Numerical Investigation of Fan Performance in a Forced Draft Air-Cooled Condenser

by
Ruan Aldrich Engelbrecht

Dissertation presented for the degree of Doctor of Philosophy in the Faculty of Engineering at Stellenbosch University

Supervisor: Prof. C.J. Meyer
Co-supervisor: Prof. S.J. van der Spuy

December 2018

Declaration

By submitting this dissertation electronically, I declare that the entirety of the work contained therein is my own, original work, that I am the sole author thereof (save to the extent explicitly otherwise stated), that reproduction and publication thereof by Stellenbosch University will not infringe any third party rights and that I have not previously in its entirety or in part submitted it for obtaining any qualification.

Date: December 2018

UNIVERSITEIT·STELLENBOSCH·UNIVERSITY
jou kennisvennoot • your knowledge partner

Plagiaatverklaring / Plagiarism *Declaration*

1 Plagiaat is die oorneem en gebruik van die idees, materiaal en ander intellektuele eiendom van ander persone asof dit jou eie werk is.
Plagiarism is the use of ideas, material and other intellectual property of another's work and to present it as my own.

2 Ek erken dat die pleeg van plagiaat 'n strafbare oortreding is aangesien dit 'n vorm van diefstal is.
I agree that plagiarism is a punishable offence because it constitutes theft.

3 Ek verstaan ook dat direkte vertalings plagiaat is.
I also understand that direct translations are plagiarism.

4 Dienooreenkomstig is alle aanhalings en bydraes vanuit enige bron (ingesluit die internet) volledig verwys (erken). Ek erken dat die woordelikse aanhaal van teks sonder aanhalingstekens (selfs al word die bron volledig erken) plagiaat is.
Accordingly all quotations and contributions from any source whatsoever (including the internet) have been cited fully. I understand that the reproduction of text without quotation marks (even when the source is cited) is plagiarism.

5 Ek verklaar dat die werk in hierdie skryfstuk vervat, behalwe waar anders aangedui, my eie oorspronklike werk is en dat ek dit nie vantevore in die geheel of gedeeltelik ingehandig het vir bepunting in hierdie module/werkstuk of 'n ander module/werkstuk nie.
I declare that the work contained in this assignment, except where otherwise stated, is my original work and that I have not previously (in its entirety or in part) submitted it for grading in this module/assignment or another module/assignment.

Studentenommer / *Student number*	**Handtekening / *Signature***
Voorletters en van / *Initials and surname*	**Datum / *Date***

Abstract

Numerical Investigation of Fan Performance in a Forced Draft Air-Cooled Condenser

R.A. Engelbrecht

Dissertation: PhD Eng (Mech)

December 2018

This study aims to develop an accurate and reliable numerical model of an Air-Cooled Condenser (ACC) using Computational Fluid Dynamics (CFD). Simplified methods for modelling the axial flow fan and heat exchanger are used to limit the complexity of the computations. The actuator disk and extended actuator disk model is presented and validated using two fans with different physical characteristics. The A-fan is an axial flow fan commonly used in industrial cooling applications and the B2a-fan is an axial flow fan developed at Stellenbosch University. The heat exchanger model is based on the A-frame heat exchanger typically used in ACCs. Validation is performed with respect to heat exchanger mechanical losses and heat transfer. The operating point of each combined fan and heat exchanger unit is determined analytically and numerically under ideal operating conditions. The results are validated by comparing the kinetic energy recovery coefficient to an experimental design from literature. A numerical recovery coefficient of 0.527 was measured compared to 0.553 measured experimentally. The axial flow fan, heat exchanger and ACC model are successfully validated.

A 30 fan ACC bank in a 6x5 configuration is analysed with regard to performance under cross-wind conditions using three different fan configurations. The ACC is subjected to four different wind speeds along five directions. Comparisons are drawn between the volumetric, thermal and overall performance using the heat-to-power ratio. The so-called A-fan ACC, B2a-fan ACC and Combined ACC are considered. Major findings indicate that the performance of an ACC decreases with increasing cross-wind speed. Superior overall performance is measured for the B2a-fan ACC resulting from a 19 % increase in performance to the A-fans on the upstream periphery. Higher thermal performance is also measured as well as 6-10 % lower power consumption than the

A-fan ACC and Combined ACC. The A-fan ACC exhibits the highest sensitivity to increasing cross-wind speeds along with the highest power consumption. Heat-to-power performance is measured 9-10 % lower than the B2a-fan ACC and 7 % lower than the Combined ACC as a result.

A comparative study between the 6x5 and 3x10 ACC layout is also presented. Wind directions leads to volumetric, thermal and overall performance differences up to 23 % for the A-fan ACC in 3x10 layout for a constant wind speed. The 6x5 layout measured differences up to 5 %. The 3x10 layout is therefore considered to exhibit a higher sensitivity to wind direction. This is attributed to the asymmetrical nature of the configuration. The A-fan ACC in 3x10 layout consumes 9.70 % more power compared to the 6x5 layout. The B2a-fan ACC consumes 6.95 % more power with similar power consumption measured for the Combined ACC.

An on-site measurement methodology for determining the fan volumetric flow rate using the measured fan power consumption and resultant blade loading along with the characteristic curves to determine the flow rate is presented. This is discussed, analysed and applied to the 30 fan ACC under cross-wind conditions. Differences in predicted volumetric flow rate up to 6.45 %, measured to the numerical results, are noted for fans not subjected to distorted inflow. Predictions for upstream periphery fans shows poor correlation with differences up to 22.81 % measured. The results do indicate that the use of the blade loading for fans subject to distorted inflow gives more accurate results for flow rate predictions compared to the power consumption.

Uittreksel

Numeries Ondersoek na Waaierwerkverrigting in ’n Geforseerde-trek Lugverkoelde Kondensor

(“Numerical Investigation of Fan Performance in a Forced Draft Air-Cooled Condenser”)

R.A. Engelbrecht

Proefskrif: PhD Ing (Meg)
Desember 2018

Die doel van hierdie studie is om ’n akkurate en betroubare numeriese model van ’n lugverkoelde kondensor (LVK) te ontwikkel deur gebruik te maak van berekeningsvloeimeganika (BVM). Die kompleksiteit van die berekeninge word verminder deur vereenvoudigde metodes vir die modellering van die aksiaalwaaier en hitteruiler te gebruik. Die aksieskyfmodel en die verlengde aksieskyfmodel word aangebied en bevestig met behulp van twee waaiers, elkeen met verskillende fisiese eienskappe. Die sogenaamde A-waaier is ’n aksiaalwaaier wat gebruik word in industriële verkoelingstoepassings, en die B2a-waaier is ’n aksiaalwaaier wat ontwerp en vervaardig is by Stellenbosch Universiteit. ’n Model vir ’n A-raam hitteruiler, wat tipies in LVKs gebruik word, word ontwikkel en bevestig met betrekking tot die hitteruiler meganiese verliese asook die hitte-oordrag. Die werkspunt van elke gekombineerde waaier en hitteruiler eenheid word analities en numeries bepaal in ideale bedryfsomstandighede. Die resultate word bevestig deur gebruik te maak van die kinetiese energie herstel koëffisiënt van ’n eksperimentele ontwerp uit die literatuur. ’n Numeriese herstel koëffisiënt van 0.527 is gemeet in vergelyking met die eksperimentele resultaat van 0.553. Die aksiaalwaaier, hitteruiler en LVK model word suksesvol bevestig.

’n LVK bank van 30 waaiers met ’n 6x5 konfigurasie word geanaliseer met betrekking tot die werkverrigting in wind toestande deur gebruik te maak van drie verskillende waaierkonfigurasies. Die LVK word blootgestel aan vier verskillende windsnelhede en vyf windrigtings. Verglykings word getrek tussen die volumetriese, termiese en algehele werkverrigtinge in die vorm van die hitte-tot-krag verhouding. Die sogenaamde A-waaier LVK, B2a-waaier LVK en die Gekombineerde LVK word oorweeg. Bevindinge dui daarop dat die werkverrigting van 'n LVK afneem met toenemende windsnelheid. Hoër algehele werkverrigting word waargeneem met die B2a-waaier LVK as gevolg van 'n 19 % verhoging in stroom-op periferie waaier werkverrigting in verglyking met die A-waaier. Hoër termiese werkverrigting word ook gemeet, asook 'n 6-10 % laer kragverbruik in verglyking met die A-waaier LVK en Gekombineerde LVK. Die A-waaier LVK vertoon die hoogste sensitiwiteit vir toeneemende windsnelhede tesame met die hoogste kragverbruik. Hitte-tot-krag werkverrigting word 9-10 % laer gemeet as die B2a-waaier LVK en 7 % laer as die Gekombineerde LVK.

'n Vergelykende studie word ook aangebied tussen die 6x5 en 3x10 LVK uitleg. Windrigting lei tot volumetriese, termiese en algehele werkverrigting verskille van 23 % vir die A-waaier LVK met 'n 3x10 uitleg vir 'n konstante windspoed. Die 6x5 uitleg toon verskille van 5 % aan. Soortgelyke termiese en algehele werkverrigting fluktuasies word opgemerk. Die 3x10 uitleg vertoon dus 'n hoër sensitiwiteit aan vir windrigting wat aan die asimmetriese aard van die konfigurasie toegeskryf word. Die A-waaier LVK met 'n 3x10 uitleg verbruik 9.70 % meer krag as die 6x5 uitleg. Die B2a-waaier LVK verbruik 6.95 % meer krag met soortgelyke kragverbruiking gemeet vir die Gekombineerde LVK met die 3x10 uitleg as die 6x5 uitleg.

'n Metingsmetodiek word aangebied om die volumetriese vloeitempo van die waaier te bepaal deur gebruik te maak van die waaier kragverbruiking en lembelasting saam met die karakteristieke kurwes. Hierdie word bespreek, geanaliseer en toegepas op die 30 waaier LVK bank in kruiswindtoestande. Volumetriese vloeitempo voorspelling verskille tot 6.45 % in vergelyking met die numeriese resultate word waargeneem vir waaiers wat nie aan inlaat vloeiversteuring kondisies blootgestel is nie. Voorspelling vir stroom-op periferie waaiers wys swak korrelasie met verskille tot 22.81 % gemeet. Die resulte dui daarop dat die lembelasting vloeitempo meer akkuraat voorspel vir waaiers wat aan inlaat vloeiversteurings blootgestel word in vergelyking met die kragverbruiking.

Acknowledgements

I would like to express my sincere gratitude to the following people:

- My parents for their unending support and motivation even though an extra 2 years were added to my academic career.
- To Prof. SJ van der Spuy and Prof. CJ Meyer for their technical advice and constant motivation over the last 4 years. The words ”give it stick” will always run through my head during hard times.
- To the CRSES for funding me throughout this project.
- To Tash, the love of my life, who has been through this process before and understood when the stress levels got high. For the prayers when it appeared that nothing worked and the celebrations when it did.
- To Christ my Saviour, through which none of this would be possible as I would have given up long ago.

Aan Tash en my familie,
dankie.

Contents

List of Figures

List of Tables

Nomenclature

Constants

$\pi =$	3.141592654
$g =$	$9.81\,\mathrm{m/s^2}$

Variables

A	Area	[m^2]
a	Variable	[ ]
b	Variable, wind coefficient	[ ]
C	Constant, coefficient	[ ]
c	Chord length	[m]
cp	Specific heat	[J/kg·K]
d	Diameter	[m]
F	Force per unit volume	[N/m^3]
f	Force	[N]
g	Gravitational constant	[m/s^2]
H	Height	[m]
h	Convective heat transfer coefficient	[$W/m^2{\cdot}K$]
i	Row number, internal energy	[ ]
K	Loss coefficient	[ ]
k	Thermal conductivity, iteration number	[W/m·K]
L	Length	[m]
M	Moment	[N/m^2]
m	Mass flow	[kg/s]
N	Rotational speed	[rpm]
n	Number	[ ]
Ny	Heat transfer parameter	[1/m]
P	Power, Openings	[W,]
r	Radius	[m]
p	Pressure	[N/m^2]

Q	Heat	[W]
Ry	Characteristic flow parameter	[1/m]
S	Source term	[ ]
T	Temperature, torque	[K, N·m]
t	Time, thickness	[s, m]
u	x-direction velocity	[m/s]
UA	Overall heat transfer coefficient	[W/m^2]
V	Volume	[m^3]
v	y-direction velocity, velocity	[m/s]
w	z-direction velocity	[m/s]

Greek symbols

α	Angle of attack, viscous loss coefficient	[^{o}]
β	Thermal expansion, relative velocity angle, porosity	[1/K,^{o}]
Γ	Diffusion coefficient	[ ]
γ	Blade angle	[^{o}]
ϵ	Effectiveness	[ ]
ζ	Blade setting angle	[^{o}]
η	Efficiency	[ ]
θ	Angle	[^{o}]
μ	Dynamic viscosity	[kg/m·s]
ν	Kinematic viscosity	[m^2/s]
ρ	Density	[kg/m^3]
σ	Blade solidity	[ ]
Φ	Energy dissipation term	[ ]
ϕ	Variable, diameter	[, m]
ω	Rotational speed	[rad/s]
∇	Laplacian operator	[ ]

Dimensionless groups

Re	Reynolds number	[ ]
Pr	Prandtl Number	[ ]

Vectors and Tensors

$\mathbf{T}$	Resistance Tensor	[ ]
$\vec{u}$	Velocity vector	[m/s]

Subscripts

0	Initial
$2D$	Two-dimensional
$3D$	Three-dimensional
a	Air
b	Blade, dimension
$bell$	Bellmouth
c	Casing, chord line, contraction, condensate
ci	Inlet contraction
cr	Chord
D	Drag
dj	Jetting
do	Downstream
E	Energy
e	Effective, exit
eff	Effective
F	Fan, flap-wise
Fid	Fan ideal
f	Friction
fr	Frontal
Fs	Fan static
H	Header duct
h	Hub
he	Heat exchanger
i	Row, inlet
In	Inertial
j	Direction
L	Lift, lag-wise
m	Mean
o	Outlet, reference
$plen$	Plenum
Qu	Heat transfer per ACC
R	Radial
r	Row, relative, radial, dimension
rec	Recovery
ref	Reference

s	Steam, dimension, static, strut, screen
si	Screen inlet
t	Tube, turbulent
tb	Tube bundle
tot	Total
ts	Tower support
up	Upstream
$Visc$	Viscous
w	Width, walkway
x	Cartesian coordinate
y	Cartesian coordinate
z	Cartesian coordinate, axial
θ	Tangential
θt	Inclined tube
$i\theta$	Inlet

Abbreviations

ACC	Air-Cooled Condenser
ACCM1	Air-Cooled Condenser Methodology 1
ACCM2	Air-Cooled Condenser Methodology 2
ADM	Actuator Disk Model
BS848	British Standard 848
CD	Central Differencing
CSP	Concentrated Solar Power
CFD	Computational Fluid Dynamics
DNI	Direct Normal Irradiance
EADM	Extended Actuator Disk Model
HTP	Heat-to-Power ratio
NTU	Number of Transfer Units
OpenFOAM	Open source Field Operation and Manipulation
RANS	Reynolds-Averaged Navier-Stokes
REEADM	Reverse Engineered Empirical Actuator Disk Model
SIMPLE	Semi-Implicit Pressure Linked Equations

Chapter 1

Introduction

1.1 Background and Motivation

The generation of electricity is typically done using the Rankine cycle as shown in figure 1.1 (van Wylen and Sonntag, 1985). Water is pumped (A) to a boiler (B) where a fuel, often coal, is used to heat water to produce steam. The steam is expanded in the turbine (C) resulting in rotation of the turbine shaft. The rotating shaft is linked to the generator (E) from which electricity is generated. The water is reused by cooling the steam in condenser units (D) in order to reduce environmental impact (Cengel and Boles, 2011).

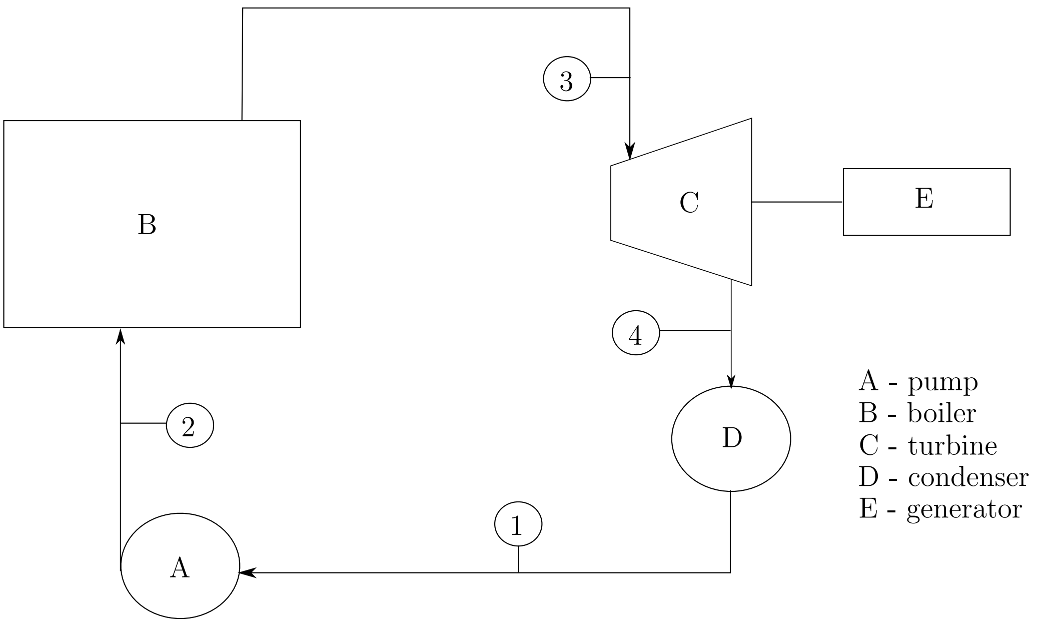

Figure 1.1: Schematic of a Rankine cycle (van Wylen and Sonntag, 1985)

The condenser units can broadly be divided into two categories based on the mechanism of cooling: *wet* and *dry*, examples of which are depicted in figure 1.2. The former is defined as the cooling of a process fluid using a combination of heat and mass transfer primarily dominated by convective heat transfer (Kröger, 1998). The process fluid is typically sprayed on packing or fill material exposing the maximum surface area to the cooling fluid, typically air. Air can enter the system either with the help of the buoyancy effect resulting in a natural draft, or with the use of axial flow fans to create a forced draft through the condensing unit. Common *wet-cooled* processes use either natural or forced-draft cooling towers. Water consumption of such a tower servicing one 600 MW(e) turbine, operating at 70 % annual capacity factor, can reach up to $10 \text{x} 10^6$ m^3. This translates to 2.5 litres per kWh(e) (Kröger, 1998).

The water requirements for such a *wet-cooling* system poses restrictions on the location where the system can be implemented. In the case where the cooling application is required in arid regions, the so-called *dry-cooling* technique can be implemented. This process involves the use of the surrounding ambient air as the heat sink where no direct contact exists between the process fluid and the cooling fluid. The capital costs of such a system is estimated to be 3.2 to 3.6 times higher than the cost of a *wet-cooled* system. A 2 % lower efficiency is also measured leading to a larger number of cooling cells required to meet the heat rejection demands (EPRI, 2004).

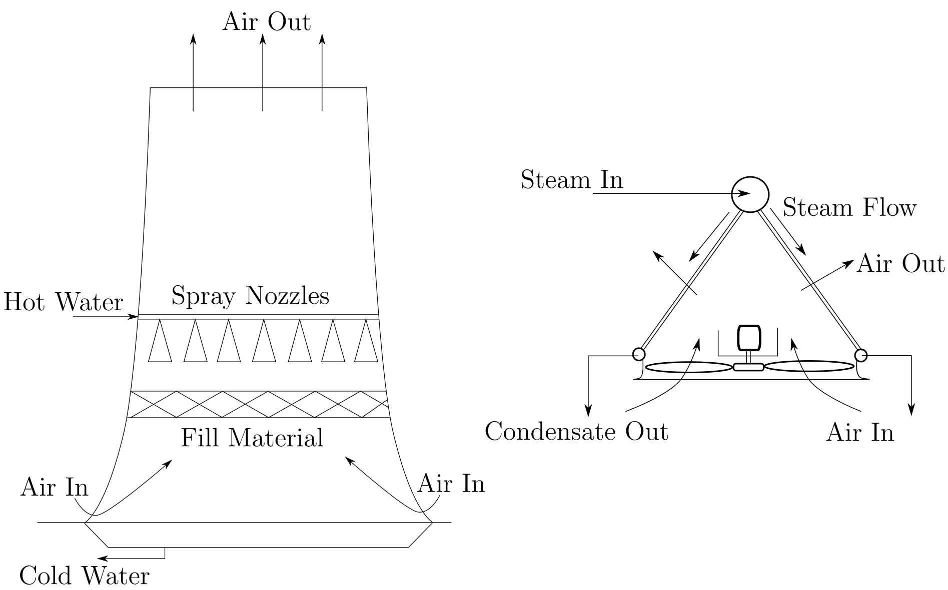

(a) Natural draft *wet-cooling* (b) Forced draft *dry-cooling*

Figure 1.2: Examples of cooling techniques

A common *dry-cooling* system makes use of the Air-Cooled Condenser (ACC) consisting of an axial flow fan used to force air through a heat exchanger carrying the process fluid. The axial flow fans can either be placed upstream of the heat exchangers in a so-called forced draft configuration or downstream of the heat exchanger in an induced draft configuration. Forced draft ACCs typically exhibit lower power consumption and lower motor running temperatures making them the preferred configuration (van der Spuy, 2011).

A typical forced draft ACC is shown schematically in figure 1.3. Air is drawn from below the platform through the fan screen into the fan inlet. The air moves through the fan and into the plenum chamber passing the walkway, fan motor and gearbox. The plenum chamber is configured in a so-called A-frame (or Delta frame) to reduce the plan surface area. The air moves through the heat exchanger bundles and is expelled into the atmosphere passing the steam duct, which serves to transport the steam from the turbine to the ACC.

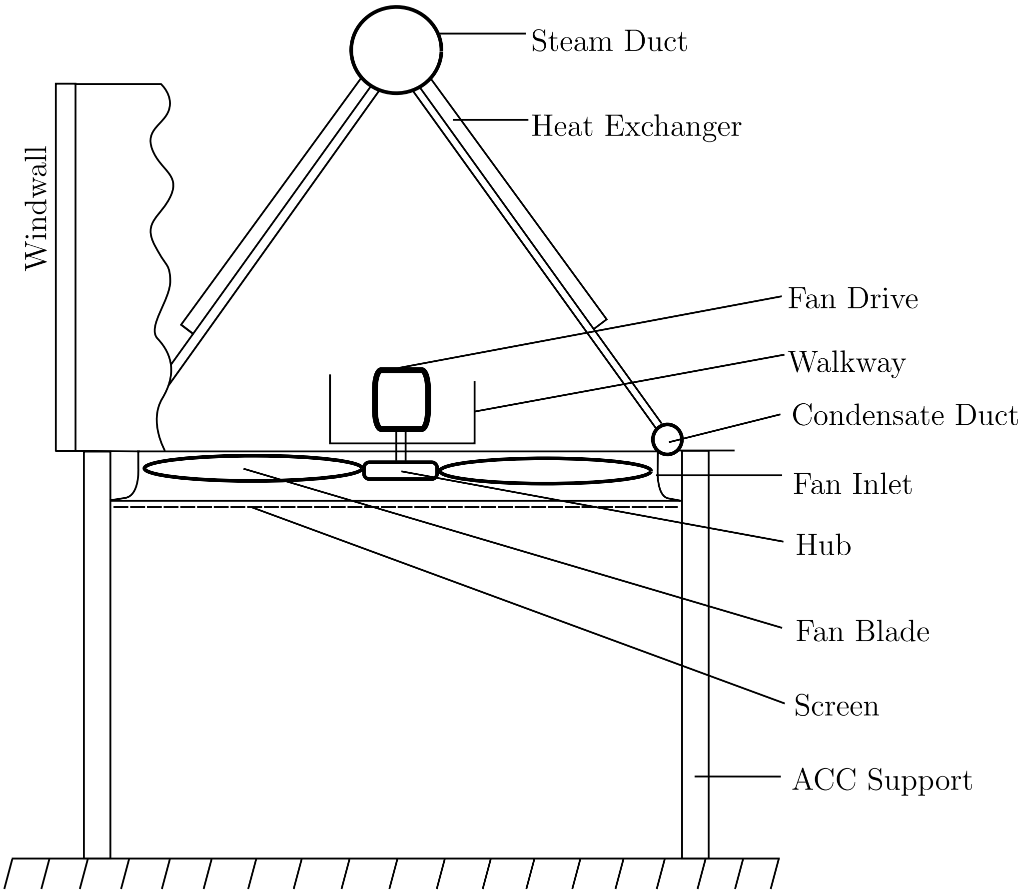

Figure 1.3: Schematic of ACC unit

Forced draft ACCs are susceptible to hot air recirculation whereby heated air is drawn back into the plenum reducing thermal performance. The addition of a windwall on the periphery is known to decrease the effect of recirculation (Monroe, 1979). Walkways and skirts on the periphery have also been shown to decrease recirculation effects (van der Spuy, 2011). Several other mechanisms affecting the performance of an ACC have also been identified. Salta and Kröger (1995) showed a direct correlation between platform height and volumetric performance of the ACC. Obstacles in the vicinity of the axial flow fan have also been shown to affect performance (Venter, 1990).

One such forced draft ACC system currently in operation is the Matimba power plant situated in Limpopo, South Africa, as shown in figure 1.4. Built by the South African electricity supply commission (ESKOM), the plant uses 288 axial flow fans, 9 m diameter in size situated approximately 45 m above ground level to service 6 x 665 MW(e) turbines (Kröger, 1998). Each fan is driven by a 270 kW electric motor with a total ACC power output rated at 65 MW (van der Spuy, 2011). The ACC bank covers a surface area of 32 300 m^2 making Matimba the largest *dry-cooled* power plant currently in operation. Two other *dry-cooled* power stations are currently under construction, namely Medupi and Kusile. Both of which house 6 x 794 MW(e) turbines serviced by an ACC system similar to the one of Matimba.

Figure 1.4: Matimba power plant showing the ACC bank

The efficient water-use of the ACC system has also contributed to an increase in potential application at large-scale concentrated solar power (CSP) plants. CSP plants are typically located in areas where the direct normal irradiance (DNI) is high and water sources are scarce. The reported inefficiency and high capital costs is, however, still seen as a significant barrier for viable use (Moore *et al.*, 2014).

The size and environmental sensitivity of an ACC presents significant challenges to design and analysis procedures. A study done by Goldschagg *et al.* (1997) at the Matimba power station indicated a drop in ACC thermal performance of 37.5 % in the presence of a westerly cross-wind measured at a speed of 6 m/s. The cooling performance of an ACC is also dependant on environmental conditions such as the drybulb temperature, which fluctuates dramatically with daily and seasonal changes (Kröger, 1998), leading to an additional design factor requiring consideration. It has also been determined that during hot or windy periods the heat rejection rate of the ACC remains constant, subsequently increasing the steam temperature and turbine back-pressure. In the case where the heat load cannot be counteracted fast enough by the system, the turbine trips (van Rooyen, 2007; van Staden, 2000). It is thus crucial to obtain an accurate and reliable representation of the performance of such an ACC system subject to different environmental conditions.

Complex flow phenomena associated with ACC performance degradation, such as hot air recirculation and flow separation at the fan inlets, resulting from cross-wind conditions are difficult to quantify due to their inherent unpredictable nature. Computational fluid dynamics (CFD) is seen as an inexpensive research tool able to model these flow phenomena. Several modelling approaches exist, the most accurate being a three-dimensional numerical model of an ACC. The computationally expensive nature has, however, seen an increase in attempts to develop simplified numerical models. The simplifications and assumptions of these models leads to inherent shortcomings and discrepancies. Balancing the shortcomings with the computational cost of each model is one of the challenges in constructing an accurate, reliable and efficient numerical ACC model.

1.2 Research Objectives

The present research builds on the pre-existing research of Thiart and von Backström (1993), Bredell (2005), Meyer (2005), van der Spuy *et al.* (2009) and Louw (2011) to investigate the performance of a 30 fan ACC using appropriate axial flow fan and heat exchanger models. The models are developed in the open source package OpenFOAM. Volumetric, thermal and overall performance of the ACC subject to cross-wind conditions is investigated. Two different fans, forming three different ACC fan combinations, along with two ACC layouts are also considered for the performance analysis.

The size of an ACC unit adds a degree of difficulty when measuring the volumetric flow rate of the axial flow fan. Modern techniques use a set of anemometers to measure the volumetric flow rate (Muiyser *et al.*, 2013; Maulbetsch and DiFilippo, 2010). This technique assumes axisymmetric flow at the outlet of the fan, which is not the case in the presence of cross-winds below the ACC (Bredell, 2005). Another technique uses the fan characteristic curves, obtained under ideal conditions, along with the fan motor power consumption to determine the volumetric flow rate. The decrease in validity of the characteristic curves, as investigated by Stinnes and von Backström (2002) under severe distorted inflow conditions, yields discrepancies when using this measuring technique under windy conditions. A new volumetric flow rate measuring methodology using the fan blade resultant bending moment is presented in this study and investigated.

The main objectives of the present study are set out as follows:

- Design and validation of an axial flow fan, heat exchanger and single ACC model
- Compare and discern performance differences measured under cross-wind conditions to the studies of van Rooyen (2007) and Joubert (2010) for a 30 fan ACC bank
- Determine and compare performance of ACCs subject to cross-wind conditions using two different axial flow fans
- Determine performance of an ACC subject to cross-wind conditions with a combination of two different axial flow fans
- Determine and compare the performance of a symmetrical and asymmetrical ACC layout subject to cross-wind conditions
- Determine the validity of using fan blade loading as a potential volumetric flow rate on-site measuring technique for axial flow fans in an ACC

Chapter 2

Literature Review

Literature is presented in chronological order focusing on the methodologies for determining the effect of distorted inlet flow conditions on the performance of an ACC. The different modelling strategies are also discussed in terms of axial flow fan, heat exchanger and ACC models. An overview of available fan blade loading experimental and numerical studies is also presented.

2.1 Air-Cooled Condensers

Monroe (1979) described the typical fan system losses which could potentially decrease efficiency in *wet* and *dry cooling* towers. The use of the fan performance curve, obtained under ideal testing conditions, and the system resistance line provides an adequate description of the fan operating point under ideal operating conditions. Monroe (1979) emphasises the correct choice of fan design such as fan diameter and fan speed to optimize fan efficiency, and to satisfy the system resistance design parameters.

Experimental tests were performed by Venter (1990) to determine the interaction between the proximity of the fan rotor and obstacles including fan safety grids, fan walkways and support beams. These interactions are defined collectively as the "system effect". Experiments were performed using a 1.5 m scale model of a commercially available fan to determine the effect of fan obstacles on the mechanical energy losses experienced by the flow passing through the fan. Mechanical energy loss coefficients were subsequently derived for use when determining fan system losses. It should be noted that fan types with different geometrical properties (hub-to-tip ratios, solidity, vortex design) were not considered.

Hot air recirculation occurs when part of the hot air plume released by the condenser bank is drawn back below the periphery cells (du Toit and Kröger, 1993), and is illustrated in figure 2.1. Building on previous research, du Toit and Kröger (1993) performed a numerical and analytical investigation on the effectiveness of the heat exchanger when recirculation occurs. The results indicate large recirculating zones present at the end of the heat exchanger cells along with a definite decrease in overall heat exchanger and volumetric effectiveness when recirculation is present. Recirculation can be mitigated by the introduction of wind walls, as well as deep plenum configurations.

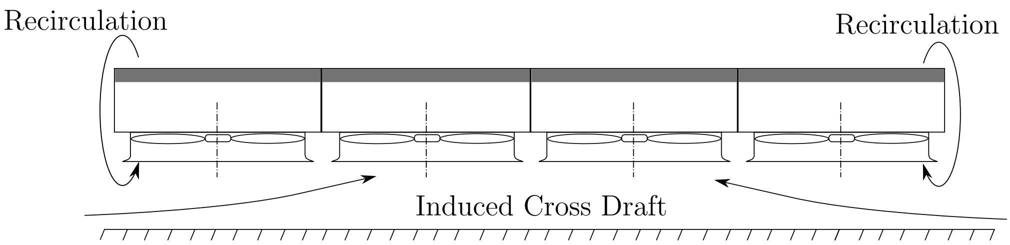

Figure 2.1: Cross-draft with recirculation at periphery of ACC

The effect of non-uniform inlet flow on the performance of ACC banks was investigated by Thiart and von Backström (1993). Neighbouring fans, buildings and cross-winds were all listed as possible reasons leading to inlet flow distortions, and is illustrated in figure 2.2. Cross-wind conditions were tested in a small-scale wind tunnel, and it was concluded that more power is required in order to achieve the same volumetric flow rate as that obtained with axisymmetric inlet-flow conditions.

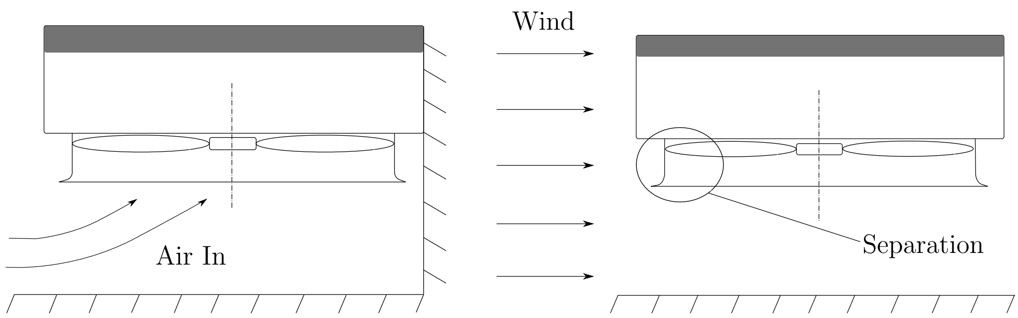

(a) Building (b) Cross-wind

Figure 2.2: Factors influencing reduction in fan performance

Salta and Kröger (1995) experimentally investigated the effect of multiple fan rows and different platform heights on the ACC volumetric flow rate. The addition of a walkway and the effect of periphery fan inlet flow distortions were also investigated. Lowering of the fan platform induced greater cross velocities at the inlet resulting in a greater degree of distortion consequently leading to a reduction in the volumetric flow rate of the ACC unit. An empirical relationship correlating the flow rate and the platform height was derived.

Duvenhage *et al.* (1996) collated data from previous studies to numerically and experimentally investigate fan inlet flow distortion effects for different platform heights and fan inlet shroud configurations. The decrease in volumetric flow rate for periphery fans was observed to be less at lower platform heights for a cylindrical inlet shroud as opposed to a conical inlet shroud. The dependence on platform height was also observed to be weaker for bellmouth inlets. The results showed good agreement with the empirical relation of Salta and Kröger (1995). The effect of increasing the cylindrical inlet shroud length was also investigated from which it was concluded that an increase in volumetric flow rate can be achieved up to a critical point. A further increase of the length results in a decrease in volumetric flow rate.

Meyer (1996) performed an experimental investigation into the aerodynamic behaviour of forced draft air-cooled heat exchangers utilising either an A-frame or normal heat exchanger configuration. Different components along with different fan types were used to formulate a set of design guidelines for an air-cooled heat exchanger. Meyer (1996) also observed a degree of kinetic energy recovery in the plenum of an A-frame heat exchanger based on the geometrical properties of the plenum and the type of fan used. This has led to Kröger (1998) classifying the plenum as a ”fan system” component due to its effect on ACC performance.

Distorted inflow conditions of axial flow fans in an ACC were investigated by Stinnes and von Backström (2002). An experimental analysis was conducted into the behaviour of axial flow fans operating under non-ideal flow conditions. Several fan types were subjected to off-axis flow and the power consumption and static pressure rise were measured. Findings indicate the fan power consumption is independent of off-axis flow up to an inflow angle of 45^o. The fan static pressure rise was also shown to be adversely affected by increasing inflow angles. These results indicate a decrease in validity of the fan characteristic curves when a fan is subject to distorted inflow conditions, as typically found in an ACC subject to cross-wind conditions.

The effect of cross-winds on inlet flow distortions was further investigated by Meyer (2005). The investigation was performed on fans at different platform heights subject to cross-winds using different inlet configurations. These include the cylindrical, conical and bellmouth inlet. A region of separated flow at the edge of the bellmouth inlet was observed resulting in a region of distorted flow upstream of the fan blades. The addition of a walkway on the periphery of the ACC bank was shown to shift the region of separation directly beneath the walkway, away from the fan inlet. This resulted in uniform flow at the bellmouth inlet and a subsequent increase in volumetric effectiveness for the periphery fans.

Van der Spuy (2011) performed an experimental and numerical analysis on the performance of fans situated on the periphery of an ACC. A multiple fan test facility was constructed with an adjustable floor as shown in figure 2.3. Moving the floor closer to the fan inlet increases the distortion of the edge fans. The addition of a walkway at the periphery of the edge fan was shown to decrease distortion at the edge fan inlet and subsequently increase fan performance. The bellmouth inlet of the edge fan was also removed with similar results reported as that of the walkway. The experimental results were compared to numerical results obtained using two different numerical fan models highlighting the shortcomings of each model. A third axial flow fan model was developed and is discussed in the following section.

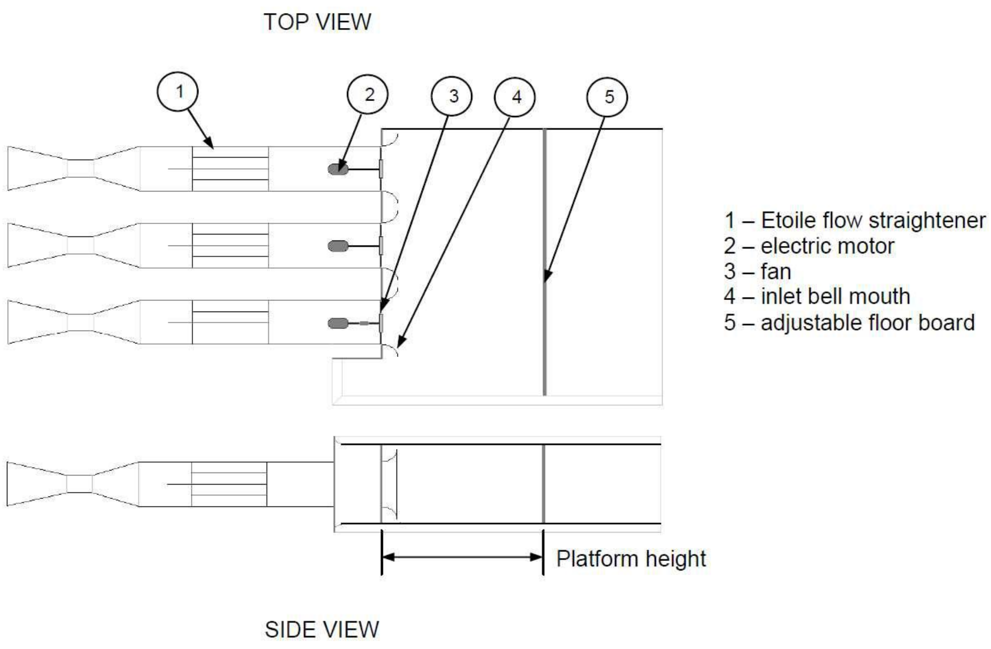

Figure 2.3: Multiple fan test facility used by van der Spuy (2011)

2.2 Fan Modelling

Three-dimensional modelling of the fan blades can be achieved with modern computing hardware. Each individual fan blade can be modelled and rotated within a reference frame to simulate flow around the blade. This modelling technique is computationally expensive requiring at least 3.5x10^6 unit cells to accurately model one fan with eight blades (van der Spuy *et al.*, 2009).

An experimental and numerical investigation performed by le Roux (2010) modelled a three-dimensional, eight bladed fan using a periodic boundary approach. The results showed good agreement to experimental results at high flow rates. Significant deviations were, however, reported at low volumetric flow rates. Several recommendations were made to address the discrepancies. Louw (2015) also modelled the same eight bladed fan as le Roux (2010) using the same approach. The numerically determined fan characteristics were validated against experimental results with a good agreement reported at all analysed flow rates. The size of the domain for both studies was in the order of 2x10^6 cells for a single blade. This illustrates the aforementioned computationally expensive nature of the three-dimensional approach and lead to the development of axial flow fan models as discussed further.

Thiart and von Backström (1993) expanded on pre-existing fan modelling techniques and developed an axial flow fan model known as the actuator disk model. Blade element theory is used to calculate the thrust and torque distributions imparted by the fan to the flow field. These are included as a force per unit volume in the Navier-Stokes equation and solved in the fan region. The model was successfully validated, however at the time it was deemed computationally too expensive and required refinement. One of the main benefits of this model is the accurate representation of the flow field immediately downstream of the fan, with tangential as well as axial velocities present in the flow field. This model was successfully implemented in a number of studies (Duvenhage *et al.*, 1996; Meyer and Kröger, 2001; Bredell, 2005; Meyer, 2005; van Rooyen, 2007; van der Spuy *et al.*, 2009)

Another model is the pressure-jump model which uses a fourth order polynomial introduced into the source term of the axial momentum equation in order to calculate a pressure at the outlet of the fan. The coefficients for the fourth order polynomial are determined from the total-to-static pressure characteristic curves determined either from experimental results or from the fan supplier data. This model does not condition the flow field at the outlet of the fan and the flow direction at the outlet is purely axial (Bredell, 2005). The popularity of this model lies in its computationally inexpensive nature and ease of implementation (Louw, 2011). The deviations reported by Stinnes and von Backström (2002) of the fan characteristics from ideal conditions subject to off-axis flow indicates a decrease in the validity of this model when analysing an ACC subject to cross-wind conditions.

Van der Spuy *et al.* (2009) performed a comparative evaluation of the pressure jump and actuator disk models for fan flow in an ACC. It was reported that the actuator disk model does not represent an accurate representation of the flow field for low volumetric flow rates due to the assumption that no radial flow is present in the model. The main findings reported a more detailed flow field with recirculation zones immediately downstream of the fan surface when the actuator disk model was used at cross-flow conditions. The pressure jump model indicated larger regions of separation at the fan inlet. Both models showed good agreement with empirical correlations at high flow rates.

The standard actuator disk model has a well documented shortcoming when predicting fan static pressure rise at low volumetric flow rates. This has led to an extensive research attempt to overcome this discrepancy. The Extended Actuator Disk Model (EADM), developed by van der Spuy (2011), is one of these models. The EADM is developed based on the results of the experimental investigation mentioned previously. The EADM extends the linear portion of the airfoil lift coefficient vs. angle of attack curve based on observations made by Himmelskamp (1945) prescribed to certain flow conditions. The drag coefficient is increased according to the lift-to-drag ratio at the corresponding angle of attack. The EADM predicts the flow characteristics at low volumetric flow rates more accurately than the standard actuator disk model. The fan static pressure rise is, however, under-predicted for flow rates well below the design flow rate.

Another model is the Reverse Engineering Empirical Actuator Disk Model (REEADM) developed by Louw (2015), also in an attempt to overcome the shortcomings of the actuator disk model at low volumetric flow rates. The main difference between the REEADM and the actuator disk model is the inclusion of the effect of the radial force on the flow downstream of the fan as the flow is predominantly radial at low volumetric flow rates (Meyer and Kröger, 2001). The radial force coefficient as well as the lift and drag coefficients were obtained from CFD simulations of a full three-dimensional fan blade. The results showed a good correlation between experimental and numerical data, however, the fan static pressure rise of the REEADM is still under-predicted for low volumetric flow rates.

2.3 Heat Exchanger Modelling

Isothermal flow losses through a small-scale A-frame heat exchanger were determined experimentally by van Aarde and Kröger (1993). The experimental set-up incorporated a process fluid duct and walkways. The effect on fluid mechanical loss of heat exchanger bundle configurations, A-frame apex angle, steam duct diameter and distance between heat exchanger bundles were determined. Correlations were derived for the total flow losses experienced by the flow based on the physical parameters of the A-frame. The correlations are still in use in the current one-dimensional analytical solution of an A-frame ACC.

Meyer and Kröger (2001) performed an experimental study to determine the effect of heat exchanger geometry on air inlet flow losses. The inlet losses of several heat exchanger geometries were determined at different flow incidence angles. The tests were also performed with the fins of the tubes aligned parallel and inclined to the incoming velocity field. The results indicate a definite correlation between geometry, fin alignment and incidence angle on the inlet air flow losses. The inlet losses are deemed independent of average air flow velocities and only dependent on the inclined angle.

van Staden (2000) modelled a heat exchanger using a porous medium configured in an A-frame configuration. The steam header duct was also included in the model. The results from the simulation of a single ACC unit was deemed inaccurate due to the pressure jump fan model not conditioning the flow field inside the plenum.

In order to reduce on computational costs, the studies of Bredell (2005), van Rooyen (2007), Owen (2010) and Louw (2011) modelled the A-frame ACC plenum in the form of the box shown in figure 2.4. The system resistance was derived in the form of a polynomial expressing the mechanical energy loss as a function of the volumetric flow rate through the heat exchanger. Significant shortcomings arise with this approach in representing an A-frame ACC. The geometrical difference between the numerical model and the A-frame give rise to incorrect flow field predictions in the plenum. The geometrical nature of the box plenum also ejects air purely in the axial direction downstream of the heat exchanger. In the case of the A-frame ACC, the orientation of the heat exchanger bundles would result in an interaction between the flow ejected from neighbouring heat exchangers as reported by van Aarde and Kröger (1993). These interactions, and subsequent effects on volumetric and thermal performance, would not have been observed by previous literature using this approach.

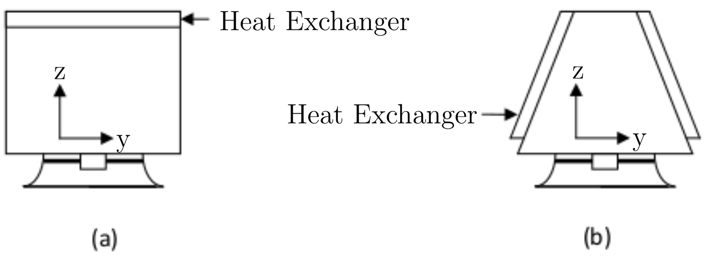

Figure 2.4: Heat exchanger represented as a) simplified and b) A-frame model (Owen, 2010)

2.4 Air-Cooled Condenser Modelling

Bredell (2005) numerically investigated the performance of two different axial flow fans in a section of an ACC bank coupled with heat exchangers using the actuator disk model. The effects of distorted inflow conditions were investigated by varying the platform height of the ACC. Findings indicated that an increase in inlet flow distortion occurs when the platform height was decreased resulting in a decrease in fan volumetric effectiveness. A performance evaluation was also performed with the addition of walkways and windscreens. The findings indicated an increase in volumetric effectiveness at the edge fans at low platform heights due to a decrease in separation at the fan inlet when walkways are installed on the peripheries. Lastly, the effect of cross-winds was modelled using an essentially two-dimensional approach. It was concluded that a two-dimensional modelling approach was not sufficient for the modelling of backflow and plume dispersion associated with the ACC, and a full three dimensional analysis would be required.

van Rooyen (2007) performed a numerical investigation into the effect of different cross-wind speeds on the volumetric performance of a 30 fan ACC using the actuator disk model. The results show a decrease in volumetric flow rate of fans in the wind upstream direction, as well as on the periphery parallel to the wind direction as the cross-wind speed increases. The reduced performance was attributed to recirculation and distorted inflow conditions. The addition of a skirt along the periphery increased the volumetric effectiveness of the fans in cross-wind conditions. It was also reported that the performance of fans in the wind downstream direction benefited from higher cross-wind speeds.

Owen (2010) investigated the flow around an ACC bank situated at El Dorado, Nevada, in the United States of America using the pressure jump model. The numerical procedure utilised a two-step iteration technique where the global flow field was coupled to the more detailed model of the ACC bank.

Increasing the power of the fans in windy conditions was investigated with the results showing an increase in performance when the fan power is increased up to 20%. Further power increase was not recommended as the net output gain of the ACC decreased.

Louw (2011) observed an increase in hot plume recirculation for increasing wind speeds across a 384 fan ACC. The effect was more pronounced with the wind direction normal to the long axis of the ACC as opposed to the short axis as more fans were exposed to inlet flow separation. The introduction of a skirt increased the volumetric flow rate through the fans situated on the periphery of the ACC as the region of separation moved away from the fan blades. The addition of an elliptical skirt, however, increased the volumetric flow rate through all cooling units. The effect of adding a screen and deflection wall was also investigated with a definite increase in overall performance observed due to the formation of a high pressure region directly below the ACC.

The approach used by Louw (2011) involved the simulation of a single fan unit and heat exchanger model under ideal conditions and comparing the results of the simulation to pre-existing fan curves for accuracy. The successful model was then used to construct a 30 fan ACC identical to the one used by van Rooyen (2007). The results of the simulation were compared to the results from van Rooyen (2007) to determine the validity of the ACC model. Once the desired accuracy was achieved, comparative studies were performed.

Several methods of decreasing inflow distortions at the fan inlet have been investigated by Dunn (2006), van Rooyen (2007), Owen (2010) and Louw (2011). These methods include the addition of screens below the ACC to improve fan performance at the wind upstream periphery. Dunn (2006) and van der Spuy (2011) investigated the effect of a periphery walkway on the volumetric performance of the periphery fans. The region of separation shifted from below the edge fan inlet to below the walkway, subsequently increasing the volumetric performance of the upstream periphery fan.

2.5 Fan Blade Loading

A numerical investigation into fan blade loading of a large scale axial flow fan was conducted by Bredell *et al.* (2006) using the actuator disk model. The blade bending moments were determined for two fans with different hub-to-tip ratios in ideal conditions, as well as different platform heights to simulate cross-winds below the ACC. The findings indicate lower resultant bending moments for the fan with a higher hub-to-tip ratio both under ideal conditions and subject to cross-wind conditions.

Muiyser *et al.* (2013) performed an on-site analysis of fan blade and gearbox shaft loading of a periphery fan at a large scale ACC. The measurements were taken using a set of strain gauges mounted at the blade neck and on the gearbox shaft. The data collection period extended over the course of five days with cross-wind speeds ranging from 2 to 20 m/s. The data collated showed a definitive correlation between fan blade loading and air flow through the fan. Larger force loads were measured at lower fan inlet volumetric flow rates. The fan blade loading was also determined to be dependent on the angle of attack of the blade. It was thus concluded that in windy periods the volumetric flow rate of the fan decreases, the distortion of the inlet air increases the blade angle of attack, and subsequently the fan blade experiences higher loads. These loads were also determined to be dependent on the azimuthal position of the fan blade. As the inlet air distortion is predominantly on one side of the fan inlet, the measured blade loading follows a cyclic nature as indicated by the blade loading vs. azimuthal position of figure 2.5.

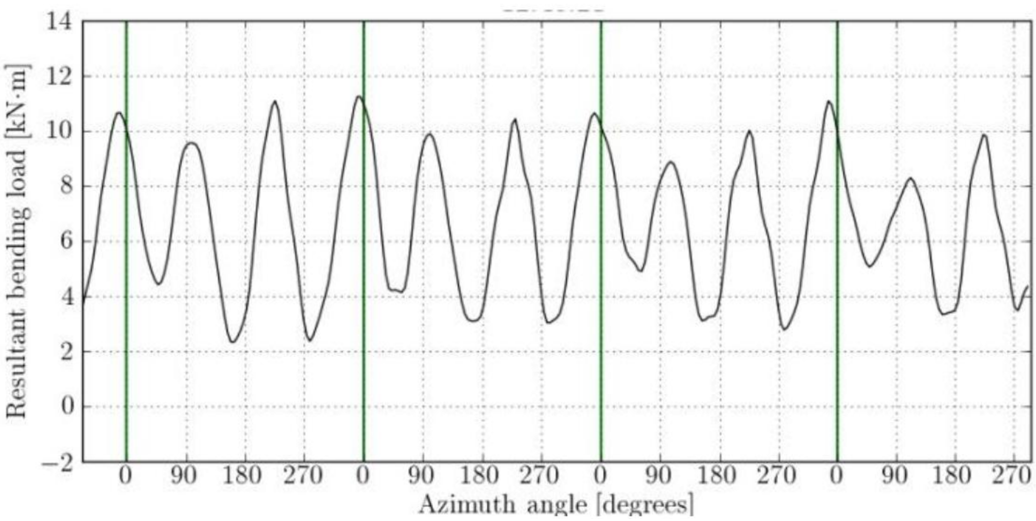

Figure 2.5: Graph showing fan blade force loading vs. azimuthal position of blade under windy conditions (Muiyser *et al.*, 2013)

Chapter 3

Numerical Model Description

CFD is defined as the analysis of, but not confined to, fluid flow and heat transfer solved using iterative procedures by means of computer simulations. This section discusses the governing equations, discretization practices and boundary conditions used in this study. A theoretical overview of the axial flow fan and heat exchanger models used and method of implementation is also discussed. The open source software package SALOME v8.0 was used for mesh generation. OpenFOAM v4.0 (Open Source Field Operation and Manipulation) was used for the CFD computations.

3.1 CFD Code Overview

3.1.1 Governing Equations

OpenFOAM solves the governing equations for fluid flow through discretization and solving of the derived linear equations. Consider the general transport equation for an unsteady, compressible system of the variable ϕ

$$\underbrace{\frac{\delta \rho \phi}{\delta t}}_{\text{transient}} + \underbrace{\nabla \cdot (\rho \vec{u} \phi)}_{\text{convection}} = \underbrace{\nabla \cdot (\Gamma \nabla \phi)}_{\text{diffusion}} + \underbrace{S_{\phi}}_{\text{source}} \tag{3.1}$$

The primary solver implemented in this study uses the Boussinesq approximation for the calculation of buoyant forces in the momentum equations. The Reynolds-averaged Navier-Stokes (RANS) governing equations derived from equation 3.1 for a steady state, incompressible solver used in the OpenFOAM models of this study are presented below.

Continuity:

$$\nabla \cdot (\bar{u}) = 0 \tag{3.2}$$

Momentum Equation:

$$\nabla \cdot (\bar{u}\bar{u}) = -\nabla \bar{p} + \nu_{eff} \nabla^2 \bar{u} + \rho_k g + F_{(u)} \tag{3.3}$$

The second last term on the right hand side is the buoyancy force derived using the Boussinesq approximation as detailed in section 3.1.4. The last term represents source terms added to the momentum equation. The effective viscosity is calculated as the sum of the kinematic viscosity and turbulent viscosity as $\nu_{eff} = \nu_0 + \nu_t$, and the bar represents a mean quantity.

Temperature Equation:

$$\nabla \cdot (\bar{T}\bar{u}) = k_{eff}\nabla^2\bar{T} + S_e \tag{3.4}$$

The last term represents a source term added to the temperature equation. The heat transfer coefficient, k_{eff}, is calculated according to:

$$k_{eff} = \frac{\nu_t}{Pr_t} + \frac{\nu_0}{Pr} \tag{3.5}$$

3.1.2 Discretization Schemes

The general transport equation shown in section 3.1.1 consists of different terms, each with its own set of discretization rules and formulations. The degree of difficulty in solving each term also differs with some, such as the convective term, posing a greater risk to stability than others. OpenFOAM provides the user with the freedom to choose an interpolation and derivative scheme for each term solved in the governing equations (OpenFOAM, 2014).

Consider the one-dimensional control volume of figure 3.1 where the term ϕ is integrated over the control volume.

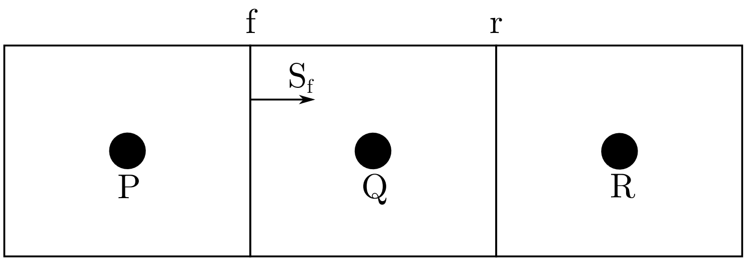

Figure 3.1: One-dimensional control volume

Applying the Gaussian theorem bounds ϕ to the cell surface in the form of integrals according to:

$$\int_V = \nabla\phi dV = \int_S dS \cdot \phi = \sum_f S_f \cdot \phi_f \tag{3.6}$$

where S_f indicates the face normal vector. The value of ϕ is required at the cell face f and as OpenFOAM stores the values of cells at the cell centres, a suitable interpolation scheme is required to determine the face value from the neighbouring cell centre values such that $\phi_f = \phi(\phi_P, \phi_Q)$. These interpolation schemes can be first order, which favours stability over accuracy such as the upwind scheme, or second order schemes which favours accuracy over stability such as the linear/central differencing scheme (CD). The discretization and interpolation scheme for each term in the governing equation requires definition. Following spatial discretization, matrices representing the linear sets of equations $Ax = b$ are formed and solved. OpenFOAM also requires specification of the linear solver used for each set of linear equations.

Table 3.1 provides an overview of the interpolation schemes used for discretisation of the gradient terms ($\nabla\phi$), the divergence terms ($\nabla \cdot \phi$) along with the respective linear solvers for each governing equation solved.

Table 3.1: Numerical solver settings

Governing Variable	**Gradient Schemes**	**Divergence Schemes**	**Linear Solver**
$\vec{u}$	2^{nd} order linear	2^{nd} order CD	Smooth solver
T	2^{nd} order linear	2^{nd} order CD	Bi-conjugate gradient
k,ϵ	2^{nd} order linear	Upwind	Smooth solver
P	least squares		Multi-grid solver

In the case of non-orthogonal meshes, where the face normal vector and the vector between the respective neighbouring cell centres do not coincide, limiting schemes are applied to increase stability. This ensures that the extrapolation of the values from the cell centres to the cell faces remain bounded to the face values of neighbouring cells (OpenFOAM, 2014). This study utilises a mesh with a combination of hexahedral and tetrahedral cells and it was thus deemed necessary to add limiting to the gradient schemes. The only gradient scheme that is not limited is the gradient of the pressure term.

Interpolation of the values in the Laplacian schemes ($\nabla \cdot (\nabla\phi)$) were all treated as second order. A correction scheme used to calculate the surface normal gradient of non-orthogonal meshes was also applied. The surface normal gradient is defined as the gradient component evaluated at the face between two neighbouring cells. Limiting of the surface normal gradient was specified as is recommended using non-orthogonal meshes (OpenFOAM, 2014).

Pressure-velocity coupling was performed with the Semi-Implicit Method for Pressure Linked Equations (SIMPLE) solver. SIMPLE is a commonly used method and uses an iterative procedure for calculating pressure-linked equations (OpenFOAM, 2014).

3.1.3 Turbulence Modelling

The realizable k-ϵ model of Shih *et al.* (1994) was used for this study. The standard k-ϵ model is the most widely used for its ability to solve thin shear layer and recirculating flows. It shows poor performance in modelling rotating and separating flow (Wilcox, 1998), which called for modifications to the model. The realizable k-ϵ model addresses these issues and provides superior performance in cases subject to these flow conditions.

The realizable k-ϵ model is presented by considering the transport equations for the turbulent kinetic energy and turbulent dissipation rate for a steady, incompressible system as:

Turbulent kinetic energy:

$$\rho(\nabla \cdot (\rho k \vec{u})) = \frac{\delta}{\delta x_j}\left[\left(\mu + \frac{\mu_t}{\sigma_k}\right)\frac{\delta k}{\delta x_j}\right] + G_k + G_b - \rho_\epsilon - Y_M + S_k \qquad (3.7)$$

Turbulent dissipation rate:

$$\rho(\nabla \cdot (\rho \epsilon \vec{u})) = \frac{\delta}{\delta x_j}\left[\left(\mu + \frac{\mu_t}{\sigma_\epsilon}\right)\frac{\delta \epsilon}{\delta x_j}\right] + \rho G_1 S_\epsilon - \rho C_2 \frac{\epsilon^2}{k + \sqrt{\nu\epsilon}}$$
$$+ C_{1\epsilon}\frac{\epsilon}{k}C_{3\epsilon}G_b + S_\epsilon \qquad (3.8)$$

The value of C_1 is defined as:

$$C_1 = max\left[0.43, \frac{\eta}{\eta + 5}\right] \qquad (3.9)$$

where $\eta = \frac{Sk}{\epsilon}$ and $S = \sqrt{2S_{ij}S_{ij}}$. The values for the constants $C_{1\epsilon}$, C_2 and the turbulent Prandtl numbers of σ_k and σ_ϵ are defined in OpenFOAM by default as:

$$C_{1\epsilon} = 1.44 \quad C_2 = 1.9 \quad \sigma_k = 1.0 \quad \sigma_\epsilon = 1.2$$

The turbulent viscosity can be calculated similar to the standard k-ϵ turbulence model:

$$\mu_t = \rho C_\mu \frac{k^2}{\epsilon} \qquad (3.10)$$

where OpenFOAM defines the value of $C_\mu = 0.09$.

3.1.4 Buoyancy Modelling

The effect of buoyancy was included using the Boussinesq approximation. The approximation assumes incompressible conditions for the continuity, momentum and temperature equations. The buoyancy effect resulting from small density variations due to temperature changes is, however, taken into account through the addition of a source term in the momentum equation.

The Boussinesq approximation can be derived according to Kays *et al.* (2005) by noting that the density is defined as $\rho = \rho(P, T)$. This can be expanded in a Taylor series:

$$\rho = \rho_\infty + \left(\frac{\delta \rho}{\delta T}\right)_p (T - T_\infty) + \left(\frac{\delta \rho}{\delta P}\right)_T (P - P_\infty) + ... \tag{3.11}$$

The last term on the right hand side can be neglected due to the small dependence of density variations on pressure differences compared to that of the first term. The volumetric coefficient of thermal expansion is defined according to:

$$\beta = -\frac{1}{\rho}\left(\frac{\delta \rho}{\delta T}\right)_p \tag{3.12}$$

Substituting equation 3.12 into the modified version of 3.11 yields the dependence of the density variation on the temperature ratio:

$$\rho = \rho_\infty (1 - \beta(T - T_\infty)) \tag{3.13}$$

OpenFOAM designates the calculated density of equation 3.13 as the kinematic density and the thermal expansion coefficient is calculated for an ideal gas according to:

$$\beta = 1/T_\infty \tag{3.14}$$

The buoyancy source term is calculated and added to the momentum equation in the form (Mills, 1999):

$$M_z = \rho_k g = g_z \frac{\rho_\infty - \rho}{\rho} \tag{3.15}$$

It must be noted that even though a density field is calculated in OpenFOAM using equation 3.13, the governing equations are still deemed as incompressible and density variations are ignored. The density used for all subsequent analytical and numerical analyses is therefore taken as 1 kg/m^3.

3.1.5 Boundary Conditions

Solving any system of linear equations requires the proper definition of boundary conditions for each set of equations. The boundary conditions specified in OpenFOAM can be classified either as a Neumann or Dirichlet boundary condition.

The boundary conditions used by the current study include:

1. **Fixed velocity boundary:** The inlet boundary condition is used to specify the inlet velocity vector of the flow domain. This is considered as a Dirichlet boundary condition and requires definition for all three momentum equations.

2. **Zero gradient pressure boundary:** The pressure inlet boundary is maintained as a Neumann condition by specifying it as a zero gradient boundary. This allows the value of the pressure to vary across the boundary.

3. **Fixed total pressure boundary:** To imitate an atmospheric boundary the value of the total pressure is fixed to a value coinciding with the atmospheric pressure. Accurate representation of the flow field requires these boundary conditions to be applied to areas of fully developed flow where large and inconsistent gradients in the flow field are not present.

4. **Wall:** The boundary conditions typically applied to a wall include a no/zero-slip boundary condition for velocity where the viscous shear stresses are calculated using predefined empirical correlations. The k-ϵ turbulence model necessitates the use of these wall functions, and the boundary conditions of the k and ϵ values on walls are specified using standard wall functions.

5. **Temperature boundary:** The temperature boundary is set as a combination of a Neumann and Dirichlet boundary. The temperature is set as a fixed value when the flux direction through the boundary is into the domain. The temperature of flow exiting the domain is set to a zero gradient boundary condition.

3.2 Numerical Models

The numerical models developed for the ACC and implemented in OpenFOAM are presented in this section. OpenFOAM provides a convenient environment for implementing custom solvers as the source code is modifiable and no external routines are required to run user defined functions.

3.2.1 Actuator Disk Model

The extended actuator disk model of van der Spuy (2011) was chosen as the axial flow fan model of this study and builds on the actuator disk model as originally developed by Thiart and von Backström (1993). The actuator disk model is therefore first discussed followed by the extended model.

The actuator disk model uses a discretized domain in the vicinity of the fan consisting of three axially aligned disks, each one cell thick. Bredell (2005) recommends placing the upstream and downstream disks half a chord length from the actuator disk. The three disks are made up of a uniform distribution of cells in the tangential and radial directions. A schematic of the actuator disk region is shown in figure 3.2.

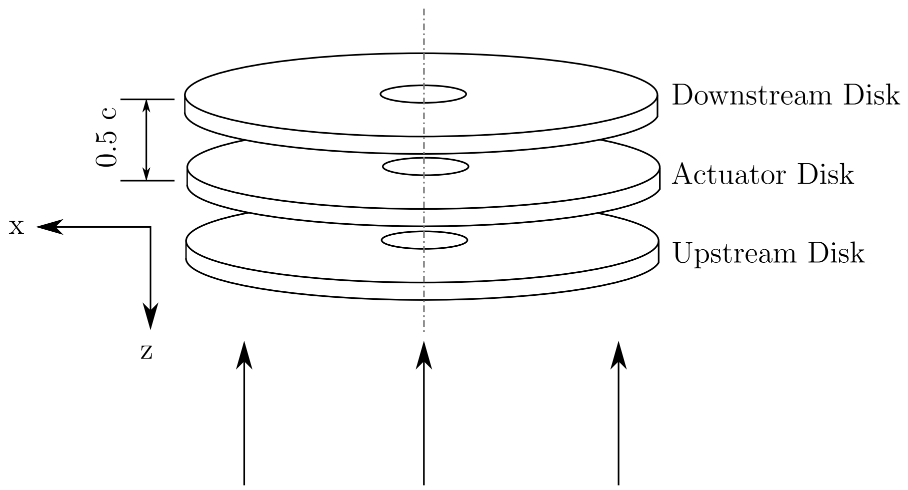

Figure 3.2: Three axially aligned disks of the actuator disk region

Blade element theory is used to calculate the source terms added to the momentum equation in the actuator disk region and is discussed by considering figure 3.3. An airfoil subject to flow experiences a lift force in a direction perpendicular to the incoming relative velocity vector. A drag force is also experienced in the direction parallel to the relative velocity vector.

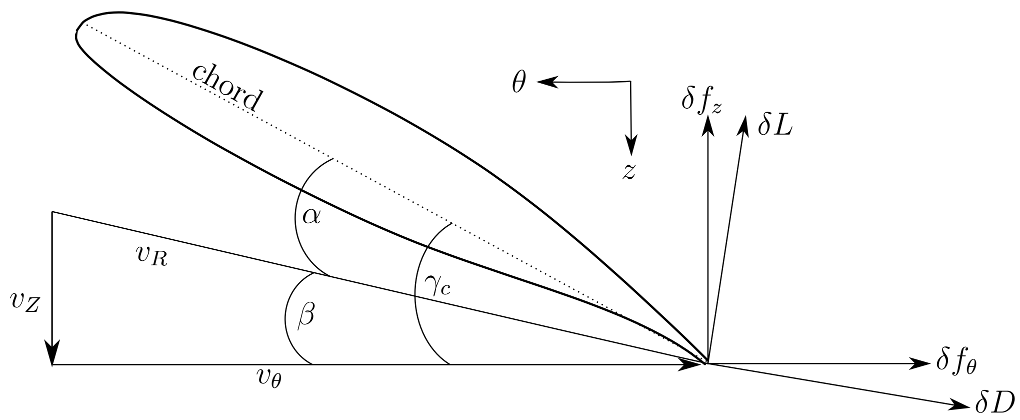

Figure 3.3: Two dimensional force components acting on airfoil

These forces can be calculated using the lift and drag coefficients:

$$\delta L = \frac{1}{2}\rho \left| v_R^2 \right| C_L c \delta r \tag{3.16}$$

$$\delta D = \frac{1}{2}\rho \left| v_R^2 \right| C_D c \delta r \tag{3.17}$$

Two axial flow fan configurations were considered for this study: a commercially available fan designated as the A-fan, and the B2a-fan originally designed by Bruneau (1994) and tested at Stellenbosch University. The physical characteristics of both fans are described in appendix A.

The lift and drag characteristics used for the A-fan were modified from those determined by Bredell (2005) using a two-dimensional numerical analysis for an angle of attack range of -90^o to 90^o. Lift and drag data outside this angle of attack range were determined from flat plate characteristics as recommended by Hoerner (1965) and Hoerner and Borst (1975). Modification of the data set was deemed necessary due to the under-prediction of power consumption as reported by Bredell (2005). The lift and drag characteristics of the A-fan only accounted for one Reynolds number as the lift and drag variation between Reynolds numbers was deemed negligible (Bredell, 2005). The characteristic graph is shown in figure 3.4.

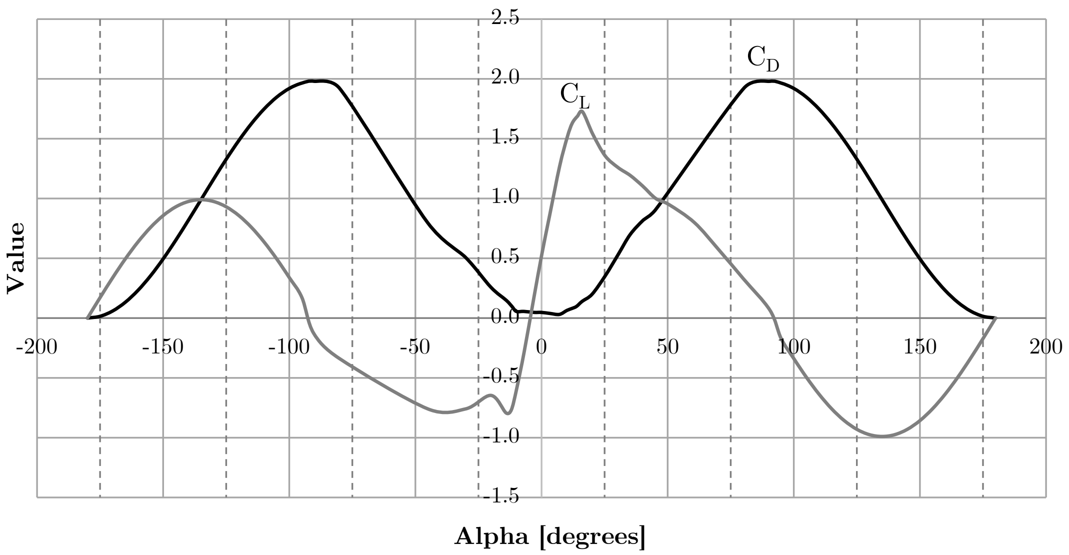

Figure 3.4: C_L and C_D distribution for the A-fan (modified from Bredell (2005))

The lift and drag characteristics of the B2a-fan were determined using data gathered from McGhee and Beasley (1979) for the NASA-LS 0413 airfoil profile. The experimental data ranged from angle of attack values of -10^o to 20^o over a set of Reynolds numbers ranging from 2x10^6 to 9x10^6. The lift and drag characteristic profile for the B2a-fan is shown in figure 3.5 for a Reynolds number of 2x10^6. The variation in Reynolds number for the lift and drag characteristics was accounted for by using a linear interpolation scheme across the Reynold data sets.

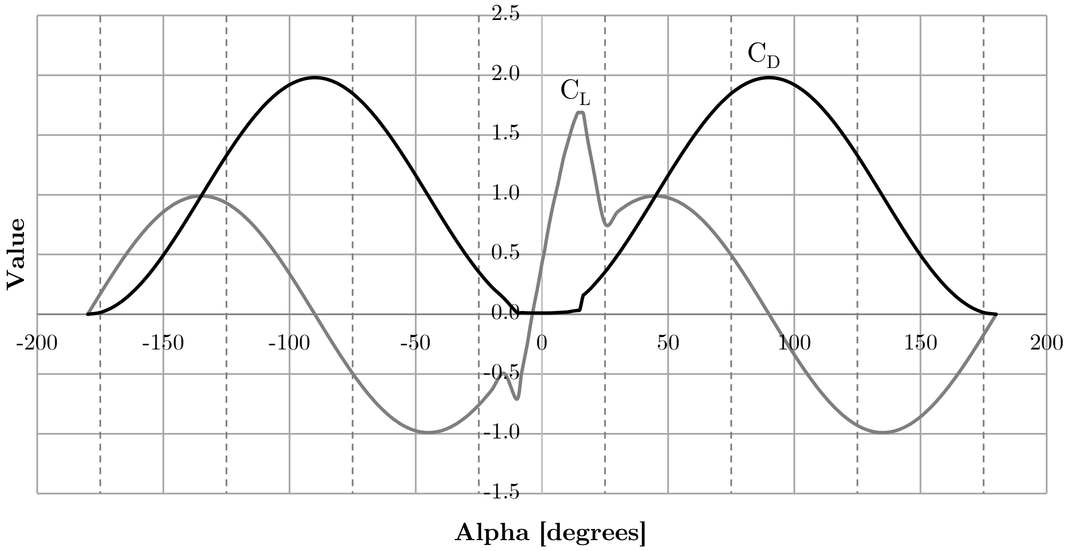

Figure 3.5: C_L and C_D distribution for the B2a-fan at Re = 2x10^6

The lift and drag data in equation 3.16 and 3.17 were determined either experimentally or numerically using flow where the velocity field was considered two-dimensional in the vicinity of the airfoil. The flow in the region of an axial flow fan, however, contains an additional tangential velocity component which reduces the validity of the determined lift and drag data (Meyer and Kröger, 2001). To compensate for this discrepancy the average velocity upstream and downstream of the actuator disk is used to calculate the relative velocity vector followed by the lift and drag forces.

The components of the relative velocity vector are used to calculate the relative velocity angle, and the angle of attack is calculated as the difference between the blade twist angle and the relative velocity vector angle:

$$\alpha = \gamma - \beta \tag{3.18}$$

The angles calculated are measured from the tangential direction as shown in figure 3.3.

The blade element in the actuator disk region exerts a force equal in magnitude but opposite in direction to the experienced lift and drag forces on the flow field. These forces are written in terms of the lift and drag forces according to:

$$\delta f_x = \delta L cos\beta - \delta D sin\beta \tag{3.19}$$

for the axial force and:

$$\delta f_\theta = \delta L sin\beta + \delta D cos\beta \tag{3.20}$$

for the tangential force.

These forces are introduced into the Navier-Stokes equations as source terms. It should be noted that the radial force contribution of the fan blade on the flow field is assumed to be negligible, and is neglected in the actuator disk model (Bredell, 2005). The axial and tangential forces are included as a specific force according to:

$$F_x = \frac{\delta S_x}{\delta V} = \frac{\sigma \delta S_x}{c \delta r t} \tag{3.21}$$

for the axial force. The tangential force can be expressed as:

$$F_\theta = \frac{\delta S_\theta}{\delta V} = \frac{\sigma \delta S_\theta}{c \delta r t} \tag{3.22}$$

The actuator disk model calculates the source terms for the momentum equation based on pitch averaged flow (Louw, 2015). The blade solidity is therefore calculated according to:

$$\sigma = \frac{n_b c}{2\pi r} \tag{3.23}$$

The momentum source terms can finally be calculated as a per unit volume body force by combining equations 3.19 to 3.23. The axial force is expressed as:

$$F_x = \frac{1}{2}\rho \left| v_R^2 \right| \frac{\sigma}{t}(C_L cos\beta - C_D sin\beta) \tag{3.24}$$

and the tangential force as:

$$F_\theta = \frac{1}{2}\rho \left| v_R^2 \right| \frac{\sigma}{t}(C_L sin\beta + C_D cos\beta) \tag{3.25}$$

As previously mentioned the radial force contribution is neglected:

$$F_R = 0 \tag{3.26}$$

3.2.2 Extended Actuator Disk Model

The extended actuator disk model of van der Spuy (2011) expands upon the original actuator disk model by augmenting the lift and drag characteristics of the two-dimensional airfoil in the presence of radial flow. Himmelskamp (1945) determined that the lift characteristics of a rotating blade increases in the presence of radial flow. Gur and Rosen (2005) also determined that the lift value of a rotating airfoil section lies between the non-rotating, two-dimensional and the inviscid flow solution.

This so-called Himmelskamp effect is incorporated into the actuator disk model by extending the linear portion of the airfoil lift characteristic curve for large angles of attack, as shown in figure 3.6. As proposed by Gur and Rosen (2005), the value of the two-dimensional drag coefficient is also adjusted according to the newly calculated three-dimensional lift coefficient according to:

$$C_{D3D} = C_{L3D}\left(\frac{C_{D2D}}{C_{L2D}}\right) \tag{3.27}$$

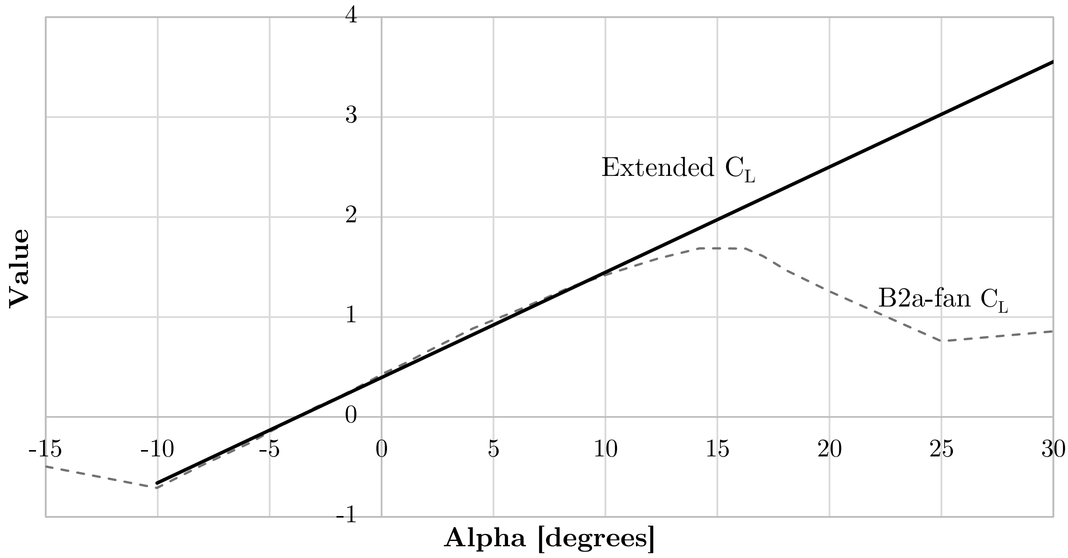

Figure 3.6: Linear extension of the lift characteristic curve for the B2a-fan

Van der Spuy (2011) noted that the suction side of the fan blade at the hub experiences stall and reverse flow at low volumetric flow rates. This decreases, and potentially nullifies, the Himmelskamp effect near the vicinity of the hub. Augmentation of the lift characteristics curve is therefore only performed above a specified radius ratio determined through an iterative procedure. The radius ratios were determined independently as the lift and drag characteristics used by van der Spuy (2011) differs from this study. The radius ratios used for the A and B2a-fan are shown in table 3.2.

Table 3.2: Radius ratio determined for the A-fan and B2a-fan

	Radius ratio
A-fan	0.45
B2a-fan	0.5

3.2.3 Heat Exchanger Model

The numerical heat exchanger model has to accurately model both the fluid and thermal dynamics of an A-frame heat exchanger. This includes changing the flow direction normal to the outlet plane, inducing a pressure drop resulting from mechanical energy losses and accurately predicting heat transfer.

Modelling the heat exchanger as an A-frame requires the use of a porous medium to force the flow in a specified direction. The fins lining the heat exchanger tubes force the flow to pass through the heat exchanger at an angle normal to the heat exchanger inlet and outlet plane. Adequate flow conditioning is thus required in order to obtain a realistic representation of the downstream flow field.

Conditioning the flow through the heat exchanger was done using the Darcy-Forchheimer principle for modelling inertial and viscous resistance in a porous medium. The flow is constrained in a direction normal to the heat exchanger inlet and outlet plane through the addition of adequate porosity. The source terms are introduced as resistance force terms calculated as:

$$F_j = -\left(C_j \frac{1}{2}\rho|\vec{u}|u_j + \frac{\mu}{\alpha_j}u_j\right) \tag{3.28}$$

where the coefficients for viscous and inertial resistance are calculated corresponding to the direction j of the flow as detailed in appendix B. This body force vector is included in the momentum equation as a source term in the heat exchanger zone.

According to van Aarde (1990), the pressure drop resulting from mechanical losses of an inclined heat exchanger can be expressed as:

$$K_{\theta t} = \frac{2\Delta p}{\rho|\vec{u_{he}}|^2} = K_f + K_e + K_{i\theta} + K_{dj} + K_o \tag{3.29}$$

which accounts for frictional, exit, inlet, jetting and outlet losses. The physical interpretation of these losses is illustrated in figure 3.7.

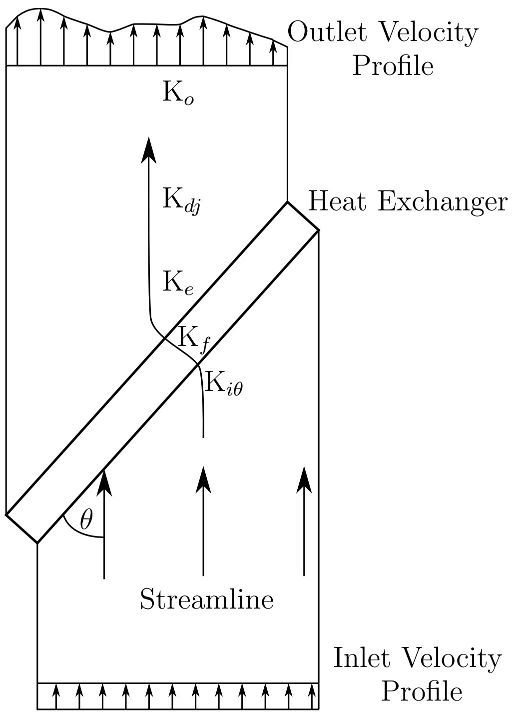

Figure 3.7: Heat exchanger analytical model

The first three terms on the right hand side of equation 3.29 can be quantified using experimental tests performed with the heat exchanger inclined normal to the flow direction ($\theta = 90^o$). The pressure loss is measured over the heat exchanger at different volumetric flow rates and converted to a mechanical loss coefficient. The newly defined heat exchanger loss coefficient, K_{he}, is expressed as a function of the characteristic flow parameter, Ry, and encompasses the frictional, exit and inlet loss coefficient according to:

$$K_{he} = K_f + K_e + K_{i(\theta=90)} = aRy^b \tag{3.30}$$

where the coefficients a and b are determined empirically.

The next loss coefficient defined is the inlet loss coefficient, $K_{i\theta}$. Mohandes *et al.* (1984) proved that for inclined finned tubes with a finite fin thickness, the inlet loss coefficient can be expressed as a function of the flow turning angle and inlet contraction loss coefficient:

$$K_{i\theta} = \left(K_c^{0.5} + \frac{1}{sin(\theta)} - 1 \right)^2 \tag{3.31}$$

The jetting loss, K_{dj}, is defined as the mechanical loss associated with the flow streamlines exiting the A-frame heat exchanger at an angle perpendicular to the heat exchanger face, and forced upwards by the presence of discharged flow from neighbouring heat exchangers (Kröger, 1998). The outlet loss, K_o, depicts losses associated with the irregular velocity profile at the outlet of the heat exchanger.

Substitution of equation 3.31 and 3.30 into 3.29 yields the following expression for modelling losses in an inclined heat exchanger:

$$K_{\theta t} = \frac{2\Delta p}{\rho|\vec{u_{he}}|^2} = K_{he}+K_{dj}+K_o+\left(\frac{1}{sin\theta_m}-1\right)\left[\left(\frac{1}{sin\theta_m}-1\right)+2K_{ci}^{0.5}\right] \quad (3.32)$$

where θ_m represents a mean flow incidence angle resulting from the flow distortion downstream of the bundle (Kröger, 1998). Meyer (2000) designated the last term on the right hand side as the mechanical loss experienced by the flow as it changes direction due to the heat exchanger fin alignment. The last loss coefficient of equation 3.32 is therefore named K_{turn} and defined as:

$$K_{turn} = \left(\frac{1}{sin\theta_m}-1\right)\left[\left(\frac{1}{sin\theta_m}-1\right)+2K_{ci}^{0.5}\right] \quad (3.33)$$

The jetting and outlet loss coefficients were not modelled in the porous region as they were accounted for by the flow field as the flow changes direction at the heat exchanger outlet. Meyer (2000) also noted that the Darcy-Forcheimmer force induces a mechanical loss over an inclined heat exchanger similar in magnitude to K_{turn} due to the flow changing direction. This suggests that the only loss coefficient which requires modelling in the porous region is that of K_{he}. This assumption was evaluated for the heat exchanger model of this study in chapter 4. A full derivation of all the loss coefficients used in this study, as detailed by Kröger (1998), is presented in appendix C.

Modelling of the heat transfer to the ambient air was performed using the effectiveness-Number of Transfer Units (ϵ-NTU) method as detailed in appendix B. A source term was included in the energy equation and calculated according to:

$$S_e = \frac{\delta Q}{\delta V} = \frac{\delta m_a}{\delta V}cp_a(T_{ao}-T_{ai}) \quad (3.34)$$

All relevant properties of the air were determined using the average of the air inlet and outlet temperatures.

The Boussinesq solver in OpenFOAM required the energy source term to be in the units of K/s. The energy source term was therefore derived and added to the temperature equation in the form:

$$S_e = \frac{S_e}{\rho_0 cp_0} \quad (3.35)$$

where the density and specific heat was calculated using the inlet air temperature.

3.3 Air-Cooled Condenser Model

The numerical model of the ACC is a combination of the axial flow fan and heat exchanger model as shown in figure 3.8 and detailed in table 3.3. The fan was up-scaled to 9.145 m and placed in a forced draft configuration to the heat exchanger. The system specifications along with the atmospheric operating conditions of the ACC are presented in appendix C.

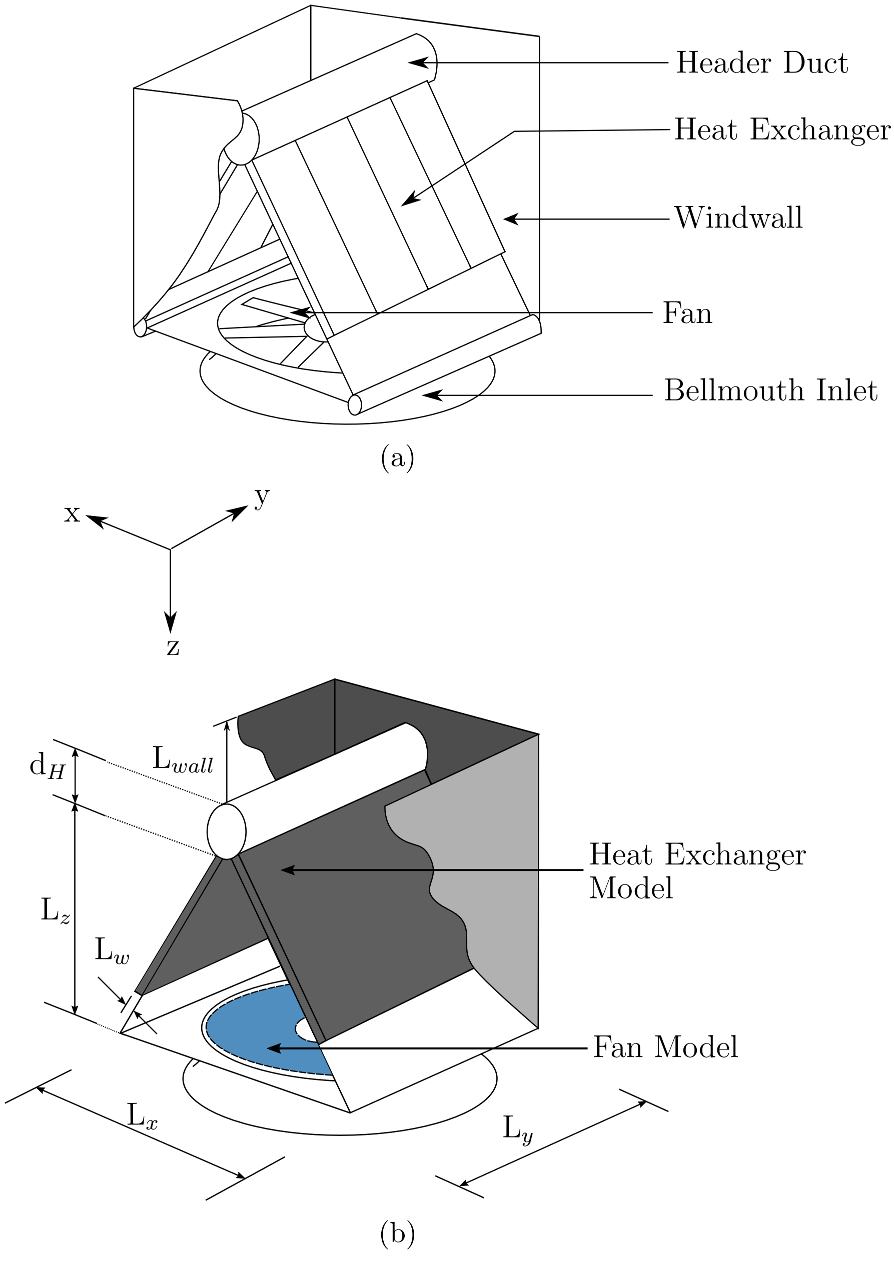

Figure 3.8: Schematic of a) ACC unit and b) numerical model with dimensions

Table 3.3: Dimensions for figure 3.8

	$\mathbf{L}_x$	$\mathbf{L}_y$	$\mathbf{L}_z$	$\mathbf{L}_w$	$\mathbf{d}_H$	$\mathbf{L}_{wall}$
Value [m]	11.8	10.56	10.03	0.24	2.34	10

The fan walkway and support struts were modelled as geometrical structures in the domain as illustrated by the schematic of figure 3.9. This differs from the approach used by Bredell (2005), van Rooyen (2007), Owen (2010) and Louw (2011). The previous studies modelled the mechanical losses of flow passing the walkway and support struts in porous regions using mechanical loss coefficients, as discussed in chapter 2.

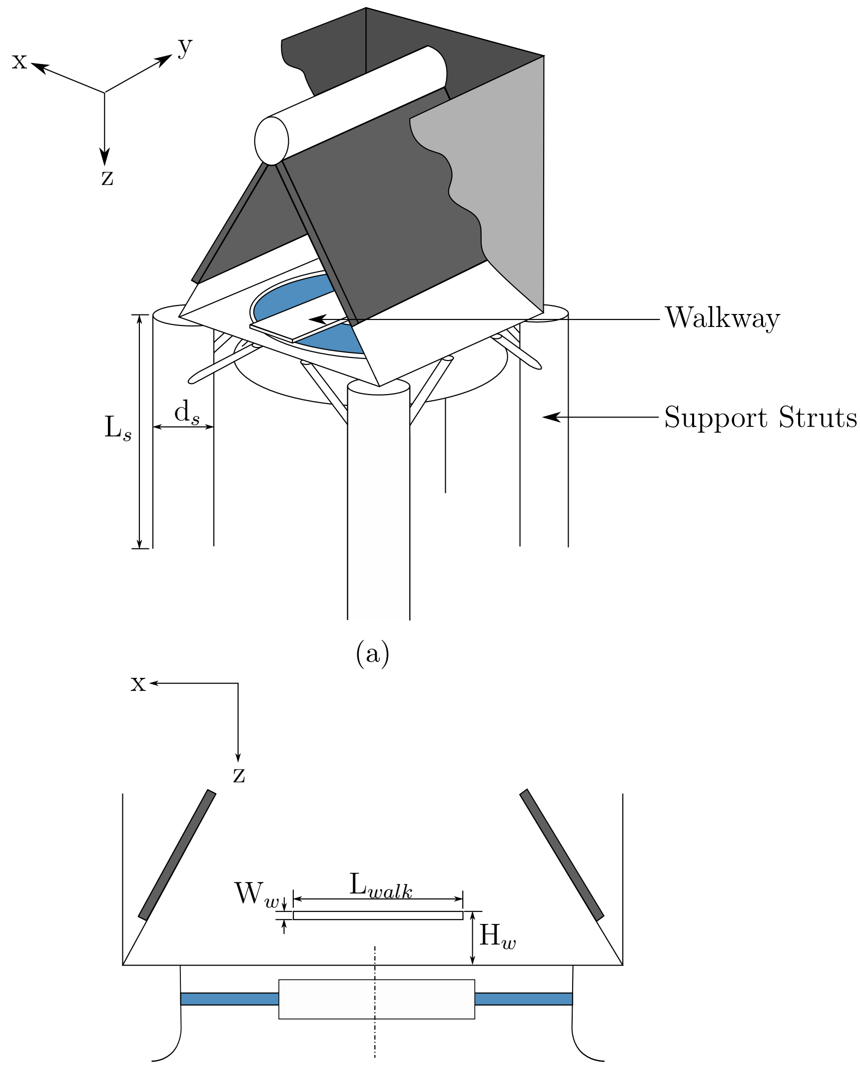

Figure 3.9: Schematic of a) numerical model with walkway and support struts and b) front view of plenum

As the flow passes through the permeable walkway a pressure drop occurs along with flow directional changes due to the mesh plate alignment. The walkway was therefore modelled as a porous region where flow was constrained to the axial direction using the previously detailed Darcy-Forchheimer force. The pressure drop over the walkway was modelled as a mechanical loss using the correlation determined by Simmons (1945) as shown below:

$$K_s = (1 - \beta_{si})/\beta_{si}^2 \tag{3.36}$$

where β_s is defined as the porosity for flow perpendicular to the screen:

$$\beta_s = (1 - d_{si}/P_{si})^2 \tag{3.37}$$

The structural characteristics of the walkway and dimensions of the ACC are indicated in table 3.4. The motor, gearbox and fan support screen were omitted from the ACC due to their relatively small, flow impeding frontal face area compared to the walkway. A comparative study between the present study modelling approach and that of previous studies is presented in appendix D and discussed in chapter 4.

Table 3.4: Dimensions for figure 3.9

	$\mathbf{L}_s$	$\mathbf{d}_s$	$\mathbf{W}_w$	$\mathbf{H}_w$	$\mathbf{L}_{walk}$	$\mathbf{d}_{si}$	$\mathbf{P}_{si}$
Value [m]	20	3	0.04	0.86	2	5e-3	20e-3

An ACC bank consisting of 30 fan and heat exchanger units was developed for comparative and performance analyses. Two different ACC bank layouts were used as shown in figure 3.10: a 6x5 layout (referred to as layout 1) and a 3x10 layout (referred to as layout 2). The analyses are presented and discussed in chapter 5 and 6.

A comparative study of ACC performance was performed using the ACCs analysed by van Rooyen (2007) and Joubert (2010) in layout 1 configuration. The lack of computer processing capacity required simplifications to be made by the previous studies. The comparative study therefore requires context through an overview of the simplifications used in the modelling procedure by each study.

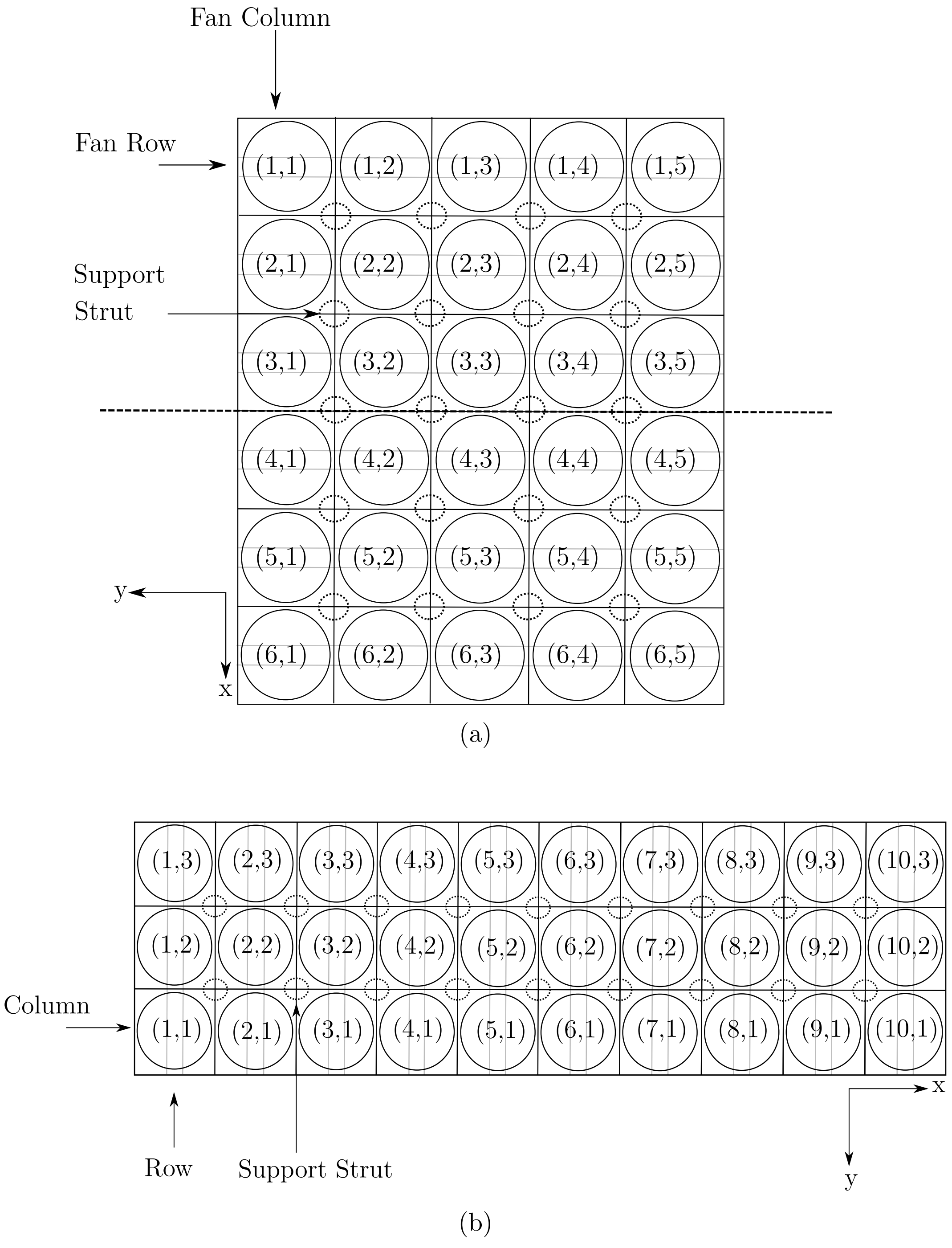

Figure 3.10: Numbering scheme used for a) layout 1 and b) layout 2 also showing the orientation of the header duct and location of support struts

These simplifications used, and which were not deemed necessary for this study, are outlined below:

- Both studies modelled the heat exchangers using box plenums.

- A symmetry plane through the ACC as shown by the dotted line in figure 3.10a was used by van Rooyen (2007). Joubert (2010) did not make use of a symmetry plane.
- Joubert (2010) made use of the pressure jump method when modelling the fan whereas van Rooyen (2007) made use of the actuator disk model.
- Only certain fans were numerically analysed by van Rooyen (2007), the fans which were not analysed were set as mass flow inlets and the mass flow was calculated using a suitable interpolation scheme. Joubert (2010) analysed all 30 fans.
- van Rooyen (2007) modelled the ACC in a separate domain as the global flow field. The two domains were coupled where the values of the global flow field were parsed as boundary condition values to the smaller domain. Joubert (2010) modelled the ACC in the global flow field.
- Both studies did not model the walkway and support struts as structures in the domain. These obstacle losses were modelled using loss coefficients in the heat exchanger porous region

3.4 Presentation of Performance Results

3.4.1 Volumetric Effectiveness

The volumetric effectiveness of a fan is presented as the ratio of the actual volume flow rate versus a specified ideal volumetric flow rate. This ratio is known as the volumetric effectiveness and is particularly useful in determining the performance of an axial flow fan subject to cross-wind conditions (Louw, 2011). It is presented in the form:

$$V_{eff} = \frac{V_F}{V_{Fid}} \tag{3.38}$$

3.4.2 Heat Transfer Effectiveness

The heat transfer through each heat exchanger is determined using the difference between the measured inlet and outlet temperatures. The heat transfer per heat exchanger, i, can be calculated as:

$$Q_{(i)} = m_{a(i)} cp_a (T_{ao(i)} - T_{ai(i)}) \tag{3.39}$$

Similar to the volumetric effectiveness, the heat transfer effectiveness for heat exchangers is determined as a ratio of the actual heat transfer of the heat exchanger versus a specified, ideal heat transfer case.

It is presented in the form:

$$\epsilon_{(i)} = \frac{Q_{(i)}}{Q_{Fid}} \tag{3.40}$$

The heat transfer effectiveness highlights the heat exchanger units which are subject to plume recirculation as well as the effect of the volumetric flow rate on the heat transfer. The total heat transfer effectiveness of the ACC can determined according to:

$$\epsilon_{Qu} = \frac{\Sigma_{i=1}^{n_F} \epsilon_{(i)}}{n_F} \tag{3.41}$$

The total heat transfer of the ACC can be determined as the sum of the individual heat exchanger heat transfer rates according to:

$$Q_{tot} = \Sigma_{i=1}^{n_F} Q_{(i)} \tag{3.42}$$

3.4.3 Power Consumption

The actuator disk model calculates the power consumption of the axial flow fan using the torque calculated by the extended actuator disk model. This provides a parameter through which performance can be measured in the form of fan power requirements. The power is calculated according to:

$$P = T\omega \tag{3.43}$$

The total power consumption of the ACC is determined as the sum of the power usage of each individual fan unit:

$$P_{Tot} = \Sigma_{i=1}^{n_F} P_{(i)} \tag{3.44}$$

3.4.4 Heat-to-Power Ratio

The heat-to-power ratio of each ACC unit is calculated as the relationship between the heat transfer rate of the heat exchanger to the power usage of the axial flow fan defined as:

$$HTP = \frac{Q_{(i)}}{P_{(i)}} \tag{3.45}$$

The heat-to-power ratio indicates combined fan and heat exchanger performance of the ACC unit. This ratio provides a parameter from which the overall performance of the ACC can be determined.

Chapter 4

Numerical Model Validation

The use of any numerical model to represent real world phenomena requires validation with a set of experimental results to ascertain the accuracy and reliability of the model. This chapter details the validation process for the axial flow fan, the heat exchanger and the ACC model.

4.1 Axial Flow Fan Model Validation

The numerical model was validated using experimental results obtained from the axial flow fan test facility at Stellenbosch University. The fan test facility shown in figure 4.1 was designed according to the British Standard 848 (BS848) and is classified as a free-inlet-free-outlet, or Type-A, facility.

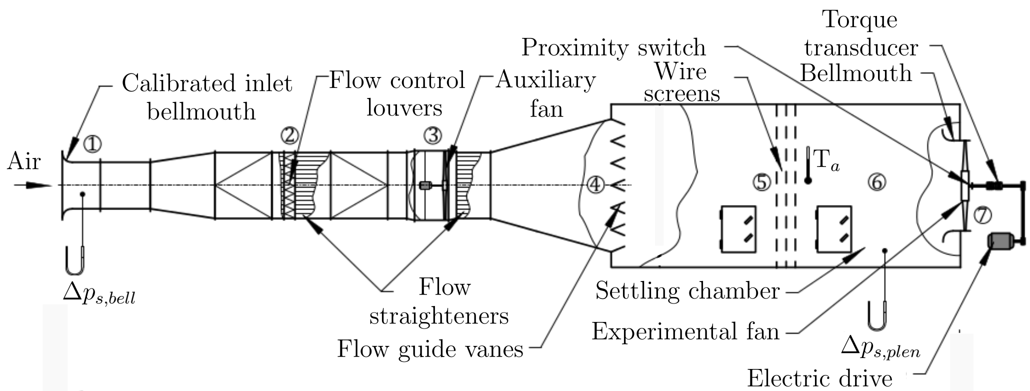

Figure 4.1: BS848 fan test facility at Stellenbosch University (Louw, 2015)

The facility allows for the testing of axial flow fans over a range of volumetric flow rates. The volumetric flow rate of air entering the test facility is measured at the calibrated bellmouth (1) and controlled by the flow control louvers (2) where after the flow is straightened through a set of flow straighteners. The auxiliary fan (3) is used to overcome the test facility system resistance.

The tangential velocity component of the flow resulting from the auxiliary fan is negated through another set of flow straighteners and flow guide vanes (4). A uniform velocity profile is attained in the settling chamber through the use of a set of wire screens (5) before entering the settling chamber (6). The inlet to the fan consists of a bellmouth (7). The air is then expelled into the atmosphere downstream of the fan.

Both fans considered for this study were validated with experimental data obtained using the fan test facility. The measured data was presented at a reference density of 1.2 kg/m^3 and an air temperature of 293.75 K. The experimental results are presented in the form of the fan characteristic performance curves in appendix A.

4.1.1 Computational Set-up

The validation process requires a computational domain and set-up resembling the fan test facility. Figure 4.2 shows the layout and dimensions of the fan test domain used for numerical validation. The dimensions correspond to the dimensions of the BS484 fan test facility used by Bredell (2005). The specifics of the boundary conditions applied to the computational domain are shown in table 4.1.

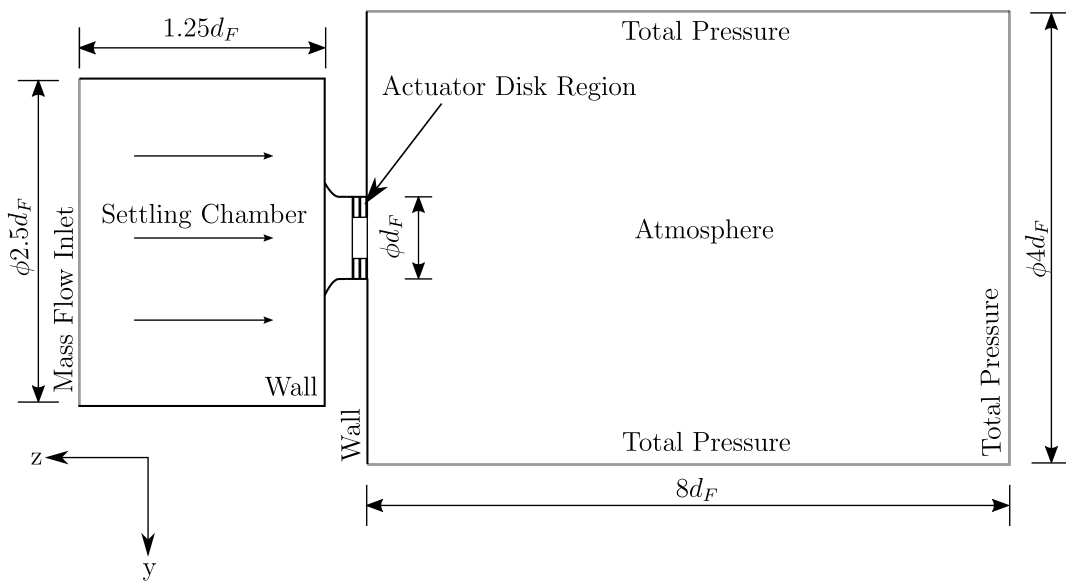

Figure 4.2: Schematic of BS848 domain along with applicable boundaries

Table 4.1: Boundary conditions used for axial flow fan validation

Boundary name	**Value**
Inlet	Velocity inlet Zero gradient pressure Turbulence intensity = 5 % Mixing length = 0.27 m
Outlet	Static pressure = 0 Pa Zero gradient velocity
Walls	No-slip walls

4.1.2 Grid Independence Study

The numerical solution for the axial flow fan model was solved on three different sized grids to determine the grid independence of the solution. Each grid focused on an increase in cell count near the axial flow fan region as well as different sized actuator disks. Van der Spuy (2011) noted negligible differences between actuator disks containing 20-30 radial, and 120-160 circumferential cells. The actuator disk of this study was discretized with 25 radial and 120 circumferential cells.

The guidelines for performing a grid refinement study as set out by Celik *et al.* for the American Society of Mechanical Engineers (ASME), defines a refinement ratio of three-dimensional grid sizes above 1.3 as good practice. In order to save on computational costs, a grid refinement ratio of between 1.4 and 1.5 was aimed for in this study. The details of each grid used for the study are detailed below:

- Case 1: consisted of $0.290 \text{x} 10^6$ tetrahedral cells and $0.033 \text{x} 10^6$ hexahedral cells. The axial length of the actuator disk was set as 15.34 mm.
- Case 2: consisted of $0.394 \text{x} 10^6$ tetrahedral cells and $0.045 \text{x} 10^6$ hexahedral cells. The axial length of the actuator disk was set as 12.27 mm.
- Case 3: consisted of $0.692 \text{x} 10^6$ tetrahedral cells and $0.083 \text{x} 10^6$ hexahedral cells. The axial length of the actuator disk was set as 9.2 mm.

The static pressure and fan power consumption, at different volumetric flow rates using the actuator disk and extended actuator disk models of the B2a-fan, were determined for each grid case. The results of the study are shown in figure 4.3 to 4.6.

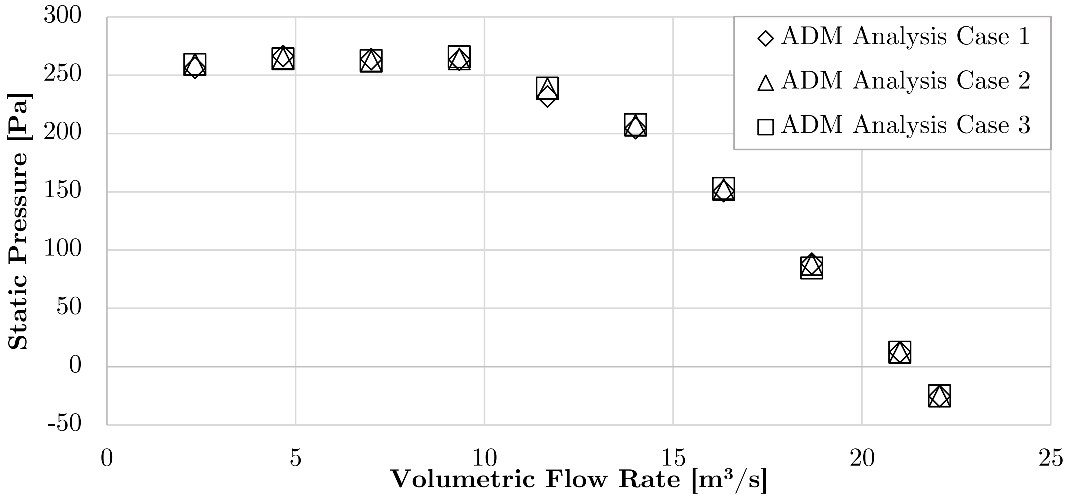

Figure 4.3: Grid analysis of static pressure rise vs. volumetric flow rate for actuator disk model (ADM) of the B2a-fan

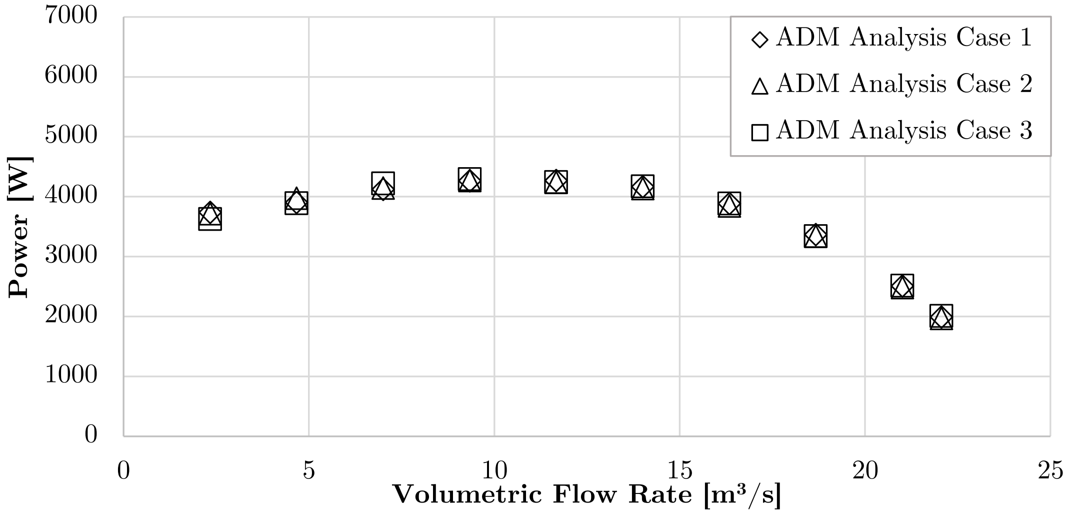

Figure 4.4: Grid analysis of power consumption vs. volumetric flow rate for actuator disk model (ADM) of the B2a-fan

The grid independence study yielded a maximum fan static pressure difference between cases of 4.39 % for the actuator disk model and 4.59 % for the extended actuator disk model. The maximum difference in power consumption was calculated as 3.10 % for the actuator disk model and 4.34 % for the extended actuator disk model. These differences are below 5 % and are thus deemed negligible. The fan static pressure and fan power consumption predictions of both axial flow fan models are therefore deemed grid independent. Grid case 2 was subsequently used for all further axial flow fan analyses of both the A-fan and B2a-fan.

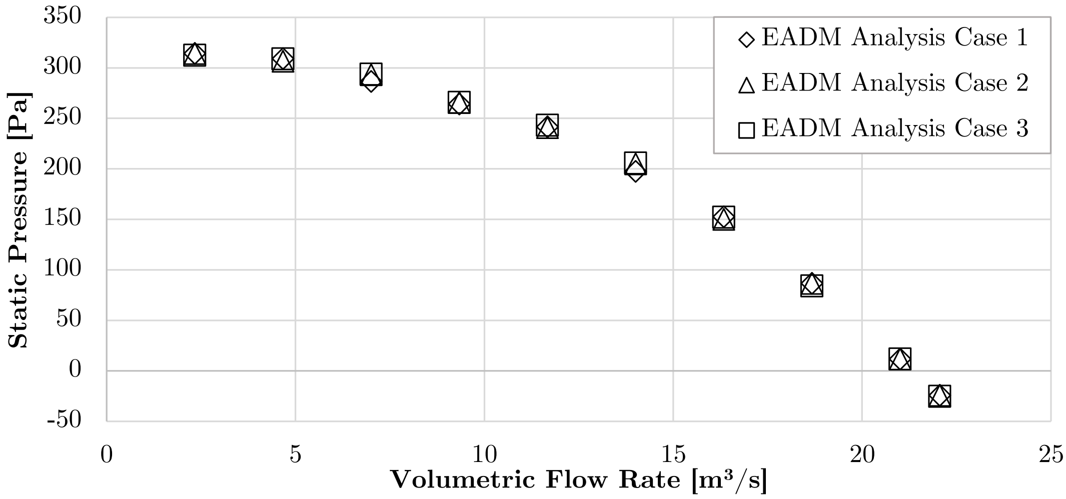

Figure 4.5: Grid analysis of static pressure rise vs. volumetric flow rate for extended actuator disk model (EADM) of the B2a-fan

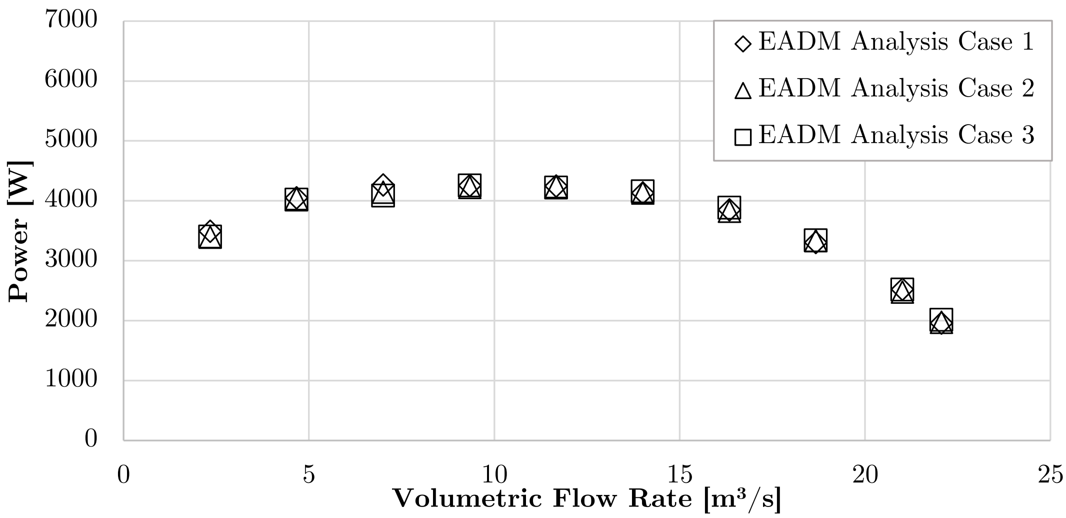

Figure 4.6: Grid analysis of power consumption vs. volumetric flow rate for extended actuator disk model (EADM) of the B2a-fan

The grid is shown in figure 4.7 and 4.8. The domain was meshed using tetrahedral cells while the actuator disk was meshed using hexahedral cells. The actuator disk was discretized using a structured mesh to facilitate data transfer for calculation of the relative velocity vector, as is deemed necessary by the model. The actuator disk region along with the positions of the upstream and downstream disks are shown in figure 4.9.

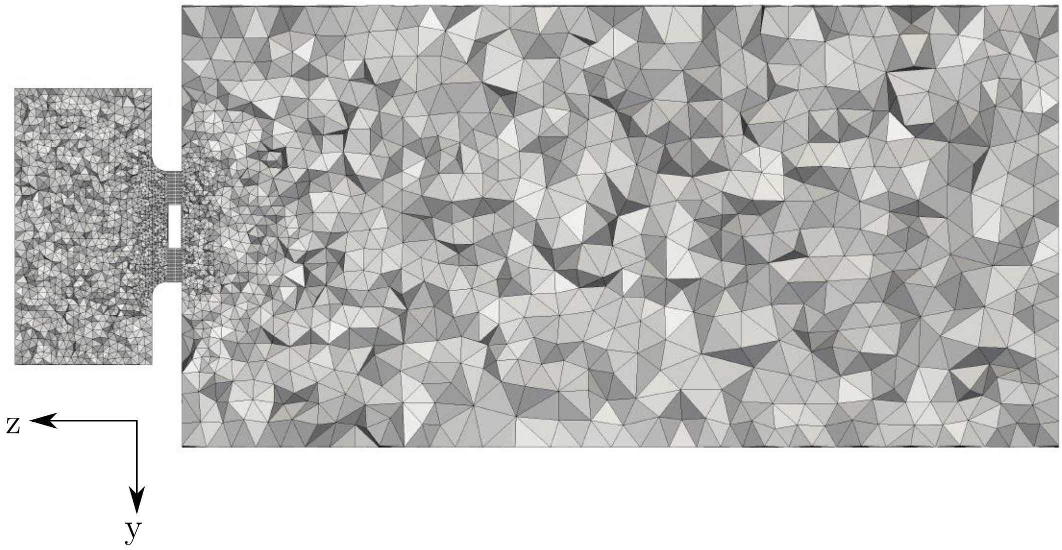

Figure 4.7: Two-dimensional section of validation domain

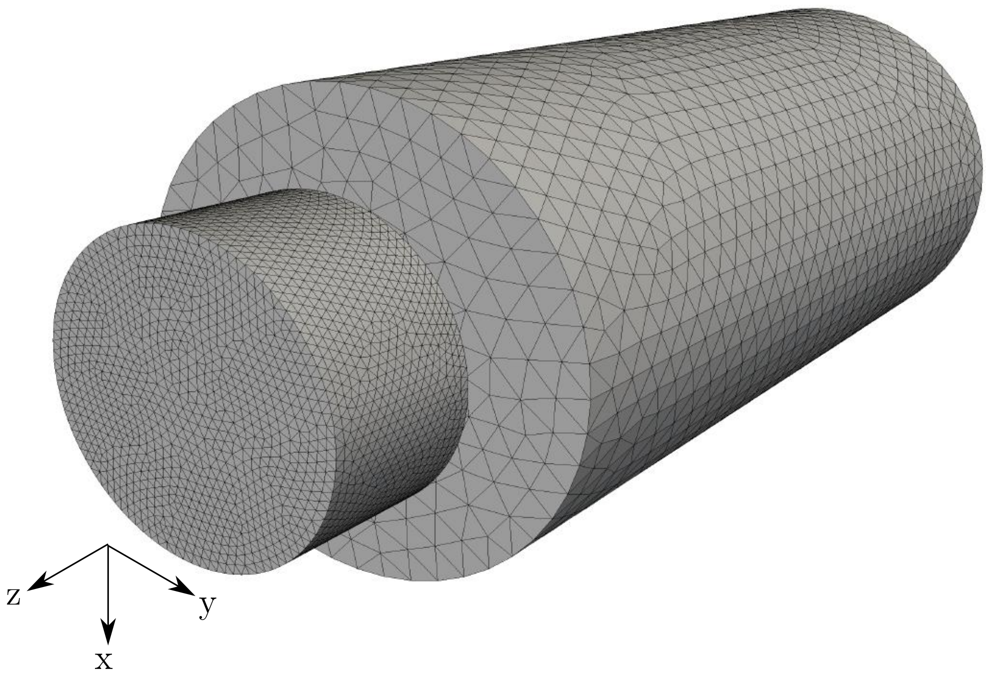

Figure 4.8: Isometric view of validation domain

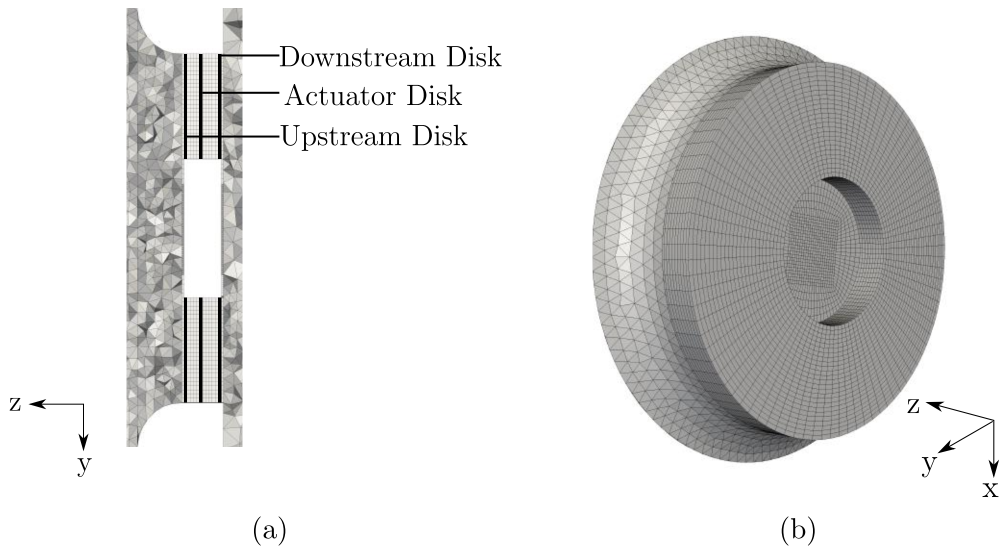

Figure 4.9: a) Two and b) three-dimensional section of B2a-fan disk region

4.1.3 Results and Discussion

The validity of the numerical model was evaluated through a comparison of the numerical and experimentally determined performance characteristics of the axial flow fan. This includes the static pressure rise and power consumption measured as a function of the volumetric flow rate. The static efficiency was then calculated. To coincide with the numerical model, the experimental results were scaled to a density of 1 kg/m^3. Figures 4.10 to 4.15 compare the A-fan and B2a-fan validation results.

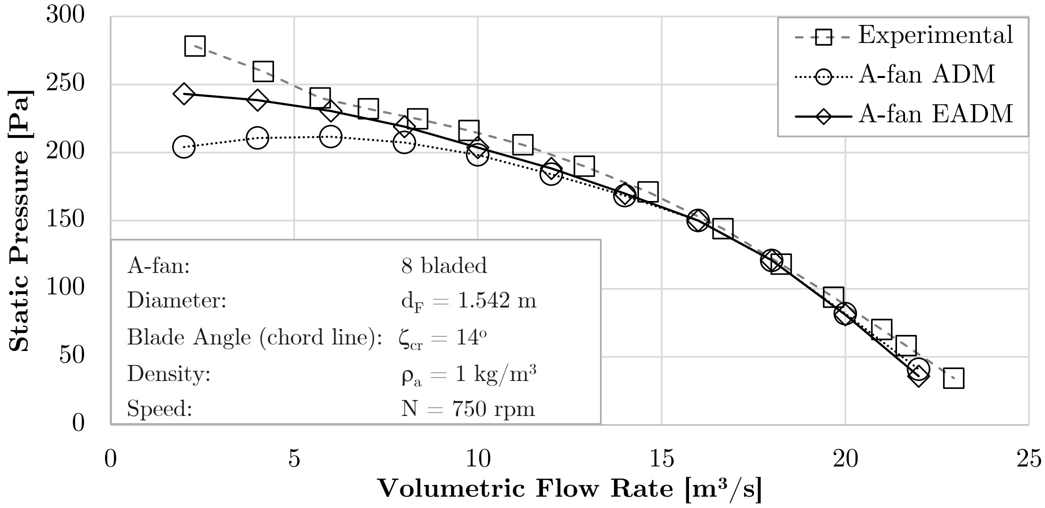

Figure 4.10: Fan static pressure vs. volumetric flow rate graph of the A-fan

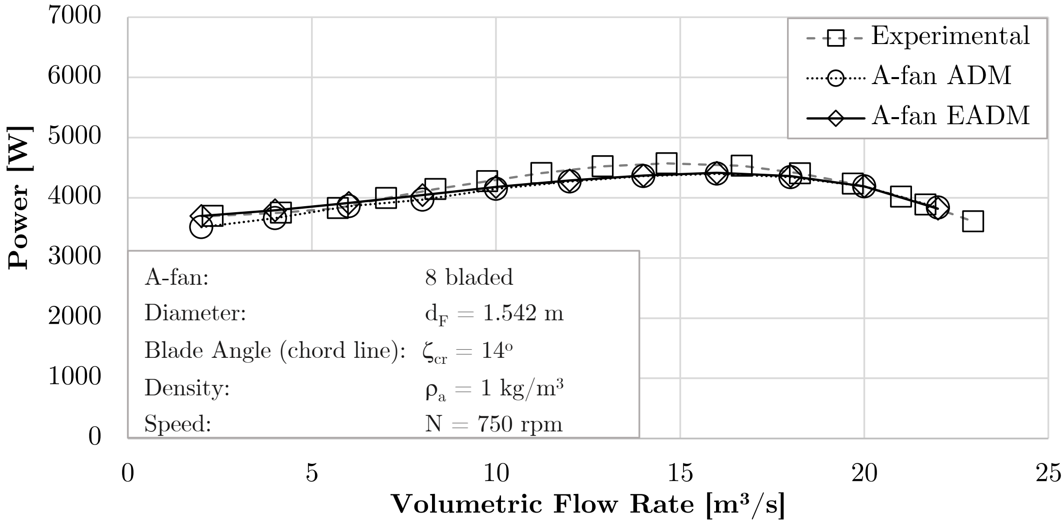

Figure 4.11: Power consumption vs. volumetric flow rate graph of the A-fan

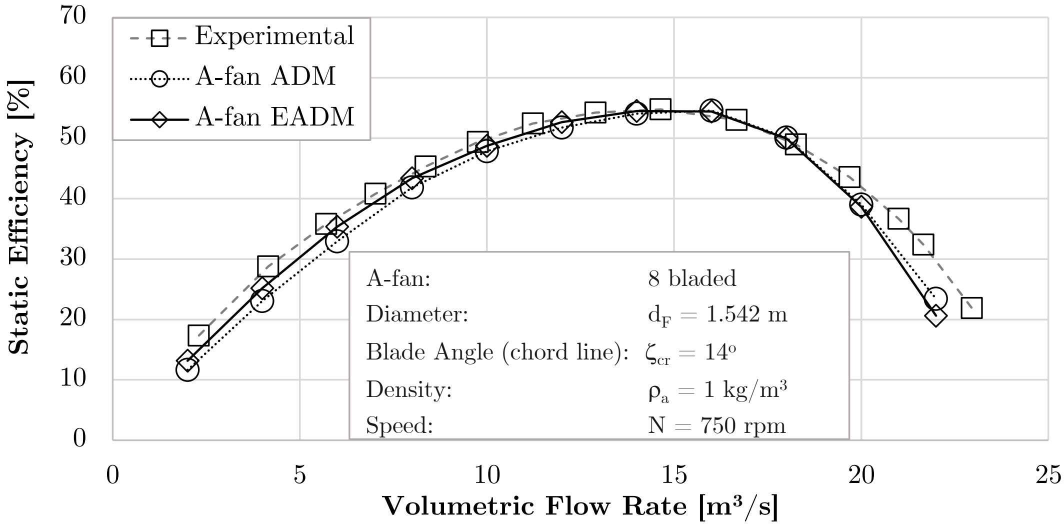

Figure 4.12: Static efficiency vs. volumetric flow rate graph of the A-fan

A good correlation is shown for the fan static pressure, power consumption and fan static efficiency for both models. Model differences are highlighted by the fan static pressure rise results. The known shortcoming of poor static rise predictions of the actuator disk model at low volumetric flow rates is observed in the case of both fans. This discrepancy is addressed by Wilkinson *et al.* (2016) and Meyer and Kröger (2001) with the most prominent factor suggested as the poor prediction of radial flow due to the omission of the radial force component. The extended actuator disk model rectifies this discrepancy and a better correlation is noted at low volumetric flow rates for both fans.

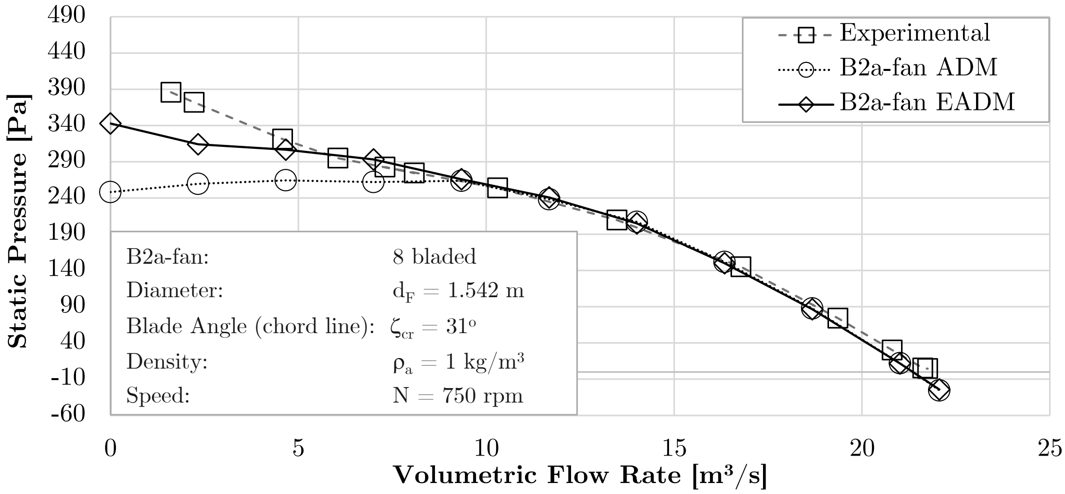

Figure 4.13: Fan static pressure vs. volumetric flow rate graph of the B2a-fan

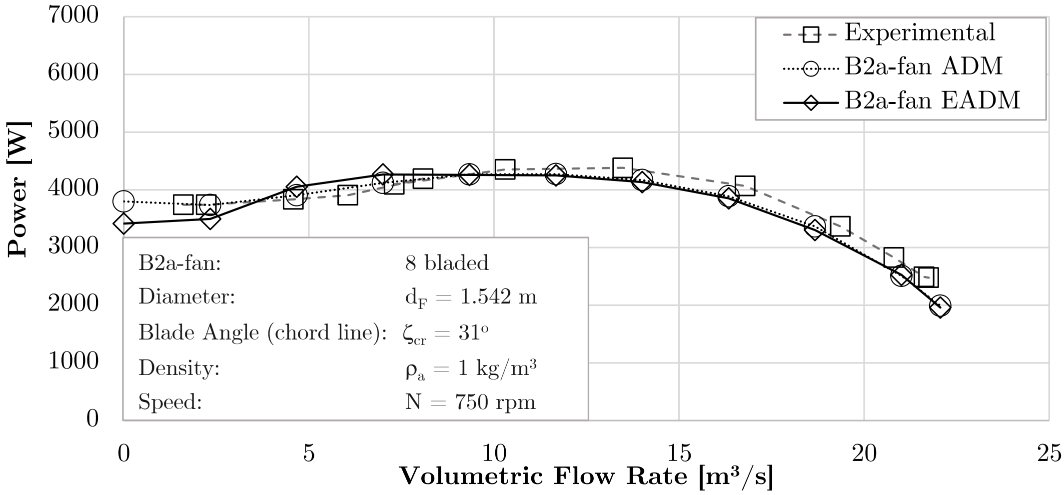

Figure 4.14: Power consumption vs. volumetric flow rate graph of the B2a-fan

The fan static pressure rise predictions of the actuator disk model indicate differences within 0.7 % for volumetric flow rates outside of the aforementioned discrepancy range. The largest difference noted for the extended actuator disk model is calculated at 15.47 % for a volumetric flow rate of 2 m^3/s in the case of the B2a-fan. This large difference between numerical and experimental results at a near zero volumetric flow rate was also observed by van der Spuy (2011) and is deemed acceptable for this study.

The A-fan and B2a-fan exhibit different flow field characteristics in the vicinity of the hub. Figure 4.16 shows the vector field of the A-fan in the vicinity of the actuator disk. A large region of recirculation forms downstream of the disk due to the small hub of the A-fan. This was also reported by van Aarde (1990) and Venter (1990) for the V-fan, which is geometrically

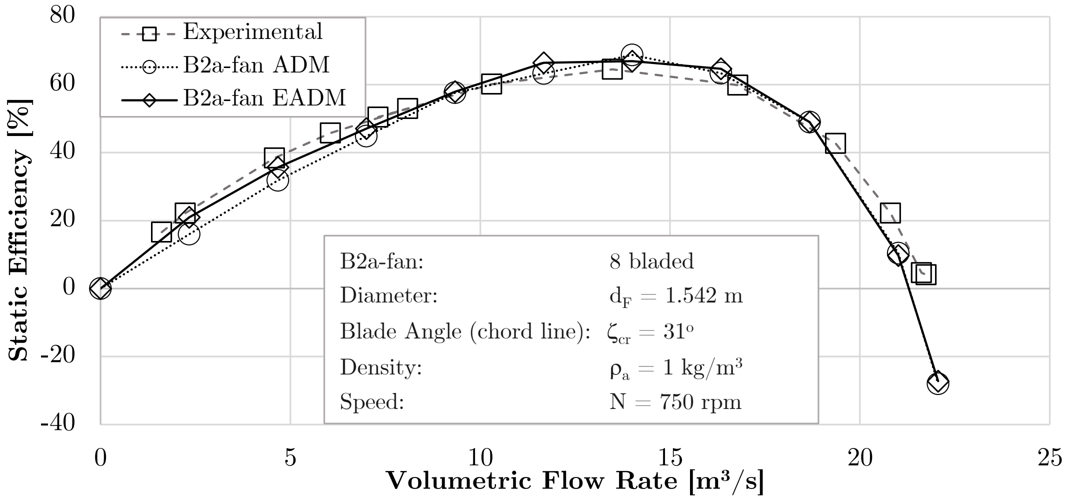

Figure 4.15: Static efficiency vs. volumetric flow rate graph of the B2a-fan

similar to the A-fan. The vector plot of figure 4.17 also indicate a region of recirculation for the B2a-fan, however, it is not as prominent as that of the A-fan. The flow is predominantly expelled in two axially aligned columns resulting from the larger hub. This was also noted by Bredell (2005).

The actuator and extended actuator disk models have been validated using experimental results in the form of the fan performance characteristic curves. The physical interpretation of the flow field in the vicinity of the axial flow fans is also consistent with previous literature.

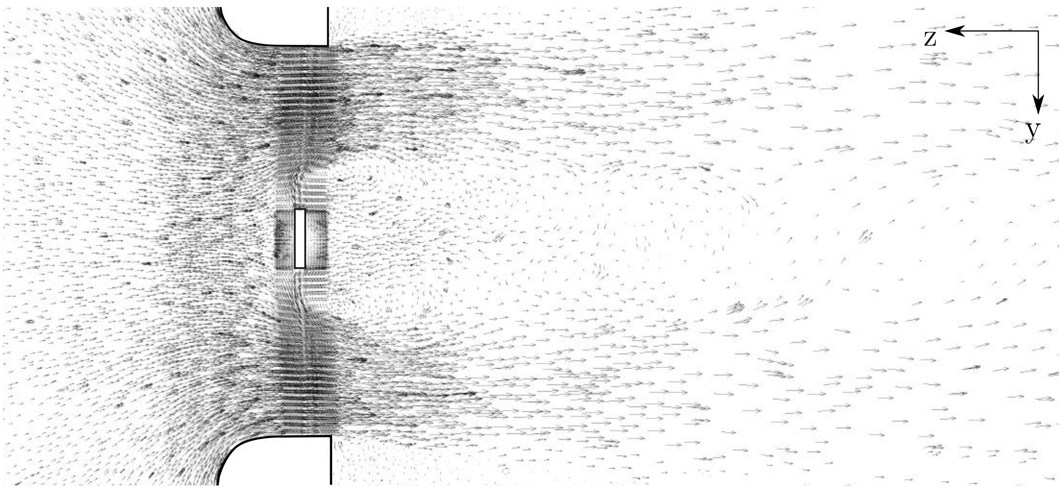

Figure 4.16: Velocity vector plot showing flow around the hub of the A-fan

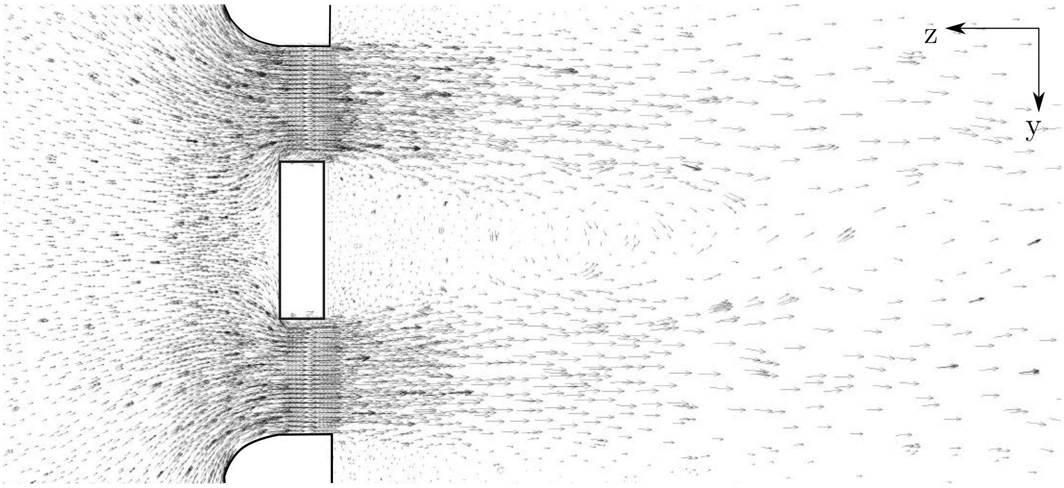

Figure 4.17: Velocity vector plot showing flow around the hub of the B2a-fan

4.2 Heat Exchanger Model Validation

The heat exchanger model was validated according to the three main components of the heat exchanger. As previously mentioned, these include the mechanical loss as the air passes through the heat exchanger, conditioning of the flow due to the fin alignment and the heat transferred to the air. The validation procedure and results are outlined below.

4.2.1 Computational Set-up

As discussed in chapter 3, development of the heat exchanger model required an evaluation procedure to determine which mechanical losses required modelling in the porous region, and which are accounted for numerically by the flow field. The procedure for evaluating the effect of the Darcy-Forcheimmer law on the heat exchanger pressure drop, as determined by Meyer and Kröger (2001), is outlined below.

Meyer and Kröger (2001) performed experimental investigations on several heat exchanger configurations to determine the contribution of the turning loss on the overall loss coefficient of the heat exchanger. The heat exchangers were placed at an angle to the incoming flow direction and the total loss coefficient was measured. The turning loss was calculated as the difference between the total measured loss (K_θ) and the loss at the same inlet air velocity in a direction normal to the heat exchanger ($K_{turn} = K_\theta - K_{\theta=90}$).

Figure 4.18a shows the computational domain used for the validation of the turning loss coefficient. The domain was modelled similar to the experimental set-up of Meyer and Kröger (2001) where the heat exchanger inclination angle θ was varied to attain a range of flow incidence angles. The inlet was set as a fixed velocity boundary of 7 m/s for all measured incidence angles. A zero gradient condition was applied for the pressure inlet boundary. The outlet pressure boundary was fixed at atmospheric conditions as stipulated in appendix C, and the velocity was set as a zero gradient condition. The sides of the domain were fixed as slip walls to ensure the mechanical energy loss measured only results from the flow directional changes. Turbulence boundary conditions were defined similar to the domain used for the axial flow fan validation, as stipulated in table 4.1.

The second validation procedure for the heat exchanger model was used to determine if the model accurately predicts the isothermal heat exchanger loss coefficient. The coefficient was derived through an experimental design whereby the heat exchanger was placed normal to the flow, and the pressure drop measured at different volumetric flow rates. The heat exchanger loss coefficient and characteristic flow parameter were calculated and an empirical correlation presented in the form:

$$K_{he} = aRy^{b} \tag{4.1}$$

This loss coefficient accounts for the frictional and exit loss associated with the heat exchanger as discussed in section 3.2.3. Similar to the experimental design, the numerical model was placed in a wind tunnel with the heat exchanger plane normal to the inlet flow direction ($\theta = 90^{o}$). The computational domain of figure 4.18b was set-up to resemble the experimental design. Similar boundary conditions of the domain used for determining the turning loss coefficients were applied. The velocity inlet boundary condition was varied, however, and the characteristic flow parameter was calculated according to equation C.5.

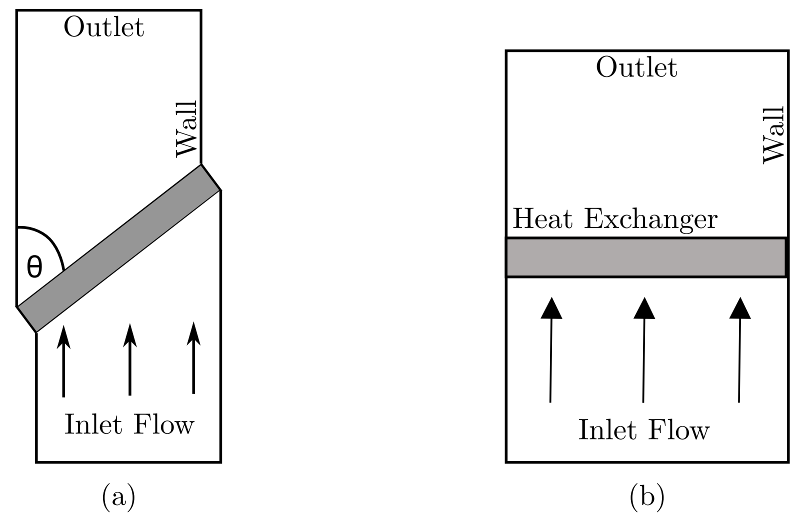

Figure 4.18: Computational domain to determine a) K_{turn} and b) K_{he}

Validation of the heat transfer was performed using an A-frame heat exchanger set-up as illustrated in figure 4.19. The numerical solution was compared to calculated heat transfer characteristics of an A-frame heat exchanger using the ϵ-NTU method as described in appendix B. The ϵ-NTU method requires heat transfer characteristics obtained through small-scale experiments using air with an axial velocity field. Even though the axial flow fan introduces a swirl component in the plenum, this uniform flow condition was used in the numerical domain of the heat exchanger model to ensure an accurate comparison to the analytical solution. Similar boundary conditions were used as the domains in figure 4.18. The inlet velocity was varied and the air outlet temperature was measured to determine the heat transfer for validation.

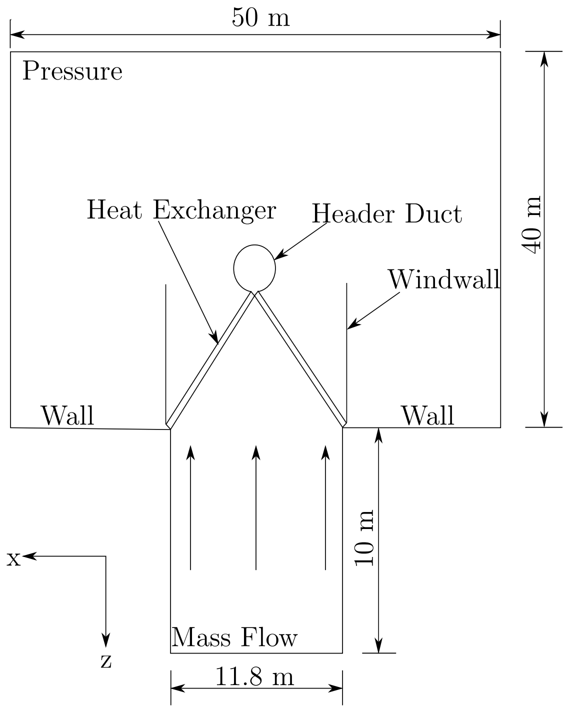

Figure 4.19: Schematic showing domain used for heat exchanger validation

4.2.2 Grid Independence Study

The domains of figure 4.18 were evaluated for grid independence using grid sizes ranging from 0.101x10^6 to 0.348x10^6 cells. The turning loss study was performed at an incidence angle of 40^o and the isothermal loss study was performed at a characteristic flow parameter value of Ry = 545 959. Differences of less than 5 % were measured and both solutions were deemed grid independent. The final domains consisted of 0.202x10^6 tetrahedral and 0.027x10^6 hexahedral cells.

A grid independence study was also performed for the heat transfer domain on grids ranging in size from 0.348x10^6 to 1.259x10^6 cells. The study was performed at a volumetric flow rate of 600 m^3/s and the heat transfer rates compared. The results are shown in table 4.2. The differences in heat transfer rates measured are small and deemed negligible. The solution is thus considered to be grid independent and the final grid consisted of 0.625x10^6 tetrahedral and 0.054x10^6 hexahedral cells.

Table 4.2: Grid independence study of heat transfer validation

Grid Size	**Heat Transfer Rate [W]**
0.348x10^6	2.347x10^7
0.679x10^6	2.310x10^7
1.259x10^6	2.282x10^7

4.2.3 Results and Discussion

The first set of results discussed is the validation of the turning loss coefficient. The heat exchanger model defines a pressure loss in OpenFOAM as:

$$\Delta p_j(U) = \frac{1}{2}K\rho|\vec{u_j}|U_j \tag{4.2}$$

where j represents the direction normal to the heat exchanger inlet plane and K being the loss coefficient. Setting the value of the loss coefficient to zero and inclining the heat exchanger to the flow direction allows for prediction of the mechanical losses purely due to the flow changing direction in the heat exchanger. The heat exchanger was inclined at an angle of 10^o, 20^o, 30^o, 40^o and 90^o to the inlet flow direction and the mechanical loss measured. This loss is associated with flow directional changes and is considered to be the turning loss coefficient.

The numerical results are compared to the experimental results of Meyer (2000) in figure 4.20 using a similar design and fin orientation as the heat exchanger of this study. It is clear that a good agreement between the numerical and experimental results exists indicating an adequate representation of the turning loss coefficient by the flow field. This substantiates the claim of Meyer (2000) that the Darcy-Forcheimmer force induces a mechanical loss as the flow changes direction. The contribution of K_{turn} should therefore not be included as a modelled loss in the porous region.

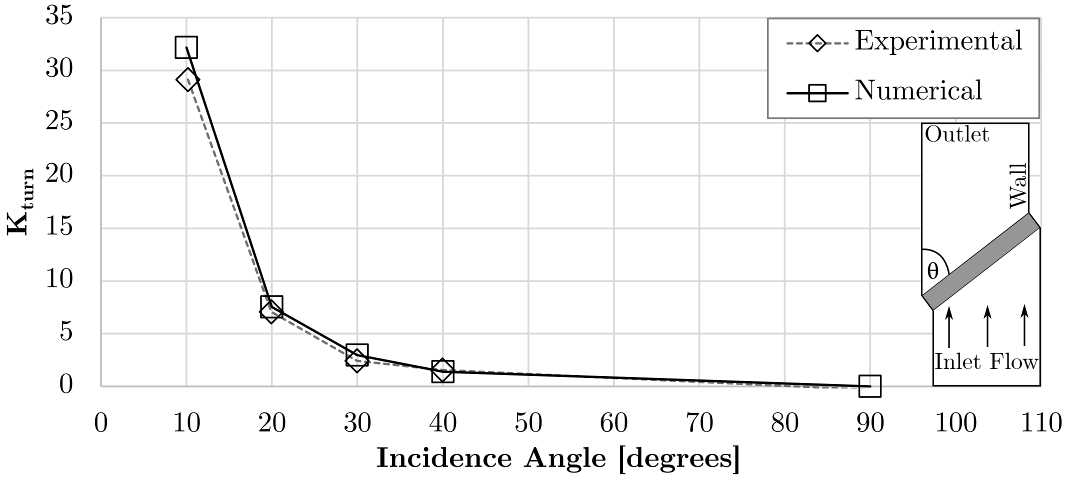

Figure 4.20: Comparison of numerical and experimental results of turning loss

Conditioning of the flow as it passed through and exited the heat exchanger was also visually validated. Figure 4.21 shows a velocity vector plot of the flow through the heat exchanger. The flow exits perpendicularly to the heat exchanger inlet and outlet plane indicating correct representation of the downstream flow field.

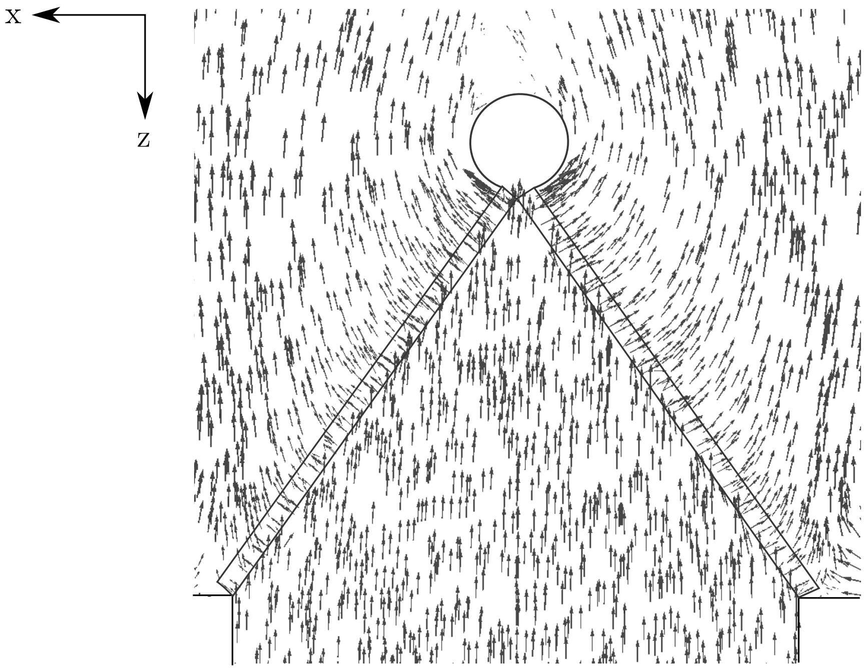

Figure 4.21: Velocity vector plot of flow through the A-frame heat exchanger

Modelling of the isothermal heat exchanger loss coefficient was validated to experimental results by varying the volumetric flow rate and measuring the pressure drop. The characteristic flow parameter and the heat exchanger loss coefficient was subsequently calculated and compared to the experimental results in figure 4.22. The experimental and numerically predicted losses correlate well indicating adequate prediction of the isothermal heat exchanger loss.

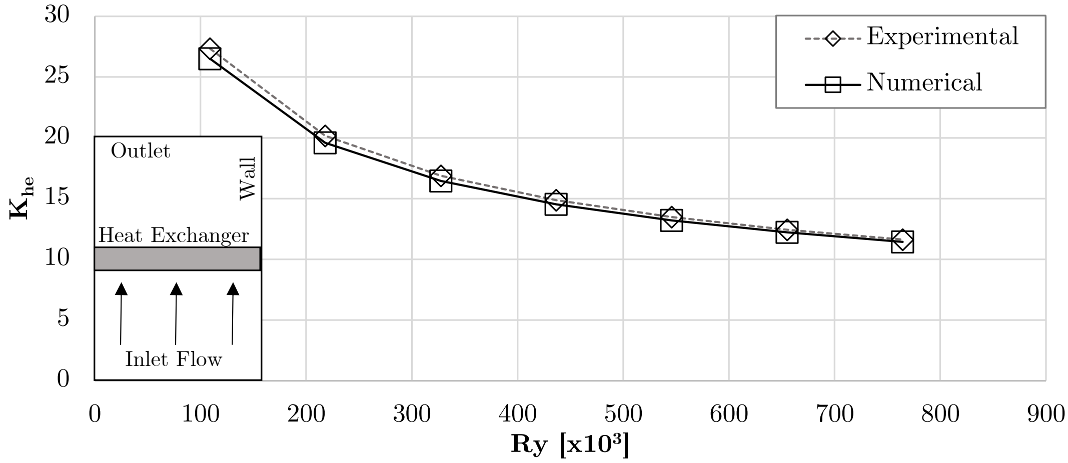

Figure 4.22: K_{he} vs. Ry experimental and numerical comparison

Finally, the heat transfer rate was compared to an analytical solution and the results are shown in figure 4.23.

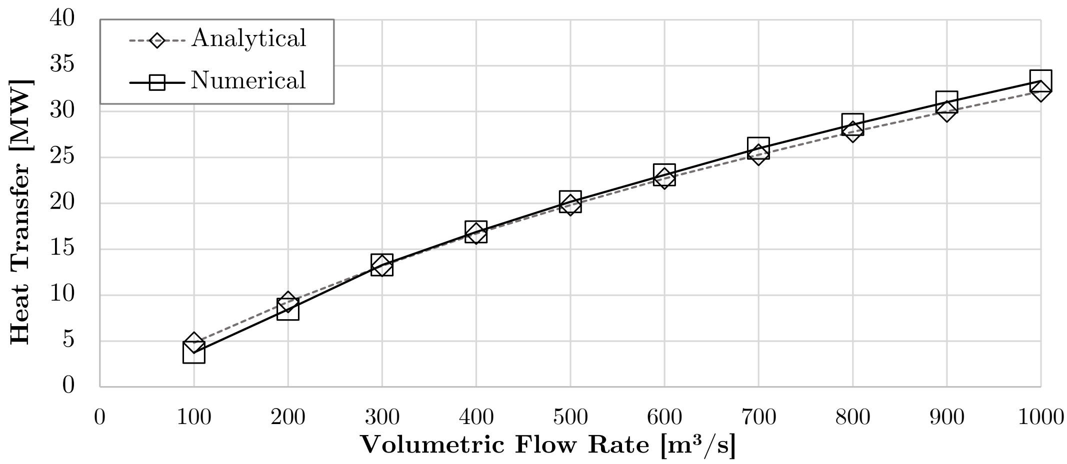

Figure 4.23: Numerical vs. analytical comparative graph of total heat transfer

The analytical solution was calculated using the ϵ-NTU method as detailed in appendix B as no experimental results for a full-scale A-frame heat exchanger was available. A good correlation between numerical predictions and the analytical solution is noted with the largest difference of 2 % calculated at a flow rate of 100 m^3/s.

Validation of the mechanical losses, heat rejected to the atmosphere as well as correct interpretation of the flow field downstream of the heat exchanger constitutes a validated numerical heat exchanger model.

4.3 Free-standing ACC Unit

The volumetric flow rate, heat transfer and fan power consumption was determined analytically and numerically under ideal conditions for a single heat exchanger and fan unit (referred to as the ACC unit) of the A and B2a-fan. The heat-to-power ratio of the ACC unit was then also determined. This calculated volumetric flow rate is taken as the operating point of the fan at the design conditions as stipulated in appendix C.

The operating point of the system was determined analytically using the one-dimensional draft equation analysis of a forced draft ACC, derived and presented in appendix C. The operating point is defined as the intercept point between the system resistance line and the static pressure characteristic curve of the up-scaled fan as illustrated in figure 4.24. The operating points were calculated for the A-fan and B2a-fan with blade setting angles of 14^o and 31^o respectively.

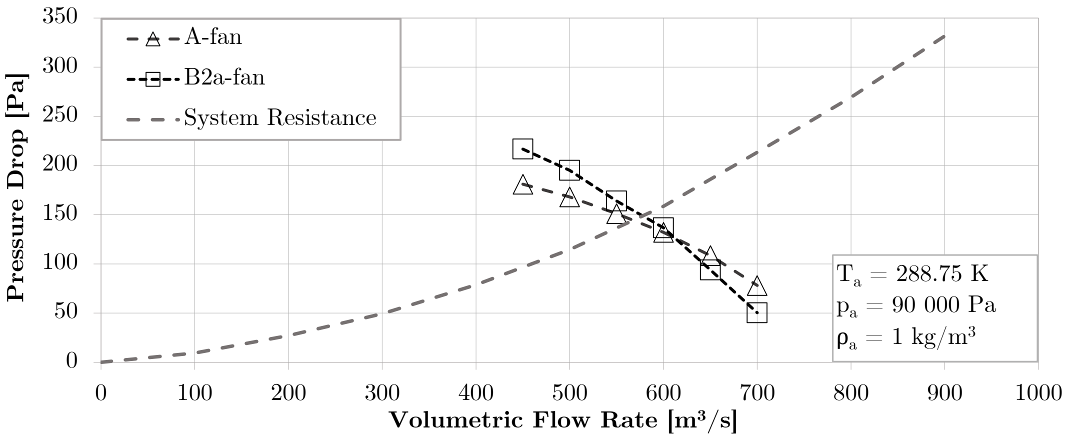

Figure 4.24: Graph showing analytically determined operating point

4.3.1 Computational Set-up

Prior to the validation procedure an analysis was performed to determine the contributions of fan obstacle losses on the performance of the ACC model. As previously mentioned in chapter 2, the mechanical energy losses resulting from flow passing through different fan obstacles were derived by Venter (1990) using the V-fan. Significant geometrical differences exist between the V-fan and B2a-fan. An analysis was therefore required to determine the validity of using these derived fan obstacle losses for the B2a-fan.

This was determined using two modelling approaches, comparatively studied in appendix D. Similar to the studies of Bredell (2005), van Rooyen (2007), Owen (2010) and Louw (2011), the first approach modelled the mechanical energy losses as air passes the fan walkway and support struts using loss coefficients in porous regions. The second approach used the ACC model described in chapter 3 whereby the support struts and fan walkway were modelled as geometrical structures in the domain. The operating points for both modelling approaches were determined and compared for the A-fan and B2a-fan. The remaining fan obstacles such as the fan motor, gearbox, safety screens and support beams were excluded.

The difference in numerically predicted operating points between modelling approaches for the A-fan (0.70 %) indicates that the flow experiences similar mechanical losses as it passes through the walkway, and around the support struts, as that measured by Venter (1990) in the derivations of the respective loss coefficients. The larger difference between modelling approaches measured for the B2a-fan (3.90 %) also indicates that a discrepancy will arise when the operating point is determined by modelling the losses using these derived loss coefficients. A more accurate representation of the operating conditions will therefore be attained when the support struts and walkway are modelled as geometrical structures in the domain for a fan with a hub-to-tip ratio larger than the A-fan.

Even though the calculated difference between modelling approaches is small in the case of the B2a-fan, modelling these losses could potentially result in incorrect predictions of flow characteristics in the plenum of the heat exchanger. It is therefore recommended that if the approach of the previous studies is to be used, the loss coefficients be evaluated on a case-by-case based on the fan. The only obstacles modelled geometrically therefore were the support struts and fan walkway.

The volumetric flow rate, fan power consumption, heat transfer rate and heat-to-power at the operating point of each fan was determined numerically by placing the ACC unit in the domain shown in figure 4.25. The following boundary conditions were used to represent ideal conditions:

- A slip condition was used for the plenum walls as no mechanical energy losses are expected at these walls (Louw, 2011).
- The hub, fan bellmouth inlet shroud, ground and support struts of the domain were modelled as no-slip wall boundaries.
- All walls used standard wall functions for the k-ϵ turbulence model.
- A total pressure boundary was used to represent atmospheric conditions.
- Temperature was allowed to vary across the boundary only on outflow. Inflow was constrained to a fixed temperature.
- Velocity was driven by pressure on inflow. Outflow was treated as a zero gradient condition.

Convergence of the numerical solution was achieved when the volumetric flow rate converged such that $|\dot{V}^{(k)} - \dot{V}^{(k-1)}| < 0.1$ m^3/s, the measured power consumption converged to $|P^{(k)} - P^{(k-1)}| < 10$ W and all governing equation residuals were below 1e-4. This convergence criteria was applied to all subsequent simulations in this study.

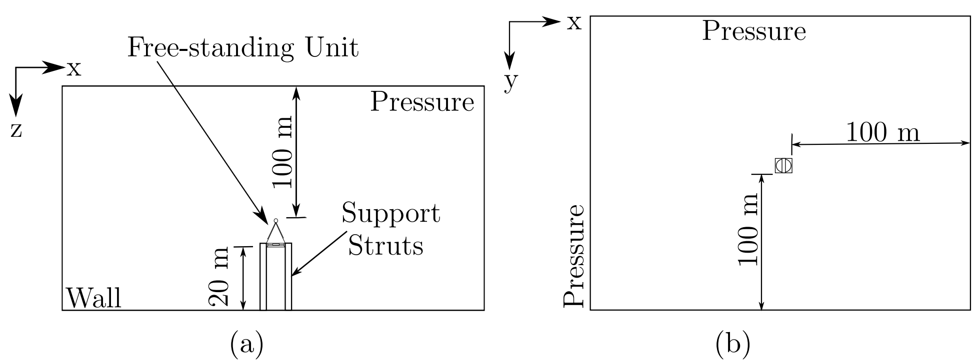

Figure 4.25: a) Side view and b) top view of domain used for a single free-standing unit

4.3.2 Grid Independence Study

The solution was checked for grid independence by measuring the volumetric flow rate, power consumption and heat transfer of the ACC unit serviced by the B2a-fan on different grid sizes. The sizes ranged from 0.899x10^6 to 1.976x10^6 cells, increasing in density in the vicinity of the ACC unit. The results of the study are shown in table 4.3 where a maximum difference of 0.15 % was measured for the volumetric flow rate, 0.24 % for the power consumption and 2.45 % for heat transfer across all cases. The measured differences are deemed negligible indicating a grid independent solution. The final mesh consisted of 1.294×10^6 cells and was used in the subsequent evaluation of the operating points.

Table 4.3: Grid dependency study of the ACC unit

Mesh Size	**Vol. Flow Rate [m^3/s]**	**Heat Transfer [W]**	**Power [W]**
0.899×10^6	618.19	2.16×10^7	130 675
1.294×10^6	618.34	2.16×10^7	130 719
1.976×10^6	617.41	2.21×10^7	130 396

The computational grid used for the analysis of the ACC unit is shown in figure 4.26 and 4.27. Both hexahedral and tetrahedral elements were used. The axial flow fan model as well as the heat exchanger was discretized using hexahedral elements to facilitate data transfer. The rest of the domain was discretized using tetrahedral elements.

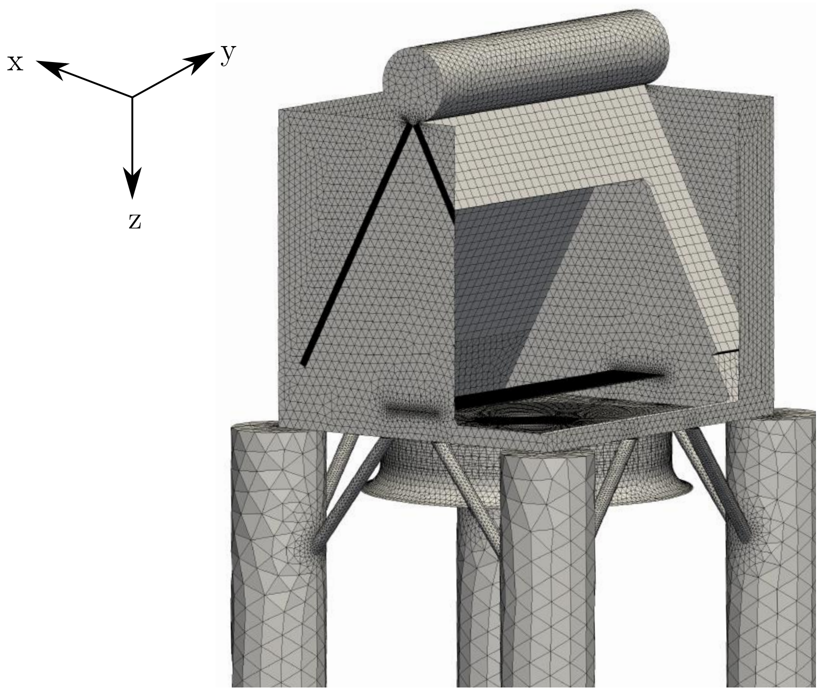

Figure 4.26: Three-dimensional view of the grid used for the ACC unit

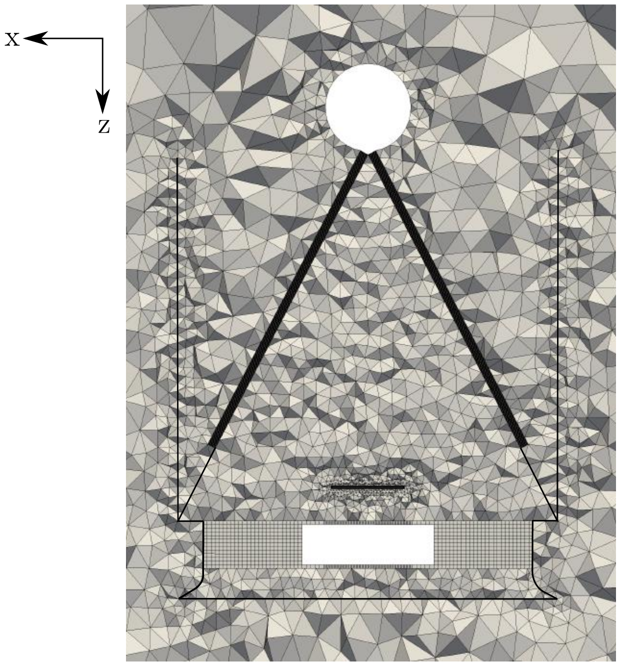

Figure 4.27: Front view of the grid used for the ACC unit

4.3.3 Results and Discussion

The numerically determined operating points are compared to the draft equation results in table 4.4, differences to the analytical solution are indicated in brackets. The axial velocity distributions and vector plots for flow in the plenum of both fans are shown in figures 4.28 and 4.29. The numerically predicted operating points over-predict the analytical solutions in the case of both fans. Possible reasons for the measured differences are discussed below.

Table 4.4: Operating points determined analytically and numerically

	Vol. Flow Rate [m^3/s]	**Heat Transfer [W]**	**Power [W]**	**HTP [W/W]**
A-fan (Analytical)	577.77	2.04e7	149 725	135.95
A-fan (Numerical)	606.11(4.91%)	2.18e7(7.24%)	147 836	147.66
B2a-fan (Analytical)	580.64	2.08e7	133 908	152.70
B2a-fan (Numerical)	618.34(6.49%)	2.16e7(5.69%)	130 719	165.33

The large tangential velocity components introduced by the extended actuator disk model in the plenum is not accounted for by the draft equation. This swirling flow, as shown by figure 4.30, results in a non-uniform distribution of air at the heat exchanger inlet. As the isothermal heat exchanger loss coefficient is calculated based on the air flow velocity, it subsequently results

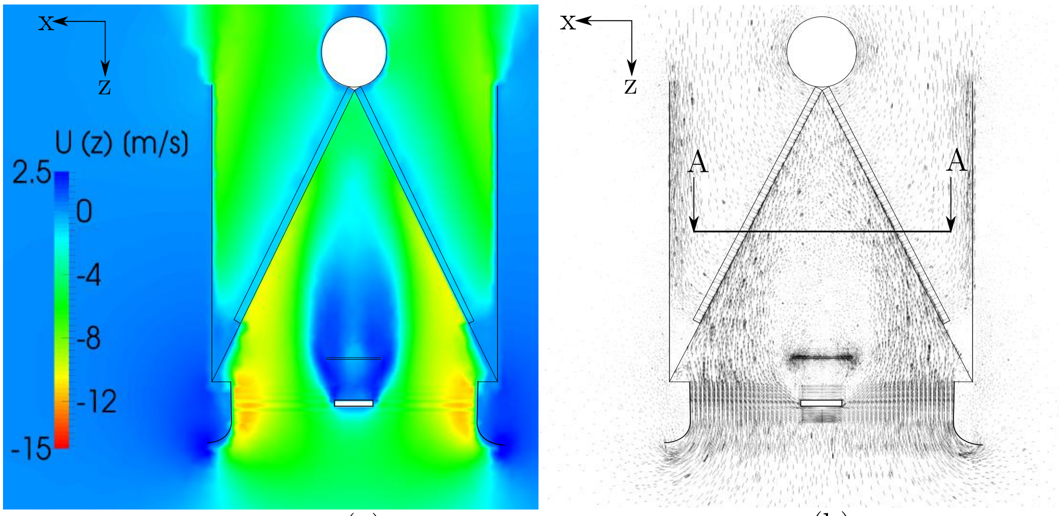

(a) (b)

Figure 4.28: a) Contour plot of axial velocity and b) velocity vector plot of flow in the plenum of the A-fan

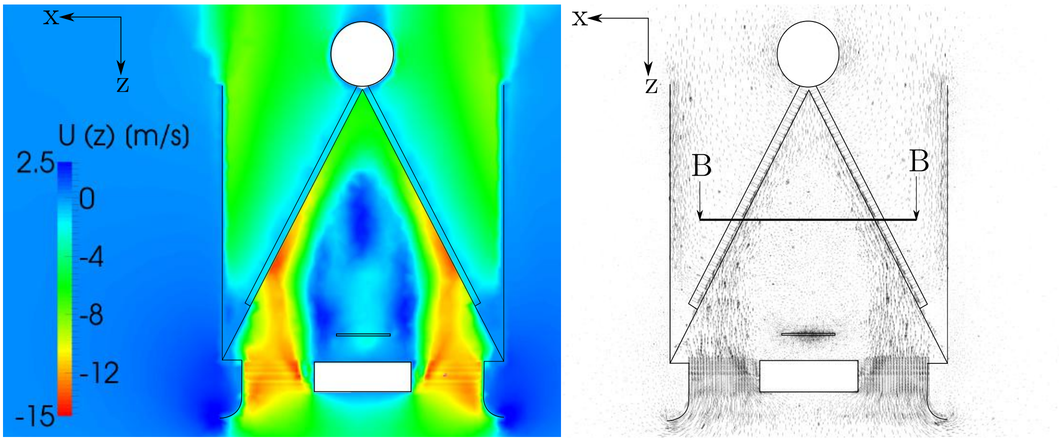

(a) (b)

Figure 4.29: a) Contour plot of axial velocity and b) velocity vector plot of flow in the plenum of the B2a-fan

in a non-uniform pressure drop profile across the heat exchanger. This non-uniform pressure drop is also expected due to the obliquity of the streamlines exiting the heat exchanger (Kröger, 1998). In the case of the pressure jump method, which does not introduce tangential velocities in the flow downstream of the fan, a better correlation was noted to the analytical model as reported by Owen (2010), Joubert (2010) and Louw (2011). This model does not, however, depict the correct characteristics of flow in the plenum of an ACC unit.

The recirculation caused by the small hub of the A-fan, and to a lesser extent the hub of the B2a-fan, also contributes to the non-uniformity of the flow

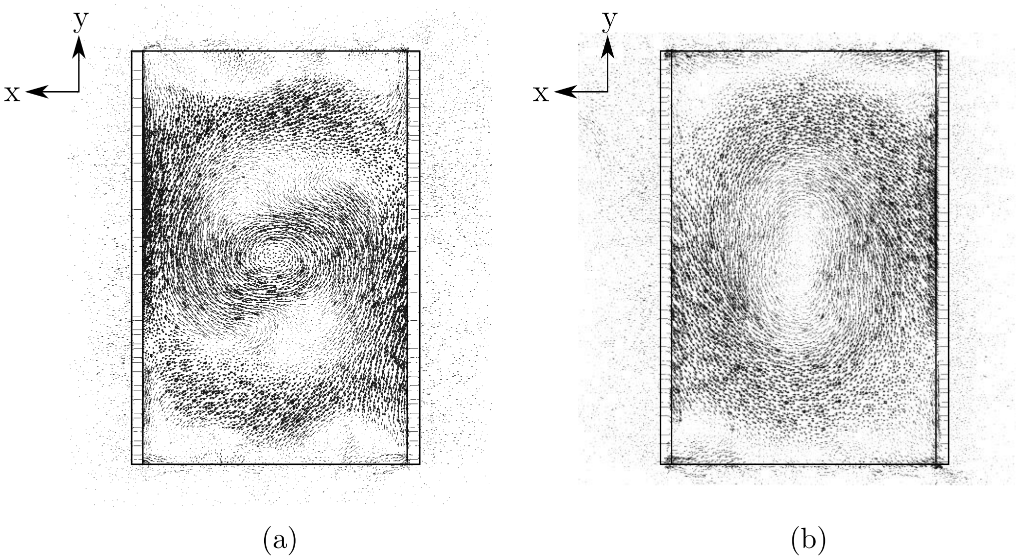

Figure 4.30: Vector plots showing swirl of a) A-fan (Section A-A) and b) B2a-fan (Section B-B)

at the heat exchanger inlet. The effect of maldistributed heat exchanger inlet flow is further accentuated by the design of the A-frame as the flow area decreases moving closer to the heat exchanger apex. As opposed to the operating points of this study, small differences between the analytical and numerically determined operating points was reported by Bredell (2005) even though the actuator disk model was used. Bredell (2005) did, however, represent the heat exchanger in the form of a box plenum as illustrated in chapter 2. This geometrical approach for modelling the plenum will not affect the flow distribution at the heat exchanger apex as observed with the A-frame plenum.

The difference in the predicted operating points between the A-fan and B2a-fan indicates that the mechanical loss as the flow passes through the walkway increases due to the recirculation effect forming at the hub of the axial flow fans. Figure 4.31 shows a vector plot of the flow inside the plenum in the vicinity of the walkway for both fans. The B2a-fan ejects the air uniformly in an axially aligned column around the walkway whereas the reverse flow region of the A-fan forms in the vicinity of the walkway. This leads to a smaller volume of air flow through the walkway in the B2a-fan case. Consequently, a smaller volume of air is affected by the mechanical energy loss resulting from the fan walkway leading to higher operating point predictions.

All the above mentioned flow phenomena leading to the differences in numerical and analytical operating points can be quantified by including a plenum kinetic energy recovery coefficient, K_{rec}, in the draft equation. The draft equation assumes that all the kinetic energy of the fan tested in the fan

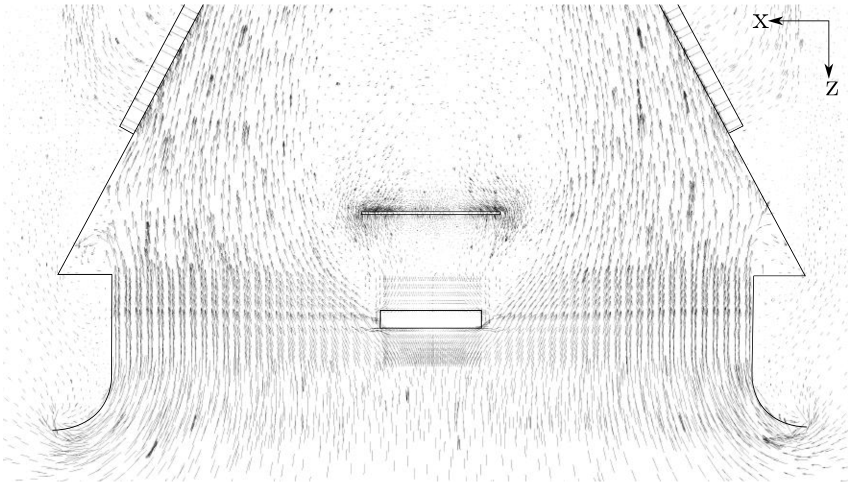

(a)

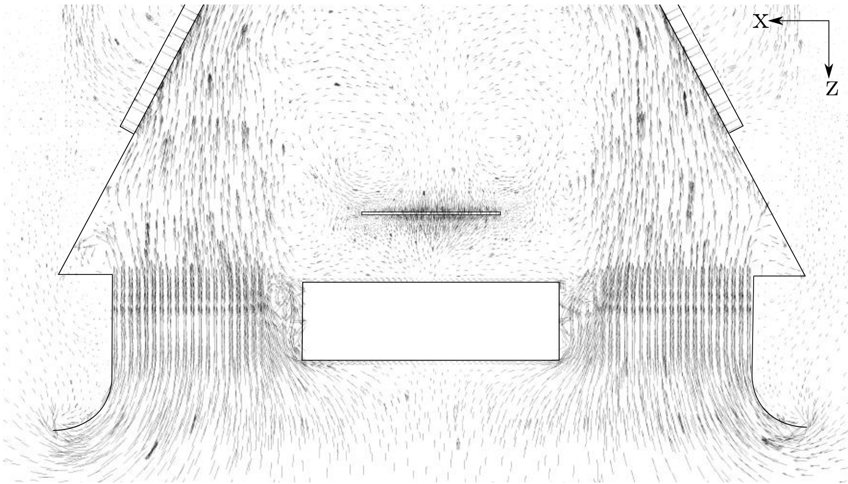

(b)

Figure 4.31: Flow in the vicinity of the walkway of a) A-fan and b) B2a-fan

test facility is dissipated in the plenum chamber. Meyer (1996) showed that this assumption is not true and a kinetic energy recovery coefficient should be included in the fan system performance characteristic term defined as:

$$(\Delta P_{Fs} + K_{rec}\rho v_F^2/2) \tag{4.3}$$

where the kinetic energy recovery coefficient is based on the mean flow velocity though the fan (Kröger, 1998). Modifying the draft equation with equation 4.3, and gradually increasing the value of K_{rec} until the analytical and numerical results match, allows for a quantification of the kinetic energy recovery in the plenum of the numerical model. A graphical depiction of this recovery effect is shown in figure 4.32. Kinetic energy recovery effectively raises the fan static pressure curve moving the intercept point of the system resistance line from V_{Fid} to V'_{Fid}, resulting in a higher predicted operating point.

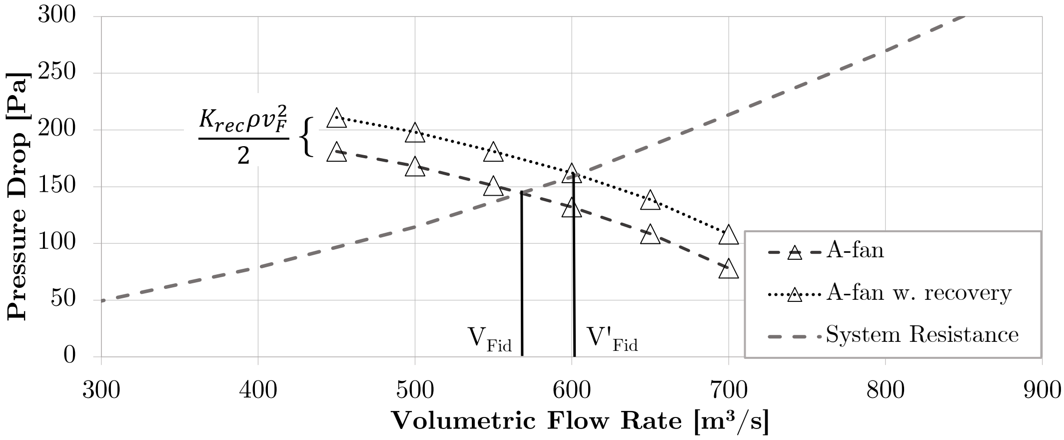

Figure 4.32: Graphical representation of K_{rec} on operating point (Kröger, 1998)

The approach was validated using the experimental results of Meyer (1996). A scale model B2-fan and an A-frame heat exchanger was used to determine the kinetic energy recovery coefficient in the plenum. The experimental set-up was designed such that the motor and gearbox housing were placed far enough downstream of the fan to have a negligible effect on the results. The walls of the fan test facility acted as windwalls on the A-frame heat exchanger. The numerical domain was set-up to represent the experimental design by removing the support struts and walkway from the computational domain. The procedure outlined above to determine the kinetic energy recovery coefficient was followed, and the results are indicated in table 4.5.

Table 4.5: Experimental and numerically determined values of K_{rec}

	K$_{rec}$
Meyer (1996)	0.553
Numerical	0.527

The results of the validation show a good correlation between experimental and numerical results. This can also be considered as an additional form of validation for the ACC unit model. Previous literature did not report the addition of kinetic energy recovery in the plenum of the ACC. As the value of K_{rec} is dependent on the geometry of the plenum, the kinetic energy recovery of the box plenum from previous studies would not be a good representation of the correct flow characteristics of an A-frame ACC. This indicates the degree to which using geometrical characteristics can have on operating conditions of a numerical model of an ACC.

4.4 Summary of Findings

This chapter served to detail the validation procedures undertaken for the axial flow fan, heat exchanger and ACC model. The extended actuator disk model is based on the actuator disk model and therefore both were validated using the performance characteristics of the A-fan and B2a-fan. The actuator disk model under predicted the fan static pressure rise for low volumetric flow rates which was addressed by the extended model. Significant deviations were, however, noted at very low flow rates. This was deemed to be outside the expected operating range of the ACC. Fan power consumption showed a good correlation for both models. Physical characteristics of the flow downstream of the fans were also observed to coincide with that reported by previous literature.

The heat exchanger was validated with specific focus on the mechanical flow losses, heat transfer and flow directional conditioning. An evaluation was conducted to determine the appropriate mechanical loss modelling approach. It was found that only the isothermal heat exchanger loss coefficient required modelling in the heat exchanger region. The model was successfully validated with regards to all three aforementioned heat exchanger characteristics.

An ACC unit was formed by combining the heat exchanger model with an up-scaled fan model. It was determined beforehand that the coefficients used to model flow losses resulting from obstacles in the vicinity of the fan are not appropriate for use with the B2a-fan. The derivations of the coefficients by Venter (1990) was only performed using the V-fan. The fan walkway and support struts were included as geometrical structures in the domain.

The operating point of the A-fan and B2a-fan ACC unit was determined and it was noted that kinetic energy recovery leads to an over prediction of the numerical results to the analytical solution. This was validated by comparing the numerically measured recovery coefficient to an experimental design from which a good correlation was noted. The successful validation of all models constituted an accurate and reliable numerical model of an ACC.

Chapter 5

Performance Evaluation of ACC Bank in 6x5 Layout

This chapter details the numerical procedure for the analysis of the 30 fan ACC bank in a 6x5 layout configuration, schematically shown in chapter 3. A description of the computational domain is presented, followed by a comparative analysis of ACC bank performance to the studies of van Rooyen (2007) and Joubert (2010). A performance evaluation of the ACC bank is discussed focusing on ACCs with three different fan configurations subject to different cross-wind speeds and directions. An overview of the factors affecting volumetric and thermal performance, as determined through an analysis of previous literature and phenomena observed in the performance evaluation, is also presented in the appropriate sections.

5.1 Computational Description

5.1.1 Computational Set-up

The ACC was subjected to various cross-wind speeds and directions, and the volumetric flow rate through the axial flow fans, fan power consumption and heat transferred by the heat exchangers were determined. The wind was modelled as a velocity distribution of the form shown in figure 5.1 defined as:

$$v_z = v_{ref}\left(\frac{z}{z_{ref}}\right)^b \tag{5.1}$$

where the coefficient, b, was set as 1/7 defined by van Rooyen (2007). The specified velocity was taken as the measured velocity at the platform height.

Figure 5.1 shows the domain dimensions and profile created by the distribution in equation 5.1. The boundary conditions used for the validation of the ACC unit in chapter 4 were also used for the ACC performance analysis.

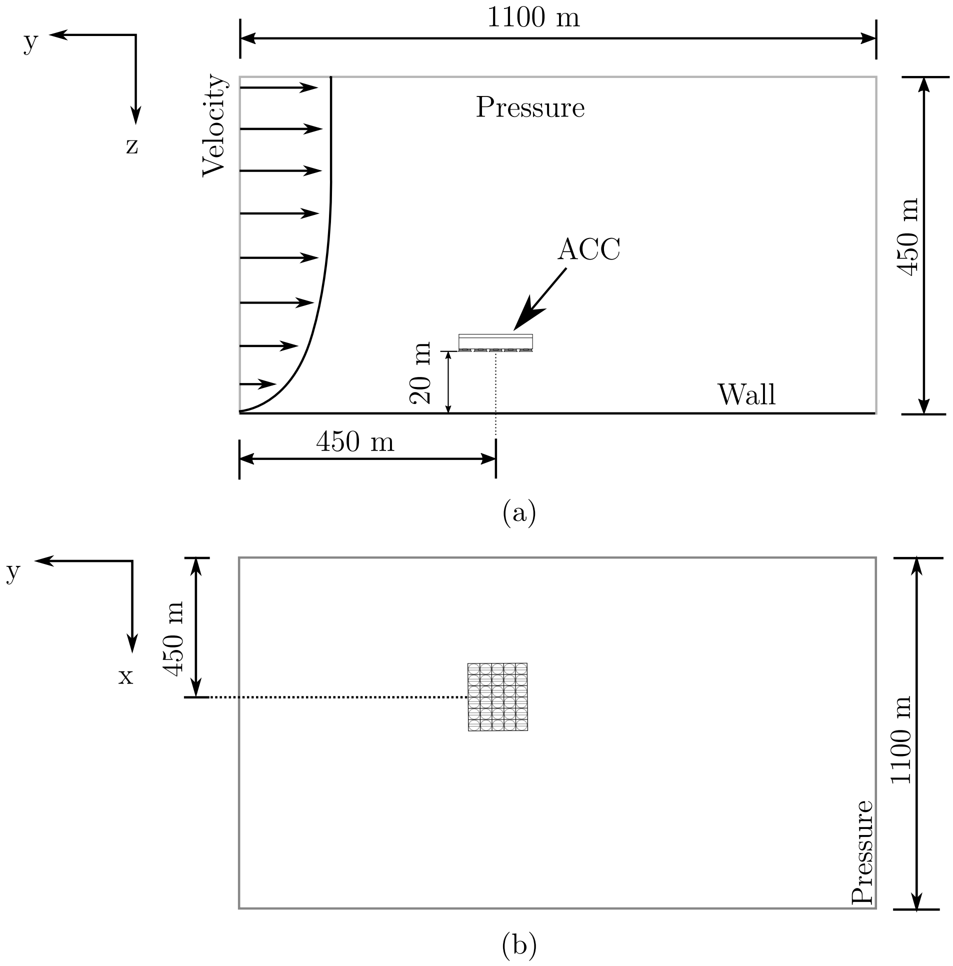

Figure 5.1: Schematic of a) side view and b) top view of numerical domain

5.1.2 Grid Independence Study

A grid independence study was performed using three different cases with the cell counts of each case set out in table 5.1. The concentration of cells for each case was increased in the vicinity of the heat exchanger and the fan inlet where the largest variable gradients were expected.

Table 5.1: Cell counts for grid dependence study

Designation	Cell Count
Case 1	8.671×10^6
Case 2	12.539×10^6
Case 3	17.133×10^6

The three cases were subjected to no wind speed and a cross-wind speed of 6 m/s and the volumetric flow rate through individual fans, total volumetric flow rate, total power consumption and total heat transfer measured. The cell count on the inlet face was also varied and the average velocity measured to determine if the velocity distribution profile was adequately modelled. Figure 5.2 and 5.3 shows the volumetric flow rate of certain individual fans. The remaining parameters measured for the study are shown in table 5.2 and 5.3.

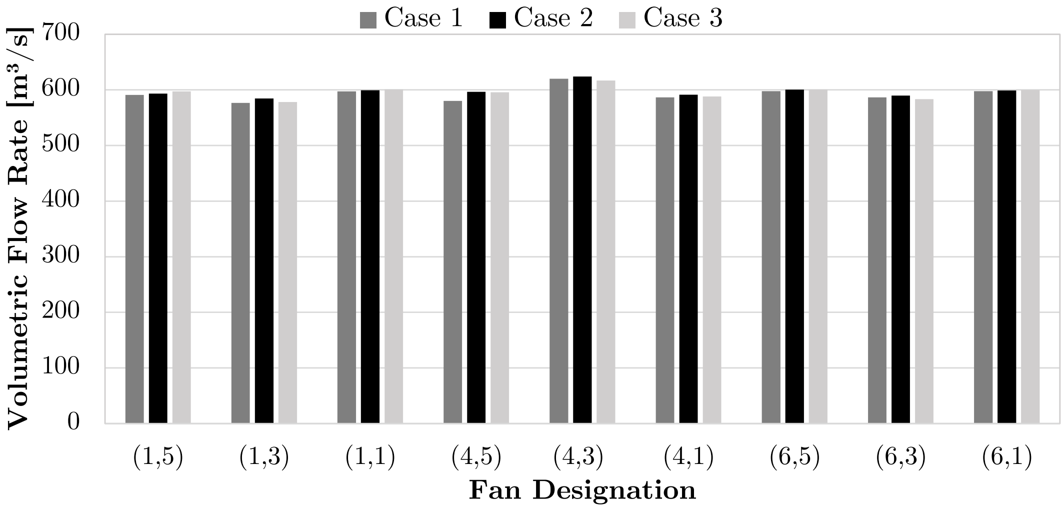

Figure 5.2: Volumetric flow rate of fans subject to no cross-wind

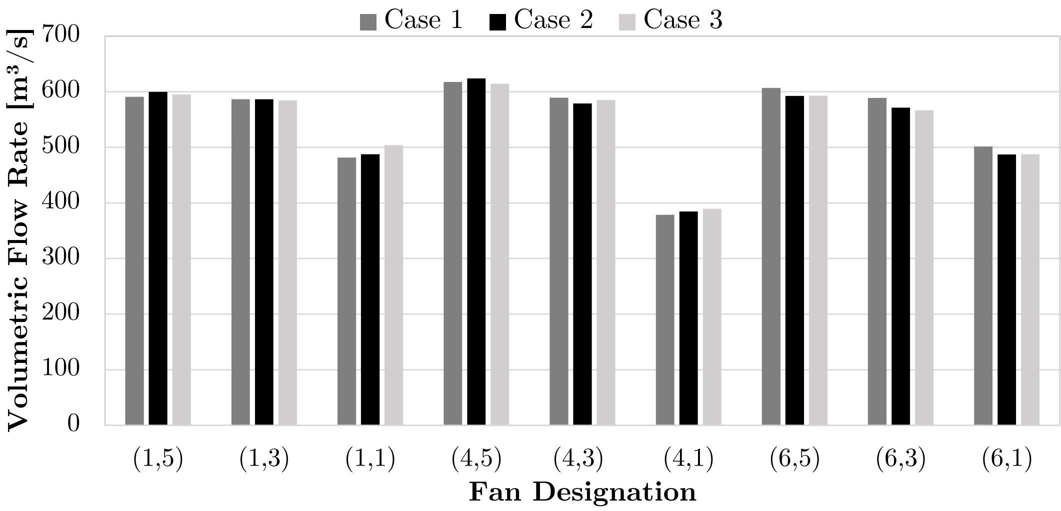

Figure 5.3: Volumetric flow rate of fans subject to 6 m/s cross-wind

The maximum difference between case values with regard to volumetric flow rate of individual fans, was calculated as 5.17 % for fan (1,1) at a cross-wind speed of 6 m/s. Maximum difference in measured parameters of table 5.2 and 5.3 were calculated as 0.51 % for total volumetric flow rate, 0.79 % for total heat transfer, 4.50 % for total power consumption and 2.66 % for the average velocity at the inlet face. The difference in case values were deemed negligible and the solution was considered grid independent. The computational grid of case 1, as shown in figure 5.4 and 5.5, was subsequently used for the comparative and performance evaluation. The higher density of cells on the inlet face near to the ground is also indicated. As the velocity profile is dependent on cell height relative to the ground, a larger number of cells was required in order to accurately capture the velocity gradients.

Table 5.2: Grid dependency study of ACC bank subject to no cross-wind

Case Number	**Vol. Flow Rate [m^3/s]**	**Heat Transfer [W]**	**Power [W]**
Case 1	18.06x10^3	62.83x10^7	3.72x10^6
Case 2	18.15x10^3	63.09x10^7	3.73x10^6
Case 3	18.13x10^3	63.07x10^7	3.72x10^6

Table 5.3: Grid dependency study of ACC bank subject to 6 m/s cross-wind

Case Number	**Vol. Flow Rate [m^3/s]**	**Heat Transfer [W]**	**Power [W]**	**Avg. Inlet Velocity [m/s]**
Case 1	16.89x10^3	59.32x10^7	3.75x10^6	6.83
Case 2	16.85x10^3	58.85x10^7	3.60x10^6	6.65
Case 3	16.87x10^3	59.27x10^7	3.76x10^6	6.66

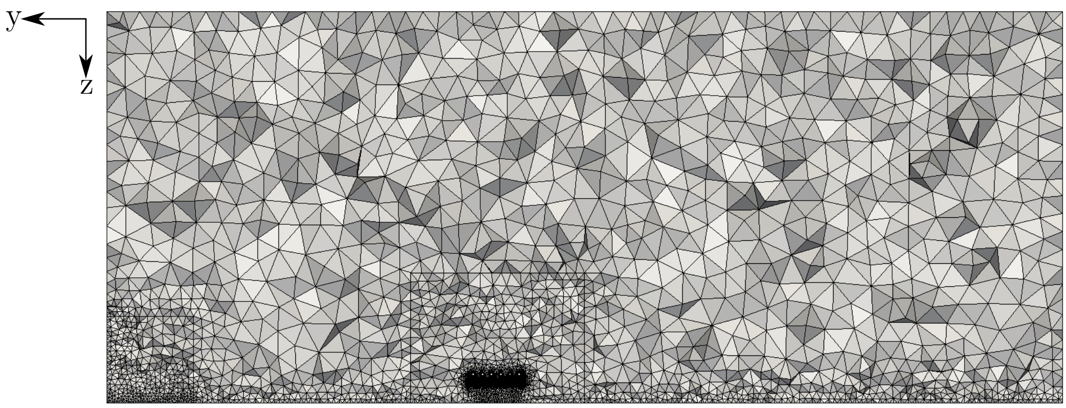

Figure 5.4: Computational grid of the domain

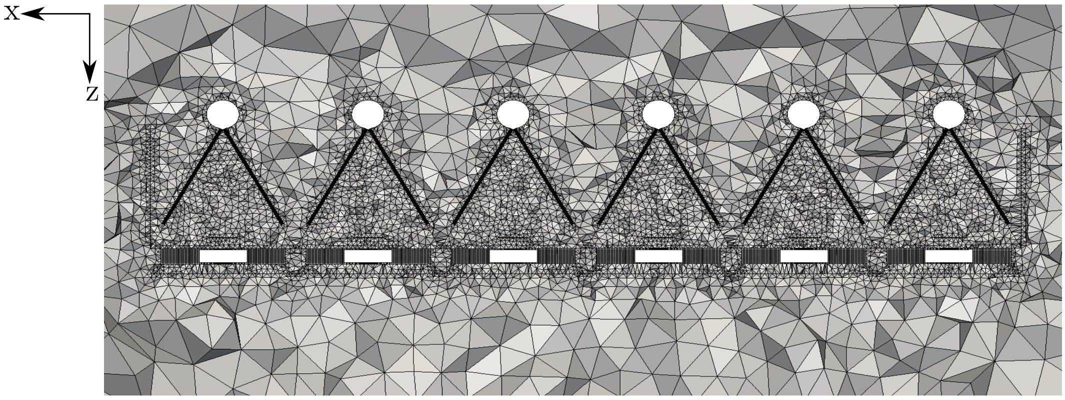

Figure 5.5: Computational grid in the vicinity of the ACC

5.2 Results and Discussion

The comparative analysis was performed using an ACC similar to van Rooyen (2007) and Joubert (2010). The ACC was set-up in a 6x5 layout using 30 B2a-fan and heat exchanger units, and subjected to different cross-wind speeds in the negative y-direction. ACC volumetric performance is presented in the form of volumetric effectiveness ratio as discussed in chapter 3. In accordance with the data presentation of the previous studies, the ideal volumetric flow rate of each axial flow fan in the ACC was taken as the volumetric flow rate determined for the free-standing B2a-fan ACC unit under ideal conditions of chapter 4. The results of the study are shown in figure 5.6.

Fans in the ACC of this study show similar volumetric performance trends to those of the previous studies on the wind downstream periphery (referred to as the downstream periphery). The volumetric effectiveness of these fans are noted to be larger than unity. This ability to exploit the wind energy is attributed to the low distortion, and relatively high momentum of the air at the fan inlet (van Rooyen, 2007).

The largest differences in predicted fan performance occurs on the wind upstream periphery (referred to as the upstream periphery). The present study predicts upstream fan performance up to 10 % higher than Joubert (2010) and 35 % higher than van Rooyen (2007). Several reasons have been identified for these differences. These include the geometrical differences between analysed ACC domains, the use of different axial flow fan models as well as the simplifications used in the numerical procedures by van Rooyen (2007) and Joubert (2010). An outline of these simplifications not deemed necessary for the current study is discussed in chapter 3.

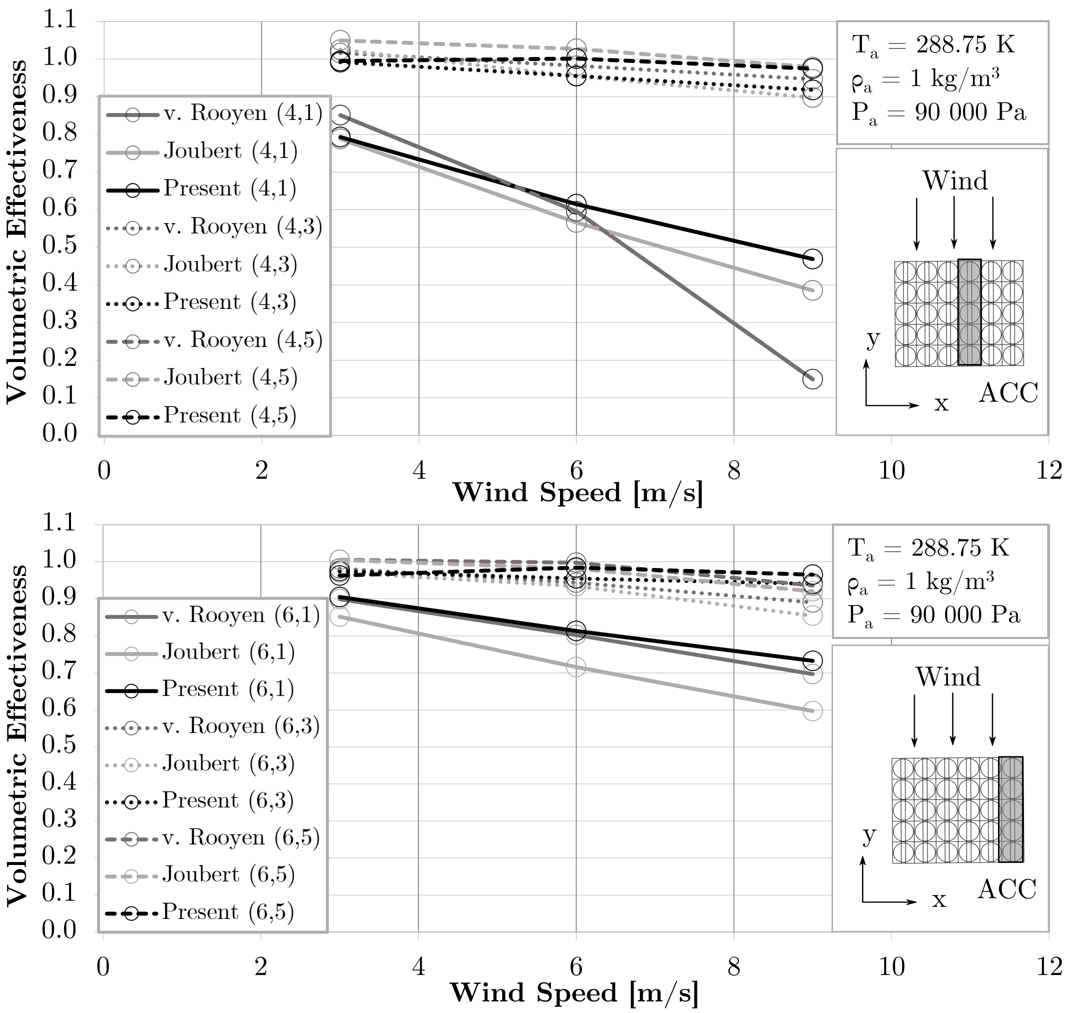

Figure 5.6: Volumetric effectiveness comparison to previous studies

A study was conducted to quantify the difference in predicted performance between the domain of the current study, where the support struts and fan walkways were modelled as geometrical structures, and a simplified domain similar to the one used by van Rooyen (2007) and Joubert (2010). The simplified domain models the flow mechanical losses passing through obstacles using loss coefficients in different porous regions. The study is presented in appendix D and the axial flow fan volumetric flow rates of the two domains are presented. The extended actuator disk model was used for both analysed domains.

Volumetric fan performance of the domain used in the present study was predicted up to 37.38 % higher for the upstream fan (4,1) at a cross-wind speed of 6 m/s compared to the simplified domain. A significant difference therefore exists with regard to ACC performance predictions, dependant on the domain used. The pressure distributions shown in figures 5.8 and 5.7 indicate a definite decrease in the size of the low static pressure region at the fan inlets of the domain used by this study, compared to the simplified domain. These regions of low static pressure indicate flow separation at the inlet and is considered to be a major contributor toward fan performance degradation (Owen, 2010; Louw, 2011), and is discussed in detail in section 5.3.1.

Lower measured air velocities below the platform results in smaller regions of flow separation present at the upstream fan inlets. The support struts decreases free-flow area reducing the momentum of the air below platform. This reduces the degree of distorted inflow at the fan blades resulting in higher upstream periphery fan volumetric performance compared to the studies of van Rooyen (2007) and Joubert (2010). As the predicted performance of the downstream fans are similar, the increase in predicted upstream fan performance leads to higher total volumetric effectiveness compared to the previous studies at higher wind speeds, as indicated in figure 5.9.

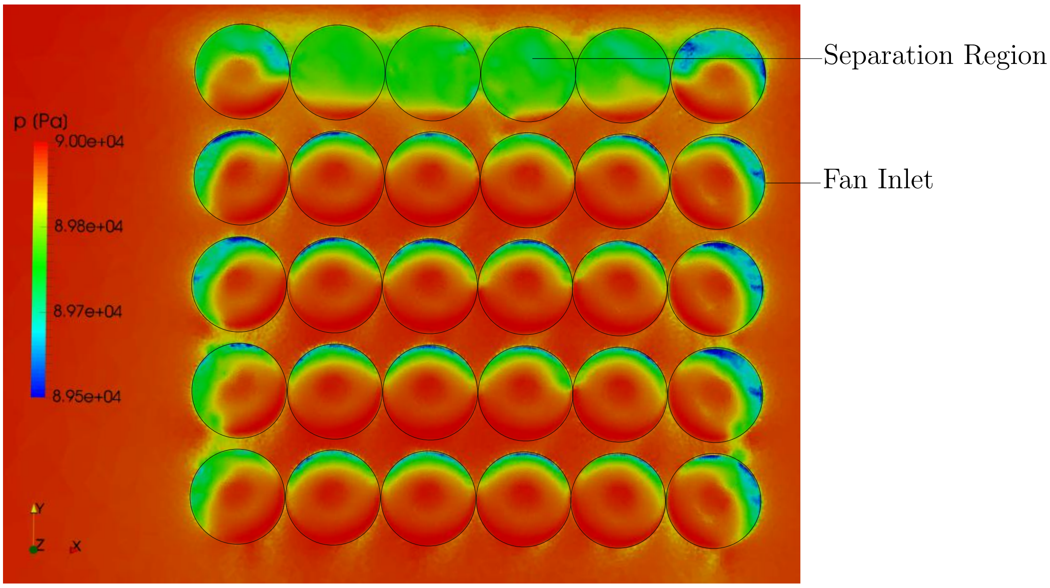

Figure 5.7: Pressure distribution at fan inlets without support struts

The ability of different axial flow fan models to accurately predict fan performance subject to distorted inflow conditions, is showcased by the difference in volumetric performance predictions of fans on the upstream periphery in figure 5.6. The actuator disk model used in the study of van Rooyen (2007) performs poorly under severe cross-flow conditions, and the pressure jump model used by Joubert (2010) exhibits inaccurate characteristics when capturing the flow field for highly distorted inflow conditions (van der Spuy *et al.*, 2009).

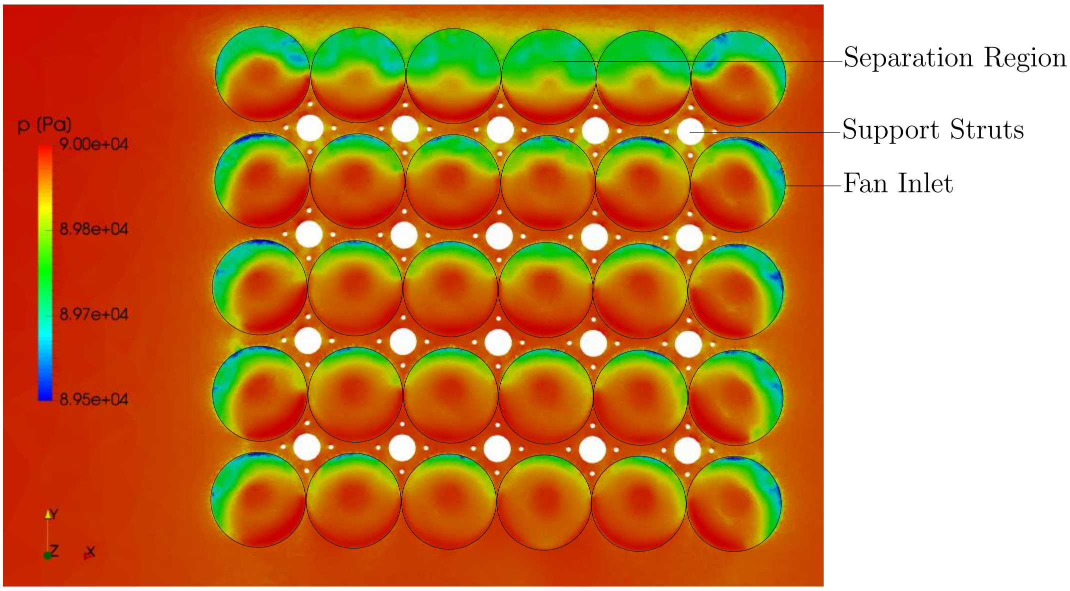

Figure 5.8: Pressure distribution at fan inlets with support struts

The extended actuator disk model used in this study addresses these shortcomings also contributing to the higher predicted upstream periphery fan performance.

Similar total volumetric and heat transfer effectiveness trends with increasing cross-wind speeds were observed between the current ACC model and previous studies, as illustrated in figure 5.9 and 5.10 respectively.

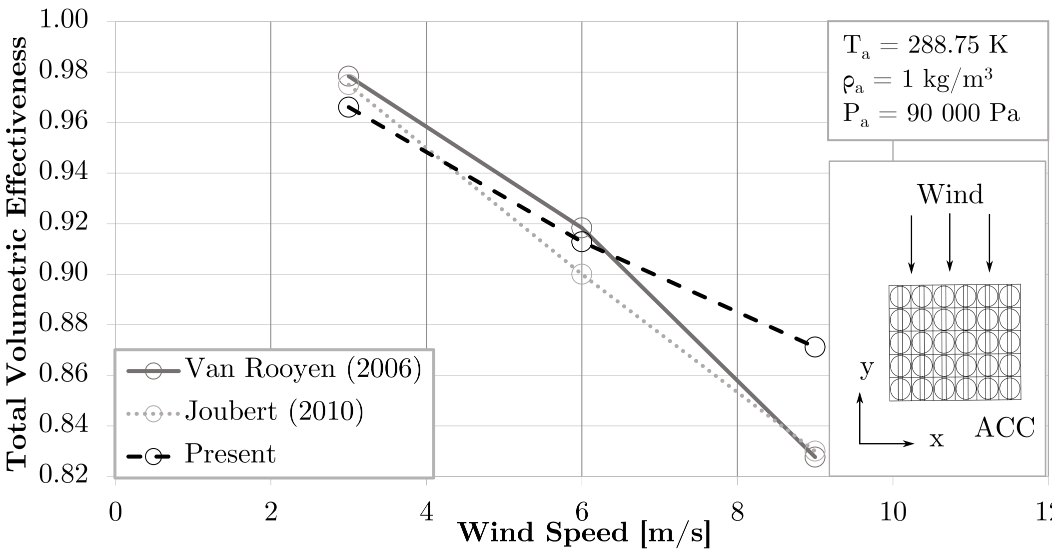

Figure 5.9: Total volumetric effectiveness at different wind speeds

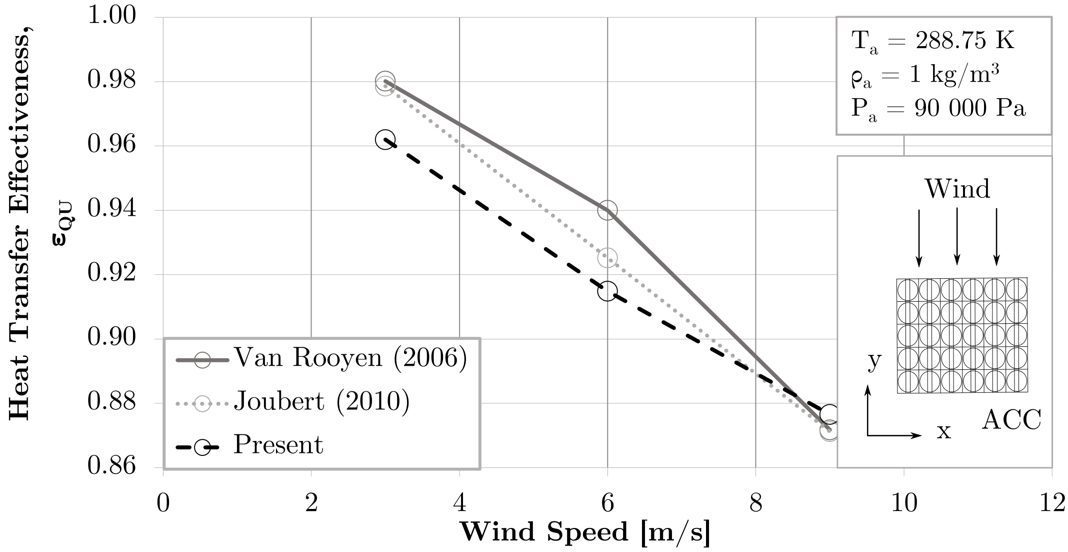

Figure 5.10: Overall heat transfer effectiveness at different wind speeds

A higher total volumetric performance was measured for the ACC model of this study at higher cross-wind speeds resulting from the previously mentioned increase in predicted periphery fan performance. Lower total heat transfer effectiveness was, however, measured for nearly all cross-wind speeds. This is due to the presence of reverse flow regions through the upstream heat exchangers. These reverse flow regions were not reported by van Rooyen (2007) or Joubert (2010). A discussion of phenomena resulting in decreased volumetric and thermal performance is presented in the following section.

5.3 Volumetric Performance Analysis

A performance evaluation of the ACC bank was performed using three different fan configurations. This section evaluates the volumetric performance of the ACCs subject to varying cross-wind speeds of 0, 3, 6 and 9 m/s in the directions normal to the long (y-direction) and short axis (x-direction) of the ACC. A discussion on the performance of the ACC subject to increasing cross-wind speeds along five different directions follows. The wind directions evaluated are illustrated in figure 5.11 with a 0^o cross-wind coinciding with the y-axis and 90^o with the x-axis.

The fan configurations considered were the A-fan ACC, consisting of 30 A-fan and heat exchanger units. The B2a-fan ACC consisted of 30 B2a-fan and heat exchanger units and the third ACC used a combination of A-fans and B2a-fans to form the so-called Combined ACC. The B2a-fans were placed on the peripheries and the A-fans in the centre of the ACC.

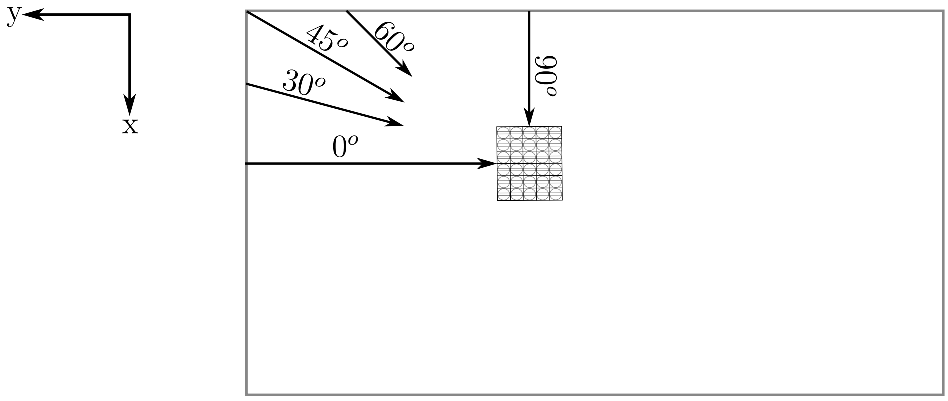

Figure 5.11: Schematic illustrating 5 wind directions used for ACC analysis

The results of the evaluation are presented in the form of the volumetric effectiveness ratio detailed in chapter 3. The volumetric flow rate of an axial flow fan in the ACC subject to no cross-wind is taken as the ideal volumetric flow rate for that particular fan when calculating the effectiveness in the ACC subject to cross-wind. Similarly, the total volumetric effectiveness of each ACC is calculated as the ratio of the total volumetric flow rate of the ACC, to the total volumetric flow rate of the ACC subject to no cross-wind.

5.3.1 Cross-Wind Speed Evaluation (y-direction)

The total volumetric flow rate and volumetric effectiveness measured for each ACC, subjected to cross-winds in the direction normal to the long axis (y-direction), is shown in figure 5.12 and 5.13.

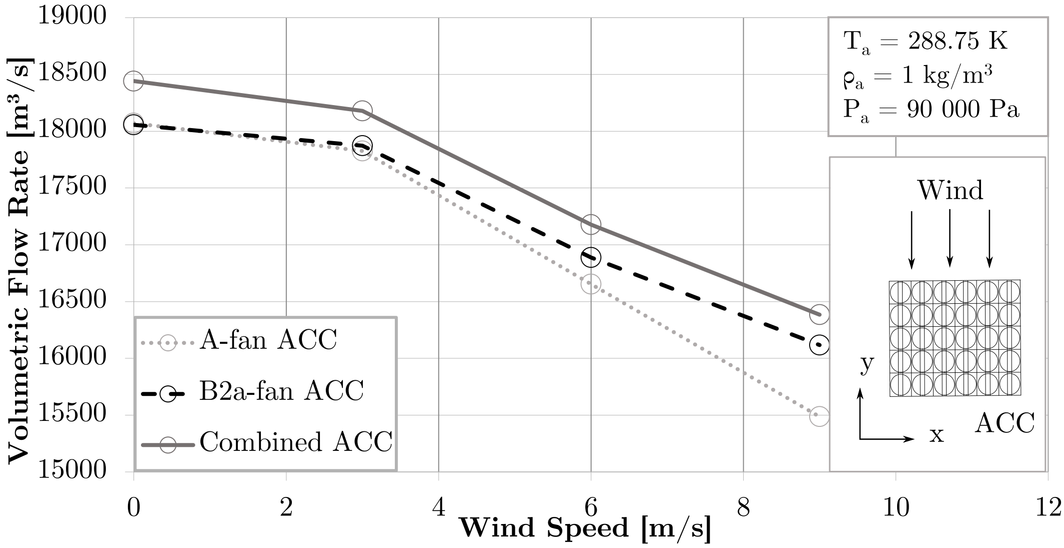

Figure 5.12: Total volumetric flow rate subject to y-direction cross-wind

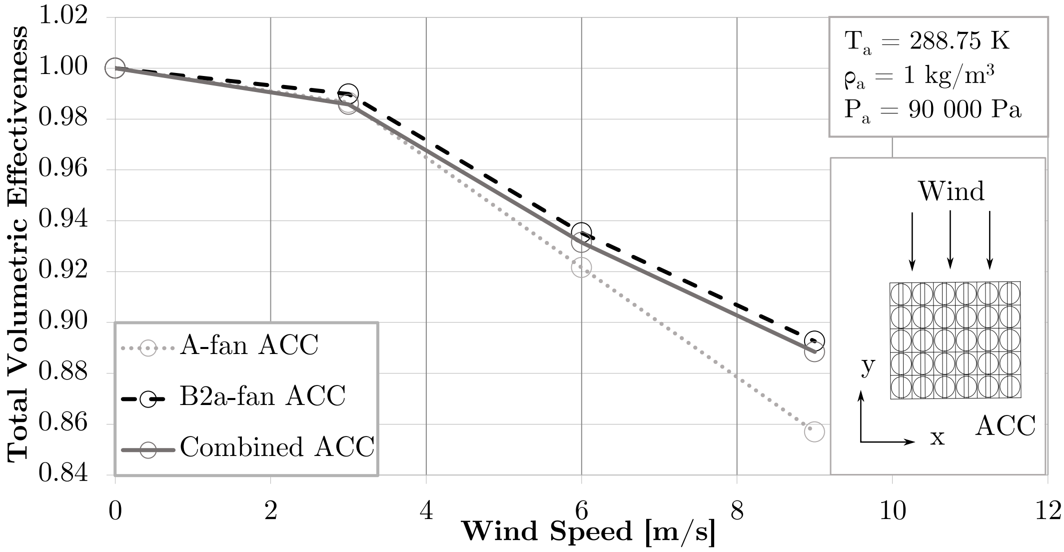

Figure 5.13: Volumetric effectiveness subject to y-direction cross-wind

An indirect relationship exists between ACC volumetric performance and cross-wind speed. The total volumetric flow rate of the B2a-fan ACC was measured as 0.26-4.08 % higher than the A-fan ACC whereas the Combined ACC showed an improvement of 1.66-5.8 % over the B2a-fan ACC. Volumetric effectiveness of the B2a-fan ACC and Combined ACC decreases by approximately 10 % for a cross-wind speed of 9 m/s, and a 14 % decrease was measured for the A-fan ACC. The decrease in volumetric performance for each ACC is explained by considering the performance of individual fans shown in figure 5.14.

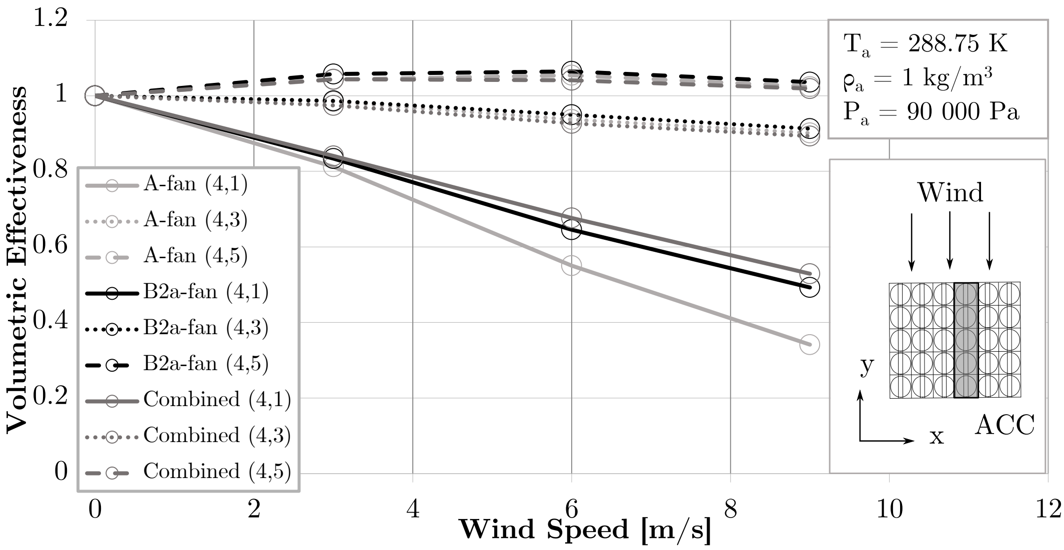

Figure 5.14: Volumetric effectiveness of fans subject to y-direction cross-wind

Individual fan performance indicates distinct differences between fans placed in different locations along the ACC. The volumetric performance of the fans on the upstream periphery decrease significantly with increasing cross-wind speed. The formation of a flow separation region at the edge of the fan inlet results in flow at the fan blades deviating significantly from ideal conditions (Joubert, 2010; Owen, 2010; Louw, 2011). The size of the separation region was also observed to increase with higher cross-wind speeds as air accelerates below the ACC platform. Several distinct flow conditions arise due to the presence of the separation region, each contributing to the decreased fan performance. The conditions are illustrated by the vector plot in figure 5.15 of the A-fan and B2a-fan on the upstream periphery subject to cross-wind, and a discussion follows.

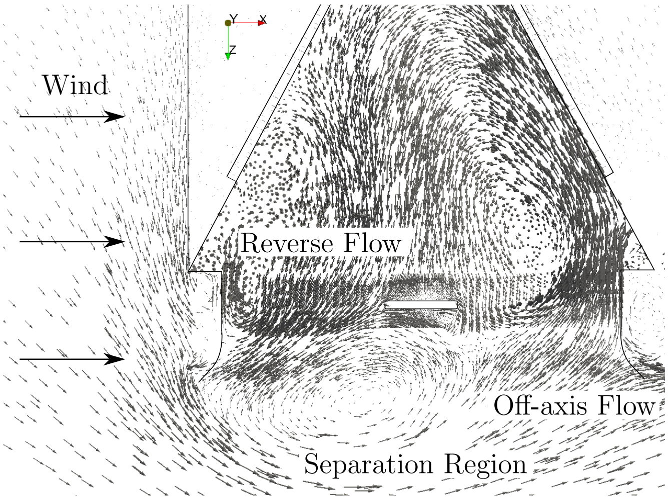

(a) A-fan

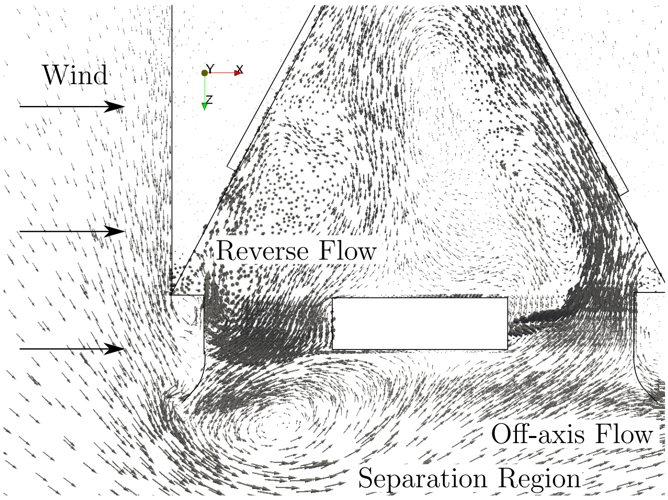

(b) B2a-fan

Figure 5.15: Vector plot of fan (4,1) subject to 9 m/s cross-wind

The flow separation forms a region of low static pressure upstream of the fan blades. The axial flow fan is thus required to overcome an additional static pressure component in order to effectively draw air into the fan inlet. Coupled with the required static pressure rise required to overcome obstacles in the vicinity of the fan blades will inevitably result in a decrease in volumetric performance. The static pressure contour plots in figure 5.16 to 5.18 illustrates the regions of separated flow as regions of low static pressure below the fan inlet. These regions of separation are also observed to affect the fans on the peripheries parallel to the wind direction, albeit to a smaller degree.

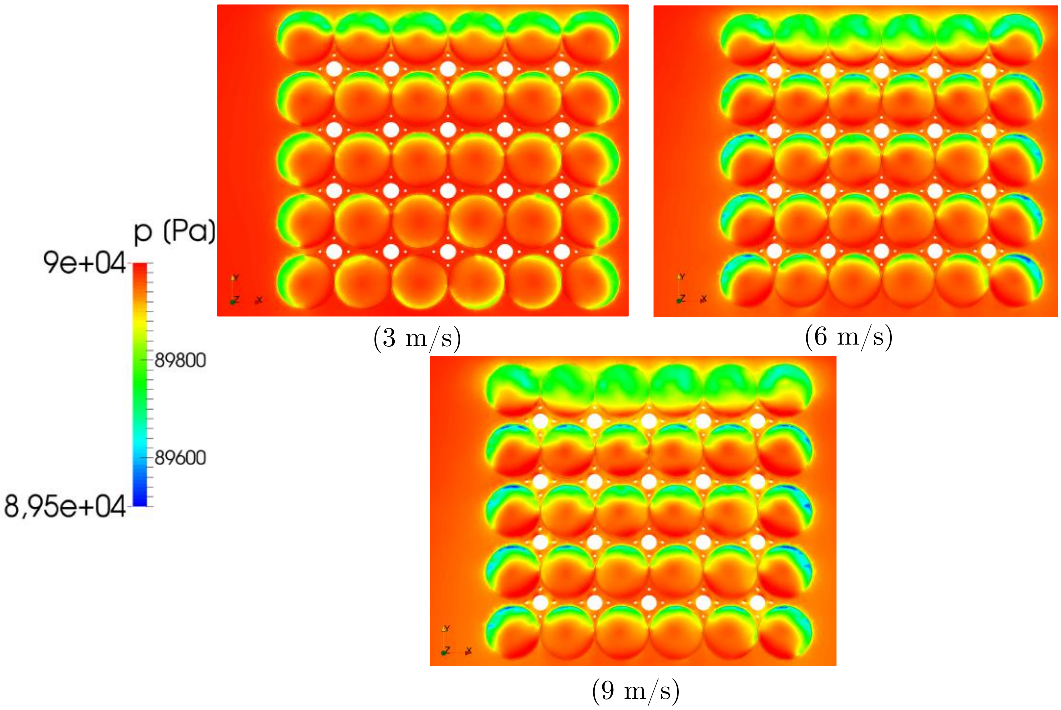

Figure 5.16: Pressure contour of A-fan ACC subject to y-direction wind

Flow separation at the inlet also forms a region of recirculating flow restricting flow to the fan blades and reducing effective blade span utilisation. This reduction of the so-called blade through-flow area, coupled with the decrease in performance due to the presence of the low static pressure region, results in air being drawn into the fan blades at an off-axis or oblique angle to the fan plane of rotation. This deviates significantly from the ideal case where flow is observed to be normal to the fan inlet plane (Joubert, 2010). Also indicated by figure 5.15 is a localised region of reverse flow present in the vicinity of the fan blades. The low static pressure region, along with the decreased fan performance, results in air leaking into the inlet. This also restricts the through-flow area of the blades reducing blade span utilisation.

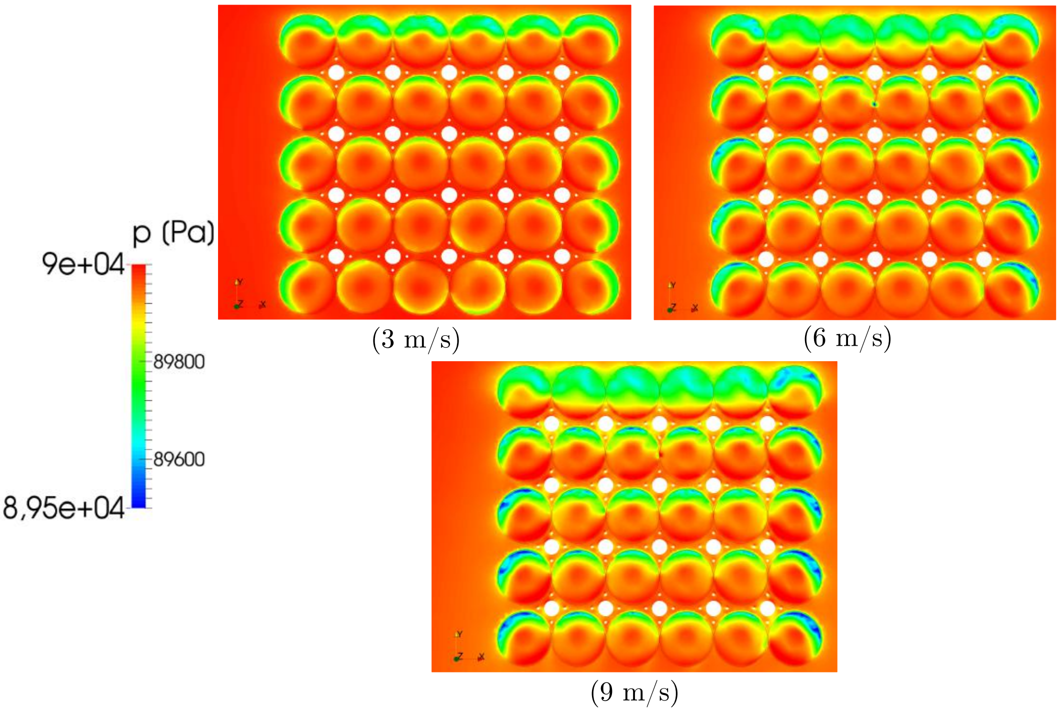

Figure 5.17: Pressure contour of B2a-fan ACC subject to y-direction wind

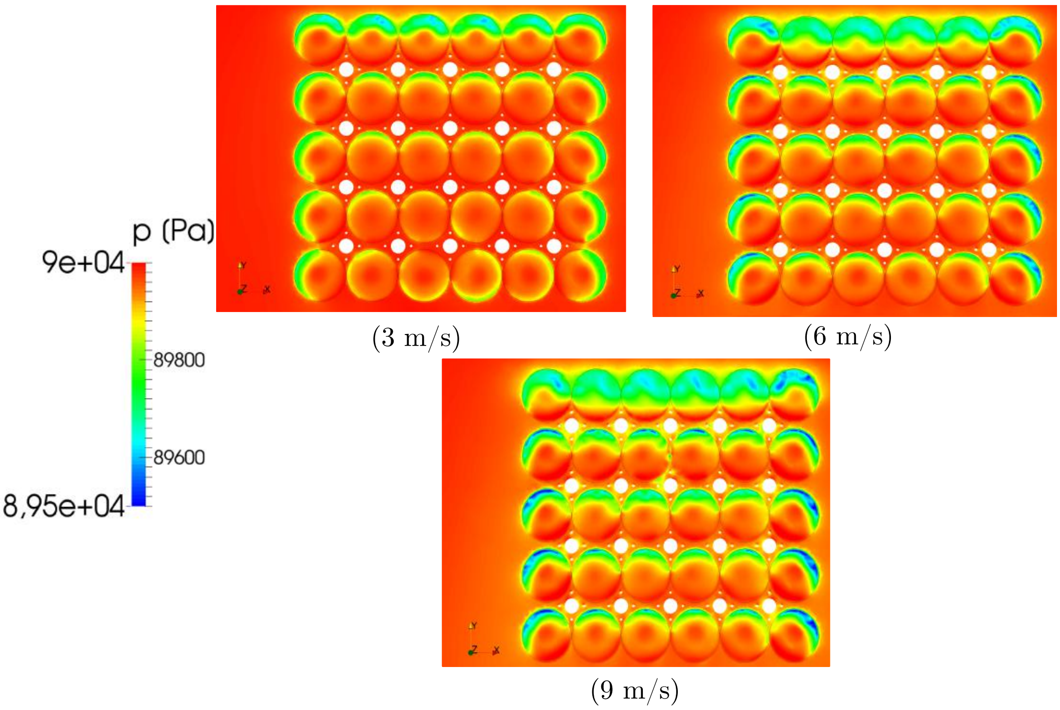

Figure 5.18: Pressure contour of Combined ACC subject to y-direction wind

Louw (2011) also noted the performance degrading effect of two-dimensional flow on the centre, upstream periphery fans. The streamlines, shown in figure 5.19, indicate that fans on the peripheries parallel to the cross-wind are able to draw air from the sides of the ACC. Streamlines in the centre of the ACC indicate constriction of the incoming wind essentially restricting flow to the centre fan to a so-called two-dimensional inlet flow. This decreases the volume of air that can be drawn into the fan inlet degrading volumetric performance.

These three-dimensional flow regions can be observed on the static pressure plots of figures 5.16 to 5.18. The flow separation region, indicating the direction from which the fan draws air, forms around a larger region of the fan inlet as the fans on the edges of the upstream periphery draws air from the sides of the ACC. The constricted and two-dimensional flow can be clearly seen affecting the fans in the centre of the upstream periphery.

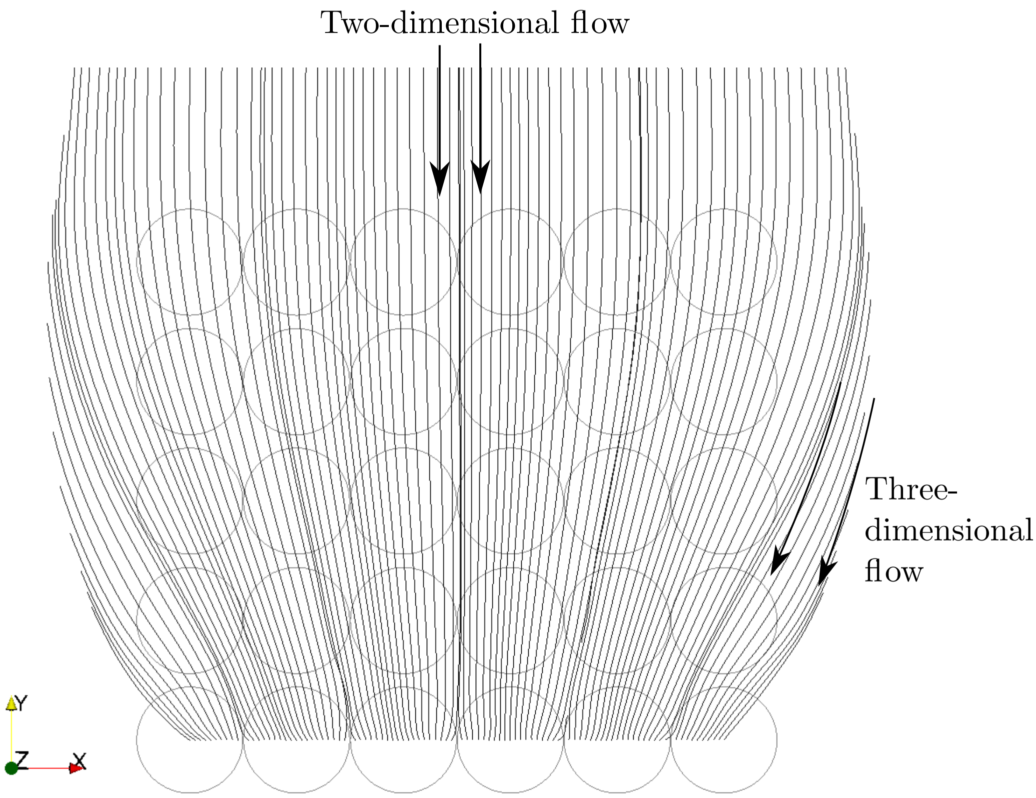

Figure 5.19: Streamlines at fan inlets showing two and three-dimensional flow

The volumetric effectiveness of fans on the downstream periphery remains within a small range for increasing cross-wind speeds. The decrease in volumetric performance of the fans on the upstream periphery is therefore considered as the largest contributor to the decrease in total volumetric performance of the ACC when subjected to cross-winds.

The measured individual fan performance of figure 5.14 also indicates a 19 % improvement in upstream periphery fan performance of the B2a-fan compared to the A-fan. This superior performance of the B2a-fan was also reported for increasing degrees of distorted inflow conditions by Bredell (2005). A possible reason for the poor performance of the A-fan was identified as the decrease in through-flow area, and subsequent effective blade span utilisation, resulting from the recirculation region present at the hub. An effective blade span utilisation of 64 % was measured at the operating point by Bredell (2005). A further decrease in through-flow area results from additional fan blade flow restriction due to distorted inlet conditions. This inevitably results in poor performance of the A-fan on the upstream periphery.

In contrast, the B2a-fan operates below stall for a range of volumetric flow rates as no flow blockage or recirculation occurs due to the enlarged hub. The dependency of the effective blade through-flow area on volumetric flow rate is reduced and a larger blade span is utilised when compared to the A-fan. Increased performance of the B2a-fan on the upstream periphery results as the effective blade span which could be utilised is only reduced by the distorted flow conditions at the inlet. This performance trend for an axial flow fan with a larger hub-to-tip ratio, and steeper static pressure characteristic curve, was also reported by Stinnes and von Backström (2002), Bredell (2005) and van der Spuy (2011).

Upstream periphery fan performance of the Combined ACC is also observed to be higher than the B2a-fan ACC, even if the same fan type was used in both ACCs. Fans in the B2a-fan ACC outperforms the fans in the Combined ACC on the downstream periphery and in the centre of the ACC. A 3-4 % increase in volumetric performance is, however, noted for the fans on the upstream periphery for the Combined ACC. This leads to the higher total volumetric flow rate measured for the Combined ACC compared to the B2a-fan ACC. Both ACCs outperform the A-fan ACC due to the poor performance of the upstream periphery A-fans.

The total power consumption of each ACC at different cross-wind speeds is shown in figure 5.20 with individual fan power consumption shown in figure 5.21. The higher measured power consumption for the ACC unit serviced by the A-fan under ideal conditions, explains the 6-10 % higher power requirement of the A-fan ACC compared to the B2a-fan ACC. The power requirement of the Combined ACC is nearly identical to that of the A-fan ACC. This is in part due to the high power requirements of the A-fans in the centre of the ACC as well as higher power consumption of the B2a-fans on the peripheries. It is expected that the increased volumetric performance of the B2a-fans on the peripheries leads to the higher fan power requirements.

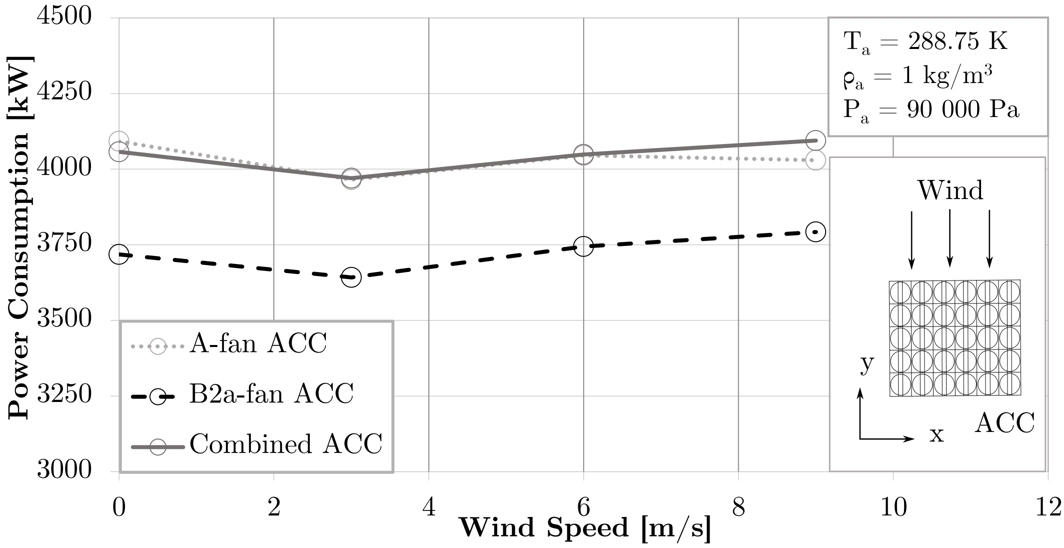

Figure 5.20: Total power consumption subject to y-direction cross-wind

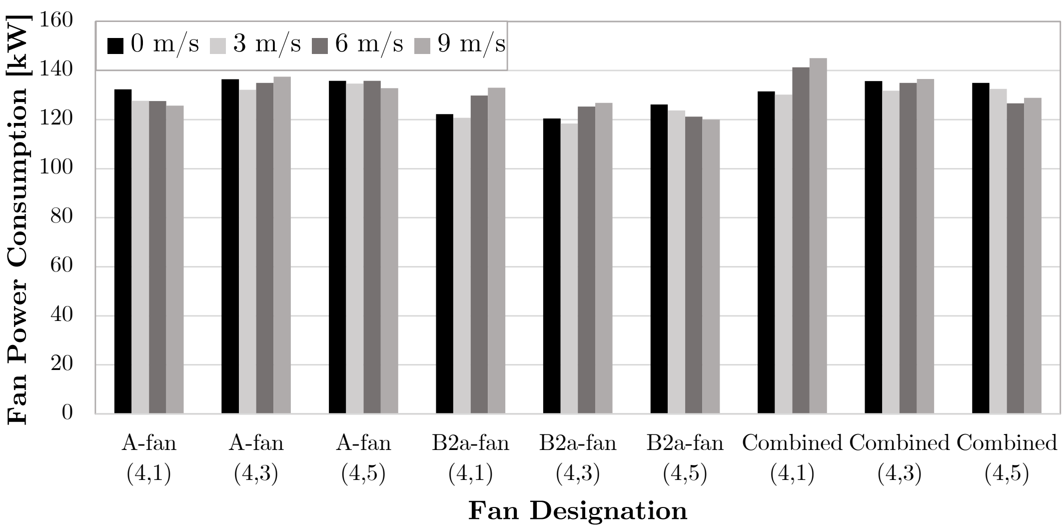

Figure 5.21: Fan power consumption subject to y-direction cross-wind

5.3.2 Cross-Wind Speed Evaluation (x-direction)

The total volumetric flow rate and volumetric effectiveness for each ACC, subject to cross-winds in the direction normal to the short axis (x-direction), is shown in figure 5.22 and 5.23. A decrease in volumetric performance with increasing cross-wind speeds is clearly observed. Higher volumetric flow rates and volumetric effectiveness is observed through each ACC, compared to the y-direction wind case, resulting from the smaller number of upstream periphery fans. The volumetric effectiveness of fans in each ACC is shown in figure 5.24.

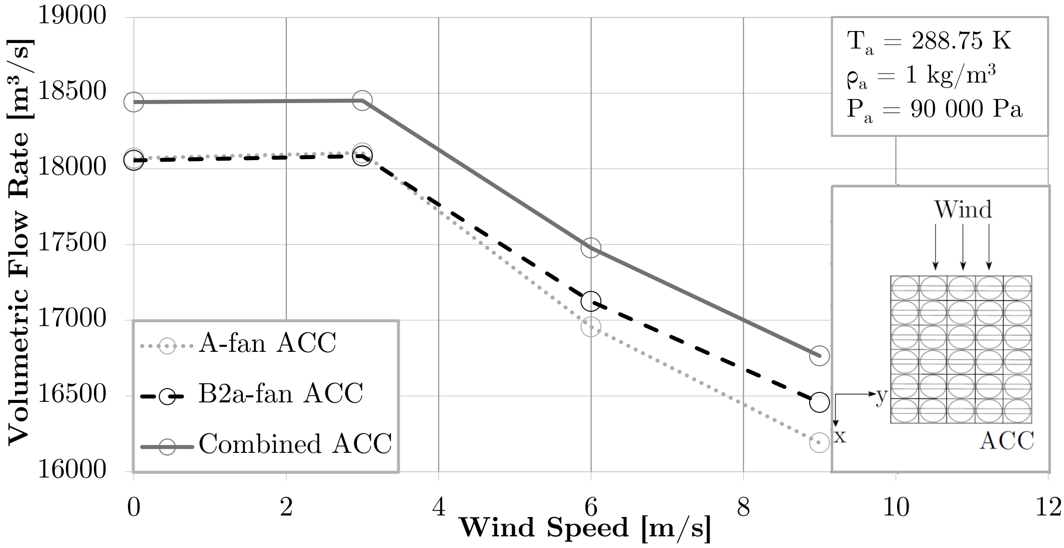

Figure 5.22: Total volumetric flow rate subject to x-direction cross-wind

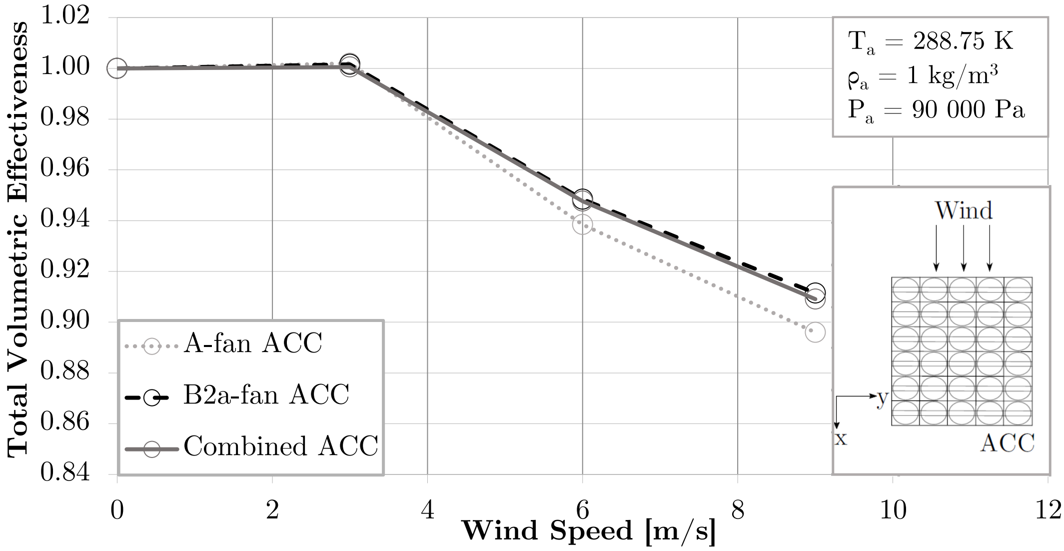

Figure 5.23: Volumetric effectiveness subject to x-direction cross-wind

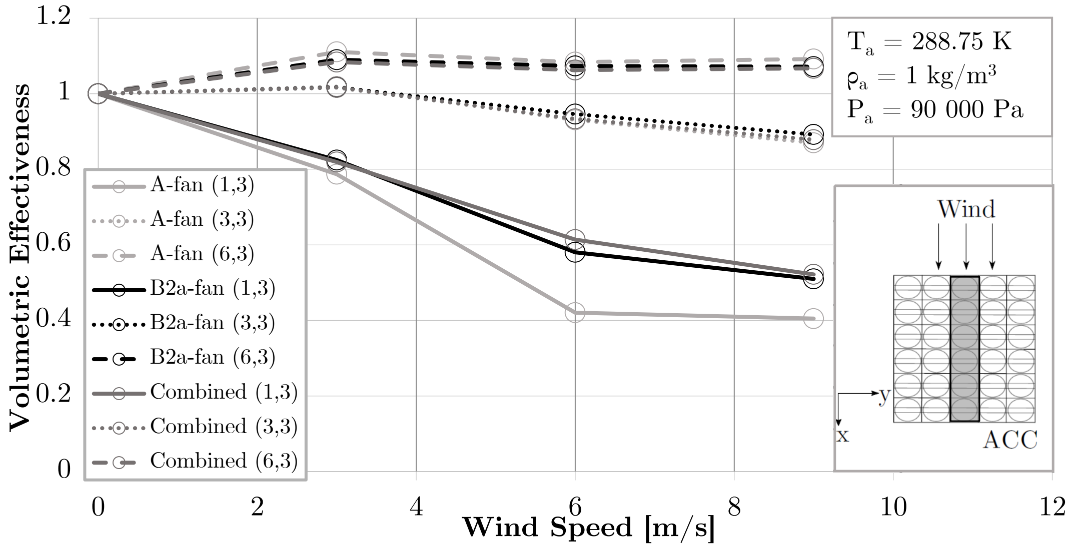

Figure 5.24: Volumetric effectiveness of fans subject to x-direction cross-wind

Orientating the cross-wind in the x-direction results in clear fan volumetric performance differences when compared to the y-direction case. A 5 % increase in volumetric effectiveness was measured for the downstream periphery fans when the long axis of the ACC is orientated parallel to the cross-wind direction. This increased length between the upstream and downstream periphery decreases the severity of distorted fan inlet flow leading to more idealised inlet flow conditions which benefits fan performance. Similar volumetric effectiveness was measured for the B2a-fans on the upstream periphery for all cross-wind speeds, compared to the y-direction case, whereas a significant decrease in volumetric performance is noted for the A-fan as the cross-wind speed increases from 3 to 6 m/s. A similar volumetric effectiveness was, however, measured for the A-fan at cross-wind speeds of 6 and 9 m/s.

This performance trend of the upstream A-fan indicates increased sensitivity of performance to flow distortion exists depending on the orientation of the ACC to the cross-wind direction. It is expected that the geometrical set-up of the ACC results in this mentioned decrease in performance. This is illustrated by comparing the inlet flow velocity vector plot of an x and y-direction cross-wind in figure 5.25. The spacing allows air to flow between the fan inlets in the x-direction case. This results in larger regions of flow separation forming at the edges, and a larger section of the fan blades experiences distorted inflow. This further restricts the through-flow area required for proper blade span utilisation. As the A-fan performs poorly under these conditions, these enlarged regions of distorted inflow results in a further decrease in performance as opposed to the y-direction case.

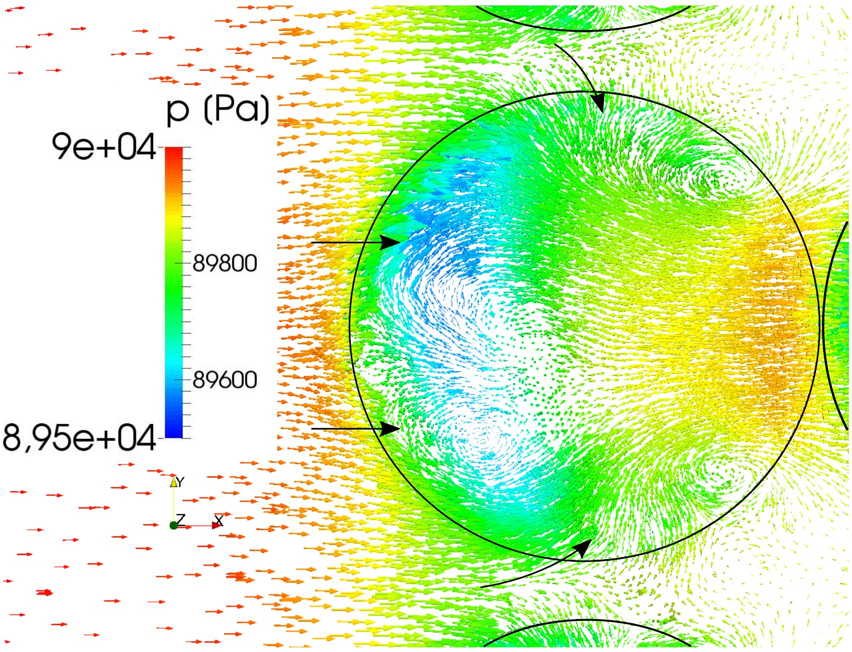

(a)

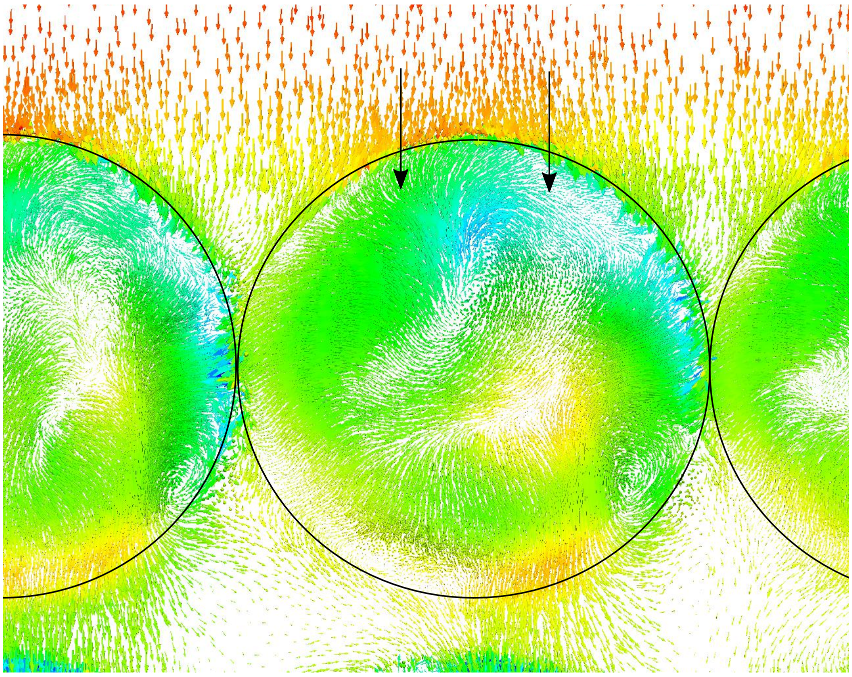

(b)

Figure 5.25: Vector plot at fan inlet for a) x-direction and b) y-direction cross-wind

These enlarged regions of flow separation present at the fan inlets are illustrated by the static pressure plots of figure 5.26 to 5.28.

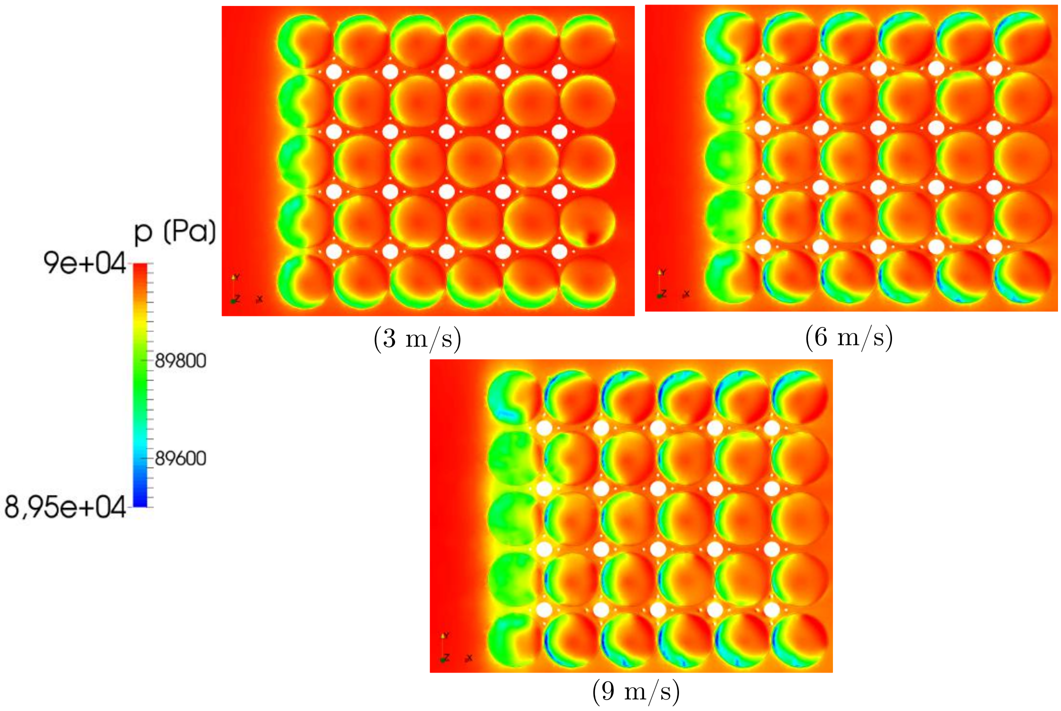

Figure 5.26: Pressure contour of A-fan ACC subject to x-direction wind

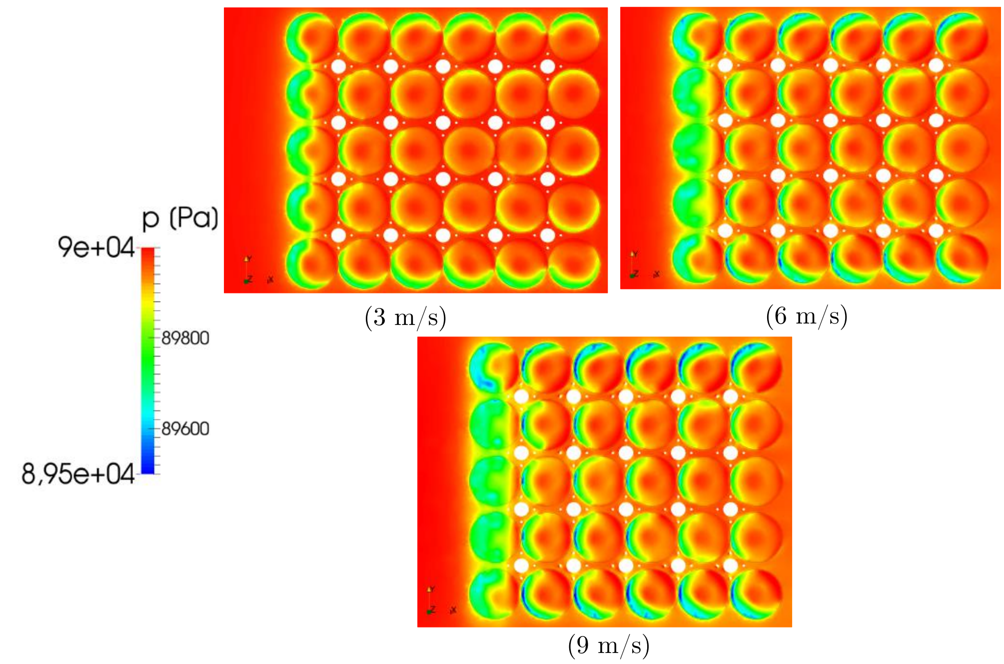

Figure 5.27: Pressure contour of B2a-fan ACC subject to x-direction wind

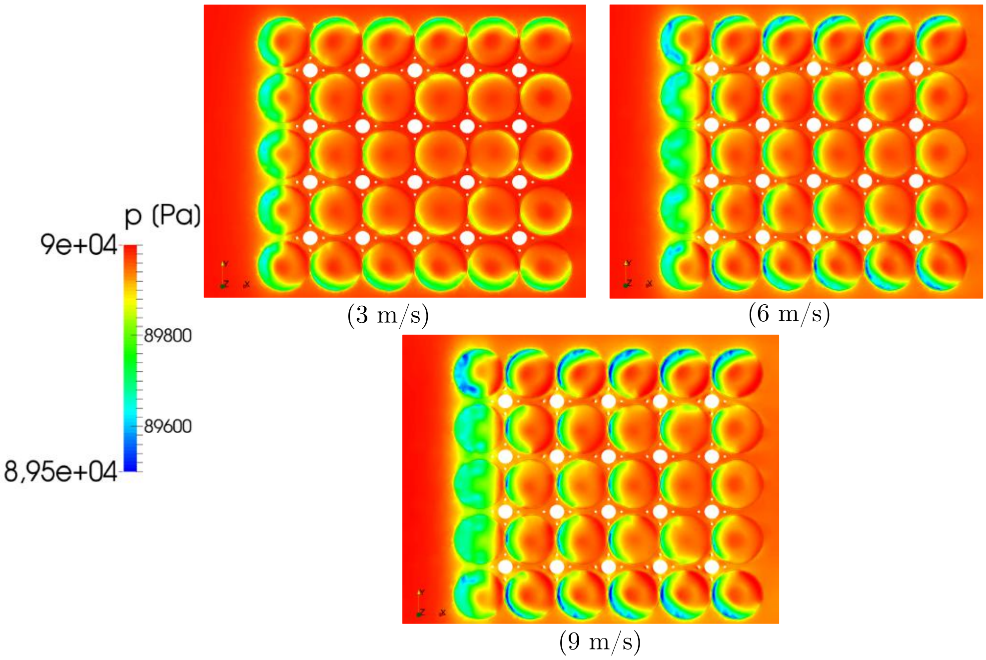

Figure 5.28: Pressure contour of Combined ACC subject to x-direction wind

Total power consumption of each ACC is shown in figure 5.29 and individual fans power consumption in figure 5.30. The power consumed for each ACC is near identical to the y-direction cross-wind case. As previously noted, higher power requirements of the A-fans results in increased power consumption of the A-fan ACC compared to the B2a-fan ACC. Increased periphery fan performance also results in higher power consumption of the B2a-fans in the Combined ACC, subsequently increasing total power consumption.

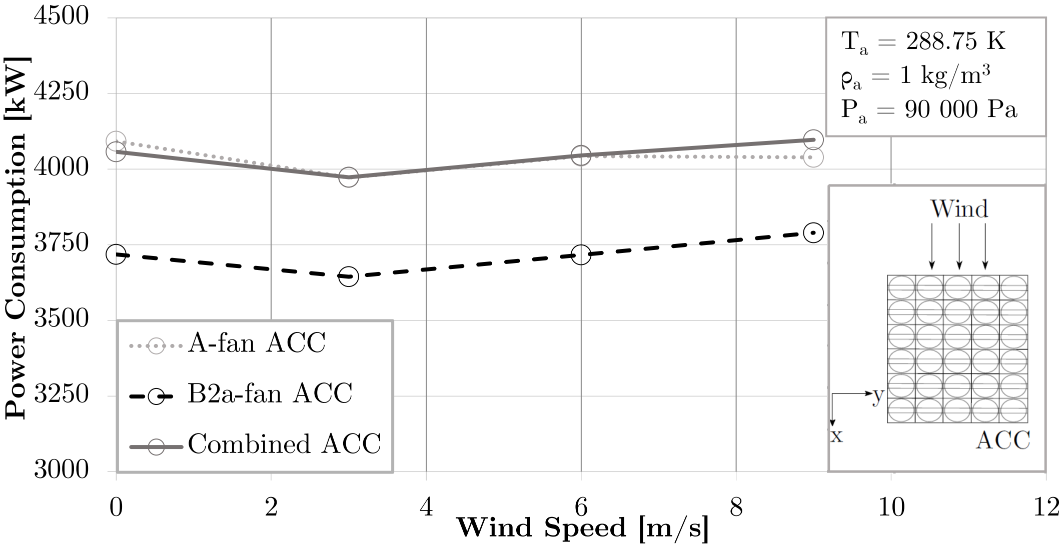

Figure 5.29: Total power consumption subject to x-direction cross-wind

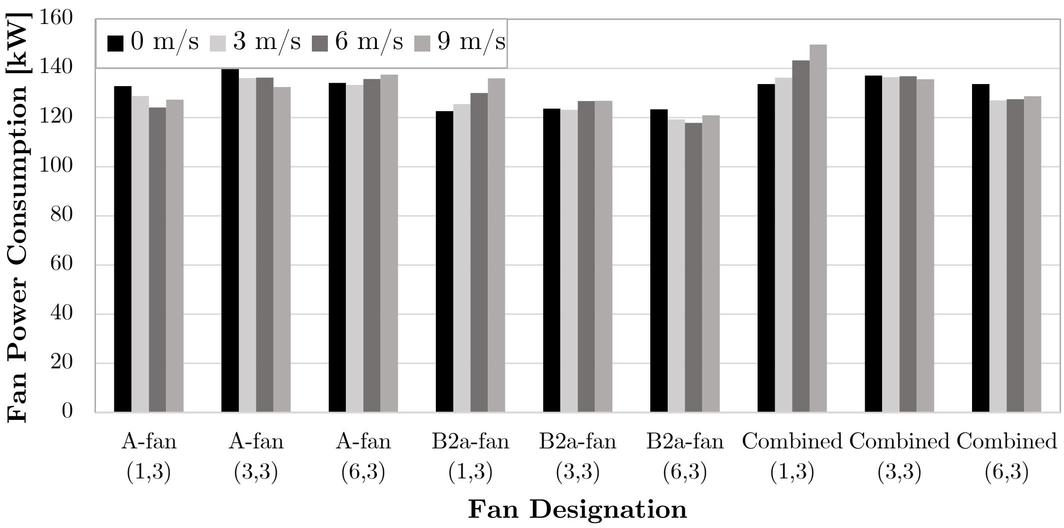

Figure 5.30: Fan power consumption subject to x-direction cross-wind

5.3.3 Wind Direction Evaluation

The total volumetric effectiveness of the ACC is shown for each cross-wind direction, at different speeds, in figures 5.31 to 5.33. Total volumetric performance fluctuations up to 4 % were measured for the A-fan ACC and 3 % for the B2a-fan ACC and Combined ACC as the cross-wind directions changes at a speed of 9 m/s. This coincides with the previous observation that volumetric performance is dependant on the ACC orientation to the cross-wind direction.

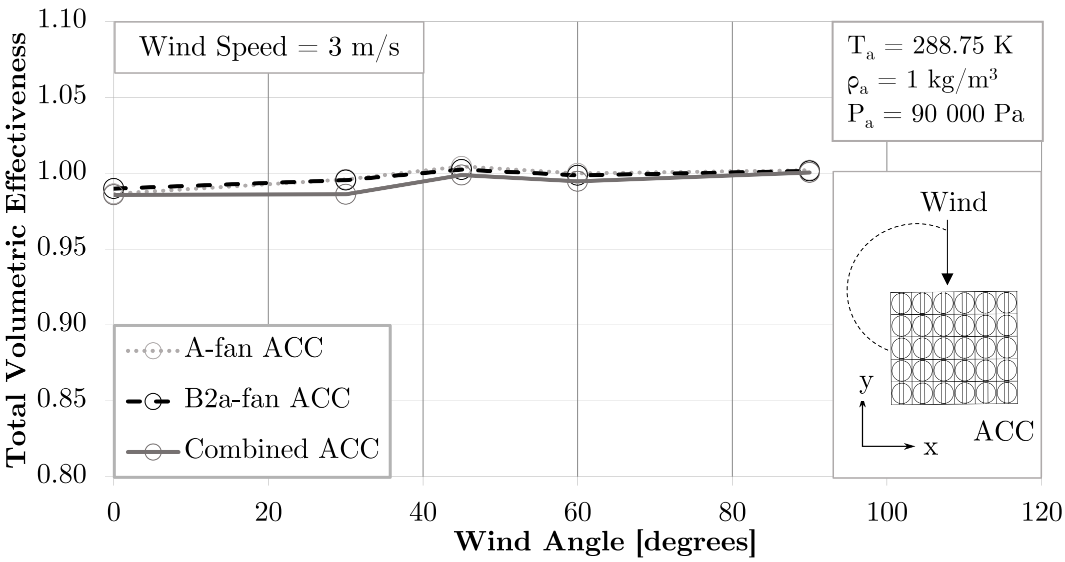

Figure 5.31: Total volumetric effectiveness for a 3 m/s cross-wind

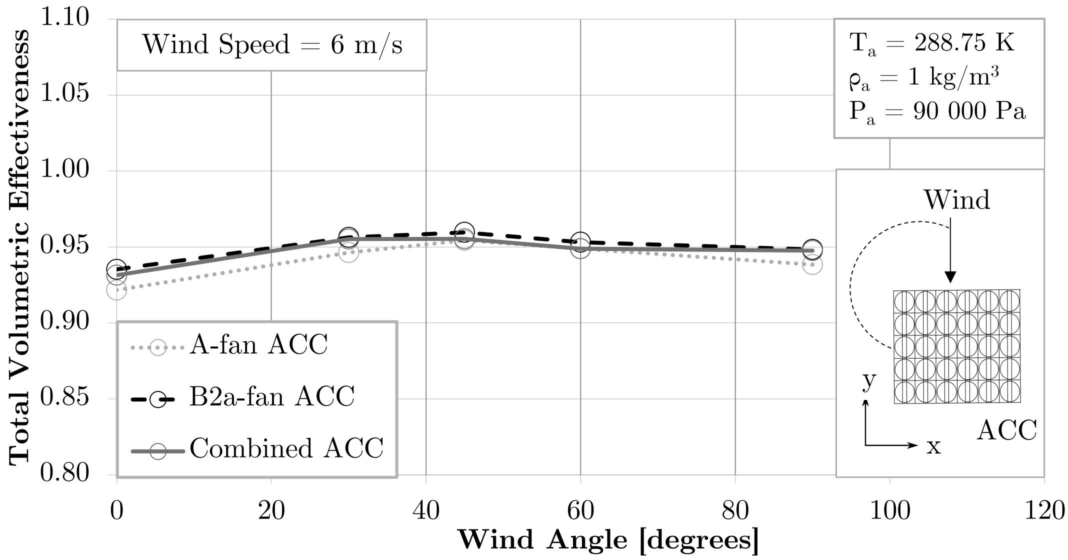

Figure 5.32: Total volumetric effectiveness for a 6 m/s cross-wind

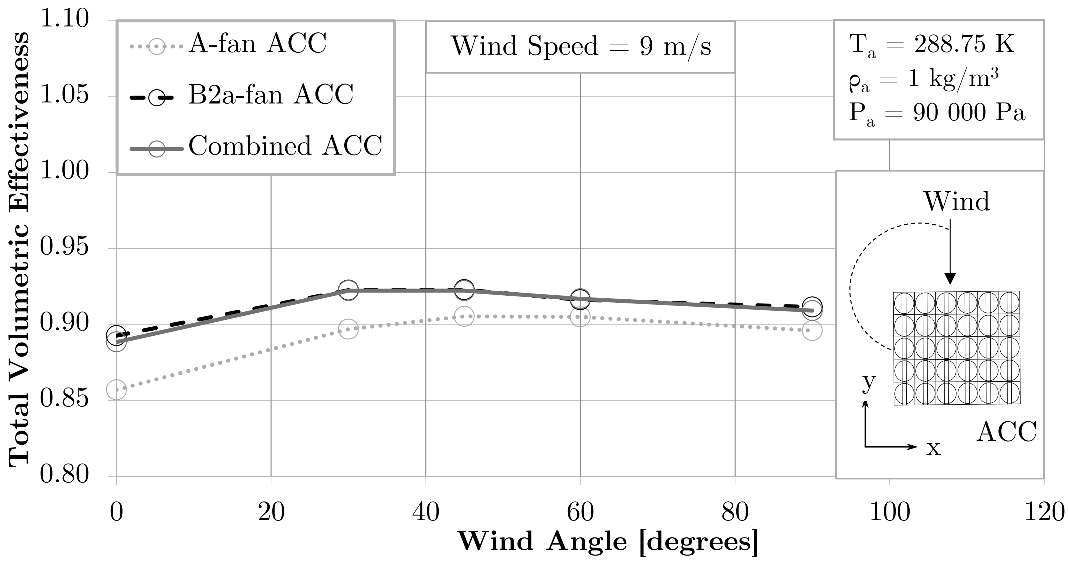

Figure 5.33: Total volumetric effectiveness for a 9 m/s cross-wind

The volumetric performance of each ACC follows a similar trend with peak performance measured for wind directions of 30-60^o. The lowest measured volumetric effectiveness was measured for a 0^o wind as the longer periphery is considered to be upstream of the wind direction. As previously mentioned, the smaller number of periphery fans benefits the ACC performance for a 90^o wind compared to the 0^o case. The higher fluctuations in volumetric performance for higher wind speeds indicates that a stronger correlation between ACC performance and ACC to cross-wind orientation exists at higher wind speeds.

The A-fan ACC shows the highest fluctuations in measured performance for different wind directions. This is indicative of a stronger correlation of ACC performance to cross-wind orientation compared to the B2a-fan ACC and Combined ACC. This is illustrated through individual fan performance in figure 5.34 and 5.35 for a cross-wind speed of 6 m/s. Similar performance was measured for the A-fan and B2a-fan in the centre and downstream peripheries of all ACCs, regardless of wind directions. The ACC performance correlation to cross-wind orientation therefore stems from upstream periphery fan performance trends highlighted by the performance of fan (4,1) in figure 5.34 and fan (1,4) in figure 5.35 for a 0^o and 90^o wind, respectively.

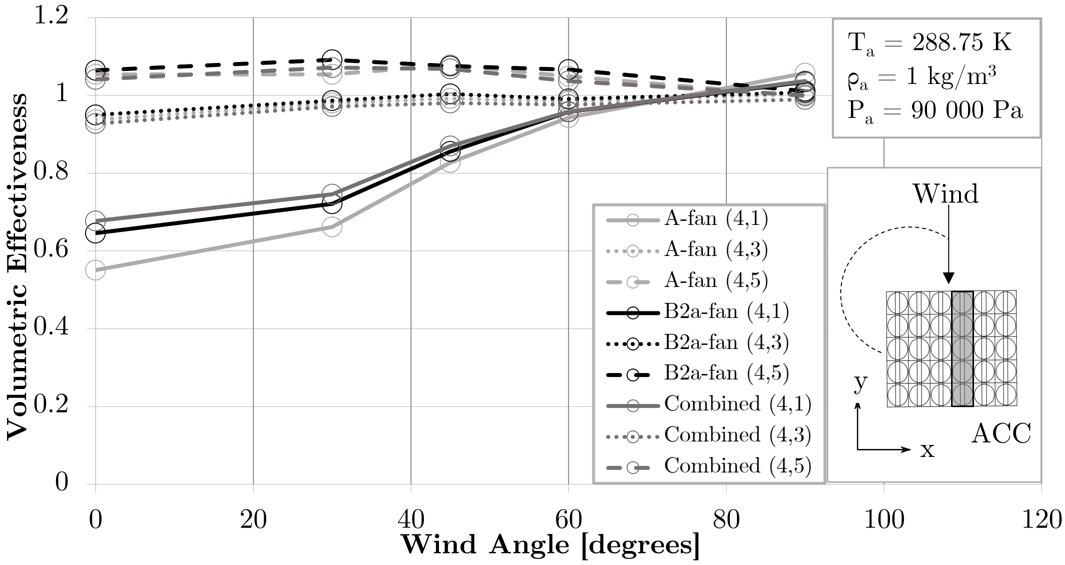

Figure 5.34: Volumetric effectiveness of fans for a 6 m/s cross-wind

The largest decrease in performance was measured for the upstream A-fan in the A-fan ACC. As downstream fan performance is observed to be constant, the increased performance sensitivity to ACC orientation therefore arises from the poor performance of the upstream A-fan. The higher measured performance of the B2a-fan in the B2a-fan ACC and Combined ACC decreases this sensitivity of volumetric performance leading to more consistent performance for different cross-wind conditions.

Peak performance for wind directions of 30-60^o is discussed by considering the performance of fan (6,4). The fan benefits from these wind conditions as an effectiveness up to 1.14 was measured. This results from relatively low distortion of the air at the fan inlet as it travels below the ACC platform. Orientating the ACC at an angle to the wind direction effectively lengthens the path the air travels below the fan inlets, further decreasing inflow distortion

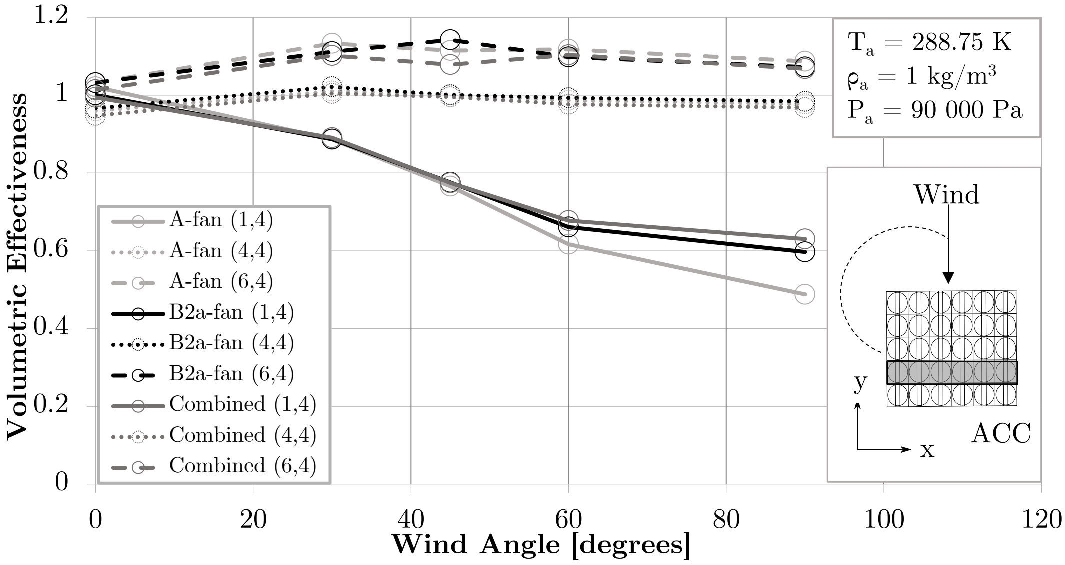

Figure 5.35: Volumetric effectiveness of fans for a 6 m/s cross-wind

at the downstream periphery. This is especially prominent along the 45^o wind direction case as wind travels diagonally across the ACC platform. Maximum volumetric effectiveness was measured for this fan at a 45^o wind direction case, as the fan is considered to be furthest from the upstream side of the ACC. This is also applicable to fans neighbouring fan (6,4), and the small separation regions are illustrated by the static pressure contour plots of figures 5.36 to 5.38.

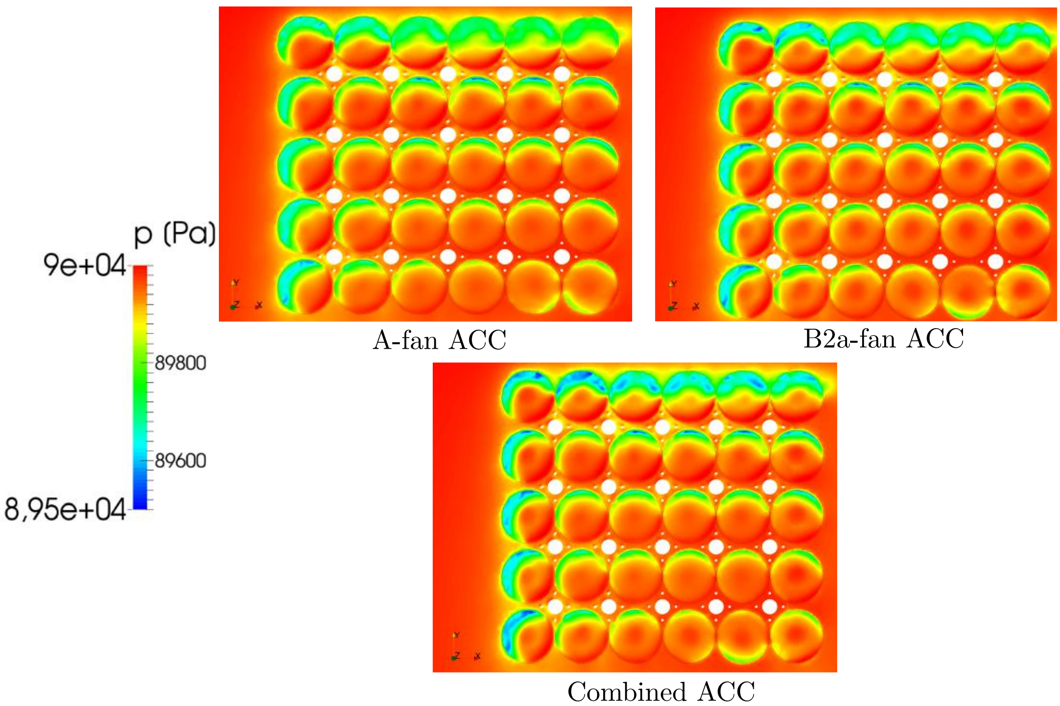

Figure 5.36: Pressure distribution of fan inlets subject to 30^o, 6 m/s cross-wind

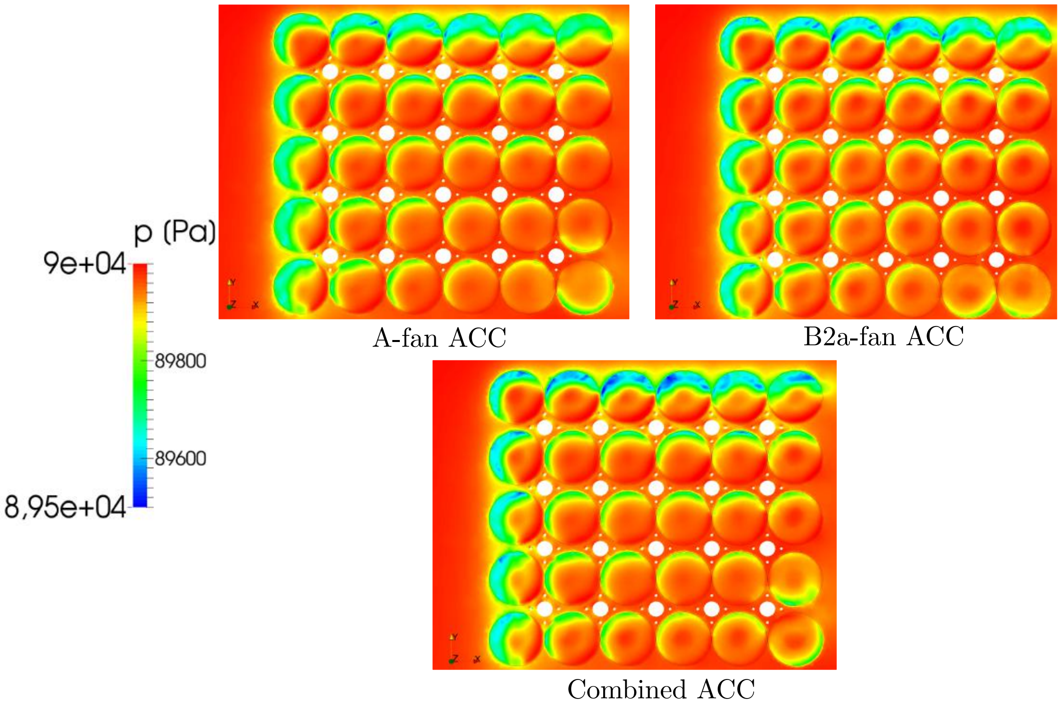

Figure 5.37: Pressure distribution of fan inlets subject to 45^o, 6 m/s cross-wind

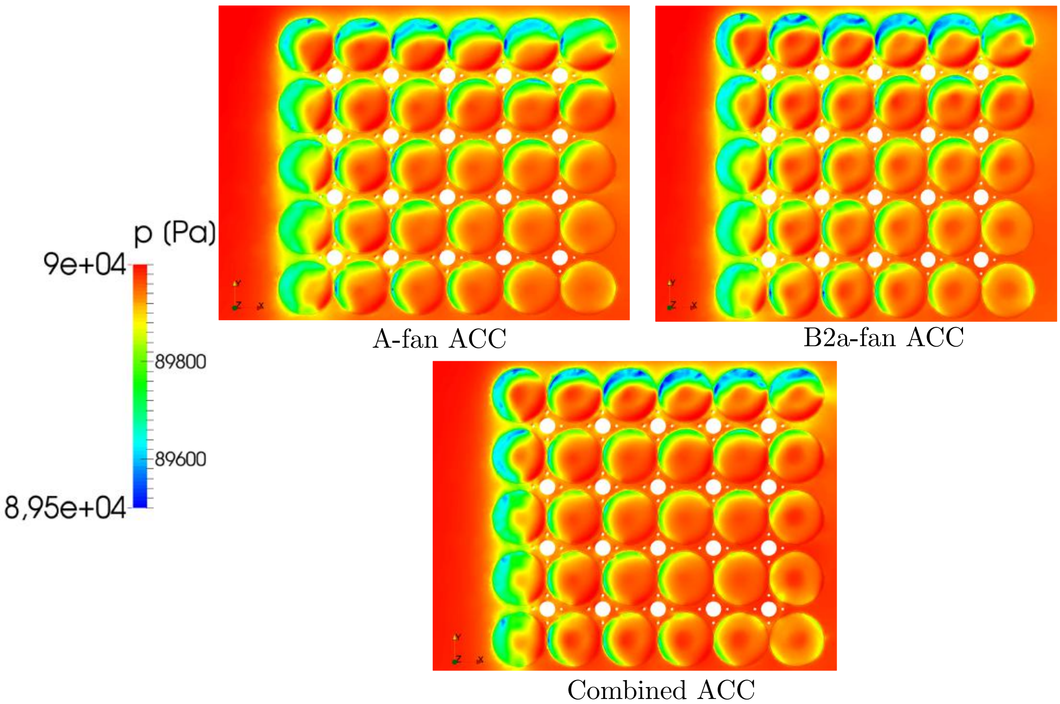

Figure 5.38: Pressure distribution of fan inlets subject to 60^o, 6 m/s cross-wind

The total power consumption of each ACC subject to increasing cross-wind speeds along different directions is shown in figures 5.39 to 5.41.

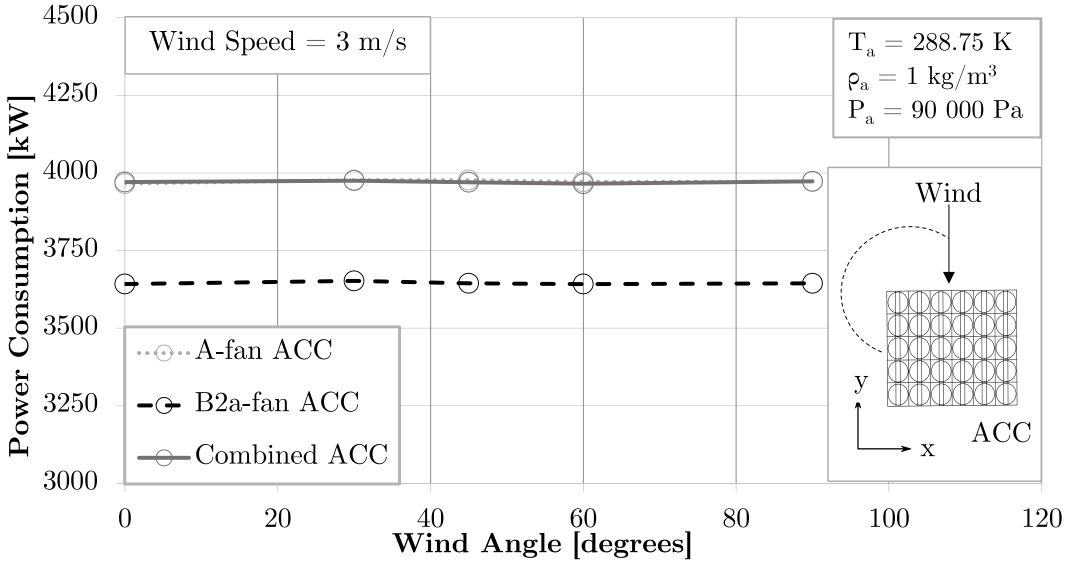

Figure 5.39: Total power consumption of each ACC for a 3 m/s cross-wind

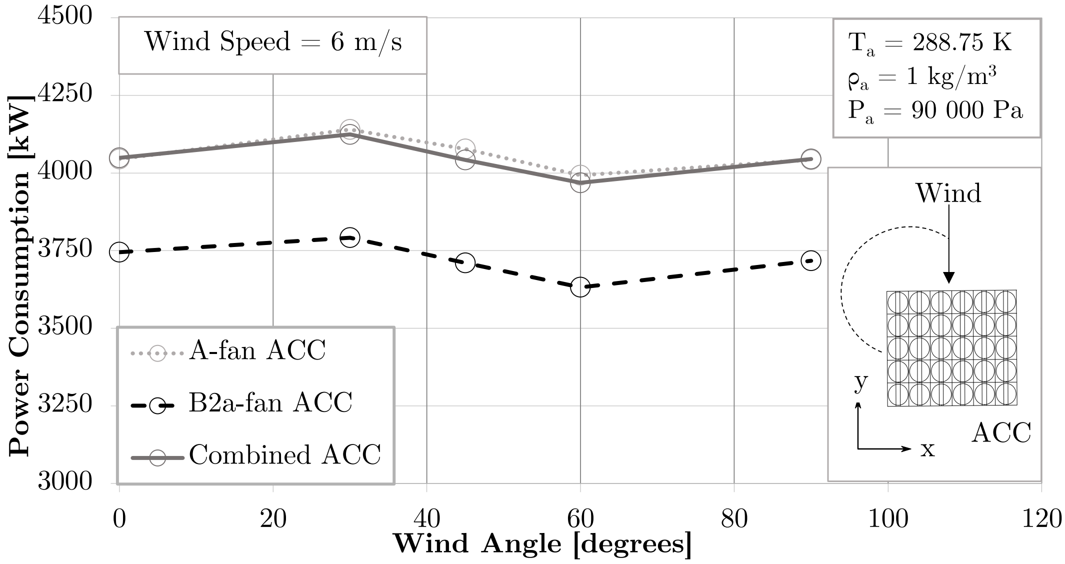

Figure 5.40: Total power consumption of each ACC for a 6 m/s cross-wind

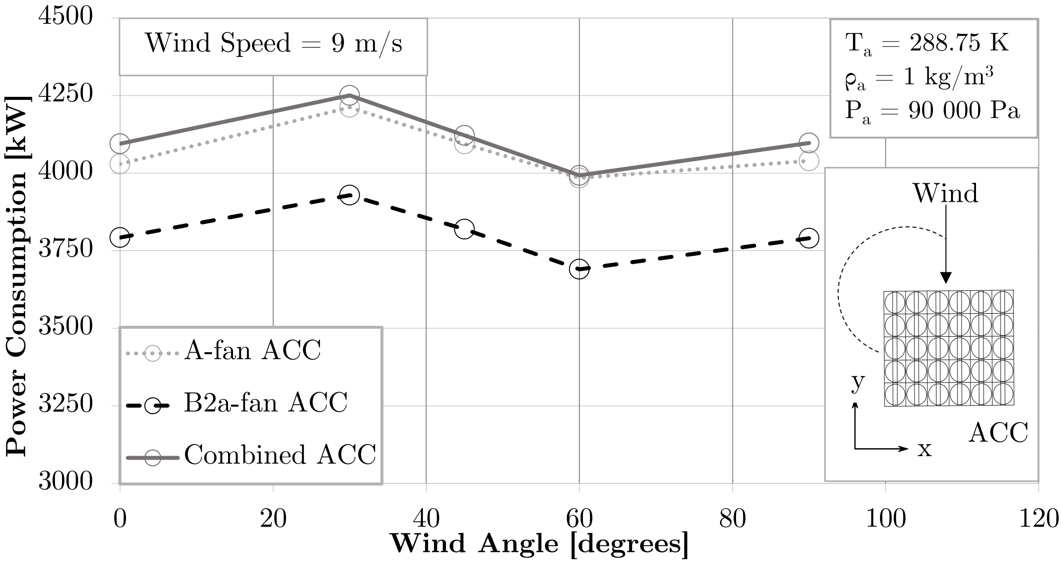

Figure 5.41: Total power consumption of each ACC for a 9 m/s cross-wind

Minor fluctuations are noted for each ACC between wind directions for a speed of 3 m/s with significant fluctuations measured at higher cross-wind speeds. The power consumed per ACC follows similar trends with a peak consumption at 30^o wind direction, due to the increased volumetric flow rate of the downstream fans, and the lowest power consumption at 60^o wind direction. Also noted is the superior performance of the B2a-fan ACC with a 7.52-9.94 % lower power consumption than the A-fan and Combined ACC. The power consumption of the A-fan ACC and Combined ACC are similar for all wind speeds regardless of wind direction.

5.4 Thermal Performance

This section details the thermal performance evaluation of the ACC bank subjected to cross-winds. Similar to the procedure followed for the volumetric performance, the thermal performance was evaluated with regard to increasing cross-wind speeds along the y and x-direction. A comparative analysis of the performance when the ACC is subjected to different cross-wind directions, as depicted in figure 5.11, follows.

5.4.1 Cross-Wind Speed Evaluation (y-direction)

The total heat transfer rates for each ACC, subjected to a cross-wind in the direction normal to the long axis of the ACC (y-direction), is shown in figure 5.42. Similar to the volumetric flow rate, a decrease in total heat transfer rate was measured for increasing cross-wind speeds. This is an expected trend as the heat transfer of the heat exchanger is strongly correlated to the volumetric flow rate through the heat exchanger. Thermal performance of the B2a-fan ACC and Combined ACC decrease by approximately 9 % when the cross-wind speed increases to 9 m/s. The A-fan ACC exhibits a higher sensitivity to cross-wind speed as the thermal performance decreases by 12 % compared to the no cross-wind case. This is due to the the poor volumetric performance of the A-fan ACC when subjected to higher cross-wind speeds.

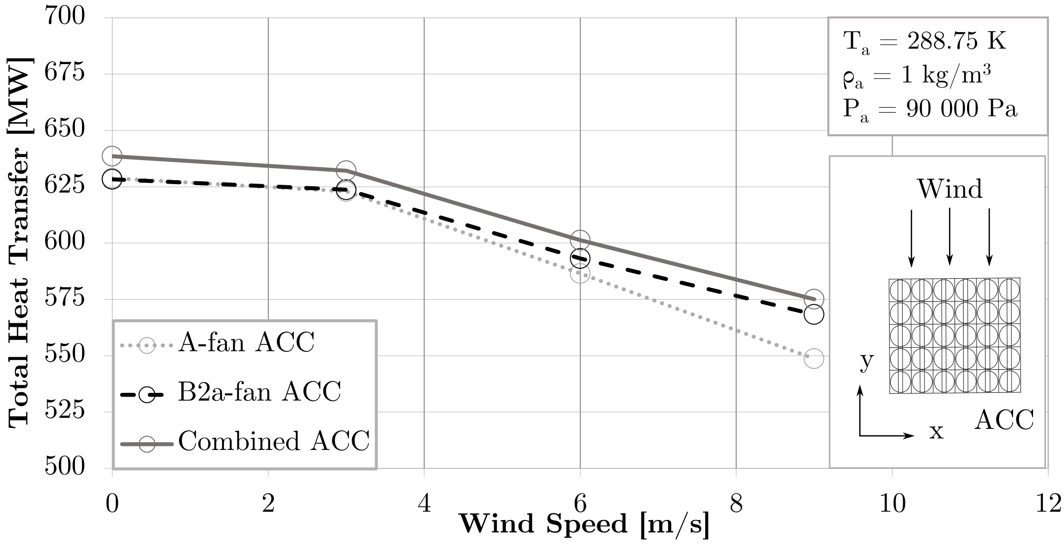

Figure 5.42: Total heat rejected by the ACC subject to cross-wind

Two phenomena have been identified leading to decreased thermal performance when an ACC is subjected to cross-winds. The first being heated plume recirculation. This occurs when the heated air expelled from the heat exchangers is drawn back into the plenum, increasing the air inlet temperature and decreasing heat transfer capabilities (Owen, 2010). It has also been observed that larger quantities of heated air is recirculated as the cross-wind speed increases. This is known to affect heat exchangers situated on the downstream periphery, and the periphery parallel to the cross-wind direction (Duvenhage *et al.*, 1996).

Decreased thermal performance of heat exchangers on the downstream periphery is discussed by considering the temperature plot of figure 5.43 which illustrates plume rise. As the cross-wind speed increases, the poor volumetric performance of the fans on the upstream periphery decreases the heat transfer capabilities of the heat exchangers. The heated air plume is therefore released closer to the downstream periphery of the ACC (Owen, 2010; Louw, 2011) and is subsequently drawn back into the heat exchanger plenum.

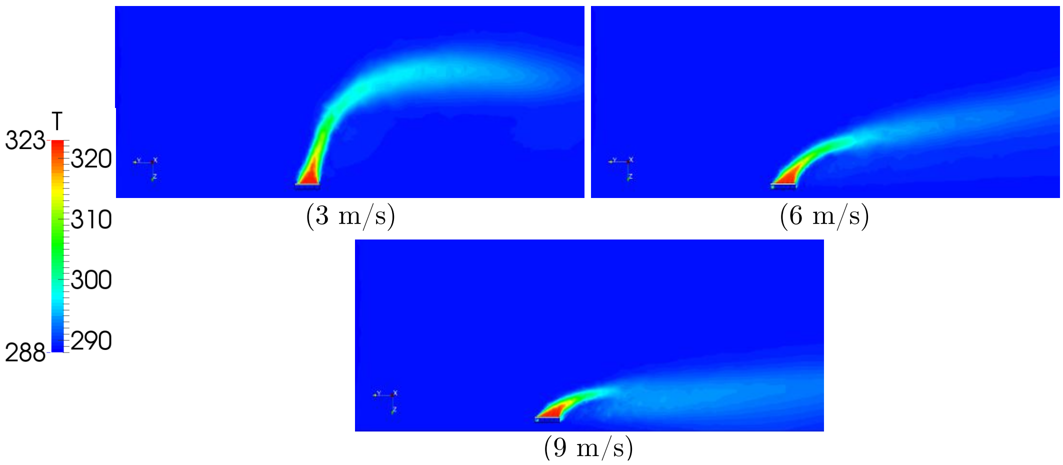

Figure 5.43: Side view through fan row 4 illustrating plume rise

Recirculating heated air also affects heat exchangers on the peripheries parallel to the cross-wind direction as the windwalls contributes to the formation of vortices. These vortices entrains heated air below the periphery of the ACC and is consequently drawn back into the fan inlets (Louw, 2011). The streamline plot of figure 5.44 illustrates vortex shedding and recirculation on the affected peripheries.

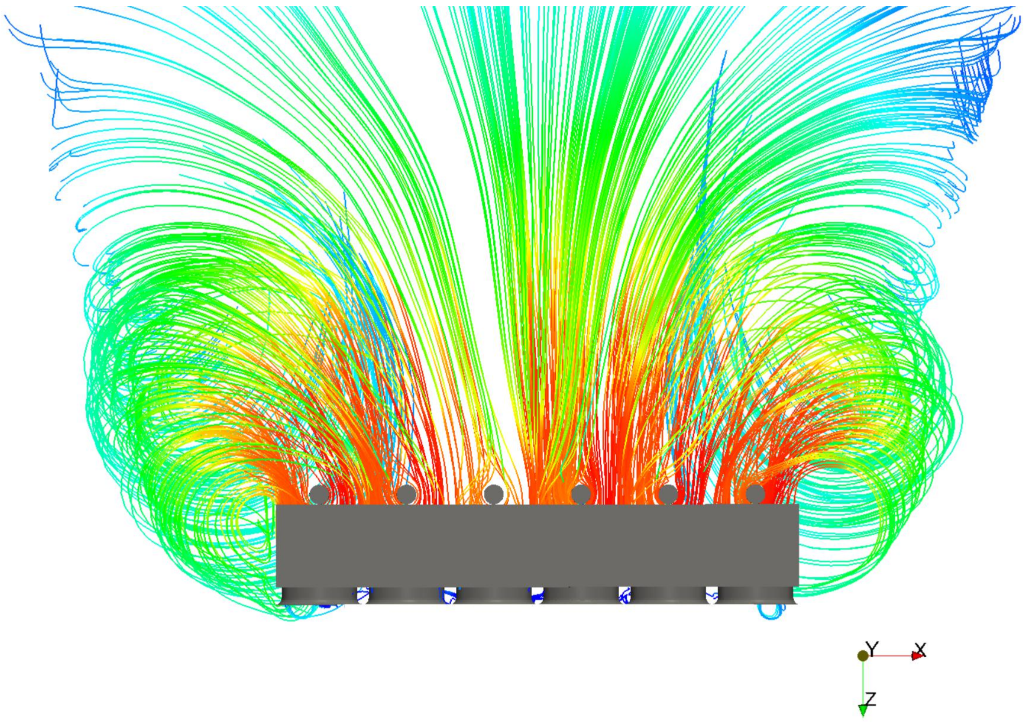

Figure 5.44: Streamlines showing recirculation and vortex formation

The second identified phenomena leading to decreased thermal performance affects heat exchangers on the upstream periphery. The previously discussed region of reverse flow, resulting from distorted inlet conditions, draws heated air from outside the heat exchanger into the plenum. This subsequently increases air inlet temperature, and compounded by reduced volumetric flow rates significantly decreases heat transfer rates.

Figure 5.45 shows the measured heat transfer rates for individual heat exchangers at a cross-wind speed of 9 m/s. The identified thermal performance degrading phenomena affecting each heat exchanger is also indicated. Distinct differences in thermal performance between the heat exchangers is observed depending on the fan type used. Higher heat transfer rates were measured for the heat exchangers on the upstream periphery serviced by the B2a-fan compared to the A-fan. As previously discussed, the increased volumetric performance of the B2a-fans under distorted inlet conditions reduces the size of the reverse flow region formed in the plenum. This consequently reduces the degree to which heat exchangers serviced by the B2a-fan is affected by reverse flow conditions. Negligible thermal performance differences were measured for heat exchangers affected by recirculation, regardless of fan type.

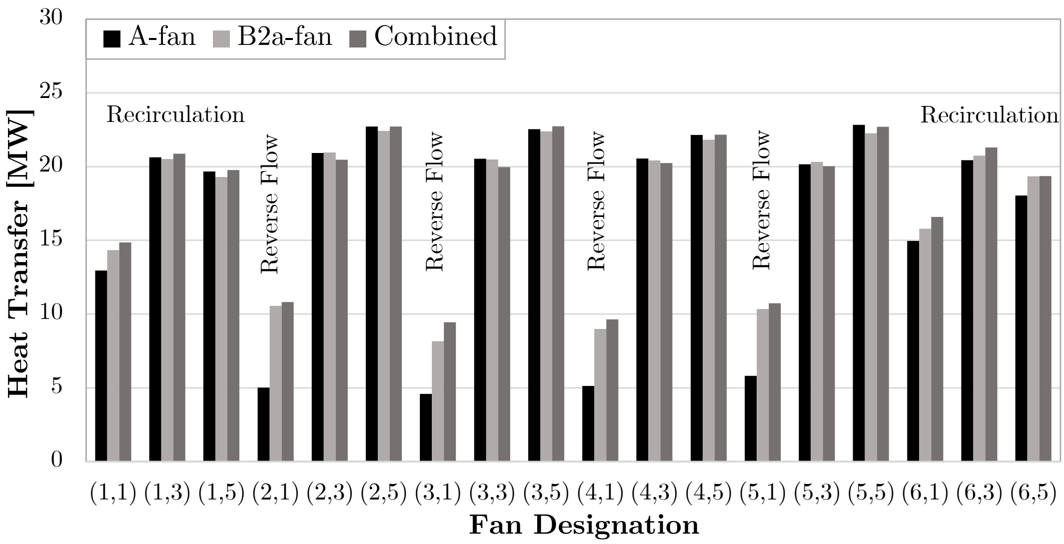

Figure 5.45: Heat transfer rates measured subject to a 9 m/s cross-wind

The air inlet temperatures of the downstream heat exchangers are shown in figure 5.46 where thermal performance was observed to be primarily affected by hot plume recirculation, illustrated by the temperature plots of figures 5.47 to 5.49. Similar inlet air temperatures were measured for the A-fan ACC and Combined ACC, even though two different fan types were used. In the case of the A-fan ACC, the plume was ejected closer to the downstream periphery due to the decreased upstream fan performance. In the case of the Combined

ACC, the higher measured total volumetric flow rate draws more heated air below the platform resulting in increased recirculating flow and higher air inlet temperatures. This is clearly indicated by the temperature plots of figure 5.47 and 5.49 respectively. The volumetric flow rate through the B2a-fan ACC, however, appears to eject the plume high enough to not affect the downstream fans to the same degree as the other ACCs. Similar thermal performance to the B2a-fan ACC was, however, measured at these heat exchangers due to higher fan performance for the A-fan ACC and Combined ACC.

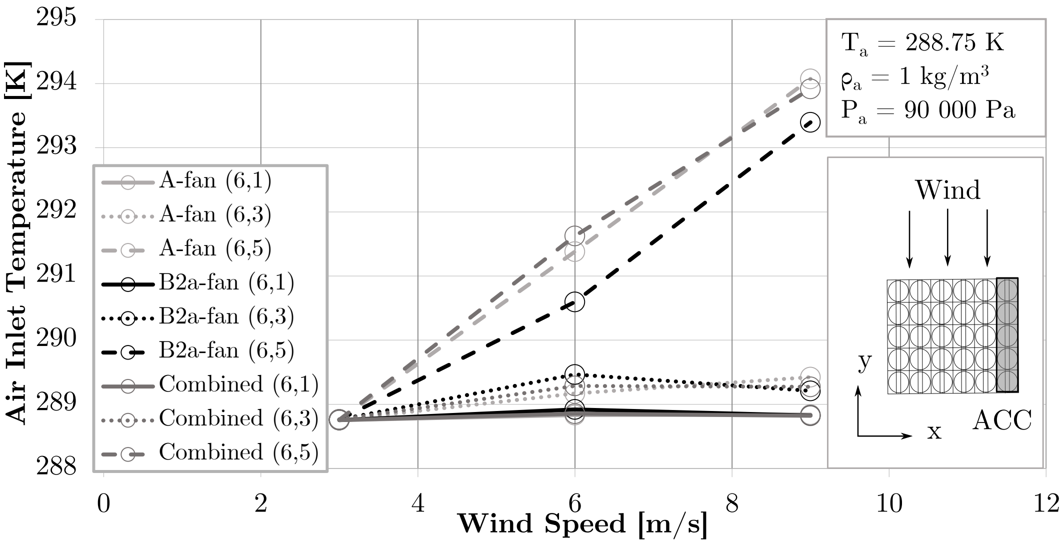

Figure 5.46: Air inlet temperatures of periphery fans

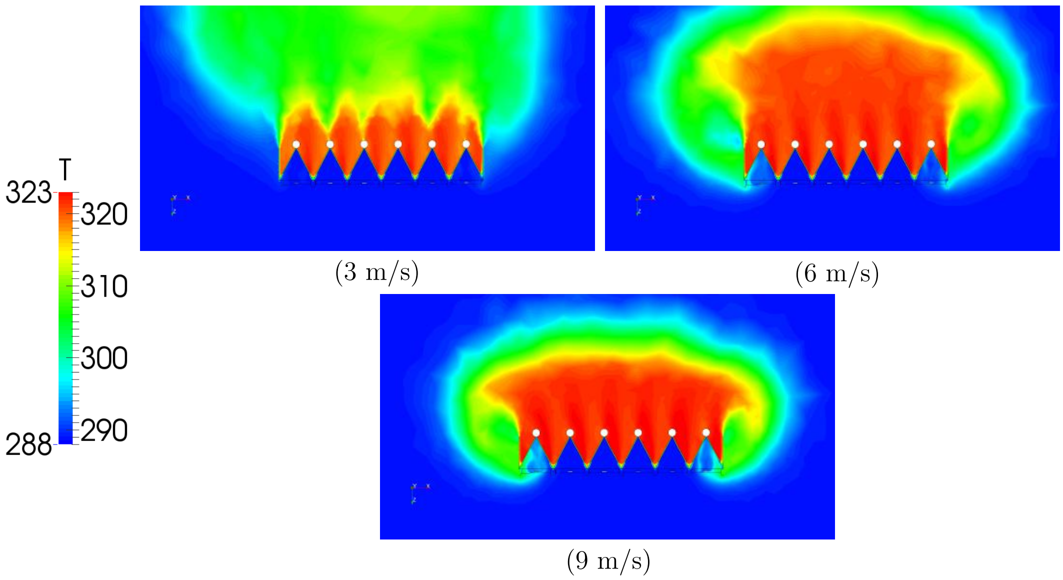

Figure 5.47: Plume recirculation through fan column 5 of A-fan ACC

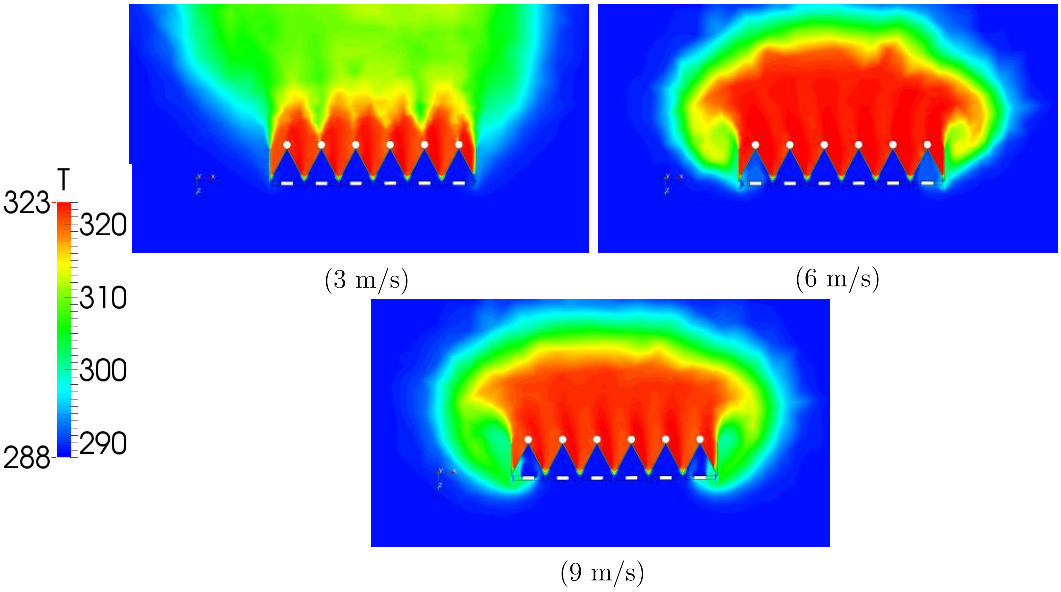

Figure 5.48: Plume recirculation through fan column 5 of B2a-fan ACC

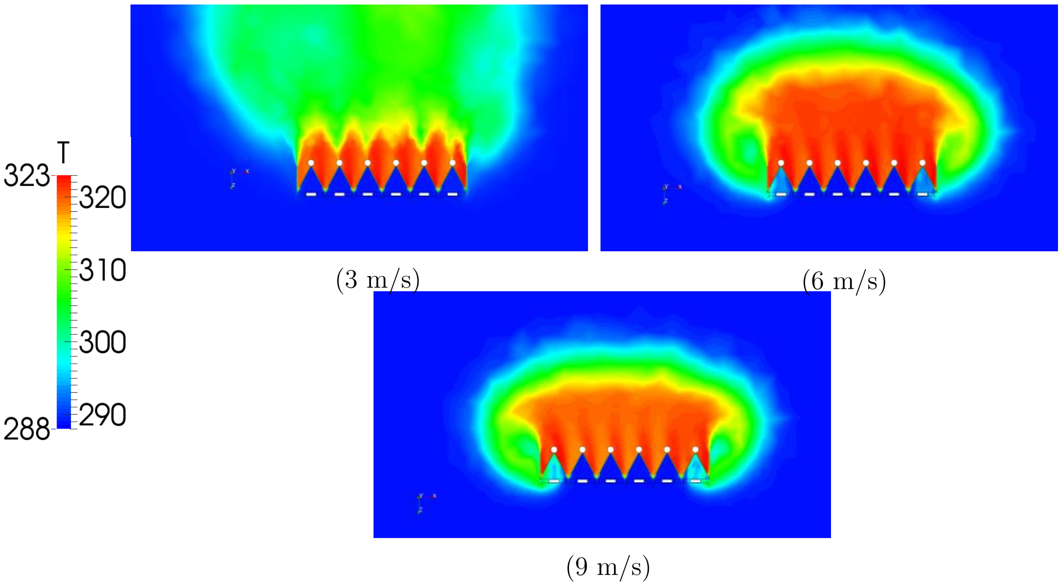

Figure 5.49: Plume recirculation through fan column 5 of Combined ACC

The air inlet temperatures of the upstream periphery heat exchangers are indicated in figure 5.50 with the temperature plots shown in figures 5.51 to 5.53. As previously mentioned, these heat exchangers are subject to reverse flow conditions. Heat exchangers serviced by the A-fan are noted to be particularly sensitive to reverse flow as indicated by the significantly higher inlet temperatures. This stems from the poor fan performance on the upstream periphery resulting in a significantly larger region of heated air drawn into the plenum of the heat exchanger. Heat exchangers in the Combined ACC are the least affected by reverse flow due to the higher upstream volumetric flow rates, as previously discussed.

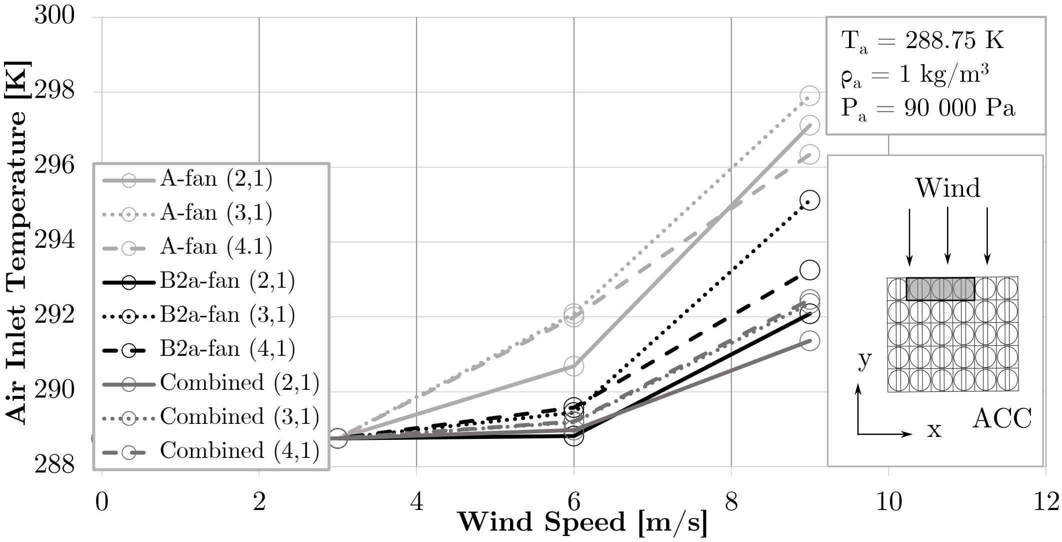

Figure 5.50: Air inlet temperature of periphery fans subject to cross-wind

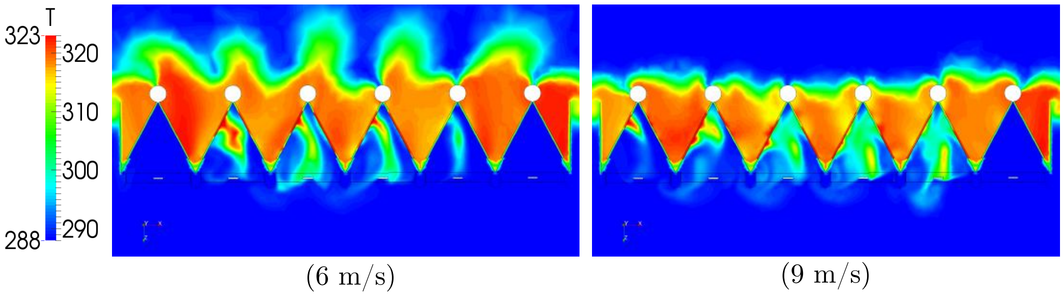

Figure 5.51: Reversed flow in the plenum of A-fan ACC periphery fans

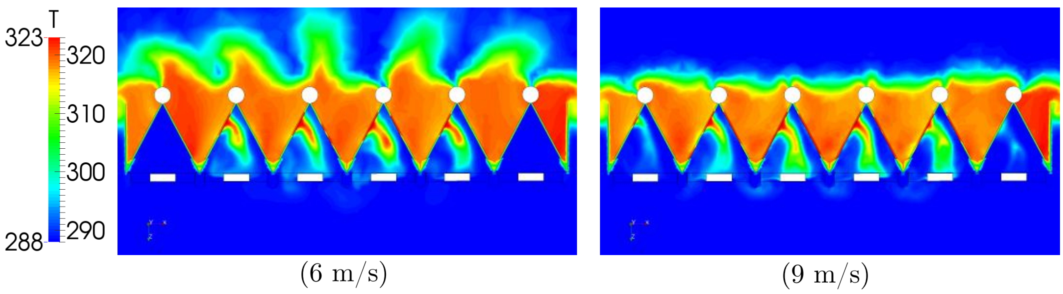

Figure 5.52: Reversed flow in the plenum of B2a-fan ACC periphery fans

Each ACC exhibits distinct differences in thermal performance for heat exchangers situated in different positions in the ACC. Similar heat transfer

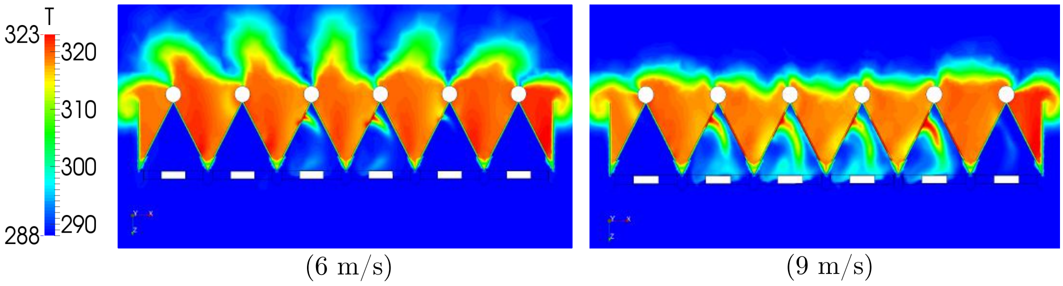

Figure 5.53: Reversed flow in the plenum of Combined ACC periphery fans

rates were measured for all ACCs at the heat exchangers in the centre and downstream periphery. The difference in thermal performance of the ACCs therefore stems from the performance of the heat exchangers situated on the upstream periphery. The increased volumetric performance of the B2a-fan yields significantly higher heat transfer rates in the case of the B2a-fan ACC and Combined ACC. This indicates the degree to which upstream fan performance can affect ACC thermal performance.

5.4.2 Cross-Wind Speed Evaluation (x-direction)

The total heat transfer rates for each ACC subjected to a cross-wind in the direction normal to the short axis of the ACC (x-direction) is shown in figure 5.54. Heat transfer rates of individual heat exchangers are shown in figure 5.55. As with the y-direction case, thermal performance decreases with increasing cross-wind speed. Performance improvements up to 2.49 % were measured over the y-direction cross-wind case resulting from the higher measured volumetric flow rates. The heat transfer of the A-fan ACC also shows the highest sensitivity to cross-wind speed compared to the other ACCs.

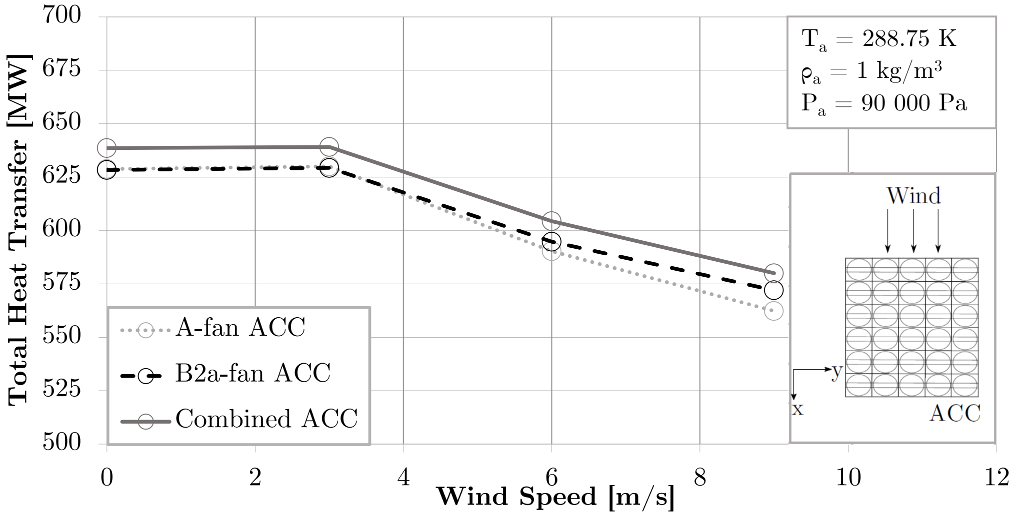

Figure 5.54: Total heat rejected by the ACC subjected to cross-wind

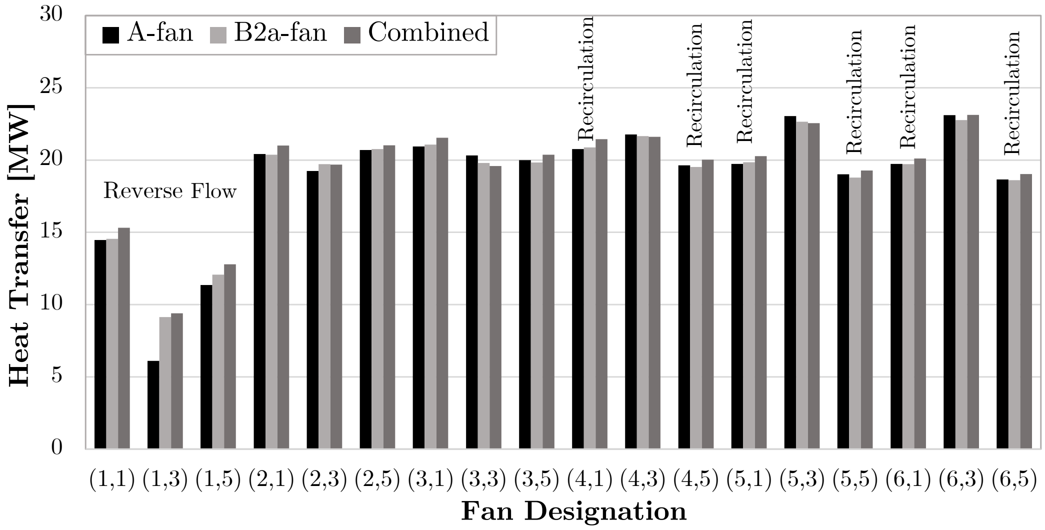

Figure 5.55: Heat transfer of fans in each ACC for 9 m/s cross-wind

Air inlet temperatures of the downstream fans, affected by recirculation, are shown in figure 5.56. Similar air inlet temperatures are observed for each ACC regardless of the fan type used. The air inlet temperatures are also observed to be higher compared to the y-direction cross-wind case. This results from increased vortex size, and subsequent heated air recirculation, as the air flows parallel the long axis of the ACC. Increased plume entrainment is illustrated by the temperature plots showing the heat exchangers on the downstream peripheries in figures 5.57 to 5.59.

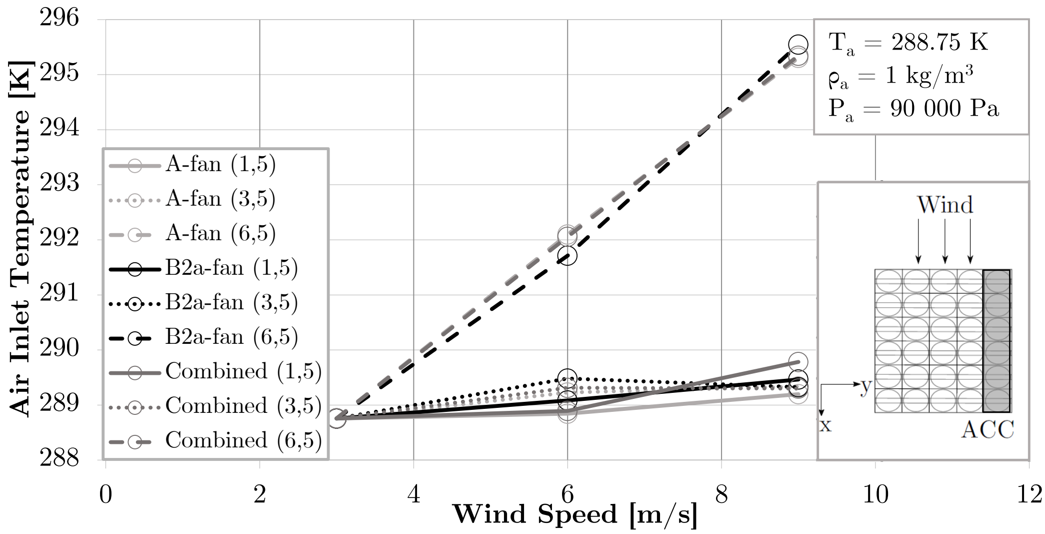

Figure 5.56: Air inlet temperatures of periphery fans subject to cross-wind

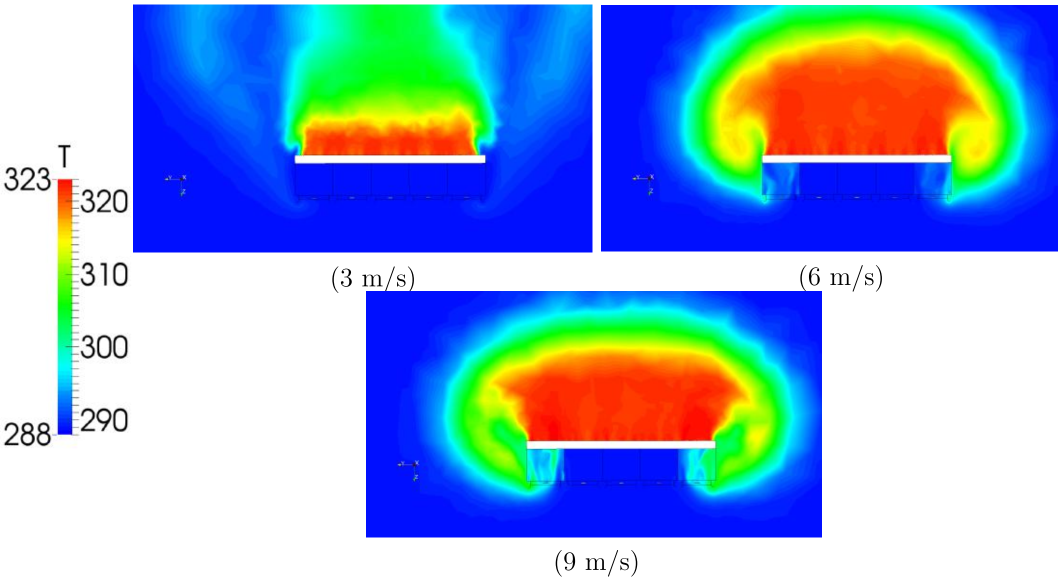

Figure 5.57: Plume recirculation through fan row 6 of the A-fan ACC

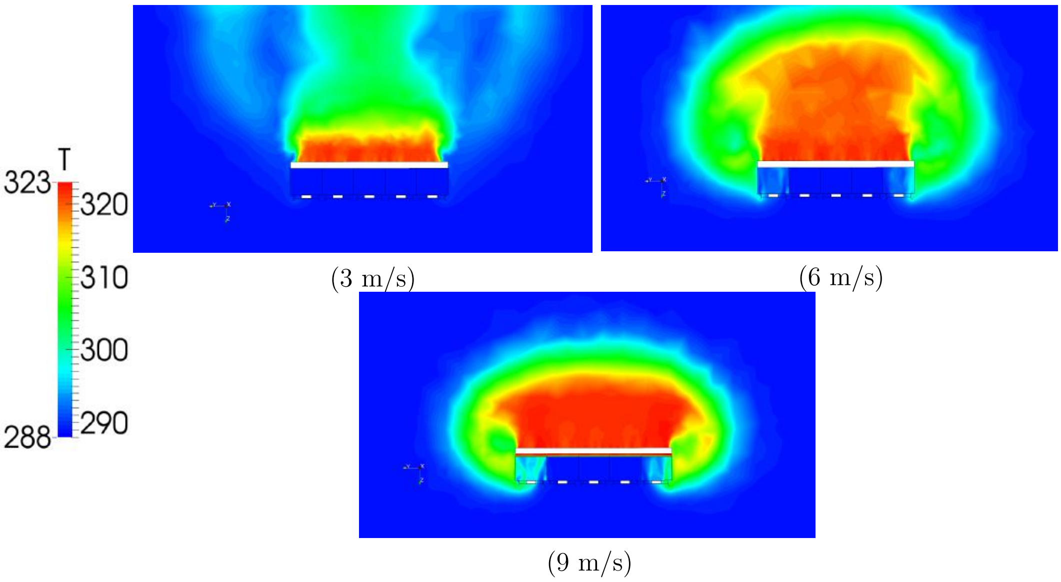

Figure 5.58: Plume recirculation through fan row 6 of the B2a-fan ACC

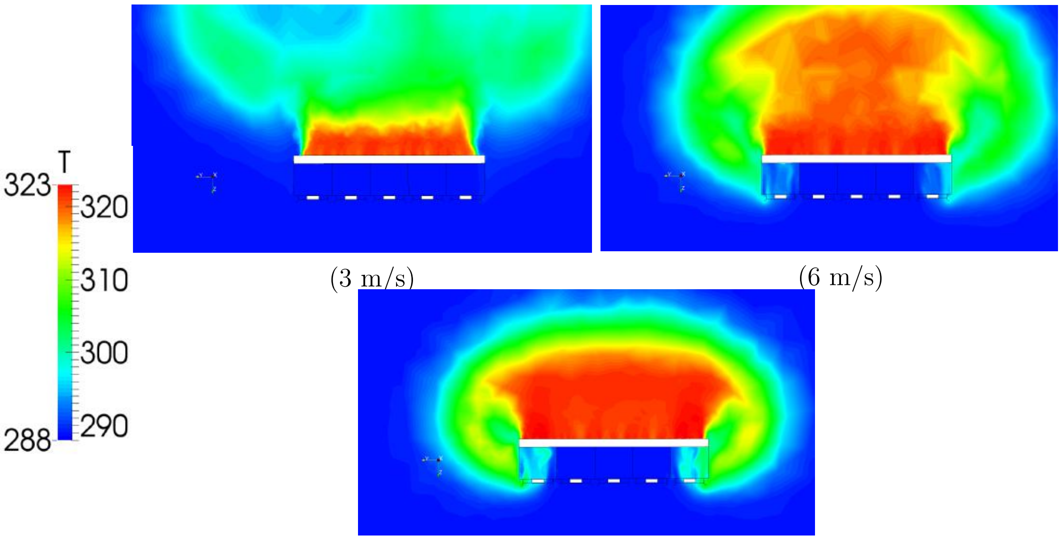

Figure 5.59: Plume recirculation through fan row 6 of the Combined ACC

The air inlet temperatures of heat exchangers situated on the upstream periphery are shown in figure 5.60. Temperature differences of approximately 1 K were measured for the B2a-fan ACC compared to the Combined ACC. Heat exchangers service by the A-fan were severely affected by reverse flow with measured air inlet temperatures in excess of 296 K. This leads to the reported poor thermal performance of the upstream periphery heat exchangers serviced by the A-fans. The reverse flow on the upstream peripheries is illustrated by the temperature plots of figures 5.61 to 5.63.

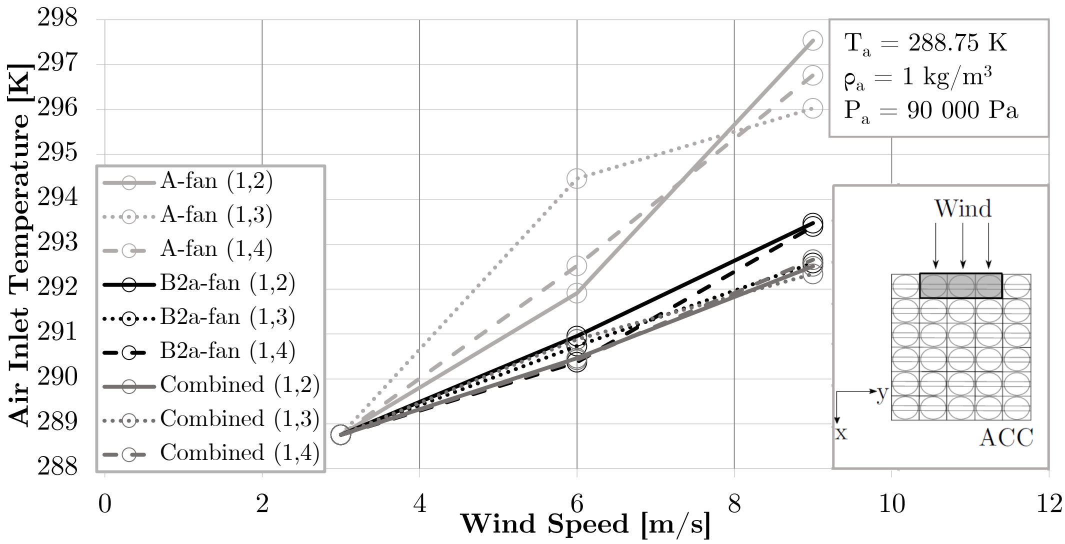

Figure 5.60: Air inlet temperature of periphery fans subject to cross-wind

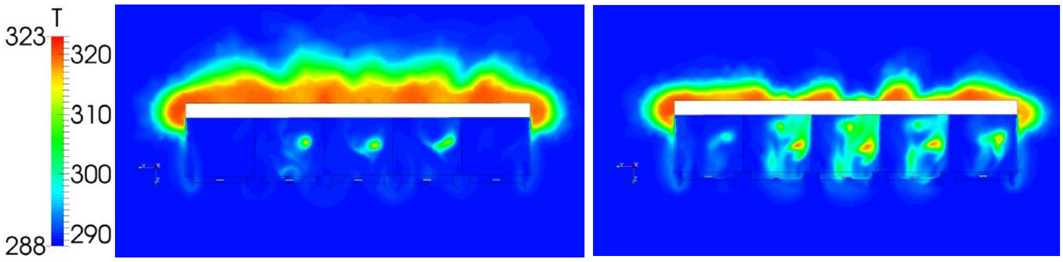

(6 m/s) (9 m/s)

Figure 5.61: Reversed flow of upstream periphery of the A-fan ACC

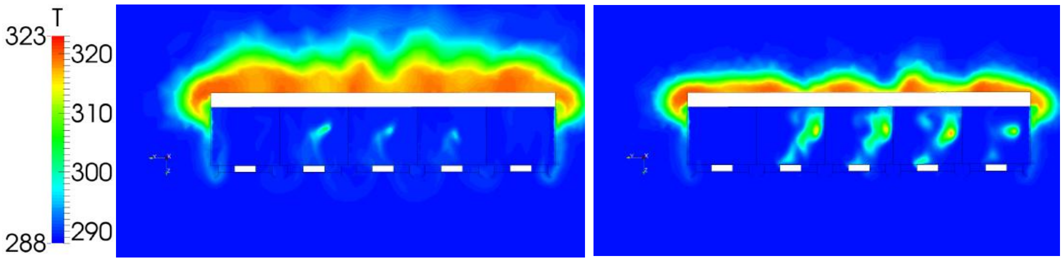

(6 m/s) (9 m/s)

Figure 5.62: Reversed flow of upstream periphery of the B2a-fan ACC

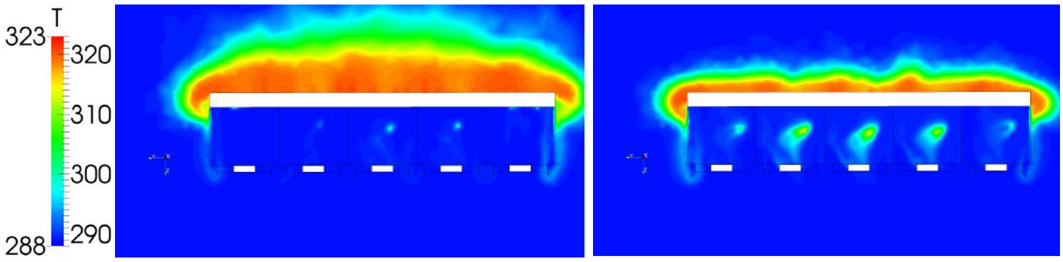

(6 m/s) (9 m/s)

Figure 5.63: Reversed flow of upstream periphery of the Combined ACC

5.4.3 Wind Direction Evaluation

The total heat transfer is shown for each cross-wind direction, along different speeds, in figures 5.64 to 5.66. Similar to the volumetric performance, the thermal performance is also dependant on the ACC orientation to the cross-wind direction. The correlation between performance and orientation is also noted to increase with higher cross-wind speeds. Maximum variation of thermal performance with cross-wind direction was measured at 4 % for the B2a-fan ACC and Combined ACC and 6 % for the A-fan ACC for wind speed of 9 m/s.

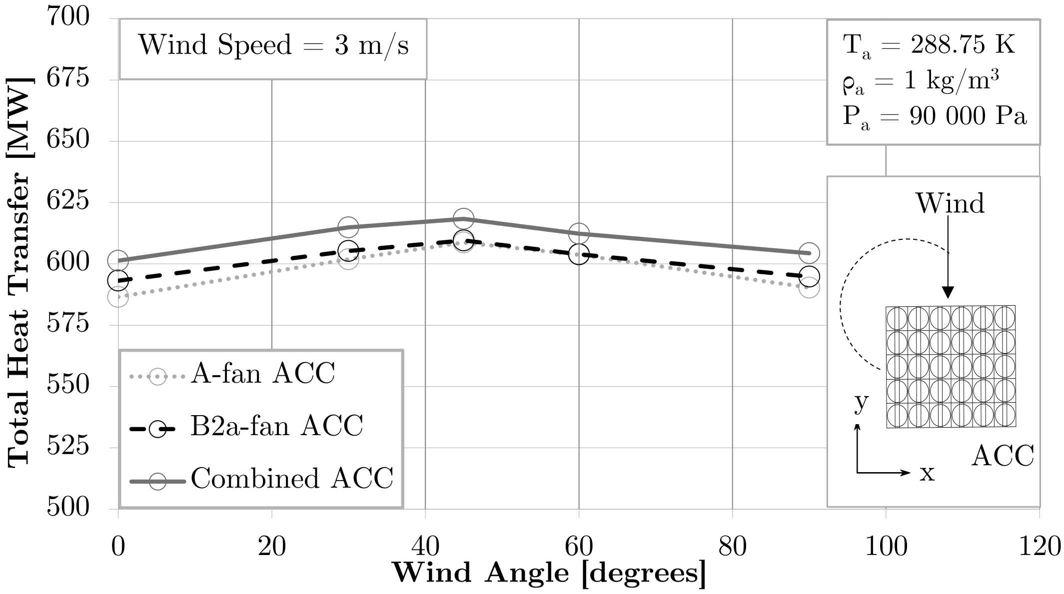

Figure 5.64: Total heat transferred for a 3 m/s cross-wind

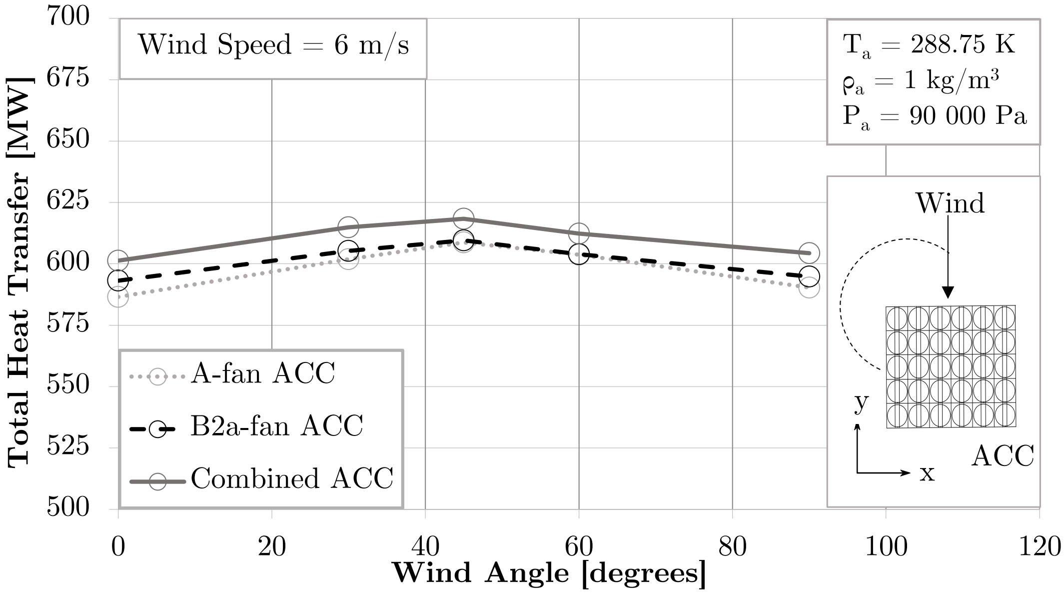

Figure 5.65: Total heat transferred for a 6 m/s cross-wind

The higher total volumetric flow rates measured for the Combined ACC lead to higher heat transfer rates compared to the other ACCs. A significant decrease in heat transfer is also noted for the A-fan ACC at a cross-wind speed of 9 m/s. As previously mentioned, the thermal performance of the ACC is primarily dependant on the heat transfer capabilities of the heat exchangers on the upstream peripheries. The poor performance of the A-fan servicing these heat exchangers lead to reduced thermal performance.

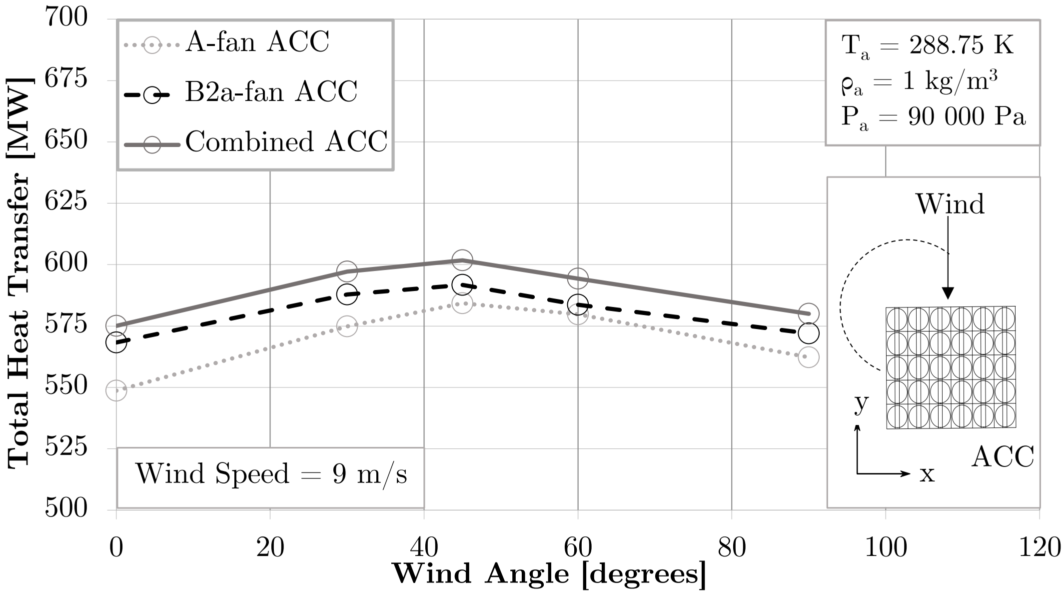

Figure 5.66: Total heat transferred for a 9 m/s cross-wind

A direct correlation exists between the volumetric performance and thermal performance with regard to cross-wind speed and direction. Minor fluctuations in heat transfer rates are therefore observed for a cross-wind speed of 3 m/s along different wind directions. Fluctuations in heat transfer for all ACCs were measured in the range of 2.84-3.78 % at 6 m/s and 4.12-6.49 % at 9 m/s. Peak thermal performance was measured for wind angles of 30-60^o resulting from the increased volumetric performance of each ACC. Also noted is the poor performance of the A-fan ACC as the cross-wind speed increases. The Combined ACC shows the highest thermal performance for all analysed cross-wind directions.

Figure 5.67 shows the heat transfer rates, and phenomenon affecting thermal performance, of individual heat exchangers for a cross-wind speed of 9 m/s. The A-fan performs poorly on the upstream periphery with near double heat transfer rates measured for the B2a-fan. The B2a-fans in the Combined ACC perform better than the fans in the B2a-fan ACC at the upstream periphery. This is attributed to the previously noted higher volumetric performance of the upstream fans. Similar heat transfer rates were measured for each ACC at the centre and downstream periphery. Reverse flow and recirculation effects on thermal performance can be compared by considering the air inlet temperature of the periphery heat exchangers shown in figure 5.68.

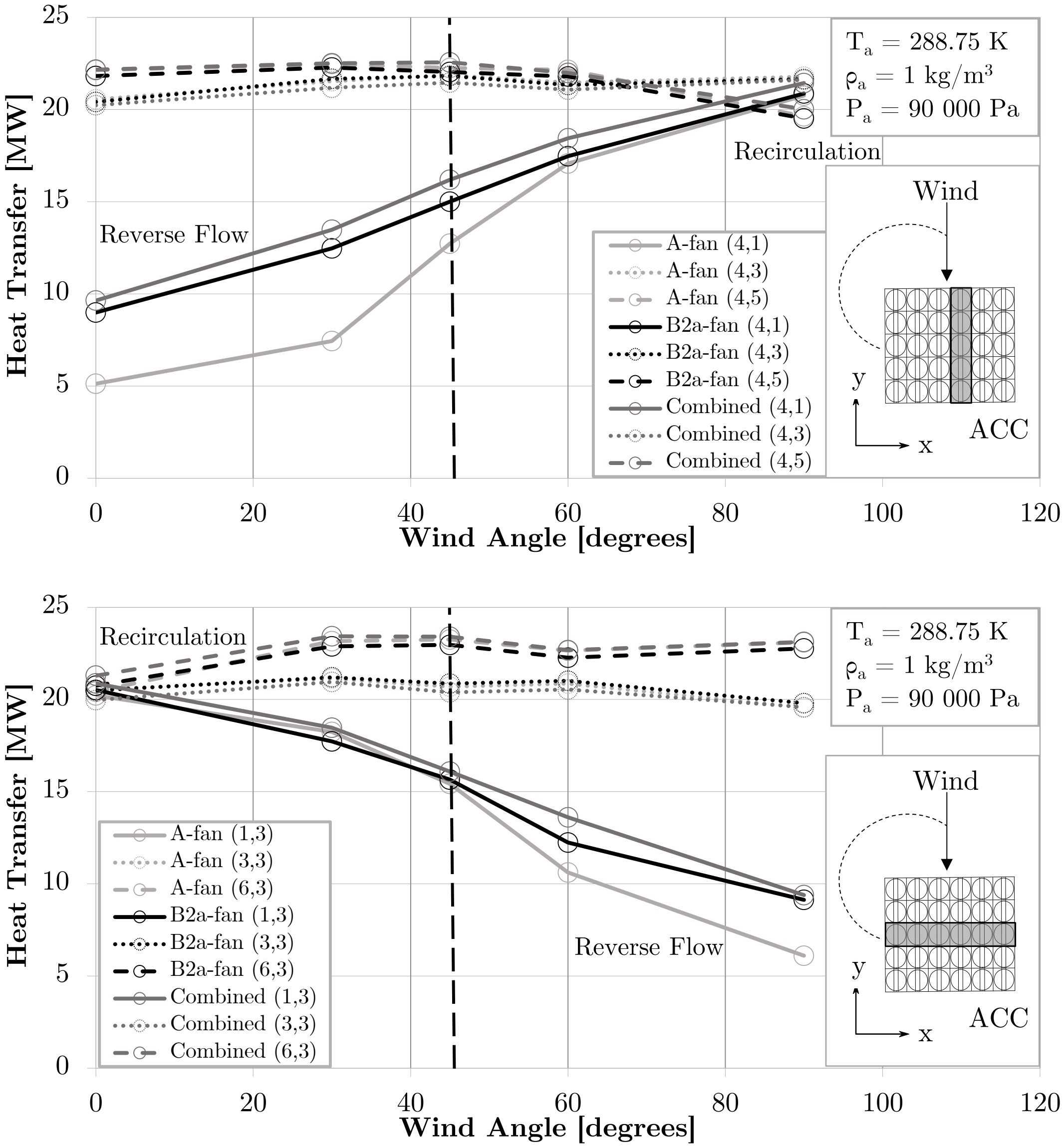

Figure 5.67: Heat transfer of individual fans for a 9 m/s cross-wind

It is clearly shown that reverse flow in the plenum of the heat exchanger results in higher air inlet temperatures for the A-fan and B2a-fan compared to recirculation. Also indicated is the aforementioned sensitivity of the A-fan to reverse flow conditions with air inlet temperatures up to 298 K measured. A 3 K lower air inlet temperature was measured for the B2a-fan ACC, and the lowest temperature was measured for the Combined ACC. Similar air inlet temperatures were measured for the heat exchangers affected by recirculation for all ACCs. Total thermal performance differences between ACCs can therefore be attributed to the performance of heat exchangers when subjected to reverse flow conditions. Minimising this effect is only achieved through the use of a suitable axial flow fan on the upstream periphery.

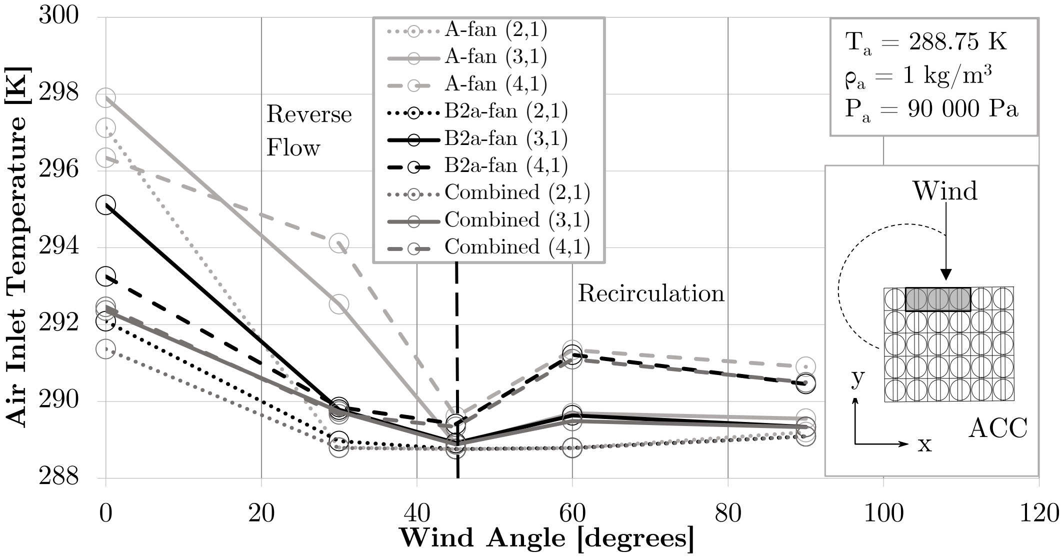

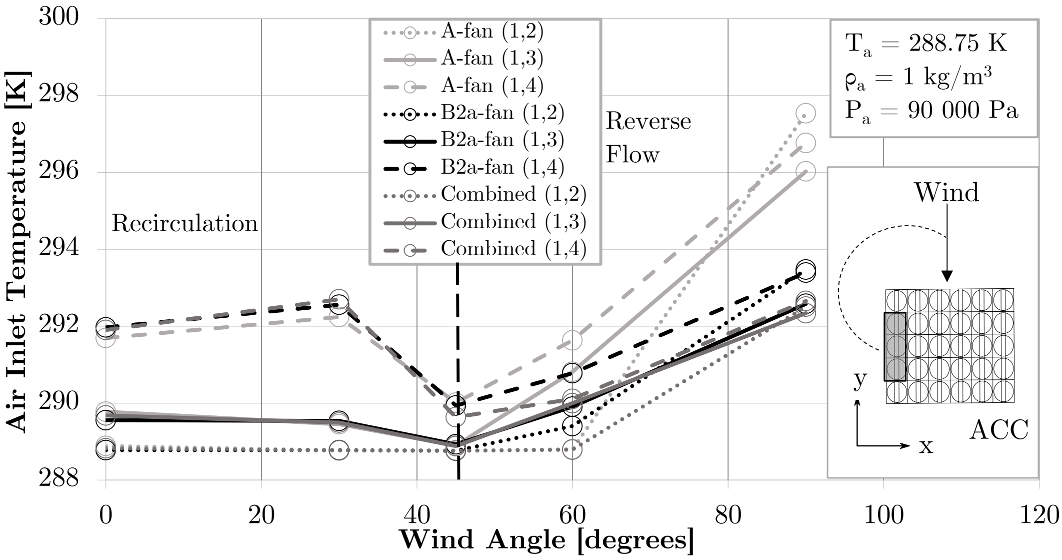

Figure 5.68: Inlet air temperatures of individual fans for a 9 m/s cross-wind

Maximum thermal performance of the ACC was measured at a cross-wind direction of 45^o for all wind speeds. The air inlet temperatures indicates that the heat exchangers are minimally affected by either recirculation or reverse flow at this cross-wind condition. Reverse flow is minimised as the wind direction is not considered to be normal to the peripheries. This leads to higher volumetric flow rates as more fans are able to take advantage of the previously discussed three-dimensional flow component. This consequently leads to the heated air plume being ejected high enough to effectively negate recirculating flow. This is illustrated by the temperature plot of figure 5.69 for different cross-wind directions. Only a small region of localised reverse flow is observed at 45^o resulting in an increase in air inlet temperature of 2 K.

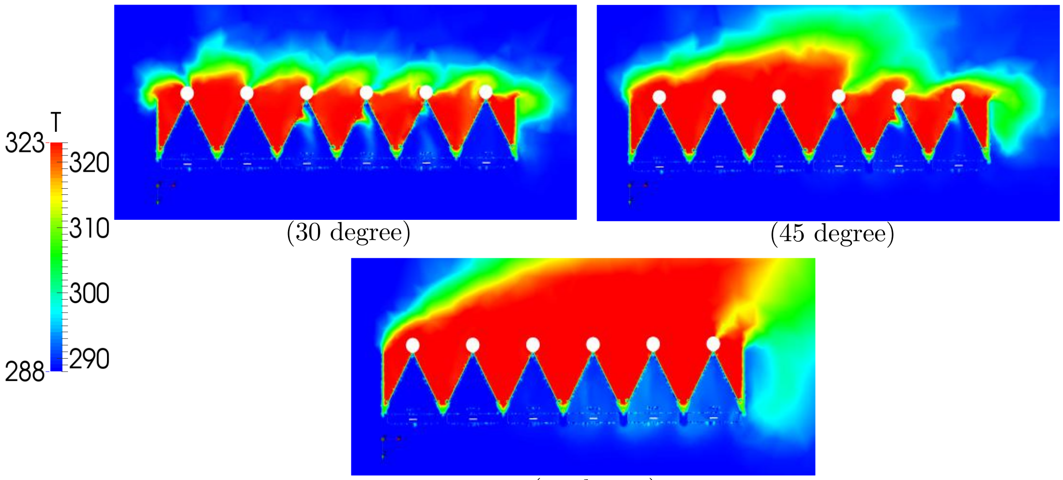

Figure 5.69: Temperature profile of A-fan ACC for a 9 m/s cross-wind

5.5 Heat-to-Power Performance

Clear volumetric and thermal performance differences exist for each ACC when subjected to cross-wind conditions. The heat-to-power ratio, defined in chapter 3, gives a measure of overall performance by combining the power consumption and thermal performance into a single performance parameter.

The heat-to-power ratio of each ACC is shown in figures 5.70 to 5.72 for different cross-wind directions. A decreasing trend of overall performance with increasing cross-wind speeds was measured, similar to the volumetric and thermal performance. A small increase in overall performance is observed for a cross-wind speed of 3 m/s resulting from decreased power consumption. Highest overall performance was measured for a cross-wind direction of 60^o for all ACCs as the lowest power consumption was measured at this wind condition.

It was previously noted that the volumetric and thermal performance shows increasing fluctuations based on cross-wind direction for higher cross-wind speeds. A similar trend is, consequently, observed for the overall performance. This relationship of performance to ACC cross-wind orientation is illustrated by comparing the difference in heat-to-power ratios of a 9 m/s cross-wind along different directions. A difference of 7.39 % in overall performance was calculated for the A-fan ACC when the cross-wind direction changes from 0^o to 90^o. A difference of 5.56 % was calculated for the B2a-fan ACC and 5.89 % for the Combined ACC. This coincides with the previously concluded observations that the A-fan ACC exhibits the highest performance sensitivity to ACC cross-wind orientation.

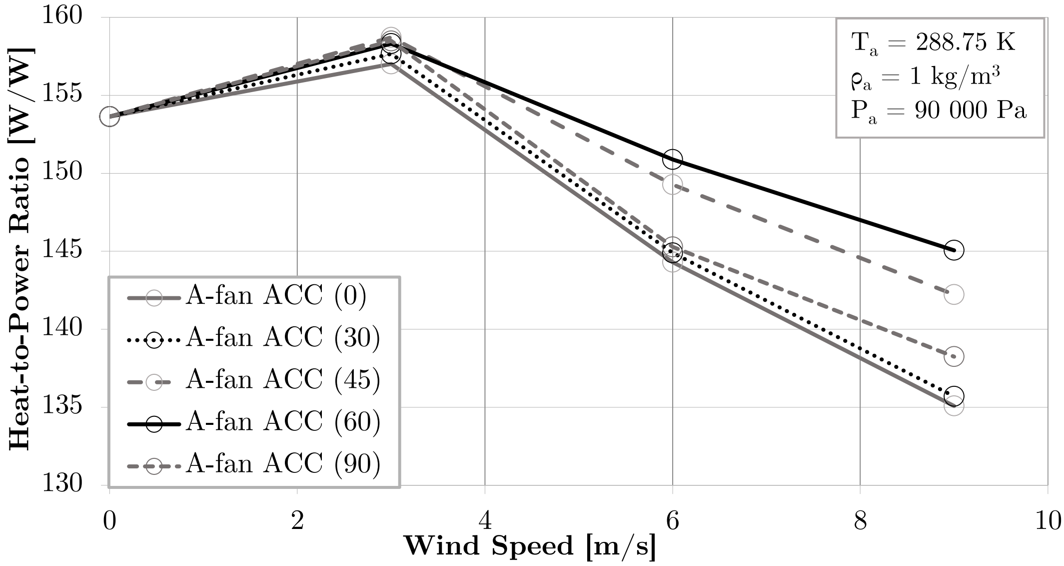

Figure 5.70: A-fan ACC heat-to-power with cross-winds (direction [°])

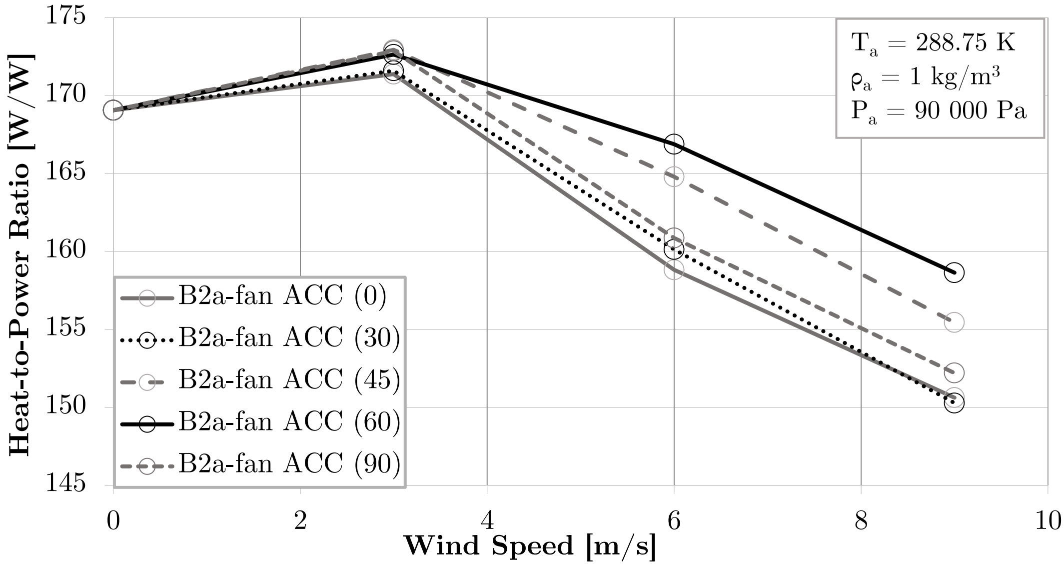

Figure 5.71: B2a-fan ACC heat-to-power with cross-winds (direction [°])

The calculated heat-to-power ratios highlights the reported volumetric and thermal performance differences of each ACC. This is depicted by the wind speed averaged heat-to-power ratios indicated in table 5.4. The significantly lower power requirements of the B2a-fan leads to the B2a-fan ACC exhibiting a 9-10 % higher overall performance compared to the A-fan ACC and a 7 % higher performance compared to the Combined ACC.

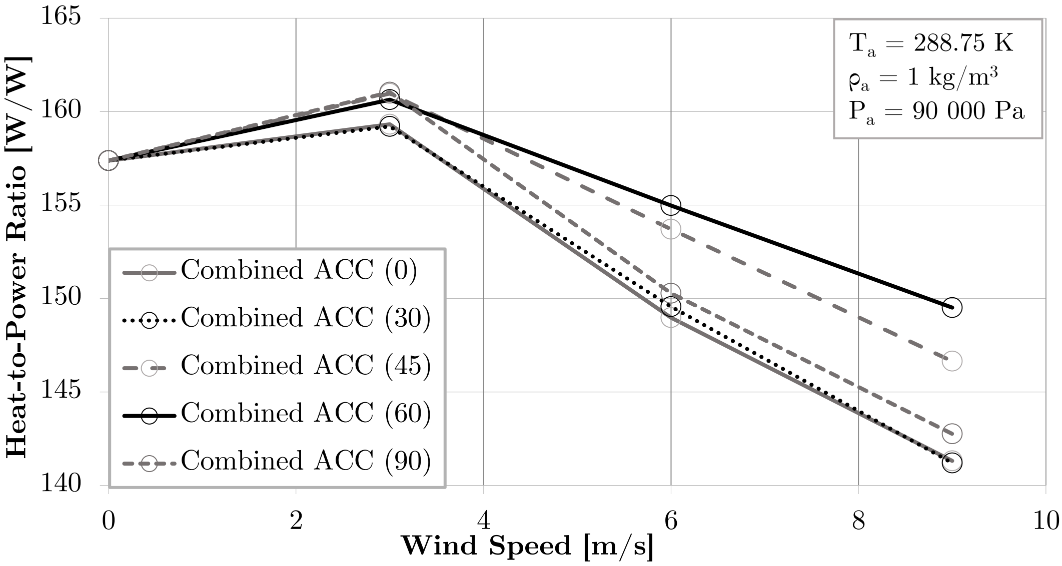

Figure 5.72: Combined ACC heat-to-power with cross-winds (direction [^{o}])

The Combined ACC shows an improvement of approximately 5 % in overall performance compared to the A-fan ACC. As the power consumption of the two ACCs is similar, the increase in overall performance stems from the higher reported heat transfer rates measured for the Combined ACC.

Table 5.4: Wind speed averaged heat-to-power ratios

Wind Direction	A-fan ACC [W/W]	B2a-fan ACC [W/W]	Combined ACC [W/W]
0^o	147.51	162.47	151.75
30^o	147.97	162.77	151.84
45^o	150.96	165.56	154.67
60^o	151.97	166.80	155.62
90^o	148.91	163.75	152.86

These calculated differences in average heat-to-power ratios for each ACC is also discussed by considering the overall performance of individual fan and heat exchanger units presented in figure 5.73 and 5.74 for an x and y-direction cross-wind respectively.

Heat-to-power ratios of 149.56-168.10 W/W were calculated for the A-fan ACC on the downstream periphery, 159.31-191.11 W/W for the B2a-fan ACC and 153.53-179.79 W/W for the Combined ACC. As the volumetric and thermal performance of each ACC was observed to be similar on the downstream periphery, the differences results from measured fan power consumption. The previously reported 6-10 % lower power requirements of the B2a-fan compared

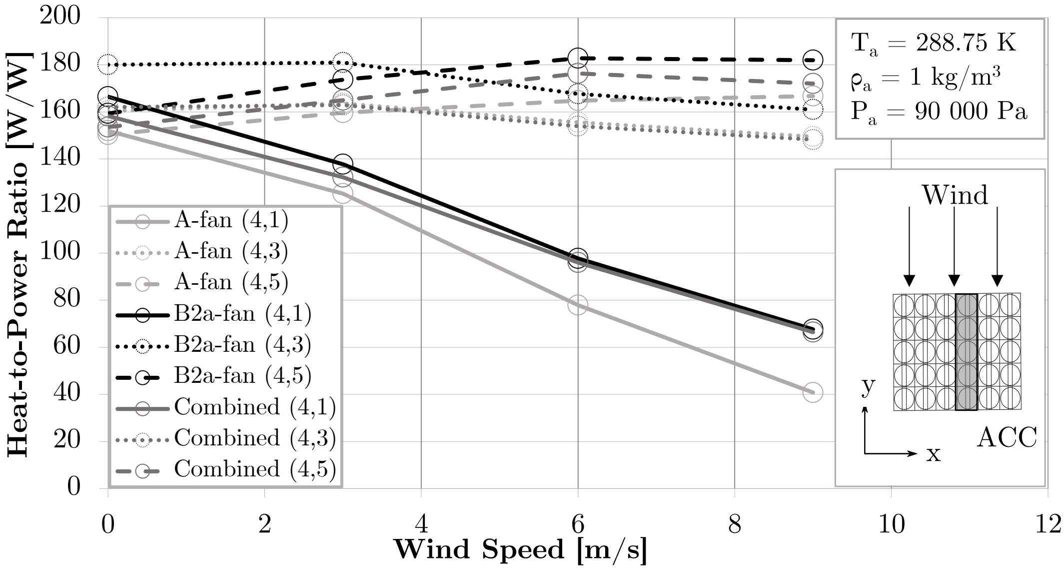

Figure 5.73: Heat-to-power ratio for fans subjected to y-direction wind

to the A-fan leads to a 6.5-13.7 % increase in performance on the downstream periphery of the B2a-fan ACC. The 3 % increase resulting from power requirements of the fan in the ACC differing from the ideal conditions. The 3-6 % lower overall performance calculated for fans in the Combined ACC, compared to the B2a-fan ACC, results from the higher measured fan power consumption.

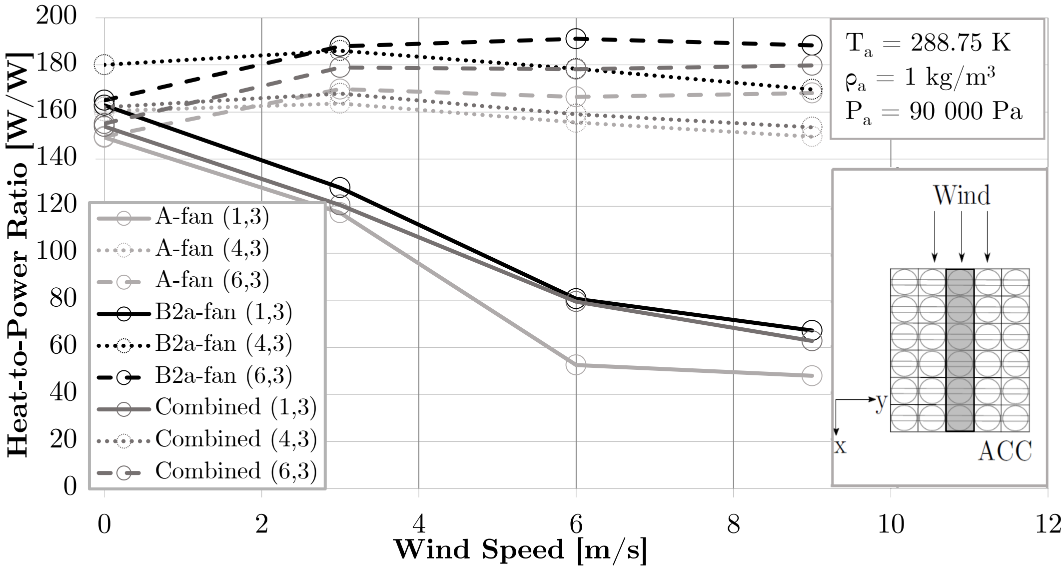

Figure 5.74: Heat-to-power ratio for fans subjected to x-direction wind

Heat-to-power ratios in the centre of the ACC were calculated as 149.52-169.48 W/W for the A-fan ACC, 160.95-186.04 W/W for the B2a-fan ACC and 148.23-167.83 W/W for the Combined ACC. The largest differences noted for overall performance was, however, calculated on the upstream periphery. The A-fan ACC showed the worst performance with a minimum calculated heat-to-power ratio of 40.80 W/W compared to 67.19 W/W for the B2a-fan ACC and 62.77 W/W for the Combined ACC. The poor volumetric performance, and consequent thermal performance, of the A-fan subject to distorted inlet conditions, coupled with the higher power requirements, results in the reported poor overall performance. These findings are in accordance with the results reported by van der Spuy (2011) for upstream periphery fan performance. Findings indicated a significant drop in the overall performance for fans subjected to distorted inflow conditions. An increase in overall performance was noted as the severity of distortion decreases.

The consistent heat-to-power ratios for the fans on the downstream periphery of each ACC indicates that the drop in overall ACC performance for increasing wind speeds is only due to the poor volumetric performance, and consequent thermal performance, of the fans on the upstream periphery. Lower upstream periphery fan performance is noted for a y-direction wind compared to an x-direction wind resulting from the lower volumetric performance as previously discussed.

The heat-to-power ratio illustrates the benefit of using efficient, high volumetric flow rate fans in an ACC. Even though the Combined ACC shows higher volumetric flow rates through the ACC at higher wind speeds, the significantly lower power consumption of the B2a-fan contributes to the superior overall performance of the B2a-fan ACC. The volumetric flow rate through fans subjected to distorted inflow conditions is considered to be one of the largest factors in reduced ACC performance (Duvenhage *et al.*, 1996; Owen, 2010). The volumetric performance of the B2a-fan ACC and Combined ACC indicates the degree to which mitigating these performance inhibiting effects can have on overall ACC performance.

It must be noted that although the heat-to-power ratio gives an indication of overall performance under increasing degrees of flow distortion, the current numerical model is unable to measure the decrease in power consumed as a result of increased air inlet temperatures and, subsequently, a decrease in density at the fan inlet resulting from hot air plume recirculation or reverse flow. This is due to the incompressible nature of the Boussinesq solver used in OpenFOAM. Inclusion of density variations in the ACC model is highlighted as an area recommended for future study.

5.6 Summary of Findings

This chapter detailed the performance evaluation of a 6x5 ACC using three different fan configurations. The A-fan ACC, B2a-fan ACC and Combined ACC were analysed with regard to performance in windy conditions.

A comparative study of the B2a-fan ACC to previous literature was undertaken. Significant differences in upstream periphery fan performance was noted. This was attributed to the geometrical differences in domains analysed as well as the different axial flow fan models used. Similar performance trends were measured for fans on the downstream periphery and the centre of the ACC. Total volumetric effectiveness and heat transfer effectiveness also followed similar trends, however, differences were noted due to the presence of phenomena not reported by previous literature.

The performance analysis of the different ACCs was performed using two wind directions to highlight the effect of cross-wind speed. This was followed by an analysis with regard to cross-wind direction. The results were presented in the form of fan volumetric performance, thermal performance of the heat exchanger and overall performance presented in the form of the heat-to-power ratio. The major findings of the analysis is presented below:

- All ACCs were characterised by a decrease in volumetric, thermal and overall performance for increasing cross-wind speeds.
- The B2a-fan shows increased performance over the A-fan on the upstream periphery. Similar performance was measured in the centre and downstream periphery.
- Fan performance on the downstream periphery and centre of the ACC was unaffected by cross-wind speed. Upstream fan performance decreased with increasing wind speed. It was thus concluded that the decrease in ACC performance for increasing cross-wind speeds was primarily due to the upstream fan performance.
- The Combined ACC showed the highest volumetric, and thermal performance, followed by the B2a-fan ACC with the worst performance measured for the A-fan ACC.
- The lower power requirements of the B2a-fan leads to a 7 % higher calculated heat-to-power ratio compared to the Combined ACC and 9-10 % higher than the A-fan ACC.
- Performance of the B2a-fan ACC and Combined ACC indicated the benefits of using an efficient, high volumetric flow rate fan for ACC applications

Chapter 6

Comparative Evaluation of ACC Bank in 3x10 Layout

This chapter details the comparative analysis of the volumetric and thermal performance of a 30 fan ACC bank in a 6x5 configuration (layout 1) compared to a 3x10 configuration (layout 2), schematics of which are shown in chapter 3. Similar to the analysis presented in the previous chapter, the A-fan and B2a-fan were used to form the A-fan ACC, B2a-fan ACC and Combined ACC. The ACCs were subjected to varying cross-wind speeds of 0, 3, 6 and 9 m/s using the velocity profile as depicted by figure 5.1. Different wind directions were also considered as depicted by figure 5.11. A discussion of the volumetric performance of the ACC is presented, followed by a discussion on thermal performance and overall performance in the form of the heat-to-power ratio.

6.1 Volumetric Performance

Similar to the analysis presented in the previous chapter, the volumetric performance of the two layouts is presented in the form of the volumetric effectiveness ratio as detailed in chapter 3. The ideal volumetric flow rate for each fan in the ACC, subject to cross-wind, is taken as the volumetric flow rate measured for the fan in the ACC subject to no cross-wind. This gives an indication of performance degradation under cross-wind conditions relative to the ideal case.

The total volumetric flow rate through each layout when no cross-wind is present is shown in table 6.1. Similar volumetric flow rates were measured for all ACCs with a 1.06 % higher volumetric flow rate measured for the A-fan ACC in layout 2 configuration compared to layout 1. Measured volumetric flow rates for the B2a-fan ACC and Combined ACC show differences less than 1 %.

Table 6.1: Total volumetric flow rate of each ACC subject to no wind

ACC Designation	**Layout 1 [m³/s]**	**Layout 2 [m³/s]**
A-fan ACC	18070.39	18262.24
B2a-fan ACC	18056.30	18159.67
Combined ACC	18441.97	18271.66

A total volumetric effectiveness comparison of each ACC in cross-wind conditions is presented in figures 6.1 to 6.3. Fluctuations in volumetric performance is noted to increase significantly for layout 2 as the cross-wind speed increases. Maximum volumetric effectiveness differences up to 23 % were measured for the A-fan ACC in layout 2 configuration as the cross-wind direction shifts from 0^o to 90^o. Smaller fluctuations were measured for the layout 1 configuration with a maximum fluctuation measured at 4 % for the A-fan ACC.

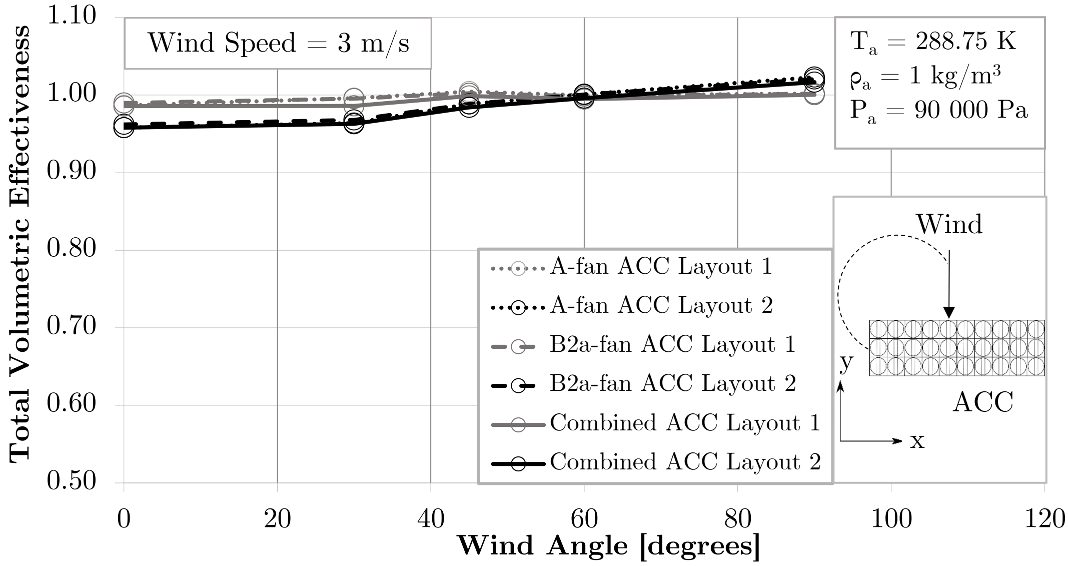

Figure 6.1: Total volumetric effectiveness comparison for a 3 m/s cross-wind

The measured differences in layout 2 performance, dependant on cross-wind direction, indicate a stronger dependence of volumetric performance to ACC orientation exists compared to that of layout 1. This stems from the asymmetrical nature of the layout 2 configuration as a significantly larger number of fans is situated on the long periphery compared to the short periphery. The decrease in volumetric performance of an ACC subject to cross-flow primarily results from the decreased performance of the periphery fans due to distorted inflow conditions, as discussed previously.

The number of fans affected by distorted inlet flow conditions decreases as the cross-wind direction shifts from 0^o to 90^o, subsequently leading to higher measured volumetric performance.

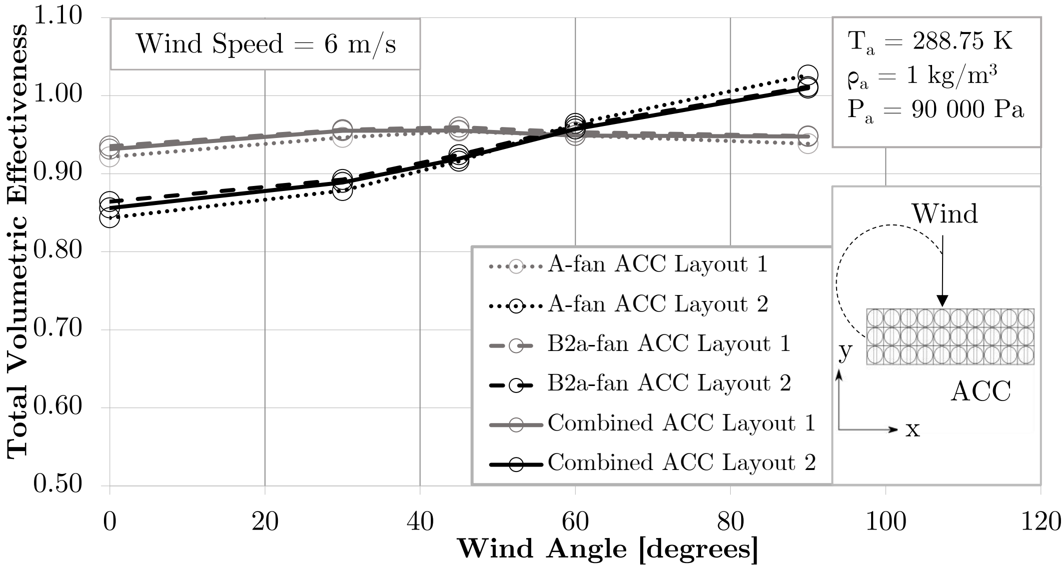

Figure 6.2: Total volumetric effectiveness comparison for a 6 m/s cross-wind

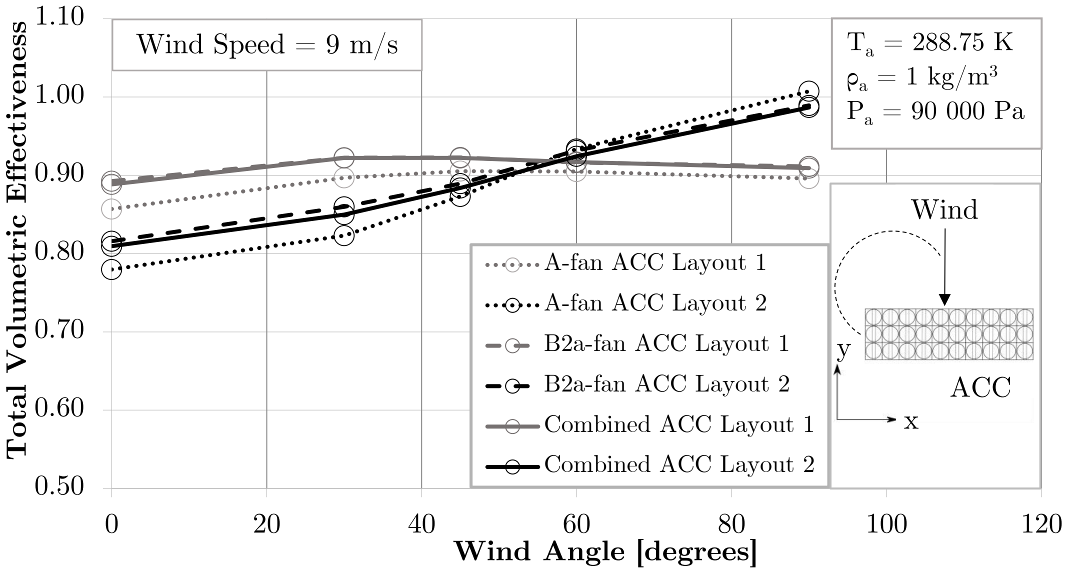

Figure 6.3: Total volumetric effectiveness comparison for a 9 m/s cross-wind

Significant performance differences are noted for each ACC using the layout 2 configuration. Poor periphery fan performance of the A-fans leads to poor total performance for the A-fan ACC in the case of a 0^o wind direction. Increased B2a-fan periphery fan performance results in the B2a-fan ACC and Combined ACC outperforming the A-fan ACC up to a cross-wind direction of 45^o. Near identical performance for all ACCs was measured at 60^o with a 2 % higher volumetric effectiveness measured for the A-fan ACC along a wind direction of 90^o. As the wind direction increases to 60^o the number of upstream fans subject to distorted inflow decreases and a larger number of fans are considered to be in the centre and on the downstream periphery of the ACC. These conditions seem to benefit A-fan performance leading to increased performance. Individual fan performance is shown and compared in figure 6.4 for a cross-wind normal to the long axis of the ACC (y-direction).

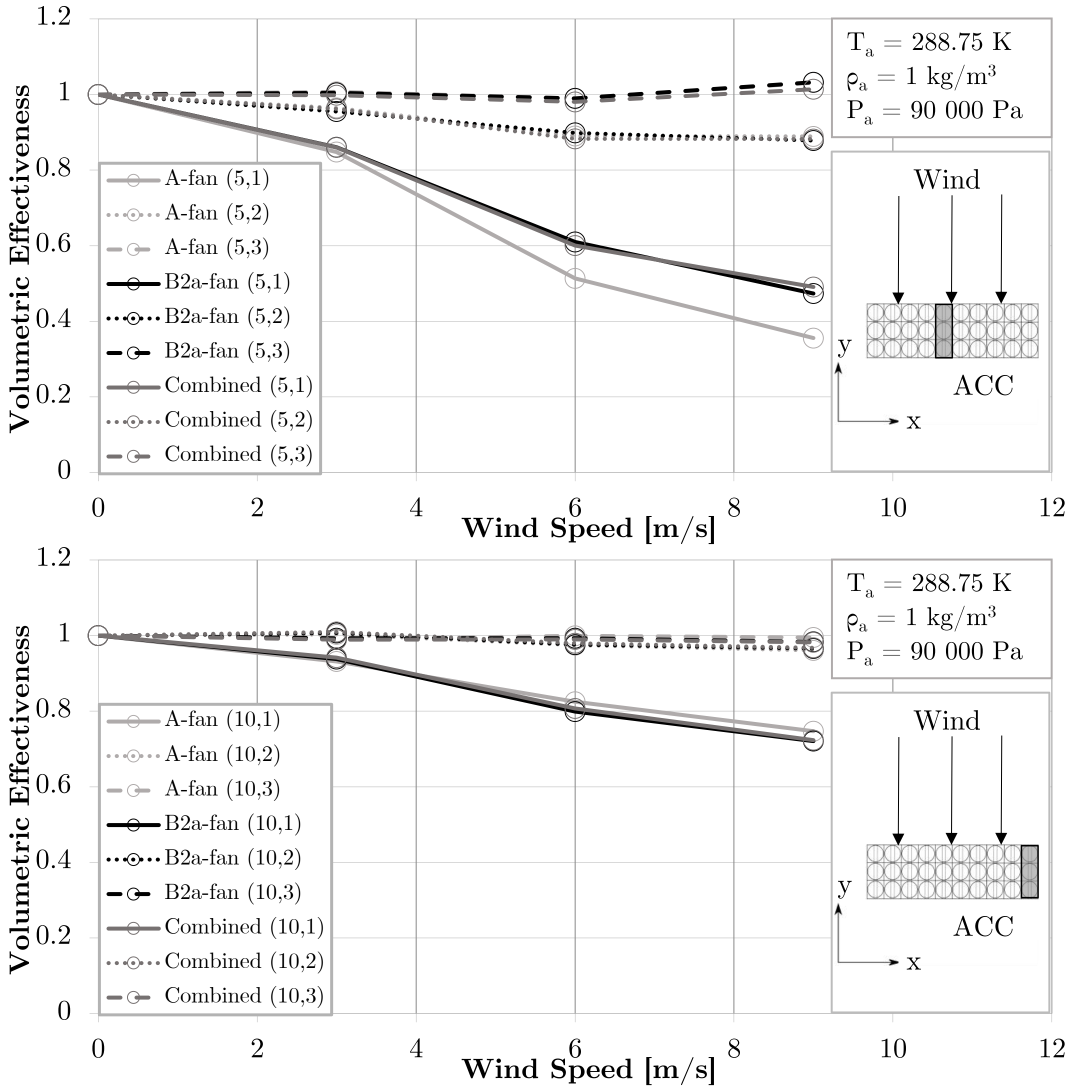

Figure 6.4: Volumetric effectiveness of fans subject to y-direction cross-wind

Similar to the case of layout 1, higher volumetric effectiveness was measured for the B2a-fans on the upstream periphery of the B2a-fan ACC and Combined ACC. A decrease in volumetric performance with increasing cross-wind speeds was measured for both the A-fan and B2a-fan in the centre and on the downstream periphery. This can be attributed to the short distance between the downstream and upstream periphery. These fans experiences distorted inflow conditions as the air flows parallel to the short side of the ACC. The air velocity below the platform has not been sufficiently reduced, and separation occurs at the centre and downstream periphery fan inlets. This is illustrated by the low static pressure regions present at the downstream periphery from the pressure distributions of figure 6.5, depicted for a cross-wind speed of 9 m/s. The low static pressure regions below the centre and downstream fans indicates flow separation leading to the previously discussed distorted inlet flow conditions, and subsequent decrease in fan performance.

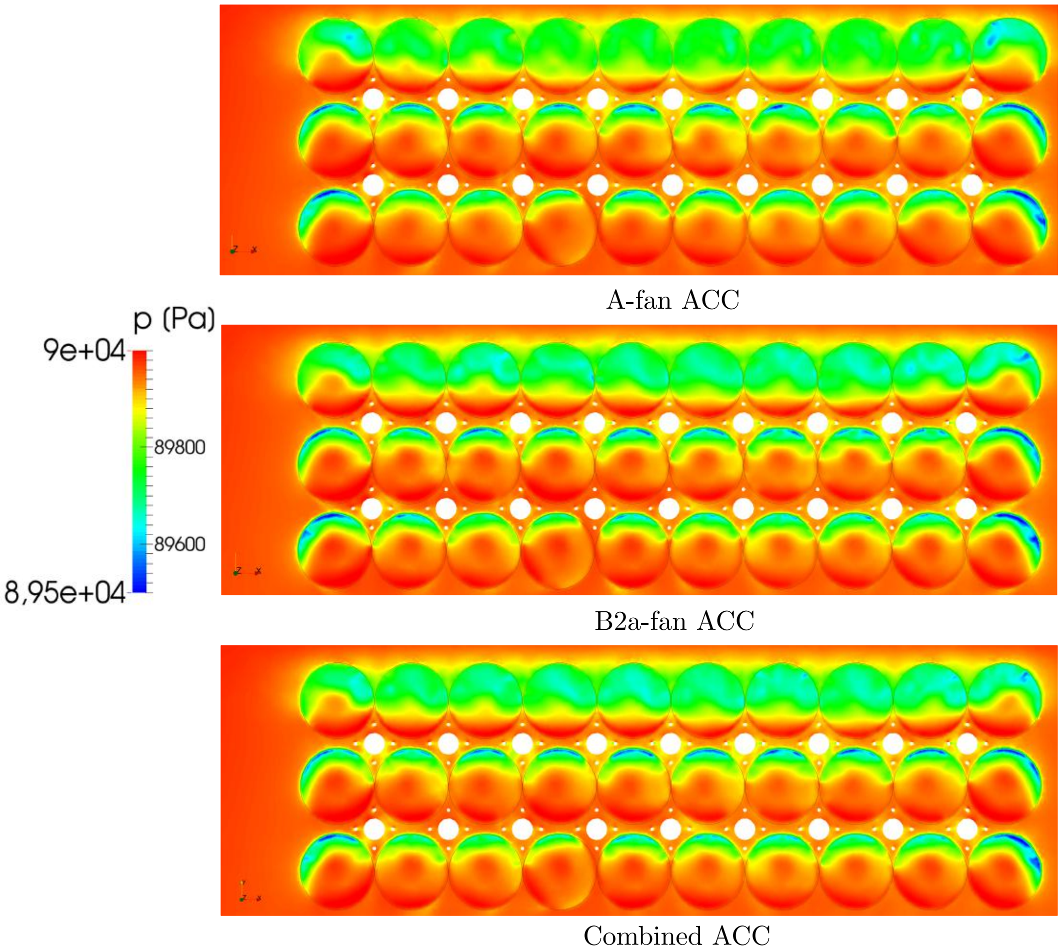

Figure 6.5: Pressure contour of ACC subject to y-direction cross-wind at 9 m/s

The increased volumetric performance of the ACC when the short axis is orientated normal to the cross-wind (x-direction) is discussed by considering the performance of individual fans in figure 6.6. The fans in the centre and downstream periphery show volumetric effectiveness in excess of 1 as a result of the low distortion at the fan inlet. As the air moves below the ACC platform along the long axis, the air velocity decreases subsequently decreasing inlet flow separation resulting in idealised inflow conditions. This low distortion at the centre and downstream fans is illustrated by the pressure distribution of each ACC at a cross-wind speed of 9 m/s in figure 6.7. Significantly smaller regions of low static pressure are observed below the fan inlets for the centre and downstream periphery fans compared to the y-direction cross-wind case.

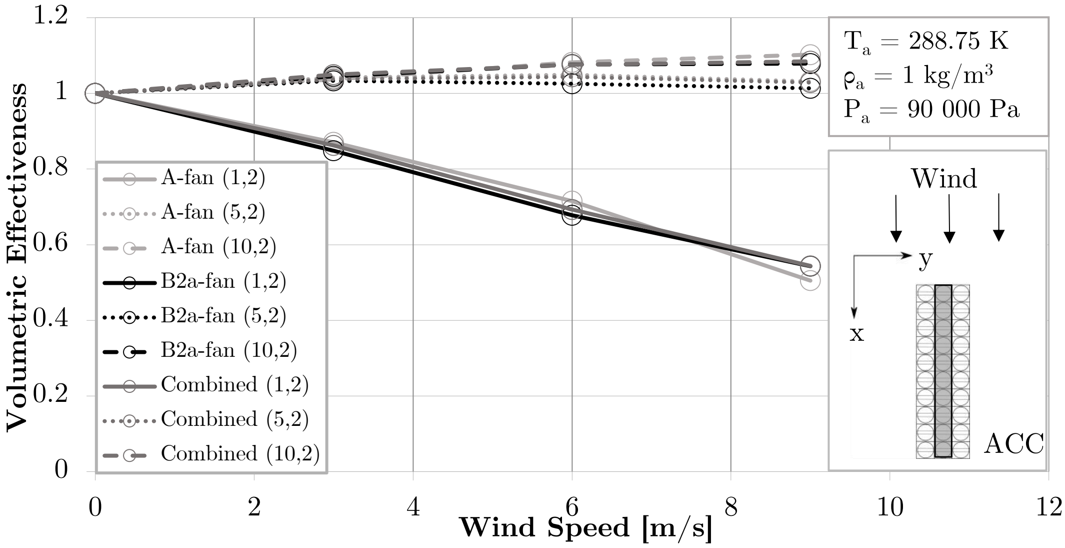

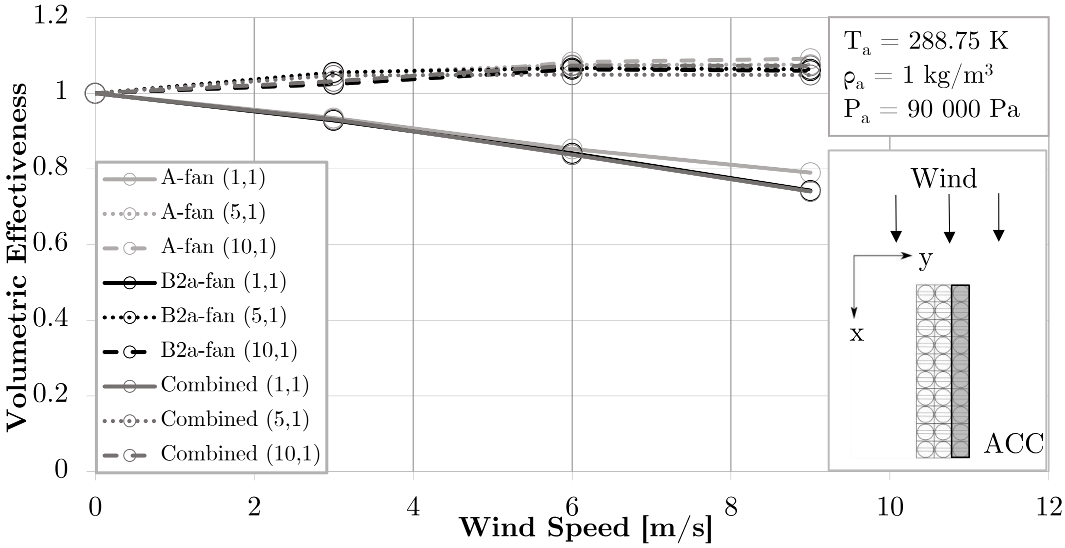

Figure 6.6: Volumetric effectiveness of fans subject to x-direction cross-wind

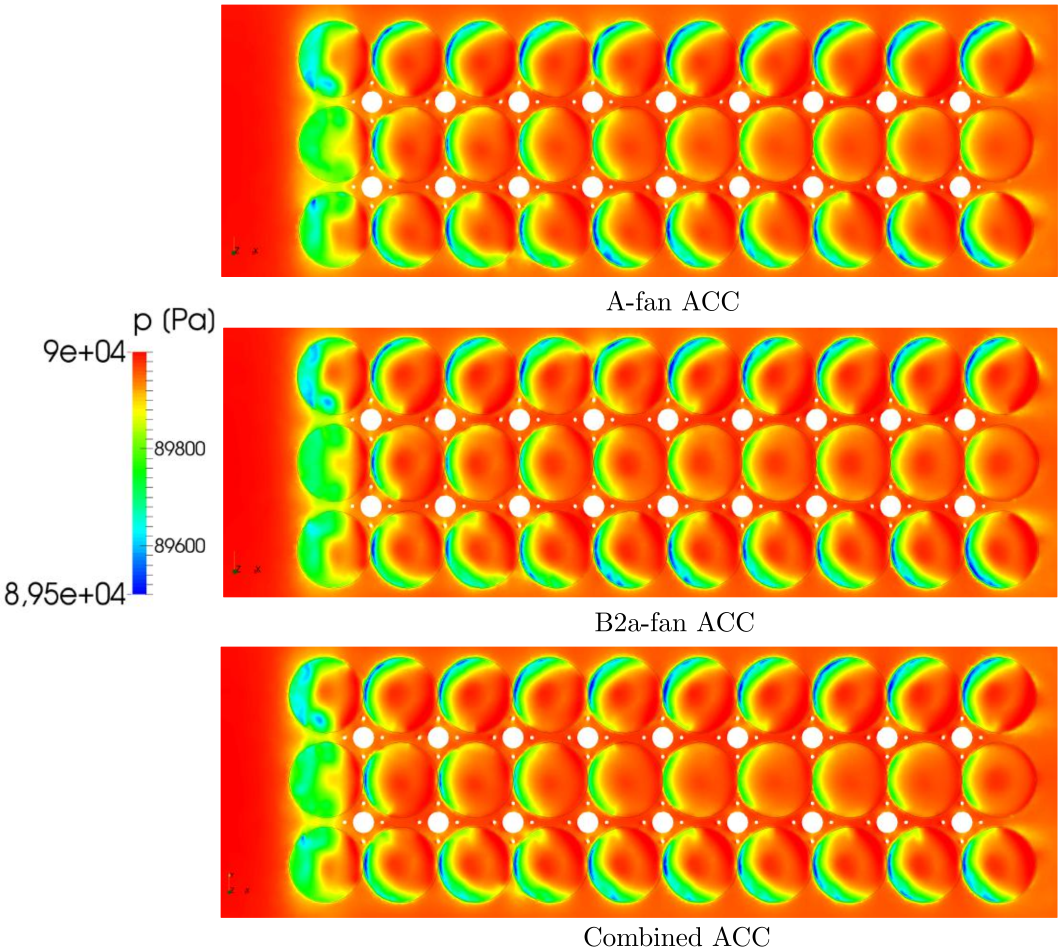

Figure 6.7: Pressure contour of ACC subject to x-direction cross-wind at 9 m/s

A volumetric effectiveness improvement up to 12 % was measured for the A-fan on the upstream periphery, and 6 % for the B2a-fan of layout 2 compared to the y-direction cross-wind case. The short upstream periphery decreases the performance degrading effect of two-dimensional flow as discussed in chapter 5 from figure 5.19. The smaller number of fans on the periphery normal to x-direction cross-wind results in less flow constriction at the centre periphery fan. This proves beneficial to both the periphery A-fan and B2a-fan performance. Higher measured A-fan performance in three-dimensional flow conditions leads to the conclusion that performance degradation resulting from two-dimensional flow is more pronounced for the A-fan compared to the B2a-fan. A larger number of fans on the peripheries parallel to the cross-wind direction is also able to exploit the three-dimensional flow component. This, added to increased periphery fan performance, results in the highest measured volumetric performance of each ACC for this cross-wind case.

The total power consumption of each ACC layout subject to cross-wind is compared in figure 6.8 to 6.10. Fluctuations in the power consumption increase for both layouts as the cross-wind speed increases. A significant drop in power consumption was measured for the ACCs in layout 2 configuration at a cross-wind of 90^o. Also noted is the 9.70 % higher power consumption of the A-fan ACC in layout 2 configuration compared to layout 1. Similarly, the B2a-fan ACC consumes up to 6.95 % in layout 2 configuration compared to layout 1 for cross-winds up to 90^o. Minimal differences were measured for the power consumption of the Combined ACC between layout configurations up to a cross-wind direction of 90^o.

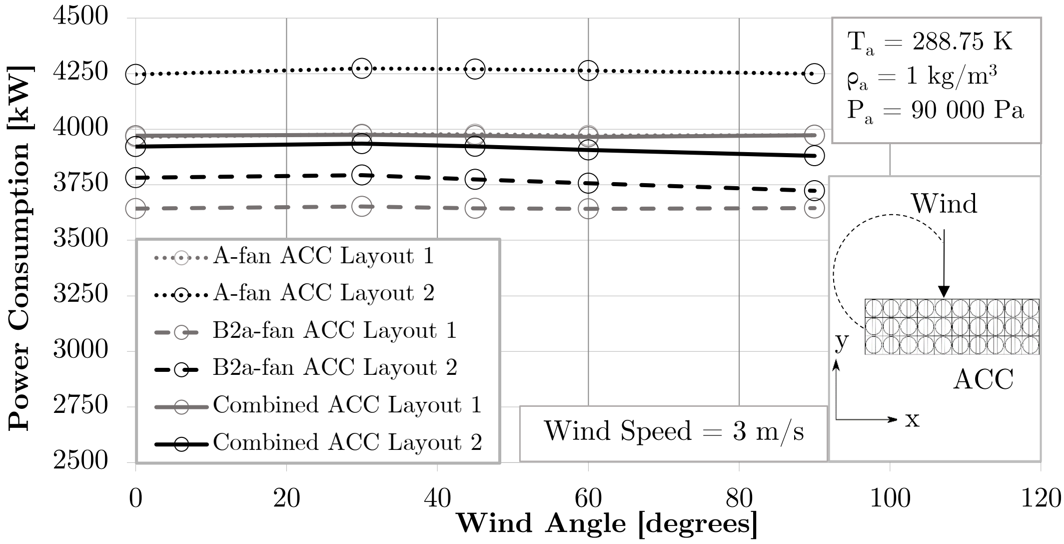

Figure 6.8: Total power consumed of each ACC subject to a 3 m/s cross-wind

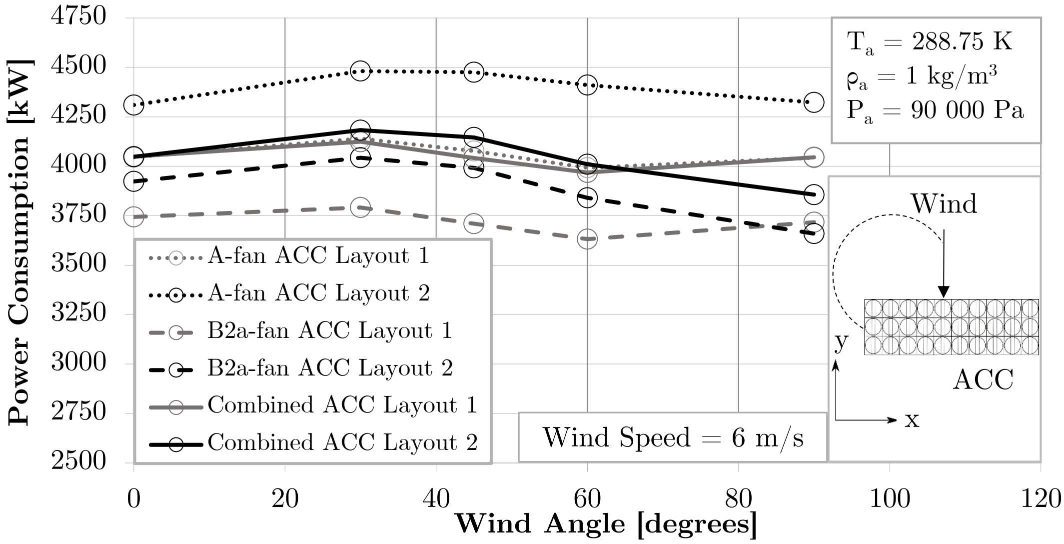

Figure 6.9: Total power consumed of each ACC subject to a 6 m/s cross-wind

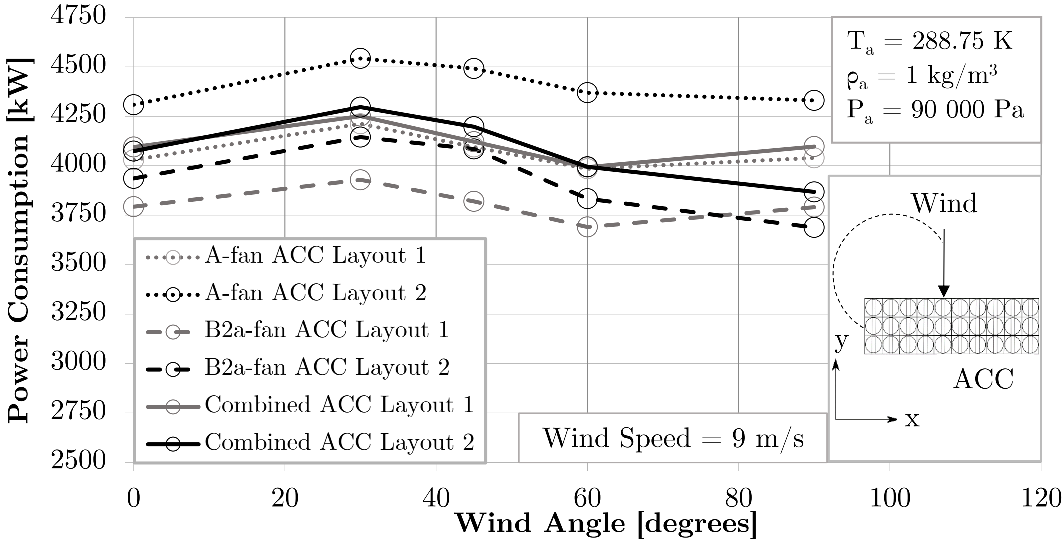

Figure 6.10: Total power consumed of each ACC subject to a 9 m/s cross-wind

ACC power consumption is discussed by considering the power consumption of individual fan units along the centre column of the layout 2 ACC, at a cross-wind speed of 9 m/s, from figure 6.11.

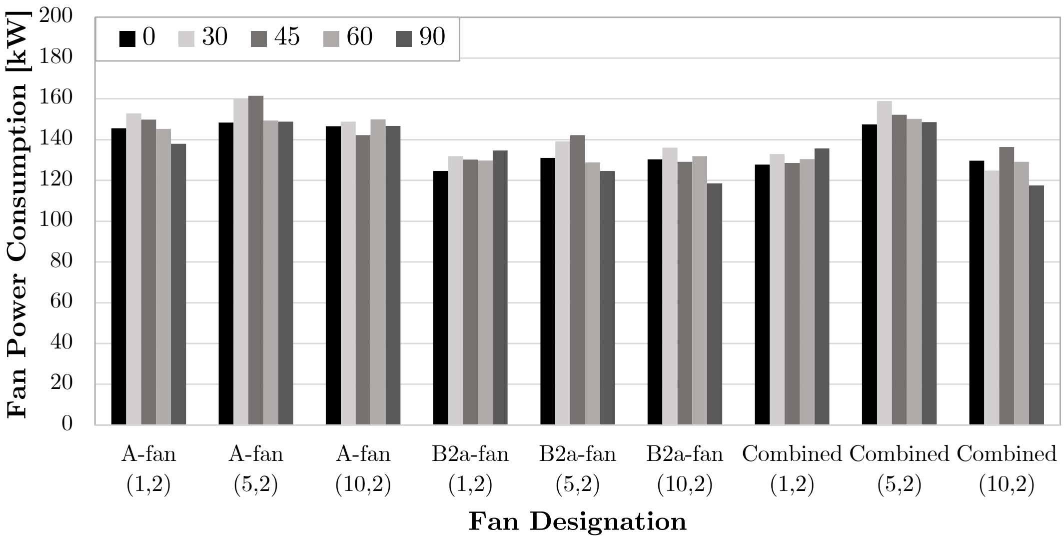

Figure 6.11: Fan power consumption subject to a 9 m/s cross-wind

The power requirements of the B2a-fan ACC and Combined ACC in layout 2 configuration decrease as the cross-wind shifts to a 90^o direction. This results from a decrease in power consumption of the B2a-fan. A possible reason could be the larger gradient of the B2a-fan power curve, shown in figure 4.14, resulting in a decrease of power requirements as the volumetric flow rate increases. The aforementioned idealised flow conditions present at the fan inlets in the centre of the ACC, and on the downstream periphery, results in these reduced power requirements. Power requirements of the A-fan is noted to show a lower dependency on cross-wind direction compared to the B2a-fan. The power requirements of the A-fan ACC, therefore, does not decrease to the same degree as the B2a-fan ACC and Combined ACC as a result.

The results of the volumetric performance analysis indicates distinct differences between layout configurations. The symmetrical nature of layout 1 yields consistent volumetric performance regardless of wind direction when compared to the performance of layout 2. If the dominant wind direction is known prior to the development of the ACC, layout 2 will yield higher volumetric performance if the short axis is orientated normal to the wind direction. Small deviations in wind direction could, however, lead to significant drops in performance for which layout 1 is better suited.

6.2 Thermal Performance

A comparative analysis of the total heat rejected to the atmosphere of each ACC is shown in figures 6.12 to 6.14. As with the volumetric performance, the thermal performance of layout 2 shows a greater dependency on ACC cross-wind orientation compared to layout 1.

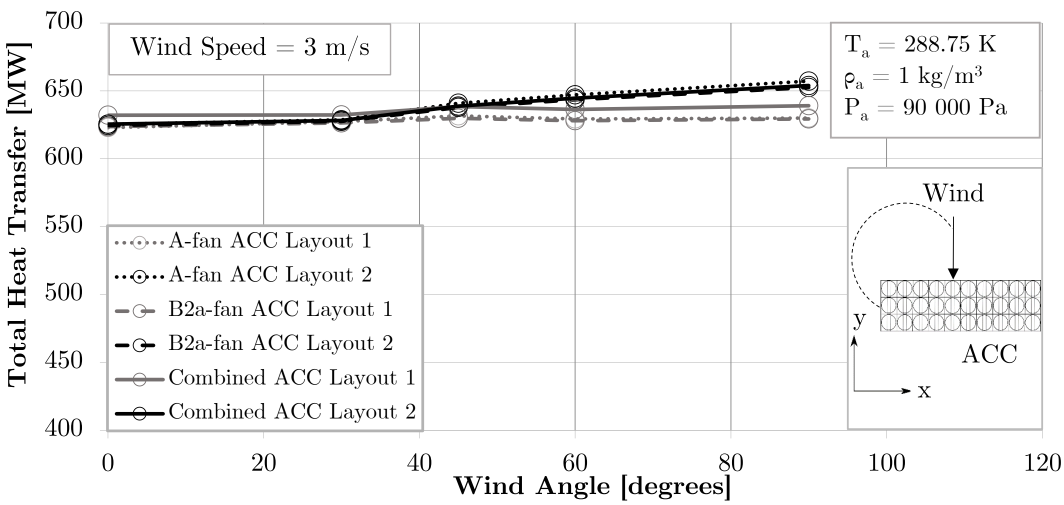

Figure 6.12: Total heat transferred for a 3 m/s cross-wind

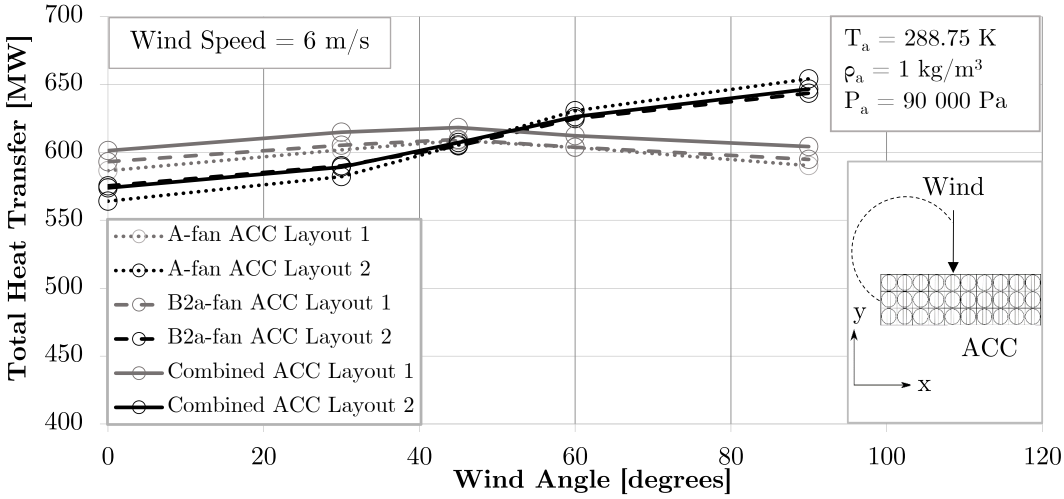

Figure 6.13: Total heat transferred for a 6 m/s cross-wind

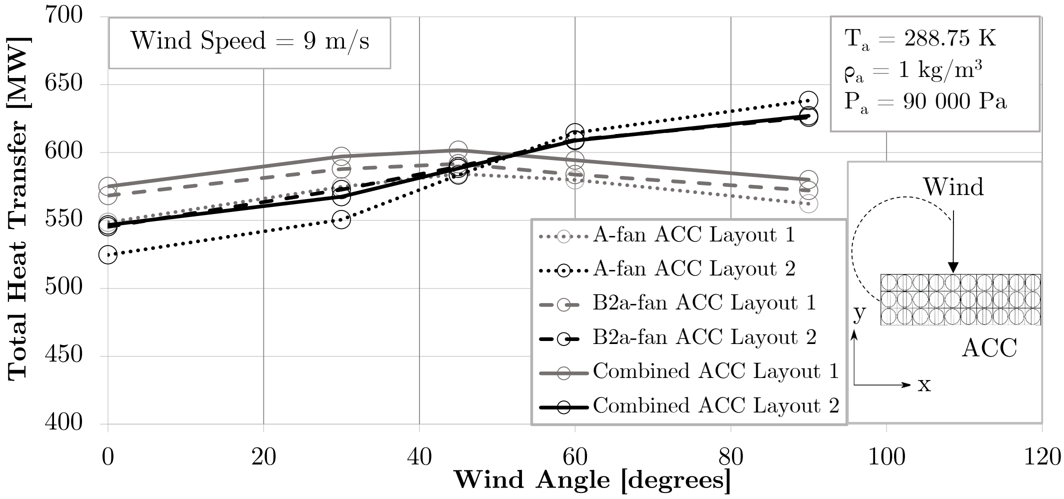

Figure 6.14: Total heat transferred for a 9 m/s cross-wind

A 21.67 % increase in heat transfer was measured for the A-fan ACC as the cross-wind direction changes from 0^o to 90^o. The B2a-fan ACC and Combined ACC exhibit a lesser dependence on cross-wind direction with a 14.7 % increase in heat transfer measured.

Reverse flow and recirculation, as discussed in chapter 5, also impede heat transfer capabilities of the heat exchangers in the layout 2 configuration. The heat transfer rates of individual heat exchangers are shown in figure 6.15 for a 9 m/s cross-wind. The lowest heat transfer rates were measured for the heat exchangers serviced by the A-fans on the long upstream periphery subject to a 0^o wind. This is primarily attributed to the poor volumetric performance of the A-fan. Similar heat transfer rates were measured for the B2a-fan heat exchangers on this periphery for both the B2a-fan ACC and Combined ACC. Increased volumetric performance of the A-fan on the short upstream periphery results in measured heat transfer rates similar for the B2a-fan in the case of a 90^o wind direction.

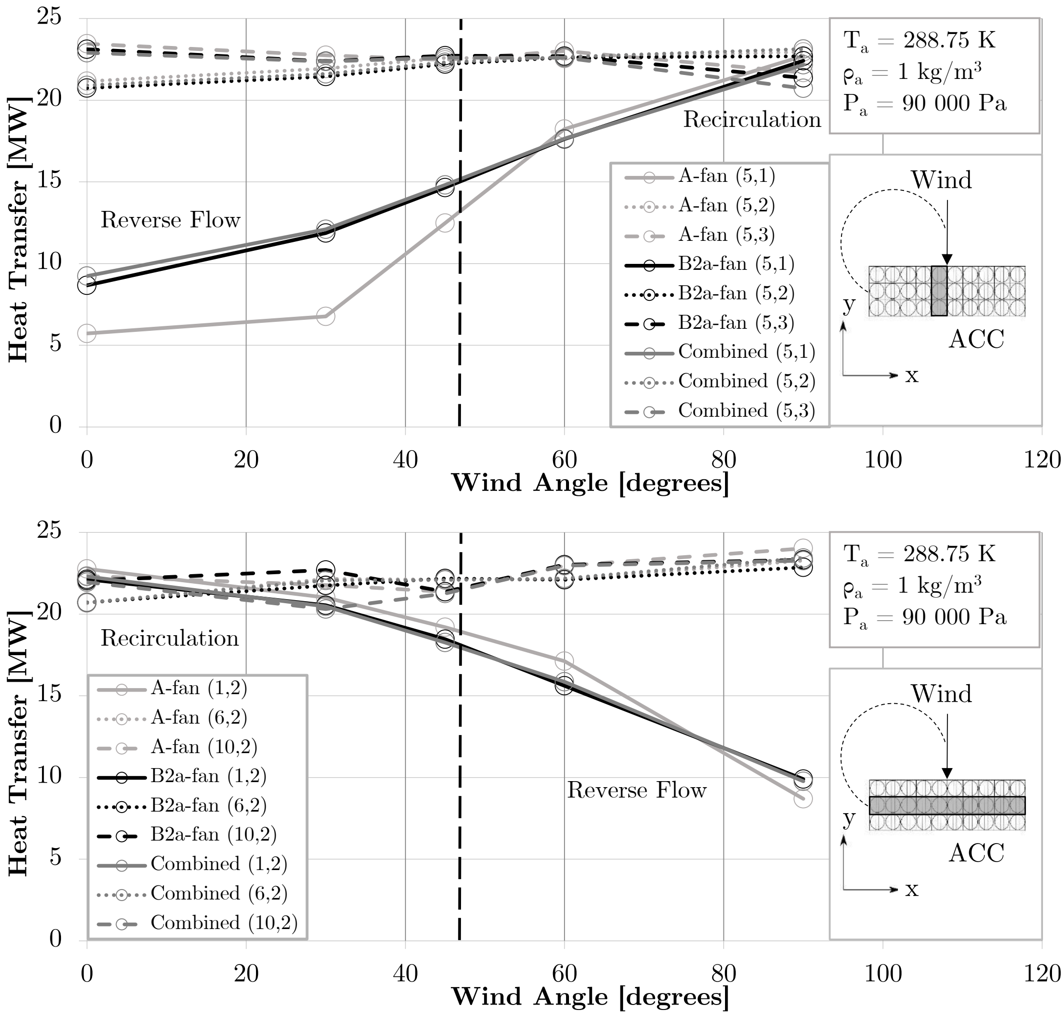

Figure 6.15: Heat transfer of individual heat exchangers for a 9 m/s cross-wind

The air inlet temperatures of heat exchangers subject to reverse flow and recirculation are shown in figure 6.16. Inlet temperatures up to 298 K were measured for the A-fan when the long periphery was orientated normal to the cross-wind direction. Orientating the short periphery of the ACC normal to the cross-wind direction decreases sensitivity of the periphery heat exchangers to the effects of reverse flow with a maximum inlet temperature of 293 K measured for the A-fan. This is due to the higher measured volumetric performance of the upstream periphery fans. The reverse flow in the upstream periphery plenums is illustrated by the temperature plots of figure 6.17.

Air inlet temperature rise due to recirculation is noted to be similar for each heat exchanger regardless of the fan type. Higher temperatures were measured when the long axis of the ACC was orientated parallel to the cross-wind direction. Heat exchangers on the short periphery show minimal sensitivity to plume recirculation effects.

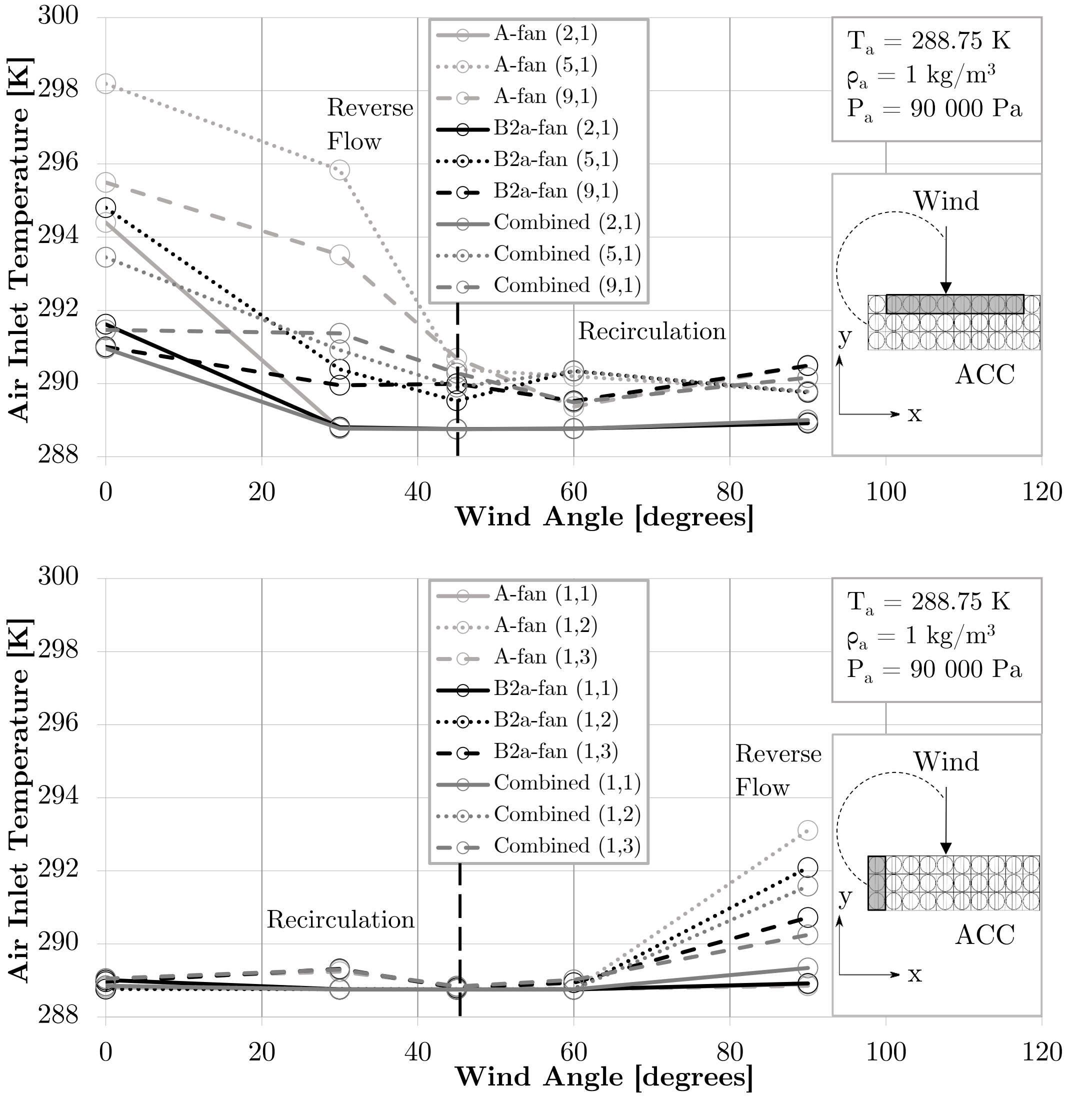

Figure 6.16: Inlet air temperatures of heat exchangers for a 9 m/s cross-wind

The effect of heated air recirculation is noted to be less compared to that of layout 1 with lower inlet temperatures measured for the affected heat exchangers. This results from the higher volumetric performance through the ACC ejecting the plume higher into the atmosphere limiting plume entrainment below the ACC platform. This only occurs when the long periphery is orientated parallel to the cross-wind direction, and is illustrated by the temperature distribution in figure 6.18 for a 9 m/s cross-wind. Also evident from the inlet temperatures is the negligible effects of recirculation when the shorter axis is orientated parallel to the wind direction. This is expected as the shorter length of the windwall impedes vortex shedding and subsequent plume entrainment.

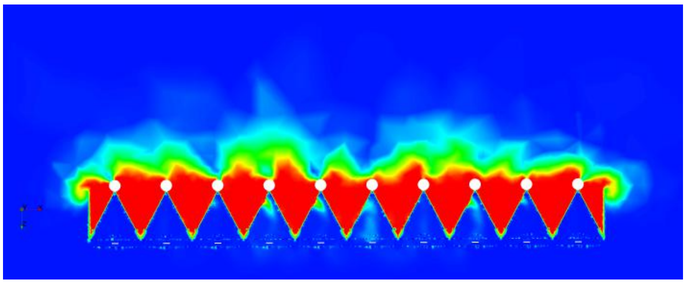

(6 m/s)

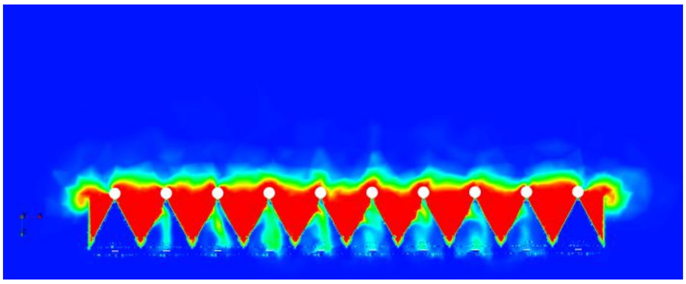

(9 m/s)

Figure 6.17: Temperature distribution of reverse flow in upstream periphery for a 0^o wind

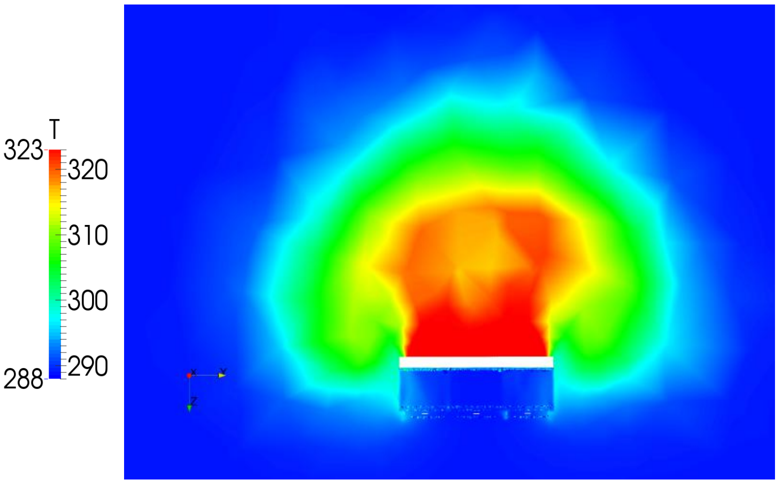

(9 m/s)

Figure 6.18: Temperature distribution of recirculation in downstream periphery for a 90^o wind

6.3 Heat-to-Power Performance

The overall ACC heat-to-power ratio is compared in figures 6.19 to 6.21 for each cross-wind direction, at different wind speeds. Similar heat-to-power ratios were calculated for each layout at 0-60^o wind directions. Differences in overall performance are noted only for a cross-wind direction of 90^o resulting from the aforementioned increased volumetric performance leading to increased heat transfer. The high power consumption of the A-fan results in the lowest calculated heat-to-power ratio, regardless of the higher measured volumetric and thermal performance, compared to the B2a-fan ACC and Combined ACC.

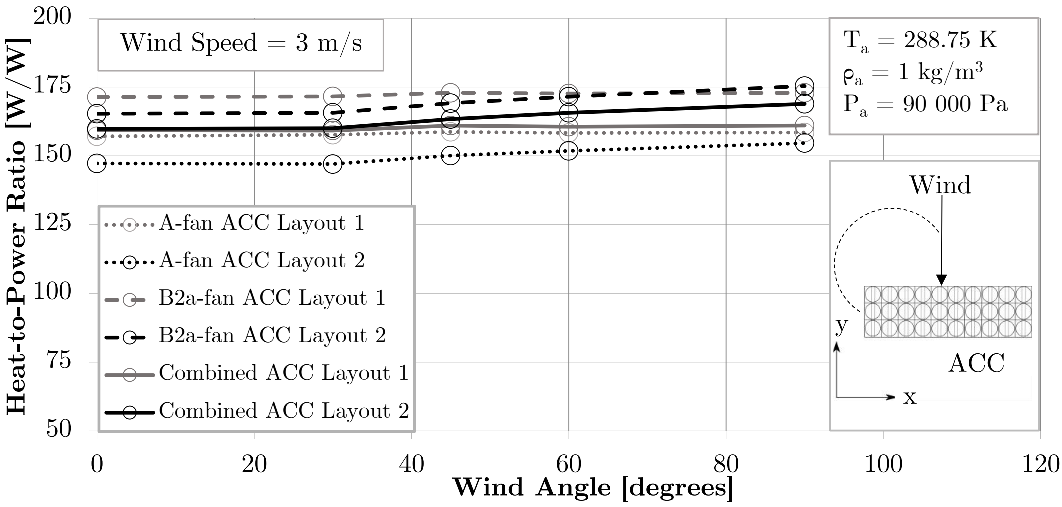

Figure 6.19: Heat-to-power ratio of each ACC subject to a 3 m/s cross-wind

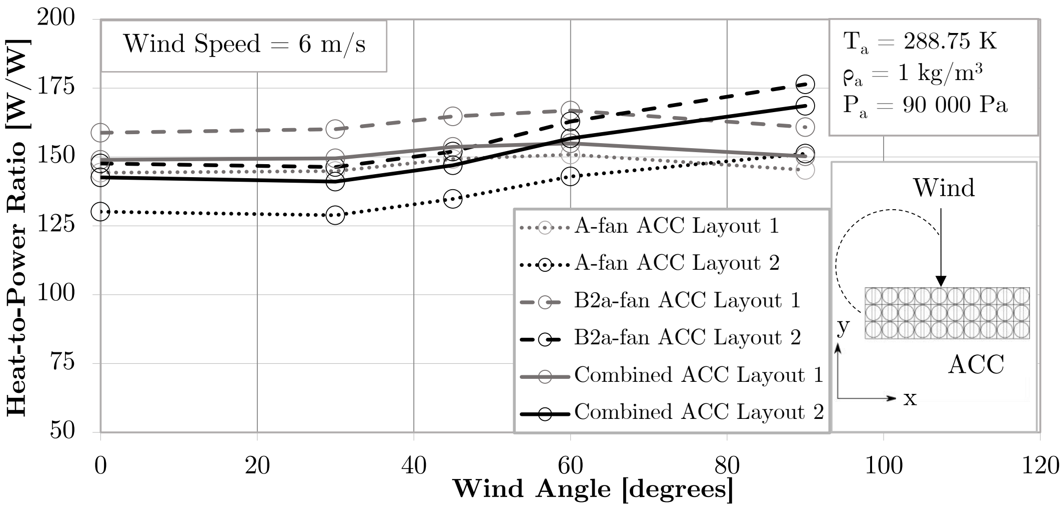

Figure 6.20: Heat-to-power ratio of each ACC subject to a 6 m/s cross-wind

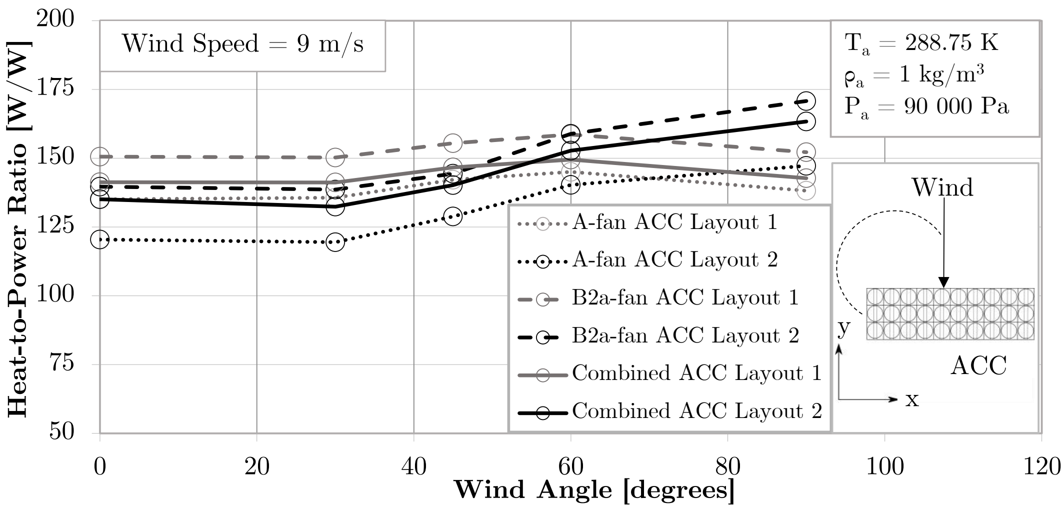

Figure 6.21: Heat-to-power ratio of each ACC subject to a 9 m/s cross-wind

The heat-to-power ratios of individual fan and heat exchanger units is shown in figure 6.22 and 6.23 for two cross-wind directions. The highest overall performance was measured for the B2a-fans on both the upstream and downstream periphery when the long periphery was orientated normal to the cross-wind direction. The A-fan and B2a-fan shows similar overall performance on the upstream periphery when the short axis was orientated normal to the cross-wind. The B2a-fan achieves superior overall performance in the centre of the ACC and downstream periphery for both the B2a-fan ACC and Combined ACC due to the lower fan power requirements. This subsequently leads to higher calculated total heat-to-power ratios compared to the A-fan ACC.

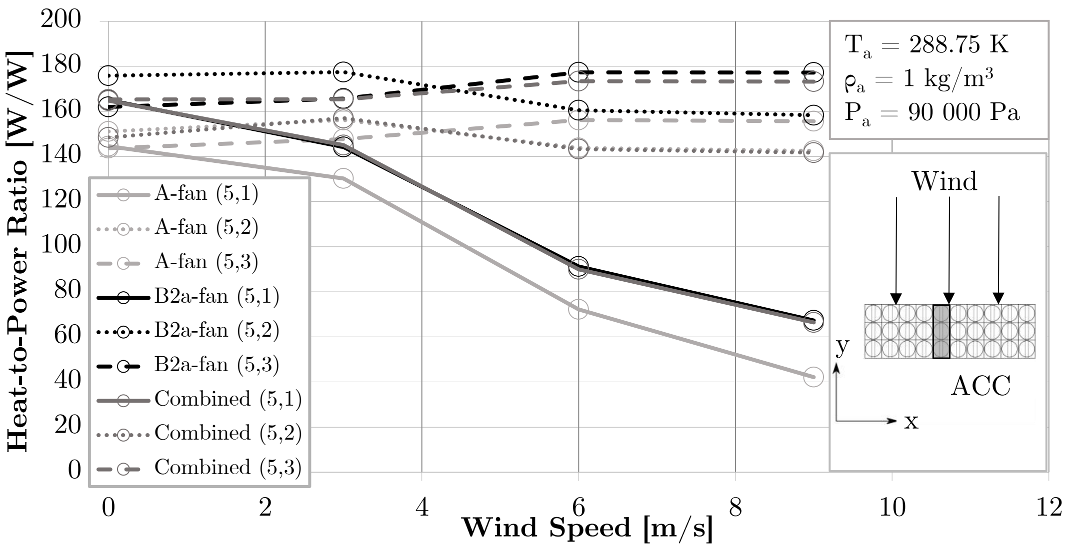

Figure 6.22: Heat-to-power ratio of fans subject to y-direction cross-wind

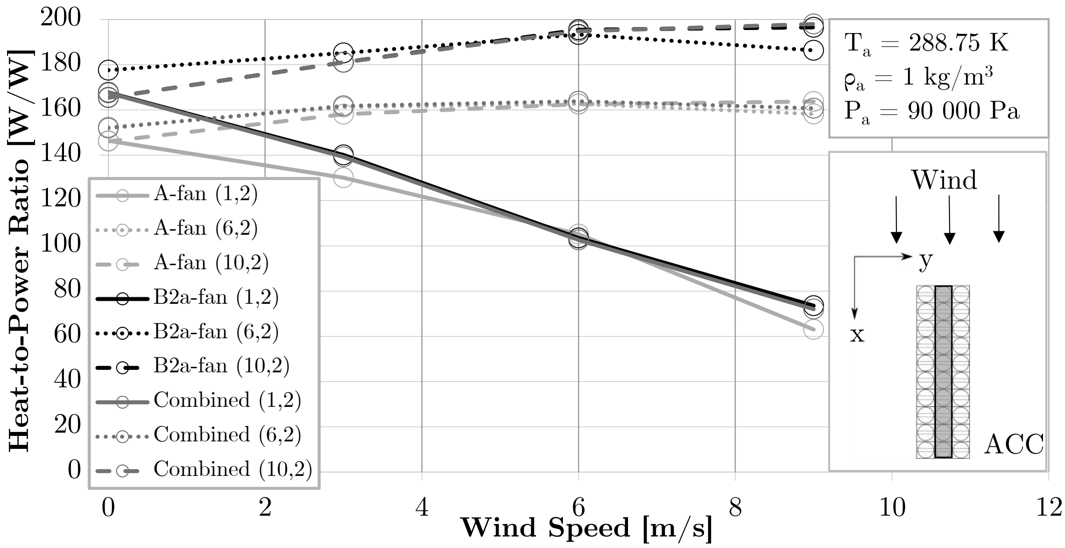

Figure 6.23: Heat-to-power ratio of fans subject to x-direction cross-wind

The noted volumetric, thermal and overall performance trends of the ACC in layout 2 configuration indicate a definite sensitivity to incoming cross-wind direction. The asymmetrical nature of the 3x10 configuration results in large performance fluctuations when cross-wind conditions change. The overall performance of layout 2 exceeds layout 1 only for specific cross-wind conditions. It can therefore be concluded that if a predominant cross-wind direction exists in the location where an ACC is required, layout 2 should be considered. The symmetrical nature of the layout 1 configuration exhibits similar overall performance for a range of cross-wind conditions. If the heat rejection rates are specified to remain within a certain range during ACC operation, regardless of cross-wind conditions, layout 1 should be considered. It is also expected that the reported performance trends for an ACC in either layout 1 or layout 2 configuration would be similar for larger sized ACCs.

6.4 Summary of Findings

This chapter served to detail a comparative performance analysis between two different ACC layouts. The 6x5 ACC was designated as layout 1 and the 3x10 layout was designated as layout 2. Similar to the previous chapter, the A-fan ACC, B2a-fan ACC and Combined ACC were subjected to cross-winds of varying speeds and directions and the volumetric, thermal and overall performance measured in the form of the heat-to-power ratio.

The major findings are discussed below:

- Decreasing volumetric, and thermal, performance of layout 2 was noted for increasing cross-wind speeds.

- The performance of layout 2 was deemed to be highly dependant on cross-wind direction due to the asymmetrical nature of the layout.
- The A-fan ACC in layout 2 showed the worst performance for the majority of cross-wind cases. A 2 % increase in volumetric performance was measured over the B2a-fan ACC and Combined ACC when the cross-wind was orientated normal to the short periphery.
- The poor upstream periphery performance of the A-fan lead to increased sensitivity to reverse flow conditions impeding heat transfer. All ACCs were similarly affected by recirculation of the hot air plume.
- Significantly higher power consumption was measured for the A-fan ACC and B2a-fan ACC in the layout 2 configuration compared to layout 1.
- The B2a-fan ACC showed the highest heat-to-power ratios, due to the lower power consumption, followed by the Combined ACC. Regardless of the increased volumetric and thermal performance measurements for the A-fan ACC in the one wind case, the higher power consumption lead to the lowest calculated heat-to-power ratios.
- The symmetrical nature of layout 1 lead to consistent performance for a variety of cross-wind conditions.

Chapter 7

Fan Blade Loading Analysis

The size and height of an ACC poses challenges when measuring the volumetric flow rate through the axial flow fan. A popular technique includes the use of anemometers placed concentrically in multiples of 4, 6 or 8 either upstream or downstream of the axial flow fan (Maulbetsch and DiFilippo, 2010; Muiyser *et al.*, 2013). Anemometers are well suited for determining fan volumetric performance when inlet flow is uniform, however non-uniform inlet flow conditions arise in the presence of cross-winds, as noted in chapter 5, decreasing measurement accuracy. This can be counteracted by increasing the number of anemometers used in the study, however this would also increase analysis cost.

An alternative method uses the fan power consumption characteristic curve along with the measured fan power consumption to determine the volumetric flow rate. The power consumed by the fan is measured using the torque exerted by the fan on the gearbox shaft. This is plotted on the characteristic curve and the corresponding flow rate is calculated. It is reported, however, that fan power characteristics deviates from the idealised case when off-axis flow conditions are present (Stinnes and von Backström, 2002). This would inevitably lead to measurement inaccuracies when this technique is employed on fans subject to distorted inflow conditions.

A new methodology for increasing measurement accuracy under cross-wind conditions is proposed by expanding on the use of the characteristic curves. An additional characteristic curve in the form of the resultant blade moment, along with the measured fan blade loading, can be used to determine the volumetric flow rate. Accuracy of the volumetric flow rate measurement can be increased through the use of the flow rate determined by the power curve. Measurement of fan blade loading can be implemented on-site with the use of the set-up as detailed by Muiyser *et al.* (2013). This chapter details the process and accuracy, determined numerically, of using the resultant blade moment as an additional data point along with the power curve to determine volumetric performance of the fan.

7.1 Measurement Theory

The blade loading was measured as the resultant moment due to aerodynamic loading. The actuator disk region consists of one disk with a concentric cell distribution. The resultant moment was therefore calculated as a blade-average moment of the entire disk. The relations for flap-wise and lag-wise moments were calculated according to:

$$M_F = \sum_{i=1}^{n_r} \frac{\delta F_{x(i)} r_{(i)}}{n_b} \tag{7.1}$$

$$M_L = \sum_{i=1}^{n_r} \frac{\delta F_{\theta(i)} r_{(i)}}{n_b} \tag{7.2}$$

Figure 7.1 illustrates the flap-wise and lag-wise bending moment applied to the fan shaft along with the applicable forces used in the actuator disk region.

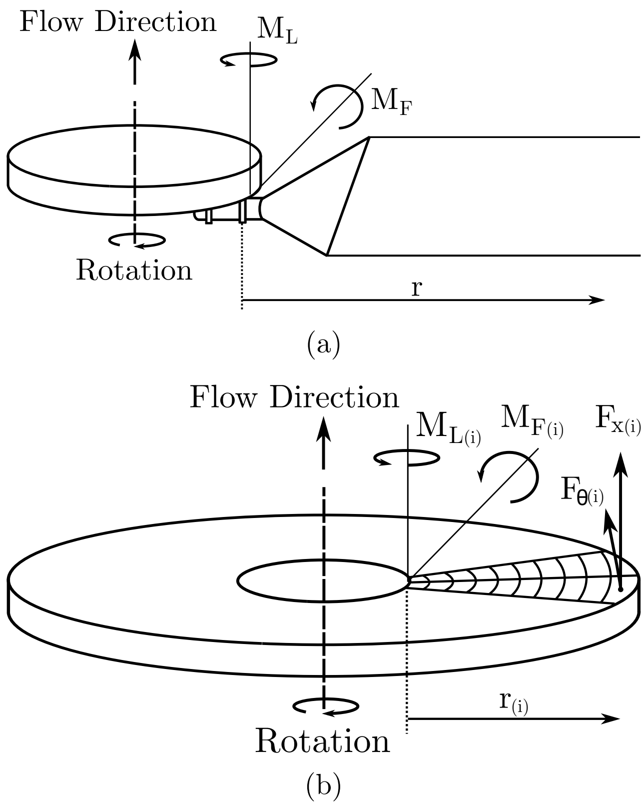

Figure 7.1: Illustration of a) measurement technique used to determine axial blade loading and b) implemented numerically

Important to consider is that the length of the moment arm is the same for the A-fan and the B2a-fan regardless of the fan hub size. The mounting of the B2a-fan blade was designed to coincide with that of the A-fan for on-site retrofitting as illustrated in figure 7.2.

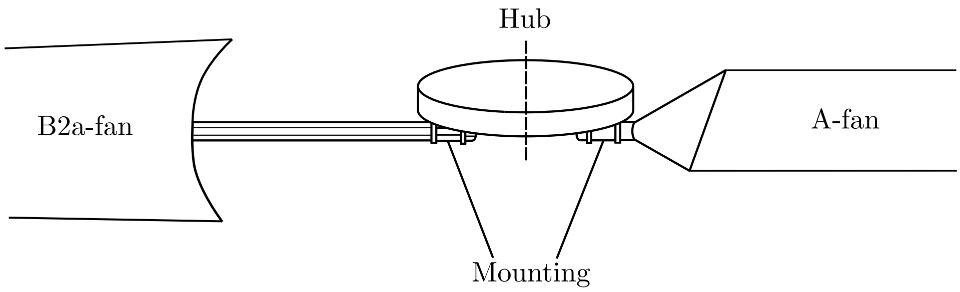

Figure 7.2: Illustration of blade mounting for the A-fan and B2a-fan

7.2 Characteristic Curve

A characteristic curve was generated for the axial flow fan using the average resultant bending moment as a function of volumetric flow rate in ideal conditions. Similar to the procedure for determining the fan static pressure rise and power consumption in chapter 4, the volumetric flow rate was varied and the bending moment measured. The procedure was performed on the 9.145 m A-fan and B2a-fan and the results are presented in figure 7.3.

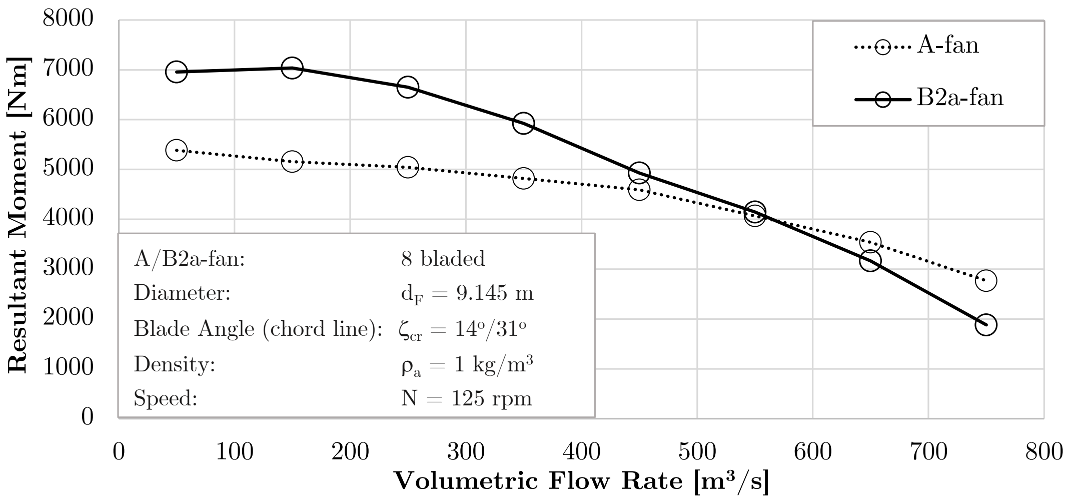

Figure 7.3: Average resultant bending moment vs. volumetric flow rate of the A-fan and B2a-fan

Muiyser *et al.* (2013) reported that the blade loading is proportional to the fan static pressure rise whereby a decrease in blade loading is noted for an increase in volumetric flow rate. This correlation between resultant bending moment, indicative of blade loading, and volumetric flow rate is observed in the results of the newly defined characteristic curve. It must be noted that the current depiction of blade loading is purely due to aerodynamic loading as the actuator disk model does not account for structural properties of the fan blade. Loads resulting from blade weight are therefore ignored in this analysis.

7.3 Free-standing Air-Cooled Condenser

The resultant bending moment was determined numerically for the single, free-standing A-fan and B2a-fan ACC unit under ideal conditions from chapter 4. The volumetric flow rate determined from the operating point was also used to calculate the resultant bending moment using the curve of figure 7.3. The difference between the measured and calculated bending moment will indicate if the characteristic curves are valid for use with a fan in an ACC set-up. The results are shown in table 7.1, and the difference between the numerical and curve-fitted results are indicated.

Table 7.1: Table indicating average bending moments of A-fan and B2a-fan ACC units in ideal conditions

Fan Type	**Numerical** [Nm]	**Curve** [Nm]	**Difference** [%]
A-fan	3759.47	3798.02	1.02
B2a-fan	3669.89	3512.22	4.49

As the proposed measurement method uses both the bending moment and power consumption of the fan, the above procedure was repeated using the fan power characteristic curve. The numerical and curve determined fan power consumption are shown in table 7.2, and the difference is also indicated.

Table 7.2: Table indicating power consumption of A-fan and B2a-fan ACC units in ideal conditions

Fan Type	**Numerical** [kW]	**Curve** [kW]	**Difference** [%]
A-fan	147 836	147 583	0.17
B2a-fan	130 719	127 799	2.28

Both the resultant bending moment and power consumption of the axial flow fans in the ACC unit indicate a good correlation between the numerical and curve-fitted data. The resultant blade moment curve, and power curve, is therefore considered applicable for both the A-fan and B2a-fan in the free-standing ACC unit. Applying the flow rate measurement methodology, whereby the volumetric flow rate is determined using the power and bending moment and plotting the points on the respective curves, and averaging the result, yields a 0.66 % and 2.89 % difference in flow rate to the numerically determined operating points for the A-fan and B2a-fan respectively. These differences are considered negligible and validates the proposed measurement method for use in a free-standing ACC unit in ideal conditions.

7.4 Air-Cooled Condenser Bank

For the sake of brevity, the analysis presented in this section will only focus on the A-fan and B2a-fan ACC in the 6x5 configuration (layout 1) subject to a cross-wind speed of 0 and 6 m/s in the y-direction. Similar results were observed for the 3x10 configuration (layout 2) as well as the remaining cross-wind directions and speeds. The power consumption of fans in the A-fan ACC subject to no wind and a 6 m/s cross-wind is shown in figure 7.4 along with the numerically determined, ideal fan power curve of the up-scaled fan. The deviations of the fan power consumption to the ideal case as reported by Stinnes and von Backström (2002) is highlighted for cross-wind conditions.

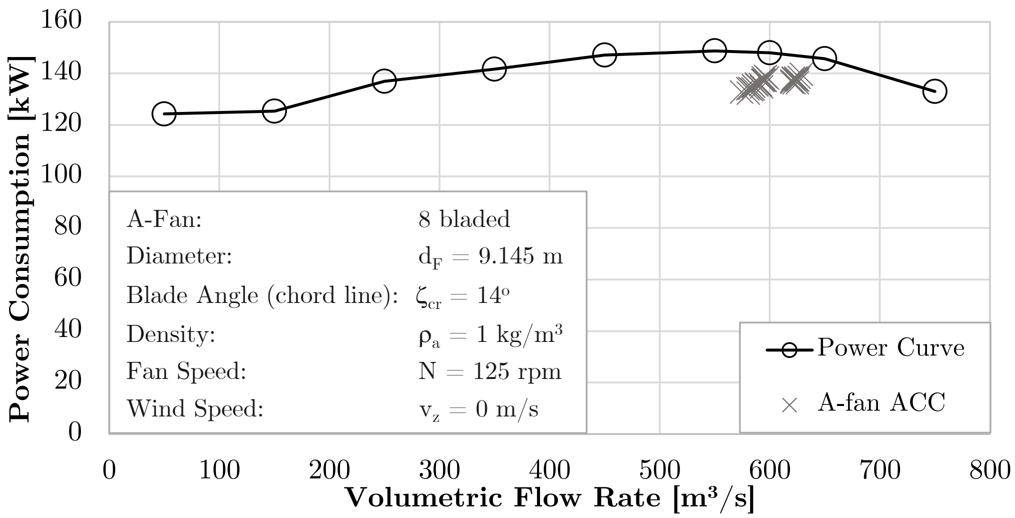

(a)

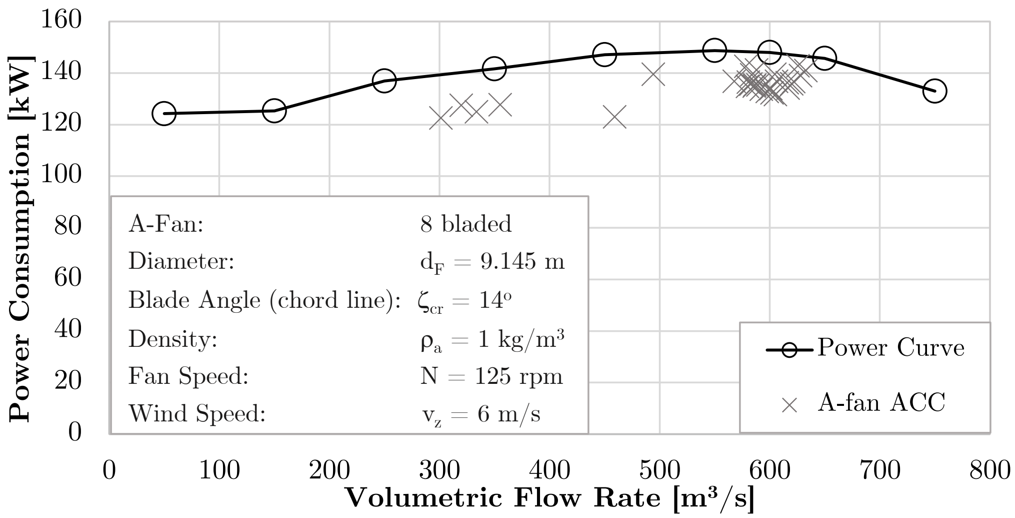

(b)

Figure 7.4: Power consumption of A-fans for a) 0 m/s and b) 6 m/s wind

The individual fan power consumption show slight deviations from the power curve when no cross-wind is present. As the cross-wind speed increases the fans subject to distorted inflow conditions deviate significantly from the ideal power curve. A similar trend is observed in the case of the B2a-fan with significant deviation noted when the ACC bank is subjected to cross-winds as shown in figure 7.5. The difference of the power consumption to the ideal case is observed to be smaller compared to the A-fans when no cross-wind is present. The reason for this is not apparent and an on-site analysis of ACC fan power consumption is recommended.

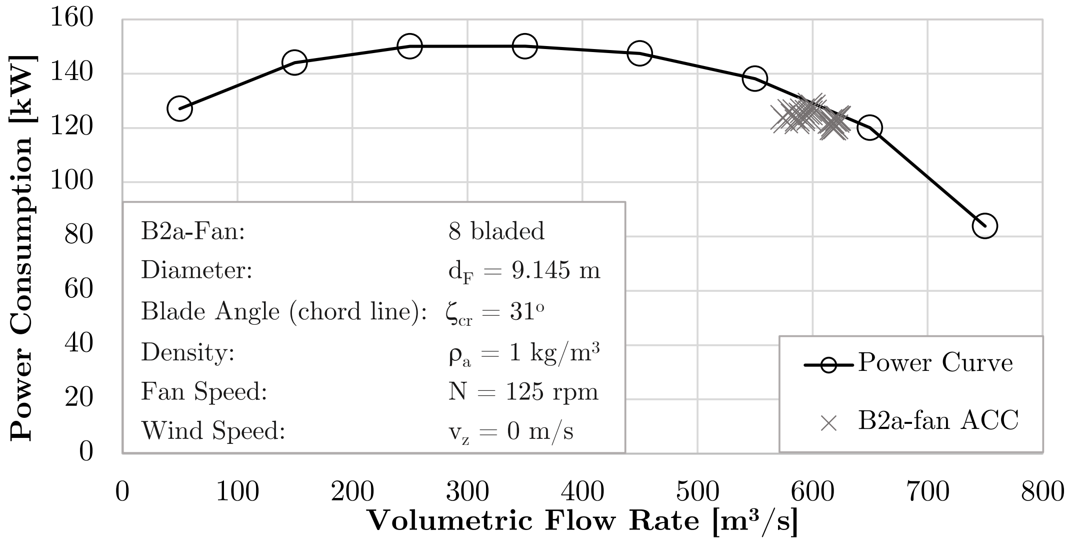

(a)

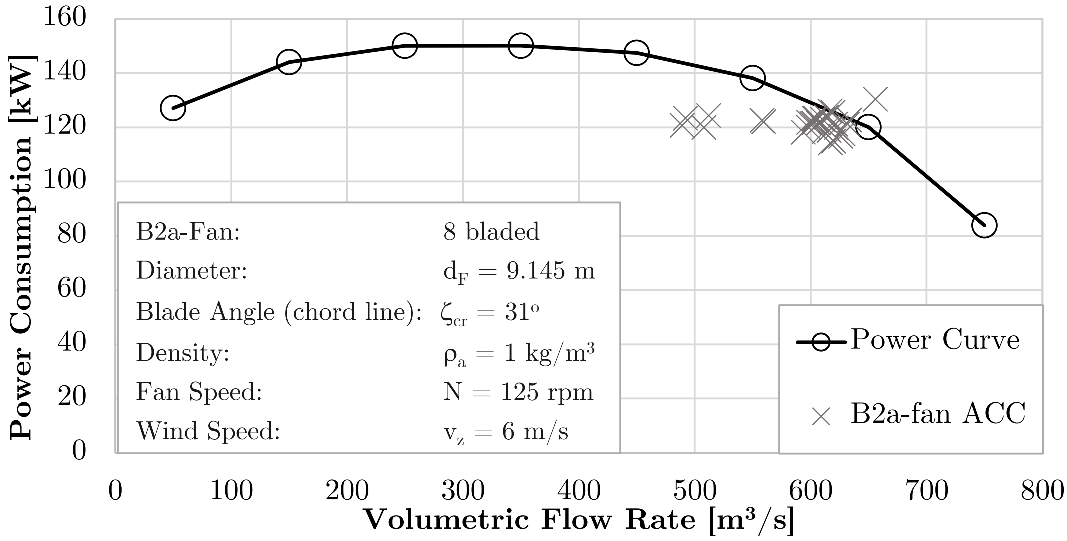

(b)

Figure 7.5: Power consumption of B2a-fans for a) 0 m/s and b) 6 m/s wind

These observed deviations of fan power consumption when the ACC is subjected to cross-winds will give rise to inaccuracies when using the power curves to determine the fan volumetric flow rates. Deviations in resultant fan blade bending moments are also observed in figures 7.6 and 7.7 when the ACC is subjected to cross-winds. Smaller deviations to the ideal characteristic curve are, however, observed compared to the fan power consumption case. An analysis follows from which the volumetric flow rate of fans are calculated using both the power and bending moment curve.

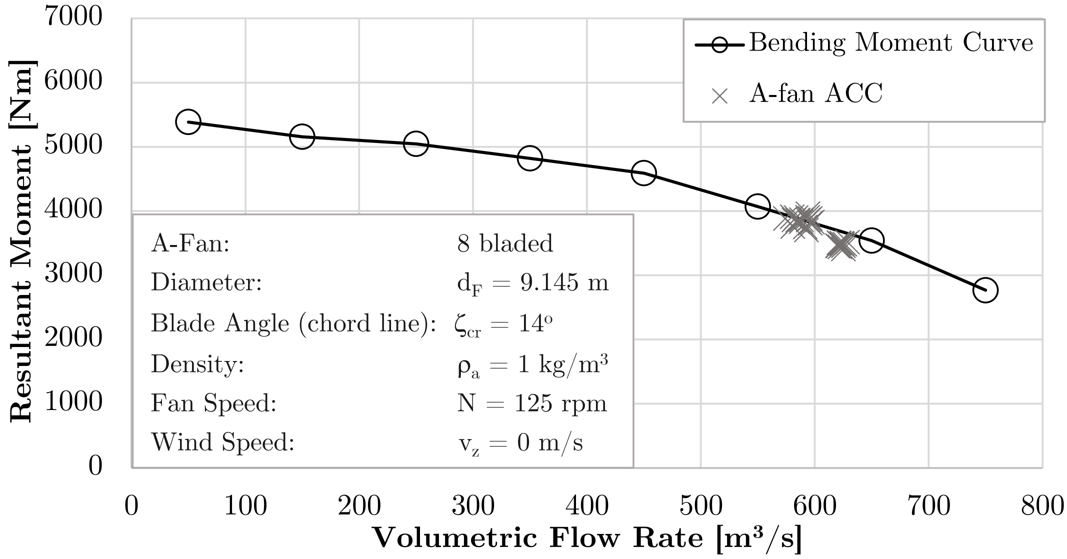

(a)

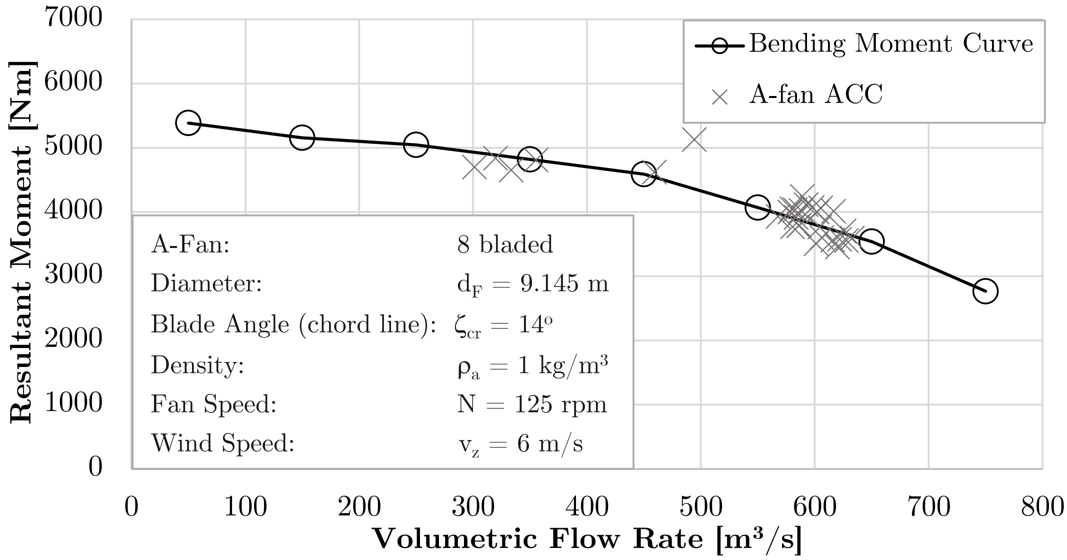

(b)

Figure 7.6: Bending moment of A-fans for a) 0 m/s and b) 6 m/s wind

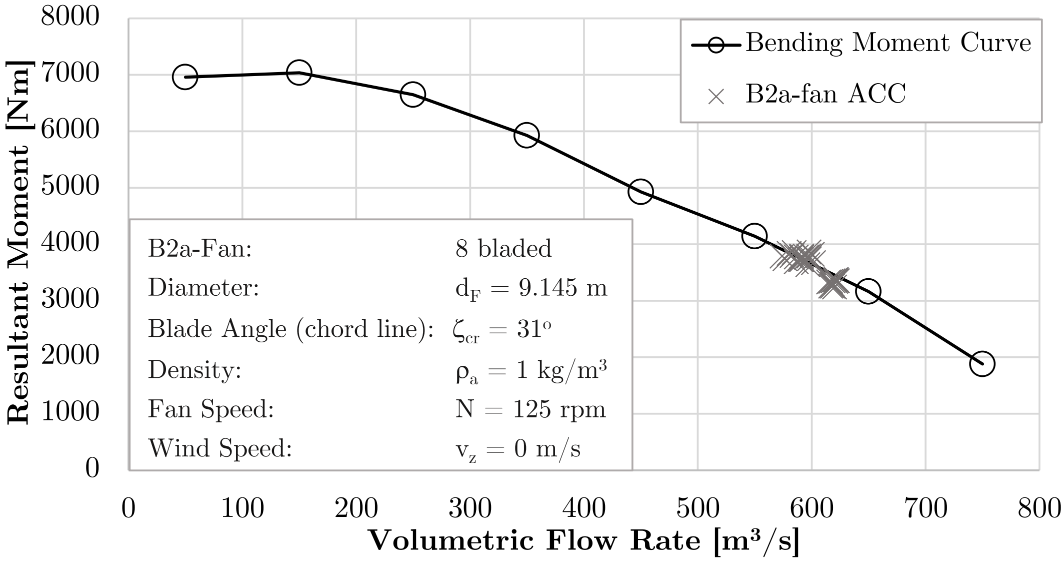

(a)

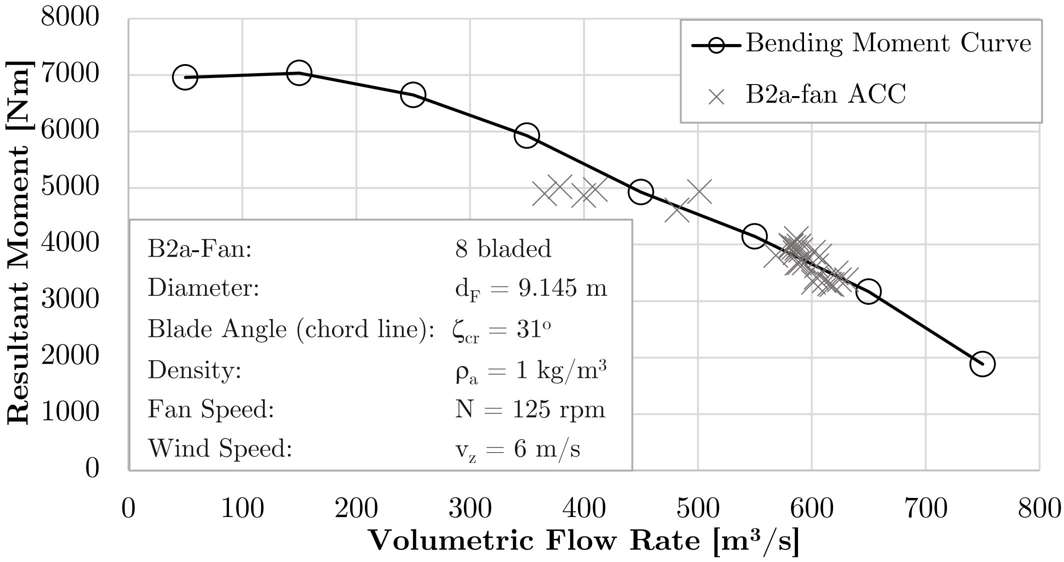

(b)

Figure 7.7: Bending moment of B2a-fans for a) 0 m/s and b) 6 m/s wind

The volumetric flow rate analysis focuses on certain individual fans in the ACC and will give an indication of the accuracy of the proposed measurement method. Three fans in the 4^{th} fan row will be used for the analysis focusing on the upstream periphery (fan (4,1)), the centre (fan (4,3)) and the downstream periphery (fan (4,5)). Table 7.3 and 7.4 shows the numerically determined power consumption, resultant blade moment and volumetric flow rates of the fans for different cross-wind speeds. The numerically predicted flow rate will be used to correlate the curve-calculated flow rates. This will give an indication of the validity of the measurement method.

Table 7.3: Table showing performance parameters of individual fans in the 4th row subject to no wind

Fan Designation	**Power Consumption [W]**	**Resultant Moment [Nm]**	**Vol. Flow Rate [m^3/s]**
A-fan (4,1)	132 333	3758.46	580.59
A-fan (4,3)	136 415	3410.52	625.04
A-fan (4,5)	135 789	3835.24	626.49
B2a-fan (4,1)	122 246	3691.06	586.55
B2a-fan (4,3)	120 431	3242.08	620.22
B2a-fan (4,5)	126 146	3837.80	580.20

Table 7.4: Table showing performance parameters of individual fans in the 4th row subject to 6 m/s wind speed

Fan Designation	**Power Consumption [W]**	**Resultant Moment [Nm]**	**Vol. Flow Rate [m^3/s]**
A-fan (4,1)	127 547	4838.88	319.70
A-fan (4,3)	134 943	3786.47	585.99
A-fan (4,5)	135 818	3454.54	619.98
B2a-fan (4,1)	129 781	5025.71	378.79
B2a-fan (4,3)	125 355	3676.30	589.11
B2a-fan (4,5)	121 246	3290.58	617.63

The method whereby the volumetric flow rates are determined from the fan power and resultant bending moment curves using the numerically determined power consumption and resultant blade moment were applied to each analysed fan. The results of the measurement methodology are shown in table 7.5 and 7.6. The flow rates determined using the power and bending moment curves are presented along with the difference to the numerically predicted flow rate on a percentage basis. Finally the difference in the volumetric flow rate when using the average of the two curves is also presented.

The results indicate distinct differences between the use of the fan power and blade moment to calculate the volumetric flow rate. In the no wind case a good agreement is observed between the average calculated volumetric flow rates and the numerically predicted flow rates for the B2a-fans. The large differences calculated for the A-fans stems from the measured difference of the power consumption compared to the ideal case. This leads to over-predicted volumetric flow rates from the characteristic curve. The results also indicate that higher accuracy is achieved if only the resultant bending moment is used for volumetric predictions. This stems from the smaller deviations to the characteristic curve as previously noted.

Table 7.5: Table showing volumetric flow rates determined using the characteristic curves for no wind

Fan	**Power** $\dot{\mathbf{V}}$ **[m^3/s]**	**Moment** $\dot{\mathbf{V}}$ **[m^3/s]**	**Power Error[%]**	**Moment Error[%]**	**Avg.** $\dot{\mathbf{V}}$ **Error [%]**
A-fan (4,1)	754.26	616.30	29.91	6.15	18.03
A-fan (4,3)	723.32	656.71	15.72	5.07	10.40
A-fan (4,5)	728.28	605.89	16.25	-3.29	6.48
B2a-fan (4,1)	641.43	590.56	9.36	0.68	5.02
B2a-fan (4,3)	648.64	645.52	4.58	4.08	4.33
B2a-fan (4,5)	625.95	573.05	7.89	-1.23	3.33

Table 7.6: Table showing volumetric flow rates determined using the characteristic curves for 6 m/s wind speed

Fan	**Power** $\dot{\mathbf{V}}$ **[m^3/s]**	**Moment** $\dot{\mathbf{V}}$ **[m^3/s]**	**Power Error[%]**	**Moment Error[%]**	**Avg.** $\dot{\mathbf{V}}$ **Error [%]**
A-fan (4,1)	169.09	337.23	-47.11	5.48	20.82
A-fan (4,3)	734.98	612.60	25.43	4.54	14.99
A-fan (4,5)	728.05	651.94	17.43	5.16	11.30
B2a-fan (4,1)	134.20	450.57	-64.57	18.95	22.81
B2a-fan (4,3)	629.10	592.34	6.67	0.43	3.67
B2a-fan (4,5)	645.40	639.59	4.50	3.56	4.03

In the case where the ACC is subjected to a cross-wind speed of 6 m/s, the volumetric predictions indicate fair agreement to numerically predicted volumetric flow rates for the fans not subject to distorted inflow conditions. Flow rate predictions using the power curve for fans on the upstream periphery deviate significantly from the numerical flow rate. In the case of the bending moment, the predicted flow rate of the A-fan subject to distorted inflow conditions correlate well with the numerical results. This is not the case with the B2a-fan as a significant difference was calculated for the flow rate using both the power and bending moment curve. Regardless of the differences calculated for each curve, the average volumetric flow rate for the A-fan and B2a-fan on this periphery shows a poor correlation to the numerical case.

The proposed use of the resultant bending moment to increase the accuracy when determining the volumetric flow rate for on-site ACC analysis is justified considering the smaller deviations from the characteristic curve compared to the fan power consumption. It can also be concluded that in the case where the fan power consumption deviates significantly from the ideal case, a higher degree of accuracy can be achieved when calculating the volumetric flow rate using the measured resultant bending moment. Even though the numerical approach to the measurement procedure provides a reliable method for increasing accuracy of volumetric flow rate prediction, it is recommended that the analysis be validated using experimental results to determine on-site applicability.

As previously mentioned, the current analysis does not include the effects of density variations on fan power consumption and blade loading. The Boussinesq solver used in OpenFOAM does not account for density variations and is deemed as an area recommended for future study. As hot air recirculation and reverse flow is present for fans in an ACC subject to cross-winds, it is expected that both the fan power consumption and fan blade loading would decrease as the density of air flowing through the axial flow fans decreases. To compensate for this decrease in measured fan power consumption and blade loading would require measurement of inlet flow temperature in order to scale the characteristic curves accordingly. Fan scaling laws applicable to resultant fan blade bending moment with density variations would also require derivation.

7.5 Summary of Findings

This chapter detailed the process by which the accuracy of on-site of fan volumetric flow rate measurements can be increased. The use of the fan blade loading measurements, along with the fan power consumption, can be plotted on the characteristic curve and the flow rate determined.

The blade-averaged resultant bending moment of the extended actuator disk model was generated as a function of the volumetric flow rate for the A-fan and B2a-fan. The results correlated with literature.

The measurement technique was applied to the free-standing ACC unit to attain the accuracy of the measurement process for ideal conditions. The numerically predicted blade loading and power consumption was compared to those determined using the volumetric flow rate plotted along the respective characteristic curve. Negligible differences were noted for both fans indicating that the free-standing unit behaves according to the characteristic curves. The volumetric flow rates were also predicted using the numerically determined resultant bending moment and fan power consumption. These were plotted on the respective curves and the flow rates averaged. The results correlated well with the numerical results.

The measurement technique was extrapolated to the 30 fan A-fan and B2a-fan ACC bank. Two cross-wind speeds along one direction was analysed. Deviations of the fan power and blade loading to the ideal curves was highlighted when the ACC is subjected to cross-winds, as reported in literature.

Blade loading deviations were noted to be less severe than the fan power consumption for both ACCs.

Volumetric flow rates were predicted using the numerically determined fan power and blade loading using the characteristic curves. Predictions showed fair correlation for fans not subjected to distorted inflow (centre and downstream periphery). Poor correlation was noted for fans on the upstream periphery using either the fan power or blade loading curves. It was, however, reported that flow rate predictions using only resultant bending moment show greater accuracy than the fan power curves.

Chapter 8

Conclusion

The research focused on the development and validation of an accurate and reliable ACC model in OpenFOAM. A performance evaluation was performed using ACCs with two different axial flow fans, as well as an ACC utilising a combination of two axial flow fans. The performance of a symmetrical and asymmetrical ACC layout were also determined under windy conditions. Finally, an alternative on-site volumetric flow rate analysis methodology was evaluated. Major findings are discussed below expanding on the summaries of chapters 4, 5, 6 and 7. A recommendation on future work follows.

8.1 Numerical Validation

Prior to the commencement of the study a literature survey was conducted with regards to previous works done on ACC modelling. Several studies were considered and different numerical modelling approaches identified. The simplifications of ACC models used in previous studies were also highlighted.

Two axial flow fans were considered in the ACC model of this study. The A-fan is an industrial fan commonly utilised for cooling applications. The B2a-fan was designed and manufactured at Stellenbosch University. Details of each fan are presented in appendix A.

The actuator disk and extended actuator disk model were considered for the axial flow fan model. The extended model was chosen for increased accuracy of fan performance characteristics predicted at low volumetric flow rates. As this model is an extension of the actuator disk model, both models were validated using fan test data obtained from a BS848 Type-A test facility. Coinciding with previous literature, the actuator disk model under-predicted fan static pressure rise at low volumetric flow rates for both fans whereas the extended actuator disk model corrected this discrepancy. Fan power consumption correlated well with experimental results for both models.

The heat exchanger was designed according to the A-frame, or Delta frame, heat exchanger format commonly used in practice. A porous region was used to model the mechanical losses in the heat exchanger. It was numerically determined that the Darcy-Forcheimmer law used to change the direction of the flow in the heat exchanger induces a pressure drop similar in magnitude to the turning loss coefficient determined experimentally by Meyer and Kröger (2001). Subsequently, the only mechanical loss modelled in the heat exchanger porous region was the isothermal heat exchanger loss coefficient. The mechanical loss and heat transfer were validated and a good correlation was noted in each case.

The axial flow fan and heat exchanger model were combined to form a free-standing ACC unit. The operating points of the A-fan and B2a-fan were determined under ideal operating conditions as stipulated in appendix C. It was determined beforehand that the inclusion of the support struts and fan obstacles as mechanical loss coefficients in the heat exchanger porous region would yield inaccurate operating point predictions. These mechanical obstacle losses were therefore not included as loss coefficients but rather the support struts and fan walkway were modelled as three-dimensional structures in the geometrical domain.

Power requirements of the A-fan were measured to be significantly higher than the B2a-fan. The volumetric flow rates at the operating points also over-predicted the analytical solution indicating the presence of kinetic energy recovery in the plenum. The recovery of the B2a-fan was validated with the results of Meyer and Kröger (1998) using a domain resembling the experimental set-up. A good correlation was noted with the experimental results. This was not reported for studies using simplified plenum geometries. The axial flow fan model, heat exchanger model and ACC model were therefore considered validated.

8.2 Comparative Study

A study on the volumetric, thermal and overall performance was done to compare three different fan configurations in an ACC. The A-fan ACC consisted of 30 A-fans, the B2a-fan ACC used 30 B2a-fans and the Combined ACC used both A-fans and B2a-fans. Each ACC was subjected to cross-wind speeds of 0, 3, 6 and 9 m/s at the platform height along different cross-wind directions. The performance characteristics of a 6x5 ACC layout (layout 1) and a 3x10 ACC layout (layout 2) were also compared.

The B2a-fan ACC was first compared to previous literature. The comparative study is discussed focusing on the performance of the different ACCs in the layout 1 configuration when subjected to cross-winds. A comparative analysis of the performance of layout 1 and layout 2 follows. For brevity, the discussion encompasses all cross-wind conditions.

8.2.1 Fan Configuration Performance Analysis

The B2a-fan ACC was subjected to cross-winds in one direction. The results were compared to the studies of van Rooyen (2007) and Joubert (2010) using the volumetric effectiveness ratio. Differences in volumetric performance of fans located on the upstream periphery were measured and attributed to the difference in domain modelling approaches, along with the improved performance of the extended actuator disk model under distorted inlet flow conditions compared to the models used by the previous studies. Near identical fan performance was measured on the downstream periphery. Higher total volumetric performance of the ACC was noted at higher wind speeds. Lower total thermal performance was also measured resulting from heat transfer impeding phenomena not observed by the previous studies.

A general trend of decreasing volumetric flow rate with increasing cross-wind speed was measured for all analysed ACCs. Fan performance on the downstream periphery was noted to be unaffected by different cross-wind speeds. The main contributor to the decrease in total ACC volumetric performance was therefore identified as the decrease in fan performance on the upstream periphery. A region of flow separation was observed to form at the fan inlet leading to distorted inlet flow consequently reducing performance. The lowest fan performance was measured for the A-fan on the upstream periphery with the B2a-fan exhibiting higher volumetric performance when subjected to distorted inlet flow. These volumetric effectiveness improvements of the larger hub-to-tip ratio B2a-fan were also reported in previous literature and attributed to the steep gradient of the static pressure characteristics.

These individual fan performance characteristics resulted in distinct performance differences measured for each ACC. In terms of volumetric performance, the B2a-fan ACC and Combined ACC exhibited similar sensitivity to cross-wind speeds. The total volumetric flow rate through the Combined ACC was, however, higher than both the A-fan ACC and B2a-fan ACC. The largest decrease in total volumetric effectiveness for high cross-wind speeds was measured for the A-fan ACC. This lead to the conclusion that the poor upstream periphery performance of the A-fan increases ACC volumetric performance sensitivity to cross-wind speed.

A decrease in total heat transfer was also measured for increasing cross-wind speed. The direct correlation between heat transfer and volumetric flow rate lead to decreasing heat transfer rates measured for the heat exchangers on the upstream periphery. Several phenomena increasing heat exchanger air inlet temperature, and a subsequent decrease in thermal performance, were identified. Heated air recirculation and plume entrainment affect heat exchangers on the downstream periphery and peripheries parallel to the cross-wind direction. Secondly, the aforementioned distorted inflow conditions present at the upstream periphery fans lead to reverse flow at the fan blades. It was observed that heated air was drawn from outside the heat exchanger back into the plenum.

Similar to the volumetric performance, distinct differences were measured in the thermal performance of heat exchangers serviced by the A-fan and B2a-fan. The poor performance of the A-fan on the upstream periphery resulted in larger regions of reverse flow and subsequently lead to the lowest measured heat transfer. This was rectified to an extent by the increased performance of the B2a-fan. Periphery fans in the Combined ACC exhibited the highest sensitivity to recirculating flow due to the increased volumetric flow rate drawing large quantities of heated air below the platform. Total heat transfer rates encompassed the measured differences between fans with the highest thermal performance was measured for the Combined ACC followed by the B2a-fan ACC, and the worst performance was measured for the A-fan ACC.

The power requirements of each fan lead to higher measured power consumption of the A-fan ACC than the B2a-fan ACC. Interestingly, similar power consumption was measured for the Combined ACC as the A-fan ACC even though both fan types were used. This was attributed to the higher measured volumetric flow rates through the periphery B2a-fans resulting in increased power requirements.

Overall performance was determined using the heat-to-power ratio. The heat-to-power ratio highlighted the advantages of using an efficient, high volumetric flow rate fan in an ACC. Due to the 7-9 % lower power consumption of the B2a-fan ACC compared to the A-fan ACC and Combined ACC, the average heat-to-power ratio across all wind speeds was calculated to be 9 % higher than the A-fan ACC and 7 % higher than the Combined ACC. Placing the B2a-fan on the periphery of the Combined ACC also yielded a 2 % increase in the average heat-to-power ratio compared to the A-fan ACC.

Performance sensitivity to cross-winds was also determined using 5 cross-wind directions. Small fluctuations in volumetric, thermal and overall performance were noted for each ACC attributed to the symmetrical nature of the 6x5 layout configuration. The A-fan ACC showed the highest sensitivity with performance differences up to 4 % measured for different cross-wind directions. The B2a-fan ACC and Combined ACC were similarly affected with performance differences of 3 % measured.

8.2.2 ACC Layout Comparative Analysis

An analysis was done in order to compare the performance of each ACC in layout 1 and layout 2 configuration under cross-wind conditions. The findings indicate a higher sensitivity of volumetric, thermal and overall performance to cross-wind direction exists for layout 2 due to the asymmetrical configuration. At higher cross-wind speeds, volumetric performance fluctuations up to 23 % were measured for the A-fan ACC as the cross-wind direction changes.

Similar performance trends to layout 1 were measured for individual fans. The A-fan showed poor performance on the upstream periphery whereas the B2a-fan showed improved performance. In the cross-wind case where the direction was normal to the short axis of the ACC, however, similar performance was measured for the upstream periphery A-fan and B2a-fan. This was attributed to a decrease in the performance degrading effect of two-dimensional flow determined to influence fans situated in the centre of the upstream periphery. This increase in periphery A-fan performance lead to the A-fan ACC outperforming the other ACCs for this cross-wind direction case. The B2a-fan ACC and Combined ACC outperform the A-fan ACC for all other cross-wind conditions.

Similar power consumption was measured for the B2a-fan ACC and Combined ACC in layout 2 configuration. The A-fan ACC consumed up to 9 % more power compared to the other ACCs. The power consumed by all three ACCs in the layout 2 configuration was measured to be significantly higher than layout 1.

Thermal performance was also noted to be highly dependent on cross-wind direction. The previously mentioned effects of recirculation and reverse flow impedes heat transfer to varying degrees depending on the ACC orientation. The large number of fans on the long periphery results in reverse flow being the dominant heat transfer impeding factor when the cross-wind is orientated normal to this periphery. In the case where the cross-wind is orientated normal to the short periphery, it was expected that the effects of plume entrainment and recirculation would significantly decrease heat transfer capabilities. This was not the case as the increased volumetric performance ejected the plume higher into the atmosphere. Similar to the volumetric performance, the B2a-fan ACC and Combined ACC showed the highest heat transfer rates apart from the one, previously mentioned, cross-wind case where the A-fan showed highest performance.

Overall performance indicated that regardless of the superior volumetric and thermal performance for one cross-wind case of the A-fan ACC, the significantly higher power requirements decreases the heat-to-power ratio below the

B2a-fan ACC and Combined ACC. Subsequently, the B2a-fan ACC and Combined ACC outperform the A-fan ACC for all cross-wind conditions. Lower measured power consumption of the B2a-fans also lead to the B2a-fan ACC outperforming the Combined ACC.

8.3 Fan Blade Loading Analysis

A method for increasing on-site volumetric flow rate measurements of large-scale axial flow fans was proposed using the resultant blade bending moment as an additional performance characteristic curve. The curve was generated using a large-scale A-fan and B2a-fan in a domain representing the BS848 test facility and plotted as a function of volumetric flow rate. It was observed to be directly proportional to the fan static pressure curve as is reported in previous literature.

The method proposed uses the measured fan power consumption and blade bending moment along with the respective characteristic curves to determine the flow rate. The average of the two data points is then taken. This was applied to the free-standing ACC unit for both fans. Power consumption and bending moments were taken at the operating point and the volumetric flow rate was used to determine these parameters using the characteristic curves. Negligible differences were measured indicating the fan operates according to the ideal characteristic curves.

The method was extrapolated to the 30 fan ACC bank in layout 1 configuration for the A-fan ACC and B2a-fan ACC. Only two cross-wind speeds along one direction was considered. Prior to the study, the numerically determined power consumption and bending moment of each axial flow fan in the ACC was plotted as a function of the volumetric flow rate, along with the respective characteristic curve obtained for each fan. The aim was to highlight the deviation of ACC fans to the ideal case under cross-wind conditions. Significant deviations were noted for the power consumption case with the resultant bending moment showing slight improvement under cross-wind conditions.

The proposed measurement method was applied to certain individual fans in order to determine the applicability for use in ACCs. The power consumption and bending moment of each fan was used to determine the volumetric flow rate using the idealised curves, and compared to the numerically determined flow rate. Both curves indicated a fair agreement to the numerical results for fans not subject to distorted inlet conditions. Average volumetric flow rates were predicted within 7 %. Fans on the upstream peripheries showed poor correlation to the numerical flow rate. The aforementioned higher deviations of the power consumption curve yielded flow rates predictions up to 60 % off the numerical results. The bending moment curves, however, showed higher accuracy when predicting the flow rate. It was thus stated that in the case where significant differences in power consumption were measured, compared to the ideal case, the bending moment curve should be used. The proposed method also requires validation using on-site measurements.

8.4 Future Work

The models developed in this study open a new area of research possibilities in the modelling of large ACC systems. The following future research could improve on the current modelling methods as well as add additional validation procedures to further enhance the reliability of the model:

On-site ACC data collection: The collection of data from an on-site ACC unit/units with regard to cross-wind performance could be used to validate the ACC model subject to different environmental conditions.

Density variation: The current model was developed using an incompressible solver incapable of predicting density variations. Development of the ACC model in a compressible solver environment capable of predicting density variations would increase validity to on-site measurement data in the presence of heated plume recirculation.

The effect of platform height: The effect of platform height on the performance of an ACC could be investigated. This would provide an insight into the optimal platform height for reduced platform construction costs and maximum performance.

Investigation of wind mitigation methods: The upstream periphery fan performance was identified as the main contributor to decreasing ACC performance with increasing wind speeds warranting a study into appropriate methods to mitigate the wind effects on fan performance. The effects of skirts and wind screens could be investigated.

Modelling of an ACC with more fan units: The 30 fan ACC could be expanded to include more fans for an investigation on the optimal number of fans for a specific application.

Effect of power station buildings: Louw (2011) performed a numerical investigation on the effect of power station building proximity on ACC performance. The ACC used by Louw (2011) used many simplifications, however, the results showed definite variations in ACC performance. The three-dimensional ACC of this study will provide more accurate performance predictions with regard to the effect of building proximity.

List of References

Bredell, J. (2005). *Numerical Investigation of Fan Performance in a Forced Draft Air-Cooled Steam Condenser*. Master's thesis, University of Stellenbosch.

Bredell, J., Kröger, D. and Thiart, G. (2006). Numerical investigation into aerodynamic blade loading in large axial flow fans operating under distorted inflow conditions. *R&D Journal of the South African Institution of Mechanical Engineering*, vol. 22, no. 2, p. 1.

Bruneau, P. (1994). *The Design of a Single Rotor Axial Flow Fan for a Cooling Tower Application*. Master's thesis, University of Stellenbosch.

Celik, I., Ghia, U., Roache, P. and Freitas, C. (). *Procedure for Estimation and Reporting of Uncertainty Due to Discretization in CFD Applications*. American Society of Mechanical Engineering (ASME), Mechanical and Aerospace Engineering Department West Virginia University, Morgantown WV (USA).

Cengel, Y. and Boles, M. (2011). *Thermodynamics: An Engineering Approach*. McGraw Hill.

du Toit, C. and Kröger, D. (1993). Modelling of the recirculation in mechanical-draught heat exchangers. *R&D Journal*, vol. 9, no. 1, pp. 2–8.

Dunn, D. (2006). *The Numerical Investigation of a Bank of Delta Plenum Air-Cooled Heat Exchangers*. Master's thesis, University of Cape Town.

Duvenhage, K., Vermeulen, J., Meyer, C. and Kröger, D. (1996). Flow distortions at the fan inlet of forced-draught air-cooled heat exchangers. *Applied Thermal Engineering*, vol. 16, no. 8 - 9, pp. 741 – 752. ISSN 1359-4311.
Available at: `http://www.sciencedirect.com/science/article/pii/1359431195000631`

EPRI (2004). Comparison of alternate cooling technologies for u.s. power plants: economic, enviornmental and other trade-offs. EPRI, Palo Alto, CA.

Goldschagg, H., Vogt, F., du Toit, C., Thiart, G. and Kröger, D. (1997). Air-cooled steam condenser performance in the presence of crosswinds. Proceedings: Cooling Tower Technology Conference, Electrical Power Research Institute, Palo Alto, California.

Gur, O. and Rosen, A. (2005). Propeller performance at low advance ratio. *Journal of Aircraft*, vol. 42, no. 2.

Himmelskamp, H. (1945). *Profile investigations on a rotating airscrew.* Ph.D. thesis, Göttingen.

Hoerner, S. (1965). *Fluid-Dynamic Drag.* Published by S.F Hoerner: Brick Town, South Africa, 1965.

Hoerner, S. and Borst, H. (1975). *Fluid-Dynamic Lift.* Published by Mrs L.A. Hoerner: Brick Town, South Africa, 1975.

Joubert, R. (2010). *Influence of geometric and environmental parameters on air-cooled steam condenser performance.* Master's thesis, University of Stellenbosch.

Kays, W., Crawford, M. and Weigand, B. (2005). *Convective Heat and Mass Transfer.* 4th edn. McGraw Hill.

Kröger, D. (1998). *Air-Cooled Heat Exchangers and Cooling Towers.* University of Stellenbosch.

le Roux, F. (2010). *The CFD simulation of an axial flow fan.* Master's thesis, University of Stellenbosch.

Louw, F. (2011). *Performance Trends of a Large Air-Cooled Steam Condenser during Windy Conditions.* Master's thesis, University of Stellenbosch.

Louw, F. (2015). *Investigation of the flow field in the vicinity of an axial flow fan during low flow rates.* Ph.D. thesis, University of Stellenbosch.

Maulbetsch, J. and DiFilippo, M. (2010). Effect of wind on the performance of air-cooled condensers. Tech. Rep., California Energy Commission.

McGhee, R. and Beasley, W. (1979). Low-speed aerodynamic characteristics of a 13-percent-thick medium-speed airfoil design for general aviation applications. *NASA Technical Paper 1498.*

Meyer, C. (1996). *Plenum Losses in Forced Draught Air-Cooled Heat Exchangers.* Master's thesis, University of Stellenbosch.

Meyer, C. (2000). *A Numerical Investigation of the Plenum Chamber Aerodynamic Behaviour of Mechanical Draught Air-Cooled Heat Exchangers.* Ph.D. thesis, University of Stellenbosch.

Meyer, C. (2005). Numerical investigation of the effect of inlet flow distortions on forced draught air-cooled heat exchanger performance. *Applied Thermal Engineering*, vol. 25, no. 11-12, pp. 1634 – 1649. ISSN 1359-4311.
Available at: `http://www.sciencedirect.com/science/article/pii/S1359431104003345`

Meyer, C. and Kröger, D. (1998). Plenum chamber flow loss in forced draught air-cooled heat exchangers. *Applied Thermal Engineering*, vol. 18, no. 9-10, pp. 875–893.

Meyer, C. and Kröger, D. (2001). Numerical simulation of the flow field in the vicinity of an axial flow fan. *International Journal for Numerical Methods in Fluids*, vol. 36, pp. 947–969.

Mills, A. (1999). *Heat Transfer*. 2nd edn. Prentice Hall.

Mohandes, M., Jones, T. and Russel, C. (1984). Pressure loss mechanisms in resistances inclined to an air flow with application to fin tubes. In: *First National Heat Transfer Conference, Leeds*.

Monroe, R. (1979). Improving cooling tower fan system efficiencies. *Combustion*, vol. 50, no. 11, pp. 20 – 21.

Moore, J., Grimes, R., Walsh, E. and O'Donovan, A. (2014). Modelling the thermodynamic performance of a concentrated solar power plant with a novel modular air-cooled condenser. *Energy*, vol. 69, pp. 378 – 391. ISSN 0360-5442. Available at: `http://www.sciencedirect.com/science/article/pii/S0360544214002904`

Muiyser, J., Els, D., van der Spuy, S. and Zapke, A. (2013). Measurement of air flow and blade loading at a large-scale cooling system fan. *R&D Journal of the South African Institution of Mehanical Engineering*, , no. 30, pp. 30–38.

OpenFOAM (2014). *OpenFOAM: The Open Source CFD Toolbox*. OpenFOAM Foundation, 2nd edn.

Owen, M. (2010). *A numerical investigation of air-cooled steam condenser performance under windy conditions*. Master's thesis, University of Stellenbosch.

Salta, C. and Kröger, D. (1995). Effect of inlet flow distortions on fan performance in forced draught air-cooled heat exchangers. *Heat Recovery Systems and {CHP}*, vol. 15, no. 6, pp. 555 – 561. ISSN 0890-4332. Available at: `http://www.sciencedirect.com/science/article/pii/0890433295900659`

Shih, T., Liou, W., Shabbir, A., Yang, Z. and Zhu, J. (1994). A new k-e eddy viscosity model for high reynolds number turbulent flows - model development and validation. *Institute for Computational Mechanics in Propulsion and Center for Modelling of Turbulence and Transition.*

Simmons, L. (1945). Measurements of the aerodynamic forces acting on porous screens. *R & M*, , no. 2276.

Stinnes, W. and von Backström, T. (2002). Effect of cross-flow on the performance of air-cooled heat exchanger fans. *Applied Thermal Engineering*, vol. 22, no. 12, pp. 1403 – 1415. ISSN 1359-4311.

Available at: http://www.sciencedirect.com/science/article/pii/S1359431102000601

Thiart, G. and von Backström, T. (1993). Numerical simulation of the flow field near an axial flow fan operating under distorted inflow conditions. *Journal of Wind Engineering and Industrial Aerodynamics*, vol. 45, no. 2, pp. 189 – 214. ISSN 0167-6105.
Available at: http://www.sciencedirect.com/science/article/pii/016761059390270X

van Aarde, D. (1990). *Vloeiverliese deur 'n A-raam vinbuisbundel in 'n lugverkoelde kondensator*. Master's thesis, University of Stellenbosch.

van Aarde, D. and Kröger, D. (1993). Flow losses through an array of a-frame heat exchangers. *Heat Transfer Engineering*, vol. 14, no. 1, pp. 43–51.

van der Spuy, S. (2011). *Perimeter Fan Performance in Forced Draught Air-cooled Steam Condensers*. Ph.D. thesis, University of Stellenbosch.

van der Spuy, S., von Backström, T. and Kröger, D. (2009). An evaluation of simplified methods to model the performance of axial flow fan arrays. *R&D Journal of the South African Institution of Mechanical Engineering*, vol. 26, pp. 12–20.

van Rooyen, J. (2007). *Performance Trends of an Air-Cooled Steam Condenser under Windy Conditions*. Master's thesis, University of Stellenbosch.

van Staden, M. (2000). *An Integrated Approach to Transient Simulation of Large Air Cooled Condenser using Computational Fluid Dynamics*. Ph.D. thesis, Rand Afrikaans Universiteit.

van Wylen, G. and Sonntag, R. (1985). *Fundamentals of classical Thermodynamics*. 3rd edn. John Wiley and Sons.

Venter, S. (1990). *The Effectiveness of Axial Flow Fans in A-frame Plenums*. Ph.D. thesis, University of Stellenbosch.

Wilcox, D.C. (1998). *Turbulence Modelling for CFD*. S edn. Anaheim: DCW Industries and Society.

Wilkinson, M., Louw, F., van der Spuy, S. and von Backström, T. (2016). A comparison of actuator disc models for axial flow fans in large air-cooled heat exchangers. In: *Proceedings of ASME Turbo Expo 2016: Turbomachinery Technical Conference and Exposition*.

Appendices

Appendix A

Fan Description

Two fans were used in the analysis of this study, namely a commercially available fan designated as the A-fan and the B2a-fan designed and tested Stellenbosch University. This chapter serves to describe the axial flow fans in terms of the physical and performance characteristics. Figure A.1 indicates the general dimensions of each fan.

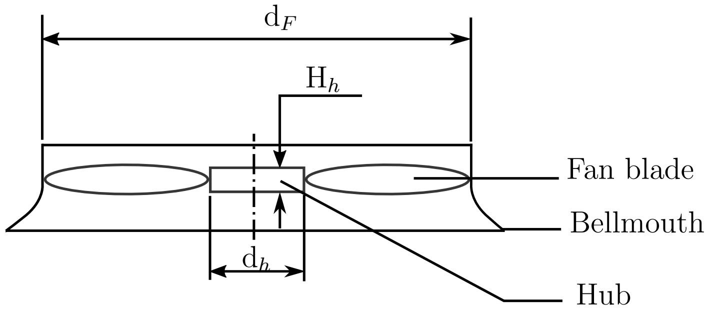

Figure A.1: Fan schematic

Fan diameter	$d_F = 9.145$ m
A-fan hub size	$d_h = 1.399$ m
B2a-fan hub size	$d_h = 3.658$ m
A-fan hub height	$H_h = 0.1829$ m
B2a-fan hub height	$H_h = 0.9145$ m
No. of blades	$n_b = 8$
Rotational speed	$N = 125$ rpm

A comparative schematic of the two fans is shown in figure A.2. Performance characteristics of both fans were determined at Stellenbosch University using a British Standard BS848 Type-A fan test facility. The experimental results were received by personal communication.

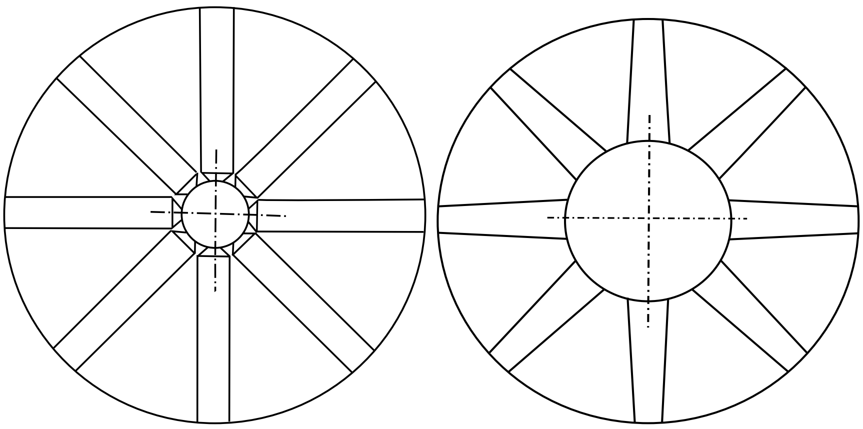

Figure A.2: Top view schematic of the a) A-fan and b) B2a-fan

A.1 A-fan

The A-fan is a small-scale model based on an existing fan used for industrial cooling applications. The fan was manufactured by a third-party and the airfoil profile designation is unknown. Bredell (2005) used an existing large-scale blade obtained from the manufacturer and determined the airfoil profile as depicted by figure A.3. The stagger angle distribution and chord length were obtained by Venter (1990) using the V-fan and is depicted by figure A.4. The A-fan and V-fan share the same physical characteristics.

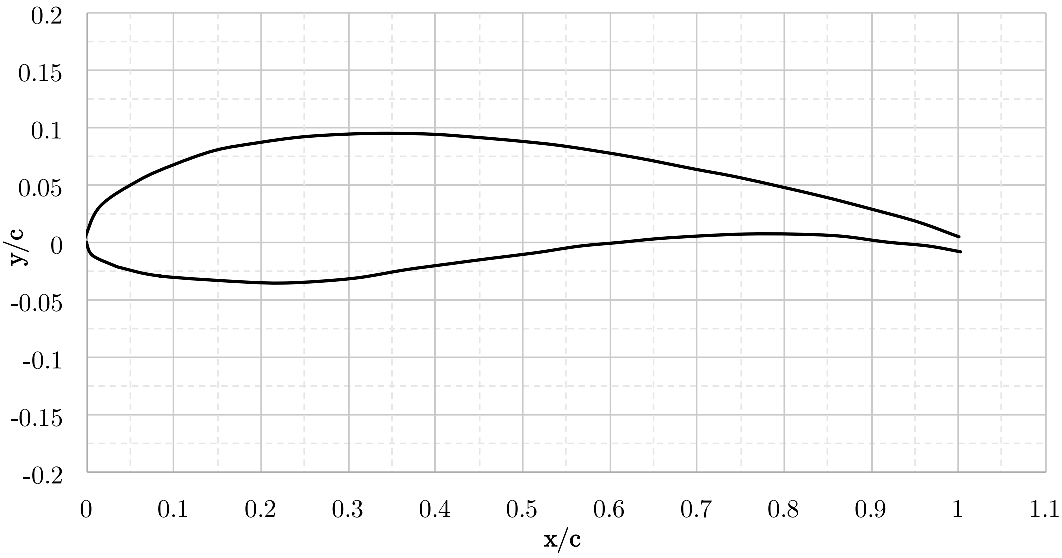

Figure A.3: Airfoil profile used by the A-fan (Bredell, 2005)

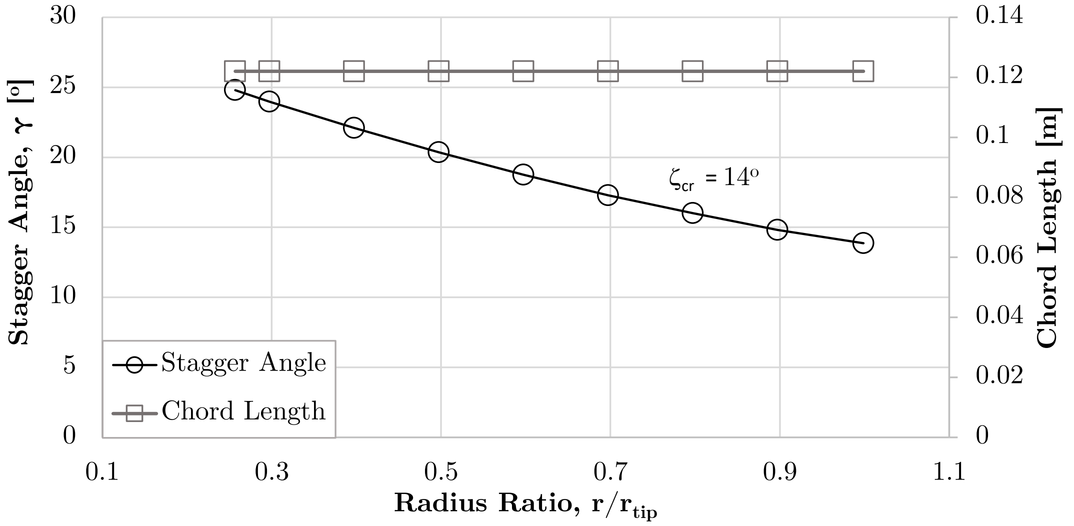

Figure A.4: Stagger angle and chord length of small-scale A-fan (Venter, 1990)

The fan was tested with a flat plate hub, a tip clearance of 3 mm and a blade setting angle of 14^o in the BS848 fan test facility. The performance characteristics obtained are shown in figures A.5 to A.7 for the fan static pressure, fan power consumption and fan static-static efficiency as a function of volumetric flow rate.

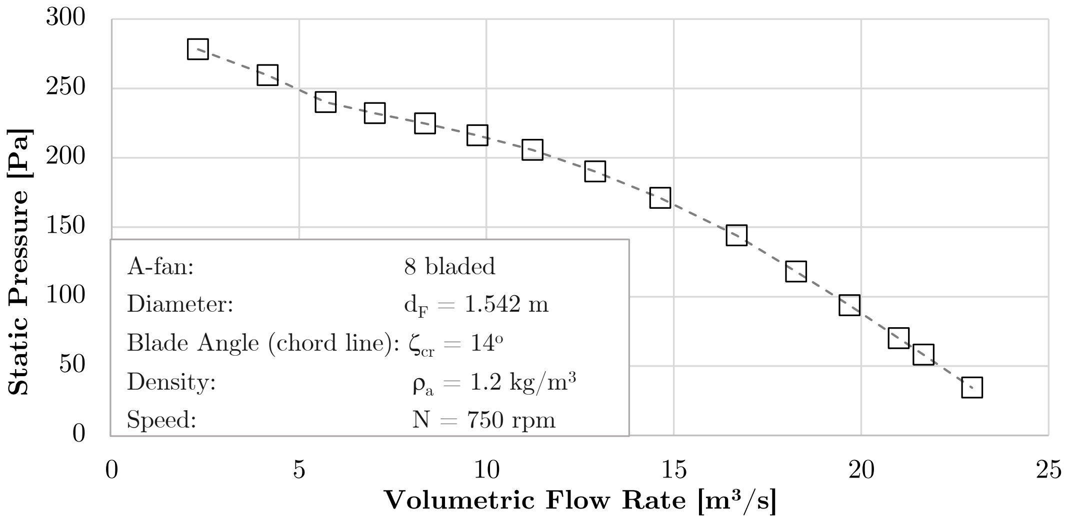

Figure A.5: A-fan static pressure vs. volumetric flow rate

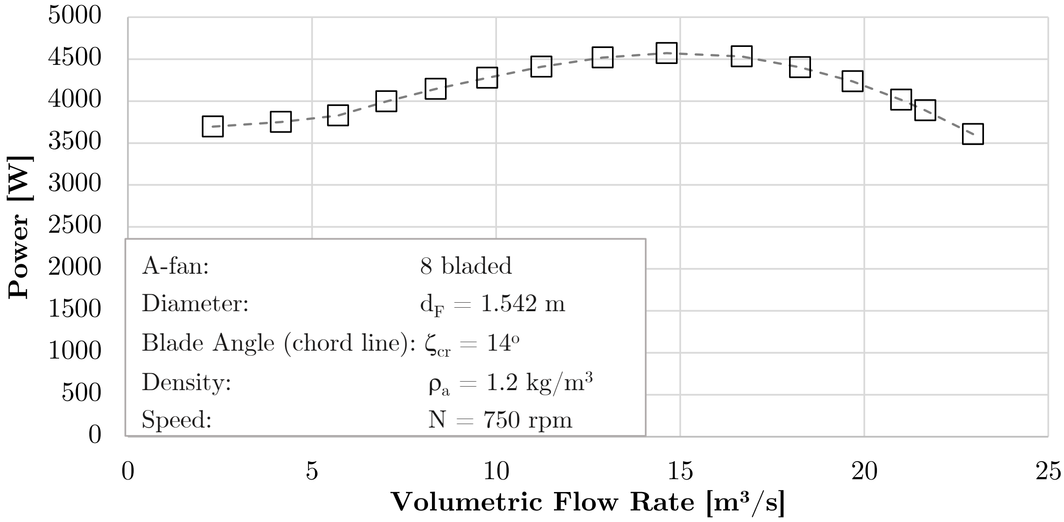

Figure A.6: A-fan power consumption vs. volumetric flow rate

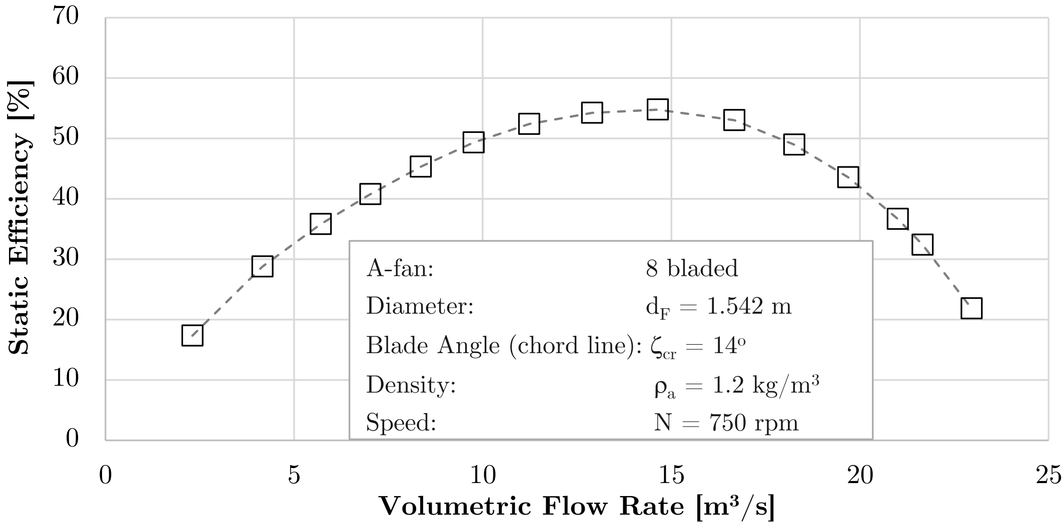

Figure A.7: A-fan static efficiency vs. volumetric flow rate

A.2 B2a-fan

The B2-fan was originally designed at Stellenbosch University for use in large-scale ACC applications by Bruneau (1994). Design specifications of the small-scale fan were stipulated as a fan static pressure rise of 210 Pa at a volumetric flow rate of 16 m^3/s. The B2-fan was vigorously tested over the period of a decade which lead to weathering of the mechanical components. A discrepancy in the hub size constructed for the B2-fan and that specified by Bruneau (1994) was also discovered. Louw (2015) reconstructed the fan with identical physical characteristics as that of the B2-fan and designated it as the B2a-fan.

The B2a-fan utilises the NASA-LS airfoil profile as shown in figure A.8 with a linearly decreasing chord length moving from the root to the tip of the blade. The thickness of the blade also decreases from 13 % at the root to 9 % at the tip. The stagger angle and chord length distribution are shown in figure A.9.

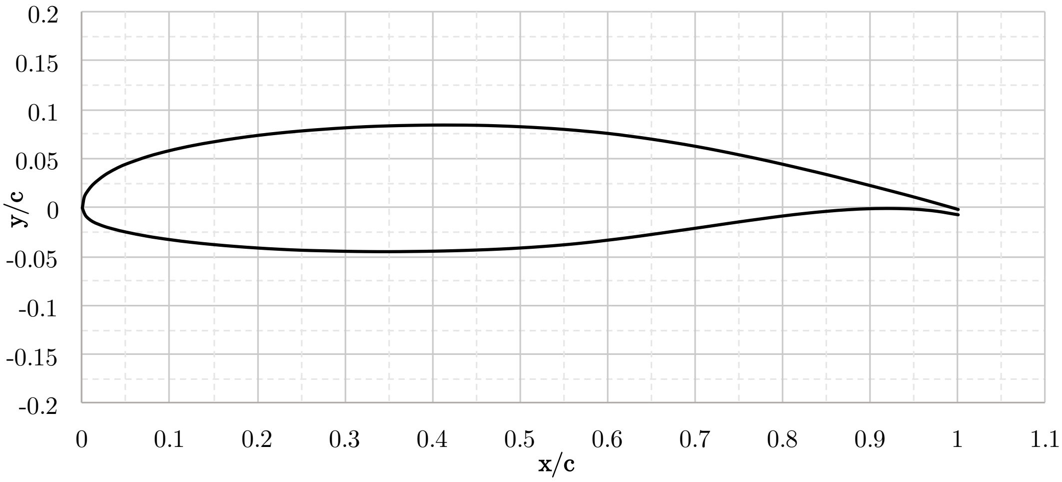

Figure A.8: NASA-LS 0413 airfoil profile as used on the B2a-fan

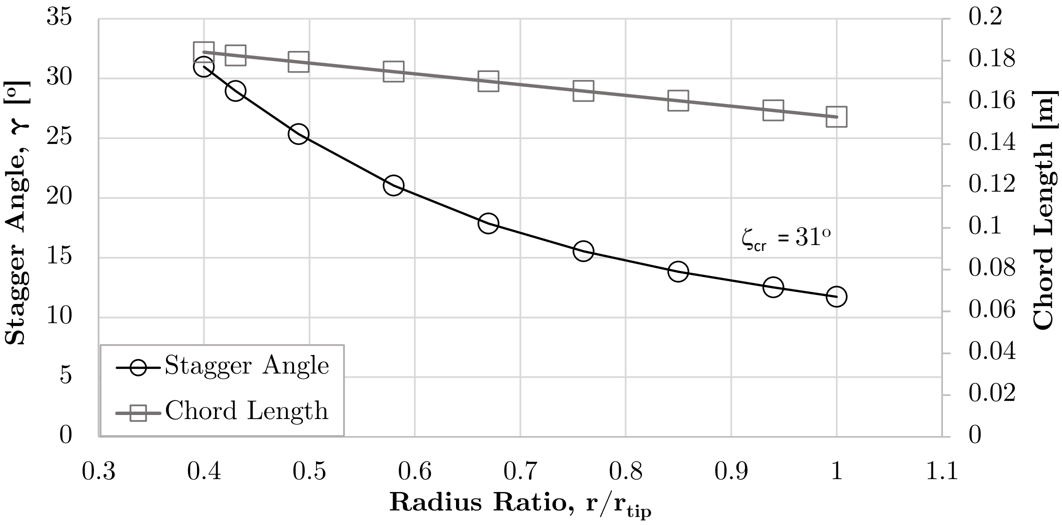

Figure A.9: Stagger angle and chord length of small-scale B2a-fan

The fan was tested in the BS848 test facility using a flat plate hub, a tip clearance of 3 mm and a blade setting angle of 31^o. The performance characteristics are presented in figure A.11 and A.12.

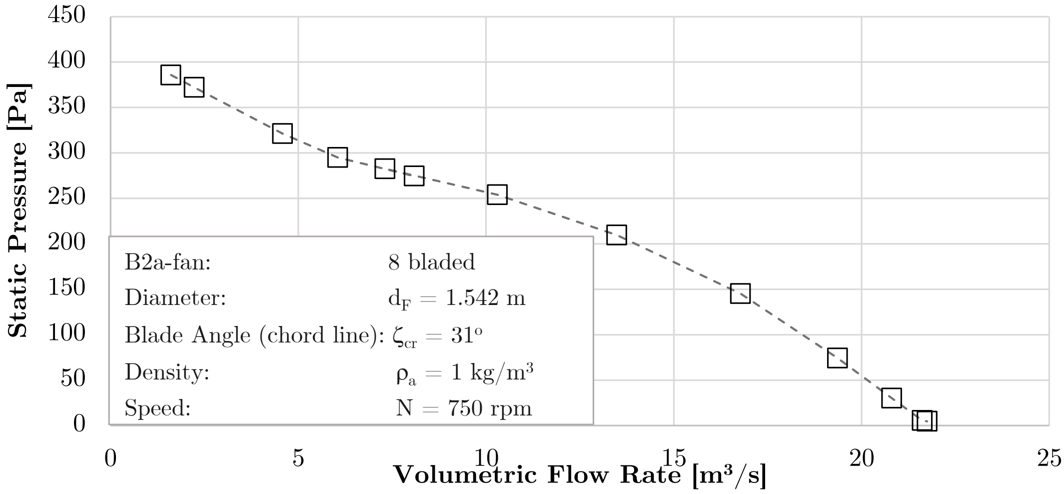

Figure A.10: B2a-fan static pressure vs. volumetric flow rate

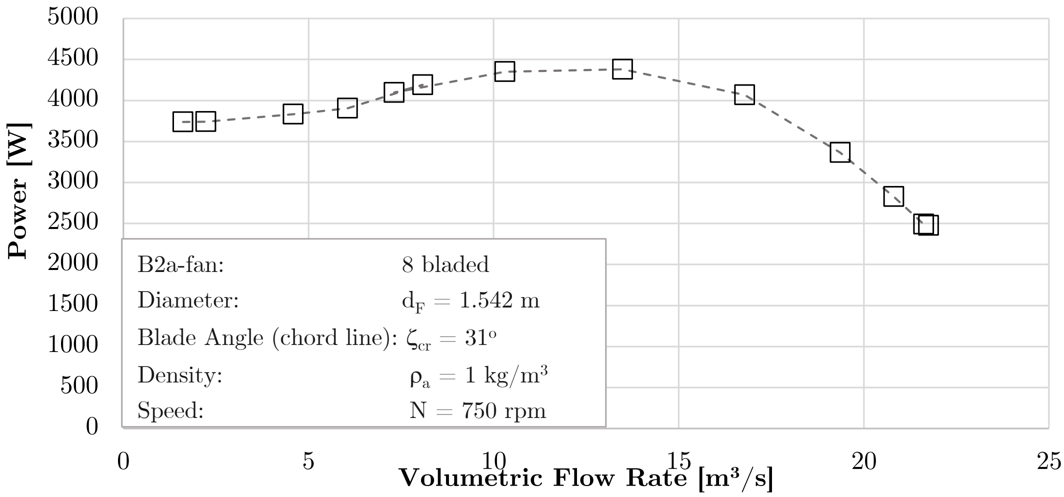

Figure A.11: B2a-fan power vs. volumetric flow rate

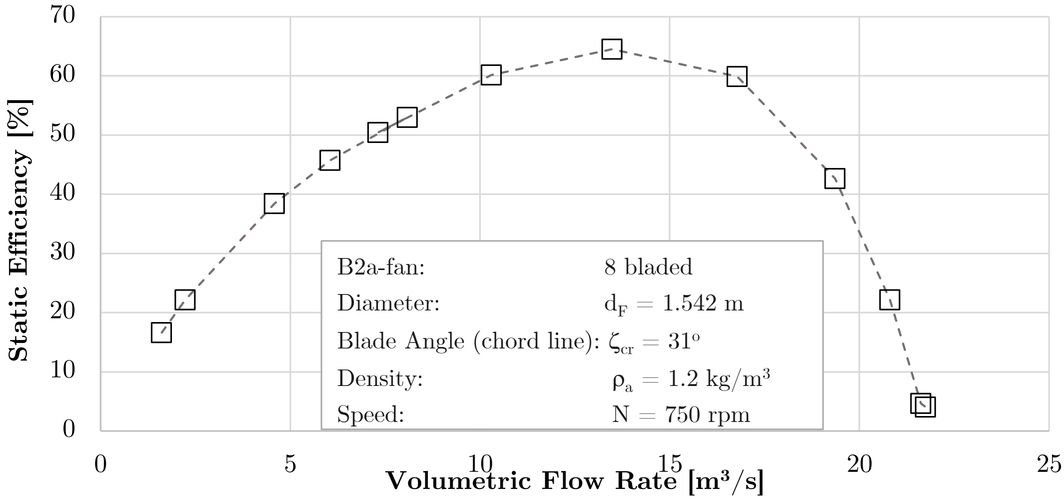

Figure A.12: B2a-fan static efficiency vs. volumetric flow rate

Appendix B

Heat Exchanger Numerical Model

The numerical model used to represent the heat exchanger is defined in this section. The three main characteristic which the model focused on is the pressure drop as air flows through the heat exchanger, flow conditioning as the air flows through the fins and heat transfer from the steam to the cooling fluid. All three aspects are discussed below.

B.1 Pressure Drop

The flow moving through the heat exchanger experiences a pressure drop associated with flow losses as detailed in chapter 3. The pressure loss coefficient K_{he} is a flow dependent pressure loss parameter and is expressed as an empirical relation obtained through isothermal experimental results according to:

$$K_{he} = aRy^{b} \tag{B.1}$$

The characteristic flow parameter is defined per tube row, i, as:

$$Ry_{(i)} = \frac{m_a}{\mu_a A_{(i)}} = \frac{\rho_a |\vec{u}|}{\mu_a} \tag{B.2}$$

This dependence on the flow properties allows the pressure loss to be added as an implicit source term in the momentum equation. This source term is calculated in OpenFOAM as a function of the velocity:

$$S_p = f(u) \tag{B.3}$$

The pressure drop is expressed as a function of velocity in the form:

$$\Delta p(u) = 1/2K\rho|\vec{u}|^2 \tag{B.4}$$

Finally, the pressure drop is added as a source term in the momentum equation by converting it into a body force:

$$S_p = \frac{(p_{a1} - p_{a7})}{L_{he}} \tag{B.5}$$

B.2 Flow Conditioning

Conditioning of the flow as it passes through the heat exchanger was done using the Darcy-Forcheimmer law of modelling resistances in a porous medium with the equation repeated below:

$$F_j = -\left(C_j \frac{1}{2}\rho|\vec{u}|u_j + \frac{\mu}{\alpha_j}u_j\right) \tag{B.6}$$

Calculation of the resistance coefficients was done using an axis transformation similarly defined by the *axesRotation* class in OpenFOAM and is discussed by considering the Cartesian coordinate system for one side of the heat exchanger in figure B.1.

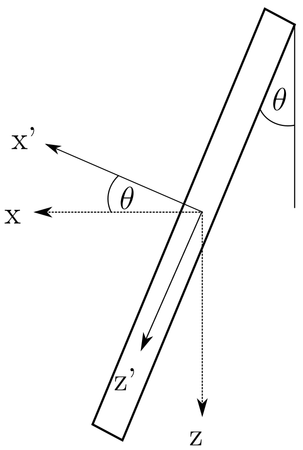

Figure B.1: Left side of heat heat exchanger showing rotating axes

The axes are transformed from the standard Cartesian coordinate system (represented by the dotted line) to the new coordinate system by creating a unit tensor corresponding to the turn direction as:

$$\mathbf{T}_{axis} = \begin{bmatrix} cos(\theta) & 0 & sin(\theta) \\ 0 & 1 & 0 \\ -sin(\theta) & 0 & cos(\theta) \end{bmatrix}$$

Two more tensors are created for each side of the heat exchanger representing the inertial and viscous resistance terms in equation B.6.

The aptly named viscous and inertial resistance tensors for the left side of the heat exchanger (as shown) is defined as:

$$\mathbf{T}_{LeftVisc} = \begin{bmatrix} 0 & 0 & 0 \\ 0 & 1 & 0 \\ 0 & 0 & 1 \end{bmatrix} 1e7$$

$$\mathbf{T}_{LeftIn} = \begin{bmatrix} 0 & 0 & 0 \\ 0 & 1 & 0 \\ 0 & 0 & 1 \end{bmatrix} 10$$

The terms multiplied into the resistance tensors are used to introduce large porosity source terms into the tensor corresponding to the z' direction ensuring low porosity in the required flow direction.

The resistance tensors are first transformed to the local coordinate system of the heat exchanger as:

$$\mathbf{T'}_{LeftVisc/In} = \mathbf{T}_{axis} \times \mathbf{T}_{LeftVisc/In}$$

followed by transforming the new local resistance tensor back to the global coordinate system using the transpose of the axis tensor:

$$\mathbf{T''}_{LeftVisc/In} = \mathbf{T^T}_{axis} \times \mathbf{T'}_{LeftVisc/In}$$

Substituting the resistance tensors into the resistance coefficients corresponding to the right or left heat exchanger, j, as:

$$C_j = \mathbf{T}_{Visc,j}$$

and

$$\frac{1}{\alpha_j} = \mathbf{T}_{In,j}$$

The Darcy-Forcheimmer resistance force is now written in terms of the resistance tensors as:

$$F_j = -\left((C_j \times u_j)\frac{1}{2}\rho|\vec{u}| + (1/\alpha_j \times u_j)\mu \right) \tag{B.7}$$

The resistance force is added to the momentum equation and only solved in the heat exchanger region.

B.3 Heat Transfer

This section details the heat transfer model used in the heat exchanger zone. The ϵ-NTU method, as laid out in (Kröger, 1998) is used to calculate the air outlet temperature for each row of tubes followed by the subsequent heat source term. The heat transferred between two mediums for a certain tube row, i, can be expressed in terms of the inlet and outlet temperature as:

$$Q_{(i)} = m_a cp_a (T_{ao(i)} - T_{ai(i)}) = e_{(i)} m_a cp_a (T_s - T_{ai(i)}) \tag{B.8}$$

The third term in equation B.8 is calculated using the effectiveness of the tube row and the steam inlet temperature. The effectiveness is calculated using the overall heat transfer coefficient according to:

$$e_{(i)} = 1 - exp\left(\frac{-UA_{(i)}}{m_a cp_a}\right) \tag{B.9}$$

The overall heat transfer coefficient for the finned tube heat exchanger used in the numerical model is a combination of the heat transfer coefficients of air and steam and is given per row, i, as:

$$UA_{(i)} = (1/h_{ae}A_{a(i)} + 1/h_c A_{c(i)})^{-1} \tag{B.10}$$

where the air side heat transfer coefficient is calculated as:

$$h_{ae}A_{a(i)} = k_a A_{(i)} Ny_{(i)} P_r^{0.333} \tag{B.11}$$

The area of the tubes exposed to the air flowing through the heat exchanger is calculated as a function of the number of bundles and the number of tubes per bundle. For the finned tube heat exchanger in this study, the exposed area of the first row is calculated as:

$$A_{(1)} = \frac{n_{tb(1)}}{n_{tb(2)}} n_b A_{fr} \tag{B.12}$$

The characteristic heat transfer parameter is a value defined in (Kröger, 1998) per heat exchanger based on the characteristic flow parameter obtained through experimental results. For the first row of tubes the heat transfer coefficient of the steam is deemed negligible (Bredell, 2005; Louw, 2011) and thus the overall heat transfer coefficient is given as $UA_1 \approx h_{ae}A_{a(1)}$. For the second row the steam heat transfer coefficient is used as 16500 J/K. Rearranging equation B.8 the outlet air temperature for row i can be calculated as:

$$T_{ao(i)} = e_{(i)} T_s + (1 - e_{(i)}) T_{ao(i-1)} \tag{B.13}$$

and for the first row

$$T_{ao(1)} = e_{(1)} T_s + (1 - e_{(1)}) T_{ai(1)} \tag{B.14}$$

The heat transfer of the subsequent tube rows can be calculated by noting that the temperature of the air leaving the previous row, $(i-1)$, is equal to the temperature of the air entering the next row, i. The total heat transfer rate can now be calculated as a summation of the heat transferred between the steam and the air for each row as:

$$\sum_{i=1}^{n_r} Q_{a(i)} = Q_{tot} = m_a cp_a (T_{ao(i)} - T_{ai(1)}) \tag{B.15}$$

The heat source term added to the energy equation can now be calculated and is defined as:

$$S_e = \frac{\delta Q}{\delta V} \tag{B.16}$$

Substitution of equation B.15 into B.16 yields the relation used to calculate the energy source term used in the numerical model:

$$S_e = \frac{\delta m_a}{\delta V} cp_a (T_{ao(i)} - T_{ai(1)}) \tag{B.17}$$

Appendix C

System Specifications

The atmospheric design conditions of the ACC analysed in this study was set-up in a near identical manner to the studies of Bredell (2005), van Rooyen (2007), Joubert (2010), Owen (2010) and Louw (2011). The air properties at which the ACC was analysed is listed along with the dimensions of the ACC. The loss coefficients are also evaluated.

C.1 Specifications for the ACC

C.1.1 Atmospheric Design Conditions

The air properties listed below was used as the thermal properties in OpenFOAM in the analysis of the ACC. This was taken as the design conditions at which the ideal volumetric flow rate was calculated.

Air temperature at ground level (dry-bulb):	$T_a = 15.6\ ^o$ C
Barometric pressure:	$p_a = 90\ 000$ N/m^2
Turbine steam temperature:	$T_s = 60\ ^o$ C

The correlations presented in Kröger (1998) were used to calculate the relevant air properties at the above-mentioned design conditions.

Density:	$\rho_a = 1$ kg/m^3
Thermal conductivity:	$k_a = 0.02535$ W/m.K
Specific heat:	$c_{pa} = 1006.609$ J/kg.K
Molecular viscosity:	$\mu_a = 1.7948e^{-5}$ kg/m.s
Prandtl number:	$Pr = 0.713$

C.1.2 ACC Platform Dimensions

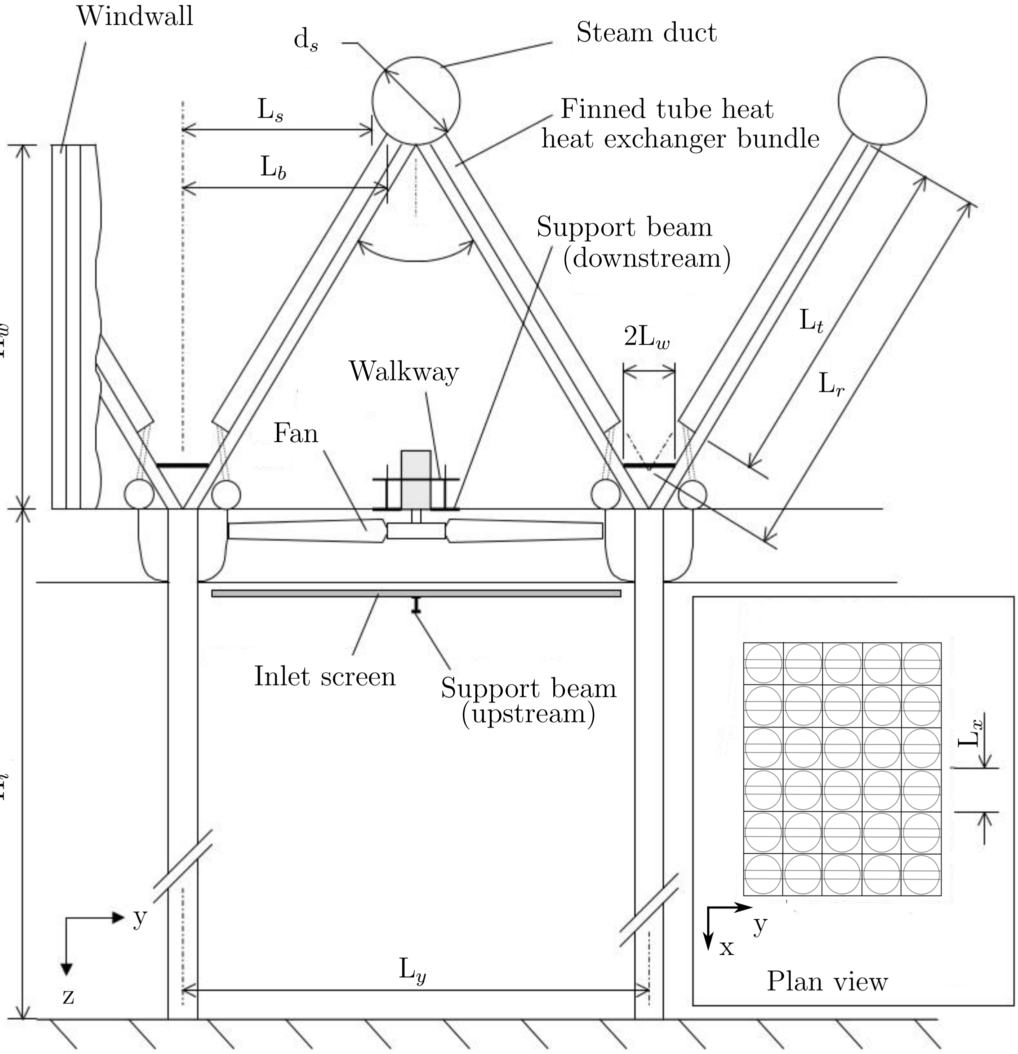

Figure C.1: Schematic of ACC Cell (adapted from Bredell (2005))

The dimensions of the ACC cell shown in figure C.1 are given below:

Average steam supply header duct diameter:	$d_s = 2.34$ m
Width of walkway:	$2L_w = 0$ m
Windwall height:	$H_w = 10$ m
Height above ground level:	$H_i = 20$ m
A-frame apex angle:	$2\theta = 56\ ^o$
Figure C.1 dimension:	$L_b = 5.28$ m
Figure C.1 dimension:	$L_r = 11.238$ m

Figure C.1 dimension:	$L_s = 4.11$ m
Figure C.1 dimension:	$L_t = 9$ m
Figure C.1 dimension:	$L_x = 11.8$ m
Figure C.1 dimension:	$L_y = 10.56$ m

C.1.3 Finned Tube Bundle Specifications

The same fin bundle heat exchanger used by Bredell (2005), van Rooyen (2007), Joubert (2010), Owen (2010) and Louw (2011) was used in this study. The specifications of the elliptical, double row, finned tube bundle is provided below:

Number of bundles serviced by one fan:	$n_b = 8$
Number of tube rows per bundle:	$n_r = 2$
Number of tubes in first row (1):	$n_{tb(1)} = 57$
Number of tubes in second row (2):	$n_{tb(2)} = 58$
Effective finned tube length:	$L_t = 9.55$ m
Frontal area of single tube:	$A_{fr} = 27.434$ m^2
Ratio of minimum to free stream flow area:	$\sigma = 0.41$
Ratio of minimum to free stream flow area at inlet:	$\sigma_{21} = 0.86$

The finned tube heat exchanger flow and heat transfer characteristics were determined empirically. The heat transfer parameter for each tube row is provided below as a function of the characteristic flow parameter as:

$$Ny_{(1)} = 583.8307 Ry^{0.4031} \tag{C.1}$$

and:

$$Ny_{(2)} = 1277.72 Ry^{0.3806} \tag{C.2}$$

The loss coefficient for the finned tube bundle was also determined empirically and is provided below as a function of the characteristic flow parameter:

$$K_{he} = 4464.831 Ry^{-0.439275} \tag{C.3}$$

The heat transfer parameter is defined by Kröger (1998) and provided below:

$$Ny = \frac{hA}{k_a A_{fr} Pr^{0.333}} \tag{C.4}$$

and the characteristic flow parameter as:

$$Ry = \frac{m_a}{\mu_a A_{fr}} \tag{C.5}$$

C.2 Forced-Draft ACC Draft Equation

According to Kröger (1998), the draft equation for a forced-draft ACC can be derived by equating the pressure differential between the inside and outside of the heat exchanger bundle at the mean heat exchanger elevation, to the sum of the resistances as the flow passes through the ACC. This can be defined by:

$$\Delta p_a = \Sigma flow\, resistances \tag{C.6}$$

Consider the forced-draft ACC illustrated in figure C.2. The variation in pressure due to elevation in the atmosphere is derived using the dry adiabatic lapse rate (DALR). Assuming a clear dry day, the temperature gradient is approximately -0.00975 K/m. The temperature at height of H_6, outside of the heat exchanger, is determined by the DALR as:

$$T_{a6} = T_{a1} - 0.00975 H_6 \tag{C.7}$$

and the atmospheric pressure at the same point:

$$p_{a6} = p_{a1}(1 - 0.00975 H_6 / T_{a1})^{3.5} \tag{C.8}$$

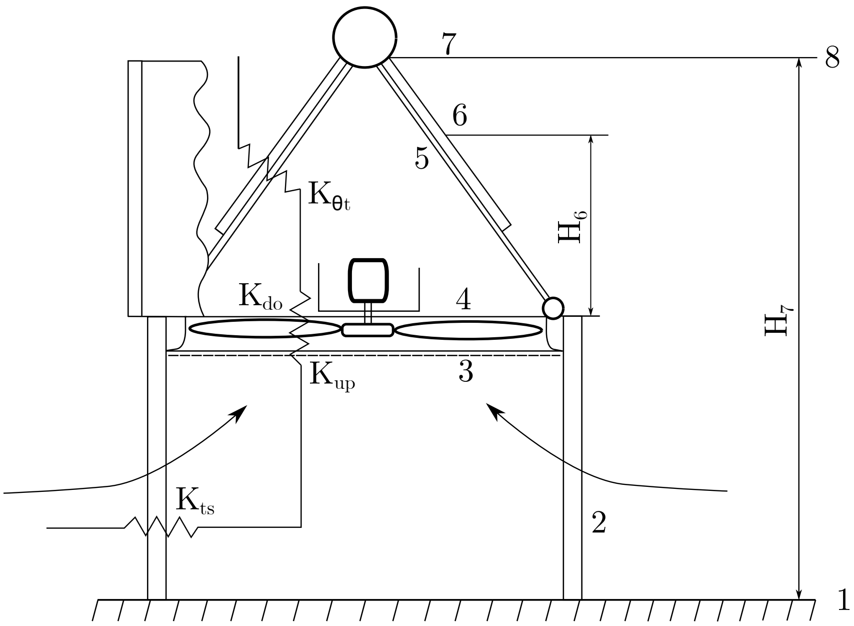

Figure C.2: Forced-draft ACC schematic (adapted from Kröger (1998))

Applying the DALR to determine the pressure differential between $H_8 = H_7$ and the mean heat exchanger elevation, H_6, derives the left hand side of equation C.6 for a forced-draft ACC:

$$p_{a1}\left[\{1 - 0.00975(H_7 - H_6)/T_{a6}\}^{3.5} - \{1 - 0.00975(H_7 - H_6)/T_{a1}\}^{3.5}\right] \quad \text{(C.9)}$$

The flow resistances are evaluated by considering the flow path through the ACC. As indicated by figure C.2, the flow experiences a mechanical energy loss due to the presence of the support struts quantified by the loss coefficient K_{ts}. The loss coefficients K_{up} and K_{do} account for the obstacles upstream and downstream of the fan respectively. These include the fan inlet screen, fan motor, gearbox, walkway screen and support beams. Finally, the losses resulting from the heat exchanger is accounted for by the coefficient $K_{\theta t}$, of which a full derivation is discussed in chapter 3.

The mechanical losses are evaluated as a function of the mass flow rate in the form:

$$\Delta p = K\frac{1}{2\rho}\left(\frac{m_a}{A}\right)^2 \quad \text{(C.10)}$$

The loss coefficients are derived based on different flow areas of the obstacles in the ACC. The coefficients K_{ts} and $K_{\theta t}$ are derived based on the frontal area of the heat exchanger, A_{fr}, whereas K_{up} and K_{do} are based on the effective fan area, A_e.

The flow properties are evaluated at the respective positions in the ACC (denoted by the numbers in figure C.2). The draft equation for a forced-draft ACC can now be derived as:

$$p_{a1}\left[\{1 - 0.00975(H_7 - H_6)/T_{a6}\}^{3.5} - \{1 - 0.00975(H_7 - H_6)/T_{a1}\}^{3.5}\right]$$

$$= K_{ts}\frac{1}{2\rho_{a1}}\left(\frac{m_a}{n_b A_{fr}}\right)^2 + K_{up}\frac{1}{2\rho_{a3}}\left(\frac{m_a}{A_e}\right)^2 + K_{do}\frac{1}{2\rho_{a3}}\left(\frac{m_a}{A_e}\right)^2 +$$

$$K_{\theta t}\frac{1}{2\rho_{a56}}\left(\frac{m_a}{n_b A_{fr}}\right)^2 - \Delta P_{Fs} \quad \text{(C.11)}$$

where ΔP_{Fs} accounts for the static pressure rise of the axial flow fan. The right hand side is typically used to determine the system resistance curve, as depicted in chapter 4. The derived draft equation does not account for flow phenomena present when the ACC is subjected to cross-winds (Kröger, 1998). These include flow separation at the fan inlet, recirculation of the heated air and reverse flow in the fans on the periphery in the upstream wind direction.

C.3 ACC Mechanical Losses

The mechanical losses experienced by the flow as it passes through the ACC obstacles is evaluated below. The loss coefficient used to represent the heat exchanger losses is evaluated with regard to variable fluid properties in appendix B.

C.3.1 ACC Loss Coefficients

The losses associated with the flow passing through the heat exchanger are derived in chapter 3 and presented as a bulk value. The losses are repeated below for convenience:

$$K_{\theta t} = K_{he} + K_{dj} + K_o + \left(\frac{1}{sin\theta_m} - 1\right)\left[\left(\frac{1}{sin\theta_m} - 1\right) + 2K_{ci}^{0.5}\right] \tag{C.12}$$

where K_{dj} and K_o are defined as the jetting and outlet loss coefficient. The last term in equation C.12 represents the loss associated with the flow turning through the heat exchanger. The parameter θ_m is a parameter calculated using an empirical relation given by Kröger (1998) as:

$$\theta_m = 0.0019\theta^2 + 0.9133\theta - 3.1558 \tag{C.13}$$

The contraction loss coefficient, K_{ci}, represents the pressure loss as the flow moves through the contracted area of the heat exchanger bundle and is defined as:

$$K_{ci} = \left[\left(1 - \frac{1}{\sigma_c}\right)/\sigma\right]^2 \tag{C.14}$$

Kröger (1998) defines the coefficient σ as the: 'ratio of the flow area between the fins at their upstream periphery to the corresponding area immediately upstream of the fins' and also provides the relation for calculating the parameter σ_c for flat plate fins as:

$$\begin{aligned}\sigma_c = {} & 0.6155417 + 0.04566493\sigma - 0.336651\sigma^2 + 0.4082743\sigma^3 + 2.672041\sigma^4 \\ & -5.963169\sigma^5 + 3.558944\sigma^6\end{aligned} \tag{C.15}$$

The jetting loss coefficient is defined as:

$$K_{dj} = \Bigg[\Bigg\{-2.89188\left(\frac{L_w}{L_t}\right) + 2.93291\left(\frac{L_w}{L_t}\right)^2\Bigg\}\left(\frac{L_t}{L_s}\right)\left(\frac{L_b}{L_s}\right)\left(\frac{28}{\theta}\right)^{0.4}$$
$$\Bigg\{exp(2.36987 + 5.8601e^{-2}\theta - 3.3797e^{-3}\theta^2)\left(\frac{L_s}{L_b}\right)\Bigg\}^{0.5}$$
$$\left(\frac{L_t}{L_b}\right)\Bigg]^2 \tag{C.16}$$

and the outlet loss coefficient:

$$K_o = \Bigg[\Bigg\{-2.89188\left(\frac{L_w}{L_t}\right) + 2.93291\left(\frac{L_w}{L_t}\right)^2\Bigg\}\left(\frac{L_s}{L_t}\right)^3 + 1.9874$$
$$-3.02783\left(\frac{d_s}{2L_t}\right) + 2.0187\left(\frac{d_s}{2L_t}\right)^2\Bigg]\left(\frac{L_b}{L_s}\right)^2 \tag{C.17}$$

C.3.2 Evaluation of Loss Coefficients

The loss coefficients are evaluated and calculated in this section. The coefficients evaluated are the ones which are dependent on the structural properties of the heat exchanger (K_{ts}, K_{up}, K_{do}, K_{dj}, K_o, K_{ci}) and not the loss coefficient dependent on the flow characteristic (K_{he}).

The mean incidence angle as given by equation C.13 is calculated as:

$$\theta_m = 0.0019(28)^2 + 0.9133(28) - 3.1558 = 23.906^o$$

The contraction ratio given by equation C.15 as:

$$\sigma_c = 0.6144517 + 0.04566493(0.86) - 0.336651(0.86)^2 + 0.4082743(0.86)^3 +$$
$$2.672041(0.86)^4 - 5.963169(0.86)^5 + 3.558944(0.86)^6 = 0.7607$$

The contraction coefficients as presented by equation C.17 is evaluated as:

$$K_{ci} = \left[\left(1 - \frac{1}{0.7607}\right)/0.41\right]^2 = 0.589$$

The jetting loss coefficient is evaluated according to equation C.16 as:

$$K_{dj} = \left[\left\{-2.89188\left(\frac{0}{9}\right) + 2.93291\left(\frac{0}{9}\right)^2\right\}\left(\frac{9}{4.102}\right)\left(\frac{4.924}{4.102}\right)\left(\frac{28}{28}\right)^{0.4}\right.$$

$$+\left\{exp(2.36987 + 5.8601e^{-2}(28) - 3.3797e^{-3}(28)^2)\left(\frac{4.102}{4.924}\right)\right\}^{0.5}$$

$$\left.\left(\frac{9}{10.6}\right)\right]^2 = 1.947$$

Finally, the outlet loss coefficient is evaluated according to equation C.17 as:

$$K_o = \left[\left\{-2.89188\left(\frac{0}{9}\right) + 2.93291\left(\frac{0}{9}\right)^2\right\}\left(\frac{4.102}{4.924}\right)^3 + 1.9874\right.$$

$$\left.-3.02783\left(\frac{2.34}{2(4.924)}\right) + 2.0187\left(\frac{2.34}{2(4.924)}\right)^2\right]\left(\frac{9}{4.102}\right)^2 = 6.516$$

The upstream, downstream and support strut loss coefficients are evaluated from Kröger (1998) based on the heat exchanger frontal area. In accordance with the domain set-up of this study whereby only the support struts and fan walkway were modelled, no upstream losses were included and the downstream and support strut losses used are shown below.

$$K_{ts} = 1.60$$

$$K_{up} = 0$$

$$K_{down} = 0.19$$

Appendix D

Development of the Air-Cooled Condenser Model

The ACC model of this study builds on the studies of Bredell (2005), van Rooyen (2007), Joubert (2010), Owen (2010) and Louw (2011). A detailed analysis of the modelling techniques used by these studies is presented in chapter 2 and 3 along with the highlighted shortcomings of the models. The development of the current model required a clarification procedure on the correct approach with regard to ACC modelling. Specific focus was placed on the mechanical losses resulting from obstacles in the vicinity of the fan. The analysis presented below details, and compares, different modelling approaches focusing on a single ACC unit, followed by a 30 fan ACC bank.

D.1 Air-Cooled Condenser Unit Model

Two variants in the methodology for modelling mechanical losses were compared for the single ACC unit. The first method (designated ACCM1) follows previous literature where the mechanical losses, repeated below in the form of the draft equation, were included as momentum sinks in different porous regions. This approach was used to save on computational cost and model complexity.

$$p_{a1} - p_{a7} \approx K_{ts}\frac{1}{2\rho_{a1}}\left(\frac{m_a}{n_b A_{fr}}\right)^2 + K_{up}\frac{1}{2\rho_{a3}}\left(\frac{m_a}{A_e}\right)^2 + K_{do}\frac{1}{2\rho_{a3}}\left(\frac{m_a}{A_e}\right)^2 + K_{\theta t}\frac{1}{2\rho_{a56}}\left(\frac{m_a}{n_b A_{fr}}\right)^2 \tag{D.1}$$

The obstacle losses in the draft equation are calculated using the effective fan area whereas the heat exchanger and support strut losses are calculated using the heat exchanger frontal area in equation C.11. This indicates where modelling of the mechanical losses should occur in the ACC. The fan obstacle losses were modelled in the axial flow fan region and the support strut loss along with the heat exchanger losses were modelled in the heat exchanger porous region. All losses were calculated in the form $\Delta p = 1/2K\rho|\vec{u}|^2$ and included in the porous region as momentum sinks according to equation B.4. The schematic of the geometrical domain is shown in figure 3.8 for this particular modelling approach.

As mentioned in chapter 2, the derived fan obstacle losses were determined using a commercially available fan. It was expected that inaccuracies would arise if these obstacle losses were used with a higher hub-to-tip ratio fan such as the B2a-fan. To determine this, the second ACC modelling methodology (ACCM2) was developed whereby the support struts and fan walkway was modelled as geometrical structures in the domain as detailed in chapter 3. The drawback of this approach is the increased mesh size in order to accurately capture the flow field in the vicinity of the struts. It is expected, however, that this would be offset by an increase in measured performance accuracy.

A measure of the discrepancy when using the obstacle losses in modelling the B2a-fan ACC can be determined by comparing the operating points of ACCM1 to ACCM2. The comparison will, however, only be valid if the same fan obstacles are modelled. ACCM1 was therefore modified by removing all the fan obstacle losses except the support struts and fan walkway loss. None of the fan obstacle losses were modelled in the porous regions in the ACCM2 case. The operating points for ACCM1 and ACCM2 were numerically determined for both the A-fan and B2a-fan.

The determined operating points are shown in table D.1. The results of ACCM1 and ACCM2 correlate well for the A-fan case. This is expected due to the geometrical similarities of the A-fan and the fan used by Venter (1990) to derive the obstacle losses. A significant discrepancy is calculated for the operating points measured for the B2a-fan case. A possible reason for this discrepancy is the aforementioned physical characteristic differences of the B2a-fan to the fan used by Venter (1990).

Table D.1: Table showing numerical and analytical operating points

	Vol. Flow Rate [m^3/s]	**Heat Transfer [W]**	**Power [W]**
A-fan (ACCM1)	601.88	2.17e7	147 934
A-fan (ACCM2)	606.11	2.18e7	147 836
B2a-fan (ACCM1)	595.11	2.13e7	129 774
B2a-fan (ACCM2)	618.34	2.16e7	130 719

D.2 Air-Cooled Condenser Bank Model

The comparative analysis between ACCM1 and ACCM2 was applied to the 30 fan ACC bank. The inclusion of support struts, and subsequent obstruction of the flow path below the platform, would impede the air flow in the presence of cross-winds. The effect on performance required quantification for the comparative analysis to the ACC models of previous studies, detailed in chapter 4. These ACCs did not include support struts in the geometrical domain but rather followed the approach of ACCM1.

ACCM1 and ACCM2 methodologies were compared by subjecting the A-fan ACC and B2a-fan ACC to cross-wind speeds of 0 and 6 m/s in the y-direction only. The measured volumetric flow rates of individual fans in the centre column of the ACC is shown in figure D.1 and D.2 for the A-fan ACC and B2a-fan ACC respectively. The most prominent difference in ACCM1 and ACCM2 performance is the volumetric flow rates measured for the upstream fans when subjected to cross-winds. The reason being that the support struts impede the flow below the ACC platform forming smaller flow separation regions at the upstream fan inlets. Downstream fan performance is observed to be relatively unaffected by the presence of support struts with differences less than 5 % measured. The increased upstream fan performance also leads to increased total volumetric flow rates as shown in figure D.3.

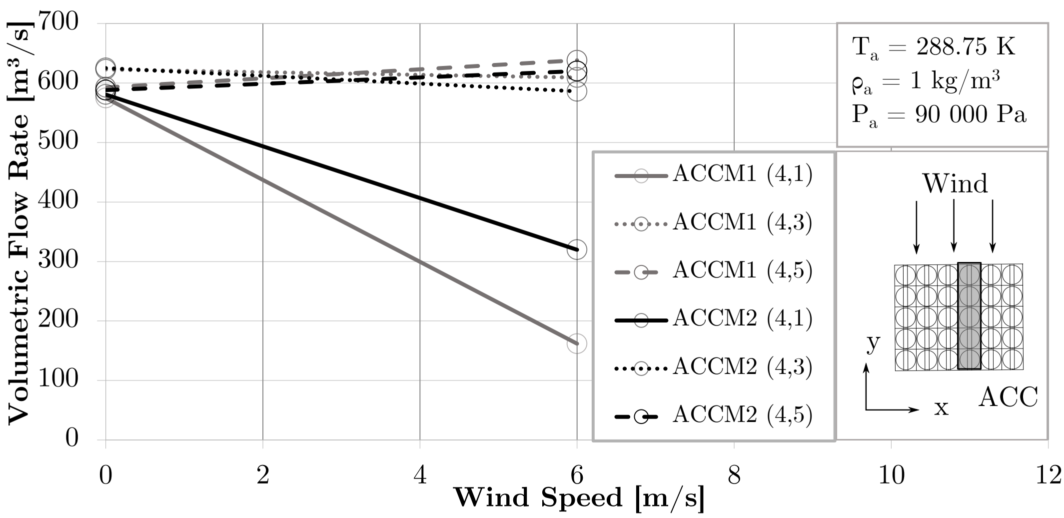

Figure D.1: Fan volumetric flow rate comparison of A-fan ACC

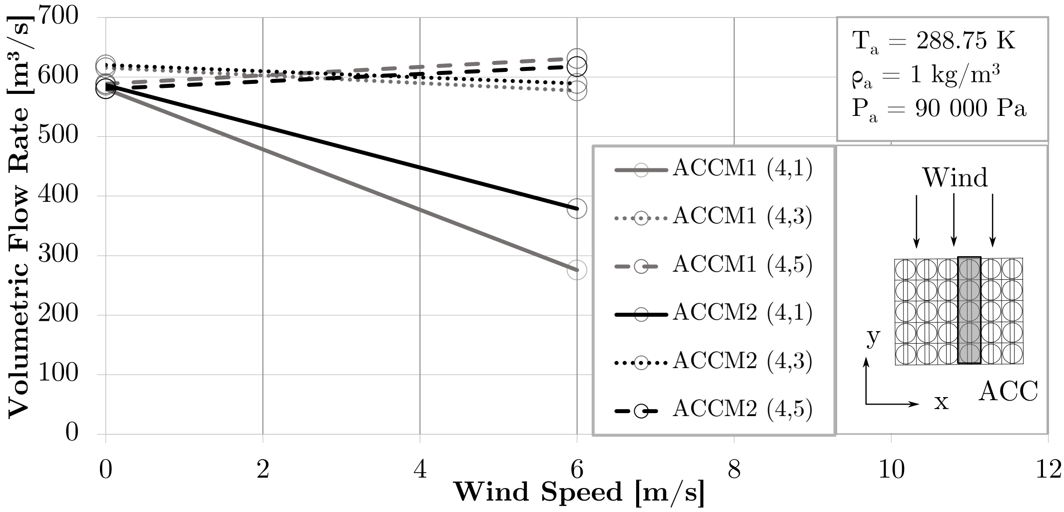

Figure D.2: Fan volumetric flow rate comparison of B2a-fan ACC

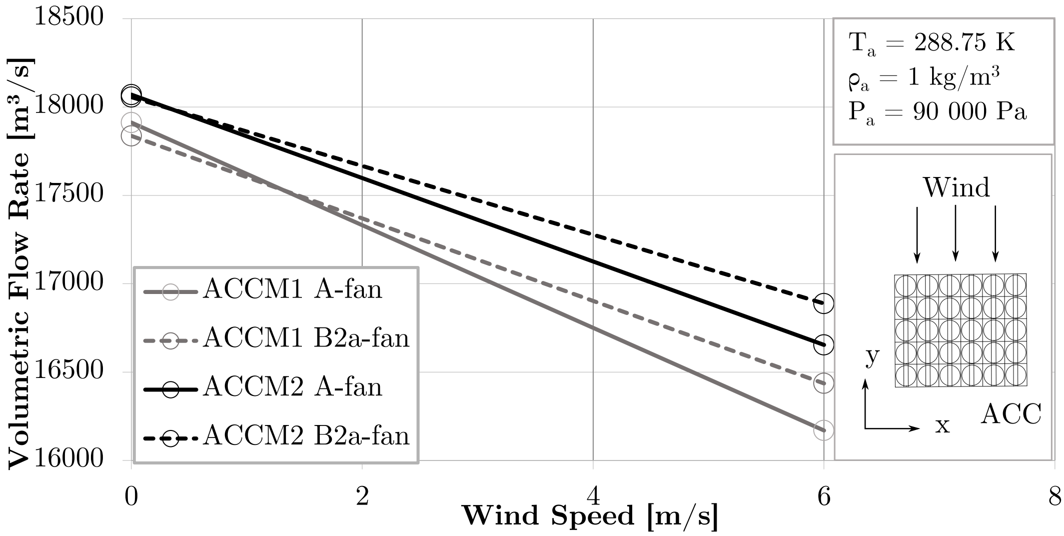

Figure D.3: Total volumetric flow rates of ACCM1 and ACCM2

The inclusion of support struts could lead to significant volumetric, thermal and overall, performance differences for upstream fan performance. In the case where accurate depictions of ACC performance is required, at the expense of additional complexity to the geometrical domain, the inclusion of support struts would be deemed a necessity. If only a performance trend analysis is required to determine ACC performance in the presence of cross-winds, the ACCM1 approach would be recommended.